

Azərbaycan Milli Elmlər Akademiyası  
Fizika-Riyaziyyat və Texnika Elmləri Bölməsi  
Fizika İnstitutu

---

4

# Fizika

Cild

XIV

2008

Bakı ✱ Elm

## A STUDY OF SURFACE MORPHOLOGY OF ZEOLITE (MAZIT) BY ATOMIC FORCE MICROSCOPY

S.D. ALEKPEROV

*G.M. Abdullayev Institute of Physics of National Academy of Sciences,  
AZ-1143, H. Javid ave. 33, Baku, Azerbaijan*

The surface morphology of zeolite (mazit) is investigated by atomic force microscopy under normal conditions. Application of "MD mode" regime has allowed receiving clear, with the high resolution, the image of topography high-abrasive surfaces with a high-developed of a relief. The analysis of surface structure in the "MD mode" regime has shown, that compaction the sample mazit, first, reduces range of the sizes surface crystallites, and, second, leads to formation of the big number of the small grains grouped near to borders of various breaks.

### 1. Introduction

Interest to nanocrystallite ceramic materials (zeolites, ceramics on the basis of various oxides) is connected with an opportunity of their practical application, for example, as high-choused catalysts of chemical reactions, absorbers of gas and etc. [1]. Zeolites (both natural and artificial) possess strongly pronounced ion-exchange and adsorptive properties, and also have rigidly sustained sizes of inputs of pores and channels (which sizes are from 0,3 up to 1,5 nm). All this allows considering them as perspective molecular filters and selective sorbets. From this point of view, the knowledge of properties and structures of the zeolites is one of ways of perfection of technological methods of their reception (first of all, compaction and sintering) [2]. The atomic force microscopy (AFM) is for today one of the basic methods of research of structural features of a surface of various types of zeolites [3].

However, at researches on air it was not possible to realize the high spatial resolution inherent in method AFM. The matter is that surfaces of zeolites are, on the one hand, high-abrasive, and with another – differ a high degree of development of a relief. Therefore, standard regimes AFM "tapping mode" and "non-contact mode" allowing investigating similar surfaces with greater difference of heights, under atmospheric conditions do not provide the sufficient resolution that is connected with presence on a surface of zeolite of the adsorbated layer [4]. Other standard regime AFM "contact mode" possesses the greatest resolution. But in this regime scanning results or in catching the probe because of a high degree of development of a relief, or to abrasion of a probe about high-abrasive a surface of zeolite [5].

In the given work the problem of reception of the image of morphology of a surface of zeolite (mazit) by method of AFM was solved under atmospheric ambience before and after compaction. For this purpose new regime AFM "MD mode" has been used (i.e. "Multi Date mode"), allowing to receive topography of a surface with the high resolution. Thus, unlike standard regimes AFM ("contact mode", "tapping mode", "non-contact mode"), it is completely excluded both abrasion of the probe, and catching of the probe at scanning a surface of the sample.

### 2. Force curve and AFM "MD mode" regime

As is known, the basic information signal at scanning a surface in AFM is the signal of a deviation cantilever on a

normal to a surface (to a plane of scanning), and also a signal of a deviation cantilever in a plane parallel to a plane of scanning [6]. Let's remind, that registration of a signal during an approach of a probe to a surface and removal from it gives power curve  $S(Z)$ , i.e. is considered a curve of dependence of size of a bend cantilever,  $S$ , from position of surface  $Z$  (if a moved element – the surface) which is set and always certain. This part of algorithm is the general for all regimes AFM. The main feature of a regime "MD mode" [7] is that the trajectory of movement of a probe at an approach-removal here essentially differs from trajectories of movement of a probe at standard regimes AFM. At an approach, the probe passes of the adsorbated layers, concerns a "pure" surface and measures its coordinates. Measurement of coordinates of topography of a surface is made in rigid contact of a probe to the sample. As the measurements are performed in full contact with the surface, resolution of "MD mode" is comparable with "contact mode" resolution. Thus, the trajectory of moving of a probe does not suppose lateral moving of a probe concerning a surface in contact that excludes abrasion or destruction of the probe. Then the probe is allocated from a surface on distance at which there is no interaction with the sample and only after that is made lateral moving to a following point of measurement. It excludes catching the probe during scanning and also lateral moving of the adsorbated layers on the surface.

Besides the probe, passing the adsorbated layers, can separately measure and their characteristics. And it means, that the regime "MD mode" allows to divide the information on a surface and the adsorbated layers on it and to receive separately both topography of a "pure" surface, and a card of distribution of thickness of the adsorbated layer on a surface [8]. Last in a regime "MD mode" turns out as follows. The probe at an approach all over again does "jump" to surface of the adsorbated layer, and after movement inside of it does one more "jump" already to a "pure" surface. Thus the coordinate of a point of a contact by a probe of a surface the adsorbated layer and coordinate of a point of a contact a probe of a "pure" surface is registered. The difference between these coordinates as a result gives thickness of the adsorbated layer in the given point of a surface. As a result, passing down-up, the probe measures characteristics the adsorbated layer and characteristics of a surface measures in contact to it already under the adsorbated layer. Therefore, first, it is possible to consider a surface "pure", and, second, influence of the adsorbated layer on the measured coordinate of a surface automatically is excluded.

### 3. Experimental results and discussion

High-abrasive surfaces mazit were tested by AFM "contact mode" and "MD mode" for comparison. The sample represented a powder consisting of grains of the spherical form, put on a graphite substrate. As grains under action of surface forces stick to a probe and remain on it the powder has been preliminary pressed under mechanical press

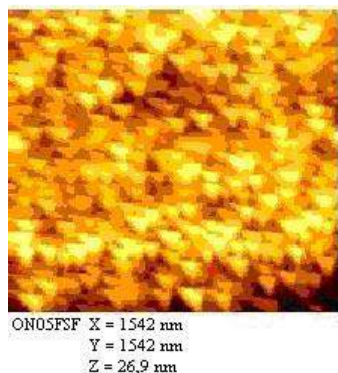


Fig. 1(a). Topographic image of a surface of mazit ("contact mode").

(diameter of pressing  $\sim 2,5 \times 10^{-2}$  m). After that, the pressed washer has been investigated on AFM. First, the sample of mazit has been investigated on AFM in a regime "contact mode". In experiment the pyramid-like probe from  $\text{Si}_3\text{N}_4$  (coefficient of elasticity cantilever 0,3 N/m was used; radius of the probe of  $\sim 120$  nm and taper angle of the probe  $\sim 55^\circ$ ). At scanning a surface in a regime "contact mode" the probe or cached, or still moved on a surface of the sample and abrasives about it as about an emery paper. And the topography of a surface in this case displayed artifact "relief". In Fig. 1 (a) the topography of a surface mazit with the area of scanning  $1542 \times 1542$  nm received in a regime "contact mode" is shown. On all area of the images certain isosceles triangles with the sizes of the sides  $70 \times 70 \times 50$  nm are observed. In this case we see not a surface, and of the pyramidal probe which has been abrasive about high-abrasive of surface mazit. The matter is that the image of data about a surface, strictly speaking, represents mathematical convolution of geometrical forms of a probe and a surface [9]. Therefore, when the probe,

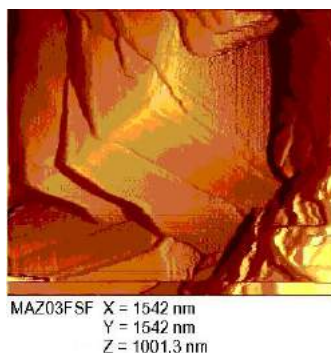


Fig. 1(b). Topographic image of a surface of mazit before compaction ("MD mode").

gradually abrasion about a surface, became more, than surface objects on the image the form of the probe was

clearly visualized, instead of a surface. For check of this fact, the probe has been separately investigated on a scanning electronic microscope. Photos of the probe, made before to the beginning of experiment and right after the end of experiment, have shown that the probe has been abrasive as a result of contact to a surface. Predictably, because of high-abrasive and strongly developed surface to receive topography of the surface of mazit in a regime "contact mode" it was not possible.

In the second experiment the surface of the same sample mazit has been investigated in a mode "MD mode". During all experiment the same probe of the conic form from W (coefficient of elasticity cantilever  $\sim 0,3$  N/m was used; radius of the probe  $\sim 15$  nm; and taper angle of the probe  $\sim 27^\circ$ ). In Fig. 1 (b) the topography of a surface mazit with the area of scanning  $1542 \times 1542$  nm received in a regime "MD mode" is shown. The image of a surface rather clear, with the high resolution (to more light tone there correspond higher point of a relief of a surface). The surface differs strongly developed relief – on the area  $1542 \times 1542$  nm the range on Z from the lowest up to the highest point of a surface reaches 1001,3 nm. Here the typical microstructure of a surface mazit is observed, in particular, steps of growth crystallites are well visible. Large crystallites have the complex form with rather sharp "broken off" edges, and finer – kvazi-spherical the form. Then, with the purpose of reception of structure of higher density, the same sample mazit has been subjected to process compaction. Last was spent by means of mechanical

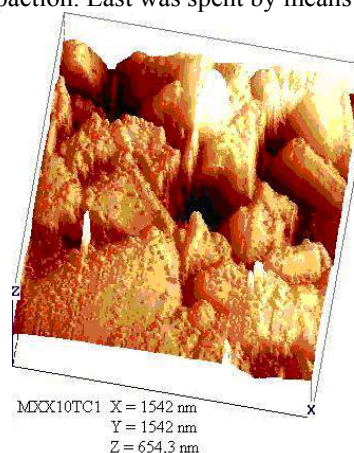


Fig. 1(c). Topographic image of a surface of mazit after compaction ("MD mode").

pressing (diameter of pressing  $2,5 \times 10^{-2}$  m; specific pressure  $\sim 4,8 \times 10^6$  kg/m<sup>2</sup>). In Fig. 1 (c) the surface mazit with the area of scanning  $1542 \times 1542$  nm after the mechanical pressing, also received in a regime "MD mode" is shown. Here too, as well as in Fig. 1 (b), the image of a surface is observed clear, with the high resolution. After compaction, the disorder of the sizes surface crystallites, naturally, became noticeably less, i.e. the relative density of structure has increased. Thus, the average sizes of a greater part surface crystallites are within the limits  $\sim (200-400)$  nm. On a surface a plenty of small grains in the size of  $16 \text{ nm} < d < 32 \text{ nm}$  which, basically, are grouped near to borders of various breaks is observed. Apparently, mechanical compaction, influencing the sample, most actively influences structure near to internal borders crystallites, as leads to formation already nanostructure crystallites.



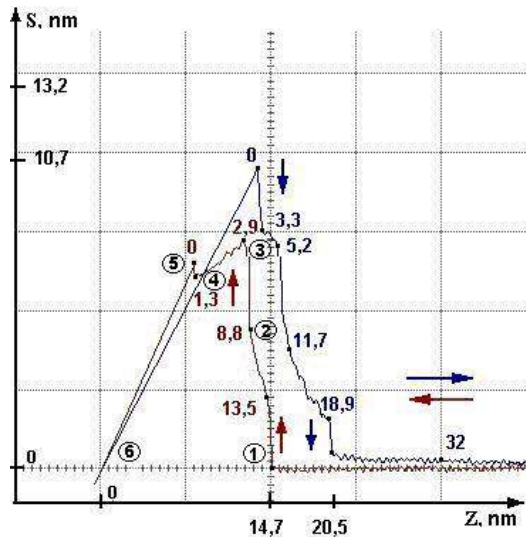


Fig. 2. Experimental force curve removed in the certain point of a surface mazit in "MD mode" regime.

In Fig. 1 (b) and in Fig. 1 (c) the clear image of a surface was observed. As the clear image obtained by the same probe is observed, it proves, indirectly, that "MD mode" is free from abrasion and catching of the probe. Both show topography of a surface the high resolution of a regime "MD mode" under normal conditions on not conductivity surface with strongly developed relief. Thus, greater advantage of a regime "MD mode" is that presence of the adsorbated layer on surfaces does not influence in no way quality of the received image of a surface. On the contrary, in addition to it, the regime "MD mode" allows to receive simultaneously and a card of distribution of thickness of the adsorbed layer on the given area of a surface [10].

Though in the given experiment such problem was not put, as an example we shall show, how the typical experimental force curve ( Fig. 2), removed in the certain point of a surface mazit in a regime "MD mode" looks (arrows force curves of an approach-removal of a probe are shown). Here we shall briefly analyze only a force curve of an approach of a probe to a surface (more detail process of registration of a force curve has been considered in [11]). On a direct horizontal part the force curve probe does not cooperate neither with of the adsorbated layer, nor with a surface. In a point 1 under influence of Van-der-Waals interaction between a probe on the one hand, and a surface of the sample with of the adsorbated layer on the other hand, the probe does "jump" aside surfaces (a vertical part from a point 1 up to a point 2) and is braked by a surface of the adsorbated layer in a point 3. On a force curve it is possible to measure, that the probe passes before registered contact to a surface of the adsorbated layer in a point of 3 distance in 11,8 nm. Further, having reached a surface of the adsorbated layer, the probe presses with accruing force, is elastic deforming it on distance of 1,6 nm (a flat part from a point 3 up to a point 4; the basis cantilever thus moves on distance of 8,5 nm). Small vertical part following it from a point 4 up to a point 5 on distance of 1,3 nm it is possible to interpret as break of the adsorbated layer by a probe and consequent "jump" of a probe to a surface mazit (a point 5). Further there is the part of direct contact of the probe with a surface (from a point 5 to a

point 6) on which in a point of crossing of zero (the point 6) cantilever is straightened (a point of contact balance). For an estimation of distance from of the probe to a surface in the given point, neglecting passage of a probe on curve Van-der-Waals of forces on the part between points C and D (Fig. 3a) also we shall consider, that the probe after "jump" to a surface at once reaches it and is based upon it (Fig. 3b).

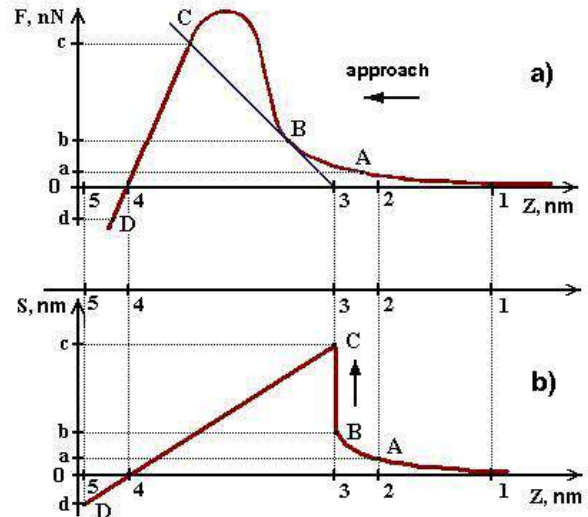


Fig. 3. The process of probe approach to the surface: Van-der-Waals interactions on the distance up  $F(Z)$  surface (a); force curve  $S(Z)$  there has been shown cantilever positions with the probe on the coordinate of surface position (b).

Obviously, that in most cases so it and occurs owing to forces of inertia and the forces of an attraction acting on a probe. So, if to consider, that in a point 5 probe gets on a surface the distance which has been passed at it by the basis cantilever, makes 14,7 nm, as is registered AFM as thickness of the adsorbated layer in the given point of a surface.

#### 4. Conclusions

So, experiment has shown that research under atmospheric conditions of a surface mazit by means of standard regime AFM "contact mode" does not give an opportunity to receive the clear image of topography of the surface. "MD mode" regime scanning has turned out to be much more effective in this sense. It has been shown, that mechanical compaction mazit with specific pressure  $4,8 \times 10^6 \text{ kg/m}^2$  leads to formation of the big number of small grains which, basically, are grouped near to borders of various breaks. Thus, the given regime "MD mode" allows receive under atmospheric conditions with the high resolution the image of topography of a surface of any samples differing high-abrasive and a high degree of development of a relief. Thus presence on such surface of the adsorbated layer does not influence in no way image of a surface. The author thanks employees of laboratory probe microscopy of Technology research and development Institute (Moscow) for the given opportunity of work on AFM and valuable consultations.

- [1] Yu.N. Barabanenkov, V.V. Ivanov *i dr.* JETP, 2006, t. 129, v. 1, s. 131-138. (in Russian)
- [2] T.I. Arbuzova, S.V. Naumov *i dr.* JETP, 2006, t. 129, v. 6, s. 10056-1063. (in Russian)
- [3] P. Grutter, W. Zimmermann-Edling, D. Brodbeck. Appl. Phys. Lett., 1992, v. 60, p. 2741-2745.
- [4] S.A. Vinogradova, A.O. Golubok, N.A. Tarasov. Nauchnoe priborostroenie, 1991, t. 1, s. 3-7. (in Russian)
- [5] U. Landman, W.D. Luedtke, M.W. Ribarsky. J. Vac. Sci. Technol. A, 1989, v.7, p. 2829-2833.
- [6] S.P. Molchanov, I.A. Chernova-Kharaeva, S.H. Abdullayeva, S.D. Alekperov. Fizika, 2005, v. XI, n. 1-2, p. 56-58.
- [7] S.P. Molchanov, V.V. Dremov, A.P. Kirpichnikov, Patent № 2145055, 2000, Rossiyskaya Federatsiya. (in Russian)
- [8] S.H. Abdullayeva, S.P. Molchanov, N.T. Mamedov, S.D. Alekperov. Physica Status Solidi (c), 2006, v. 3, n. 8, p. 2853-2857.
- [9] X.-Y. Zhang, D. Youzhen, L.A. Bottomley. J. Vac. Sci. Technol. B, 1995, v. 13, p. 1320-1324.
- [10] S.D. Alekperov. Transactions of ANAS, 2007, v. XXVII, n. 2, p. 21-27.
- [11] S.D. Alekperov. Transactions of ANAS, 2006, v. XXVI, n. 2, p. 21-28.

**S.C. Ələkbərov**

### **ATOM-QÜVVƏ MİKROSKOPİYASININ KÖMƏYİ İLƏ SEOLİT (MAZİT) SƏTHİN MORFOLOGİYASININ TƏDQIQI**

Atom-qüvvə mikroskopiyaşının köməyi ilə seolit (mazit) səthin tədqiqi normal şəraitdə edilmişdir. “MD mode” rejimin tətbiq etməsi, yüksək abraziv və relyefi yüksək dərəcədə inkişaf olan səthin topografiyasının şəklini aydın və böyük böyüdülmə ilə alınmasına imkan verdi. “MD mode” rejimi ilə səthin strukturasının analizi göstərdi ki, mazit nümunəsinin preslənməsi, birincisi, səthin kristallitlərinin ölçüsünü azaldır, ikincisi, cürbəcür sındırmaların həddlərin yanında toplaşan böyük saylı xırda dənələrin əmələ gəlməyinə səbəb olur.

**С.Д. Алекперов**

### **ИССЛЕДОВАНИЕ MORFOLOGИИ ПОВЕРХНОСТИ ЦЕОЛИТА (МАЗИТА) С ПОМОЩЬЮ АТОМНО-СИЛОВОЙ МИКРОСКОПИИ**

С помощью атомно-силового микроскопии исследована поверхность цеолита (мазита) при нормальных условиях. Применение режима “MD mode” позволило получить четкое, с высоким разрешением, изображение топографии высокоабразивной поверхности, с высокой степенью развитости рельефа. Анализ структуры поверхности в режиме “MD mode” показал, что компактирование образца мазита, во-первых, уменьшает разброс размеров поверхностных кристаллитов, а во-вторых, приводит к образованию большого числа мелких зерен, группирующихся вблизи границ различных разломов.

*Received: 14.04.08*

## PEYK MƏLUMATLARININ EMALINDA SÜNİ NEYRON DÖVRƏLƏRİNDƏN İSTİFADƏ ÜSULU

R.B. QULİYEV, A.A. ABBASZADƏ

*Təbii ehtiyatların Kosmik Tədqiqatlar İnstitutu NAKA*

B.M. ƏZİZOV

*Azərbaycan Texniki Universiteti, Az-1073, H. Javid pr., 25*

Neyron şəbəkələrinin klassifikasiyası əsas anlayışına və təbii mühitin ekoloji vəziyyətinin öyrənilməsi məsələsində alqoritmlərə baxılmışdır.

Bir çox hallarda təbii mühitdə gedən proseslərin elmi-nöqtəyi nəzərdən klassik standart riyazi modellər əsasında proqnozlaşdırılması çətin olur. Bəzi hallarda isə ümumiyyətlə mümkün olmur. Bunun səbəbi problemlərin çoxistiqamətli olması, onlar arasındakı qarşılıqlı əlaqənin çoxşaxəli olub və onların eyni qanunauyğunluqla baş verməməsidir. Bu amillər nəticəsində təbii proseslərin gedişinin proqnozlaşdırılmasının təcrübi universal üsulu mövcud deyil. Buna görə də təbii mühitdə hadisələrin inkişafı faktların statistik yığımının analizindən yox, fasiləsiz bir hadisələr toplusu kimi şərh olunmalıdır. Bu məsələlərə riyazi nöqtəyi nəzərdən baxış onu göstərir ki, formalaşdırılan məsələlərdə hətta prosesə daha böyük təsir göstərən ilkin prinsipial amillərin dəqiq nəzərə alınması qeyri mümkün olur. Buna görə də prosesin sonrakı mərhələlərinin proqnozlaşdırılması mümkün olmur və yaxud proqnozlar çox böyük xəta ilə alınır.

Bu fundamental ziddiyyətlərin aradan qaldırılmasının müasir üsulu kompüter sistemlərində yaradılan və 90-cı illərdən etibarən sürətlə inkişaf edən süni neyrodövrələrdən istifadə üsuludur [1,3]. Bu dövrələr üçün aprior biliklərin funksional paylanma xüsusiyyətləri tələb olunmur və təsnifat interaktiv rejimdə aparılır. Bu rejimdə müxtəlif aspektli əlavə məlumatlardan istifadə asanlaşır. Neyron dövrələrin arxitekturası istənilən hər hansı xüsusi bir məsələnin tətbiqinə adaptasiya oluna bilər. Bu sistem vasitəsilə təsnifat məsələlərinin həllində siniflər üzrə identifikasiyanın həyata keçirilməsi yerüstü məlumatların olmadığı halda belə mümkün olur. Son illərdə aparılan tədqiqat nəticələrinin analizi göstərir ki, bu üsulla aparılan təsnifatın dəqiqliyi istifadədə geniş yayılmış üsullara nisbətən dəqiqlik 10-30% yuxarı olur [2,4].

Süni neyron dövrələri yüksəklikləri neyronlardan ibarət olan və bir-biri ilə rabitəsi olan istiqamətlənmiş bir sistemdir. Hər bir neyron öz potensial imkanları çərçivəsində ancaq müəyyən sayda vəziyyətlər ola bilər. Hər bir neyrona giriş və çıxış xətləri birləşir. Bu xətlər vasitəsilə bir neyronun həyəcanlanması digərlərinə ötürülür.

Hər bir neyron dövrəsi özünün topologiyası ilə xarakterizə olunur. Buraya giriş və çıxışların sayı, açıq səviyyələrin sayı (giriş və çıxış dövrələri arasındakı təbəqələr) və hər bir təbəqədə olan neyronların sayı daxil olur. Topologiyasının birləşmə dövrələri tamamilə və yaxud lokal şəkildə dəyişə bilər. Bu səbəbdən süni neyron dövrələri bir və çoxtəbəqəli ola bilər. Eyni zamanda hər bir təbəqə digərinə nisbətən giriş və yaxud çıxış ola bilər.

Hal-hazırda peykdən alınmış informasiyalar əsasında bir sıra məsələlərin həllində neyron dövrələrindən istifadə olunur. Bu məqsəd üçün bir neçə növ neyron dövrələri istifadə olunur. Bunlardan ən geniş yayılmışları MLP

(çoxtəbəqəli sistem), ART (adaptiv rezonans nəzəriyyəsi), BAM(ikiistiqamətli yaddaş qurğusuna malik) və MAP (özünü tənzimləyən sistem). Qeyd olunan neyron dövrələri bir-birindən topologiyanın müxtəlif olması və öyrətmə üsulunun fərqli olmasıdır. Ən geniş yayılmış neyron dövrələri kosmik informasiya əsasında həll olunan məsələlərin xüsusiyyətindən və tələb olunan dəqiqlik dərəcəsi əsasında müəyyənləşdirilir [5].

Qeyd olunan sistemlər içərisində ən geniş yayılmışı MLP sistemidir. Bu sistemdə giriş təbəqəsində vektor göstəricisini hesablayan və növbəti təbəqəni həyəcanlandıran qovşaqlardan ibarət olur. Növbəti təbəqənin qovşaqları elə vəziyyətə gətirilir ki, onlar qeyri-xətti çevrilmələrə nəzarət edə bilərlər. Sonrakı təbəqələrin qovşaqları oxşar alqoritmlər əsasında əvvəlki qovşaqlar tərəfindən həyəcanlandırılır. Təsnifatın tam formalaşdırılması üçün tələb olunan qiymətlər sonuncu təbəqədən götürülür. Hər bir neyronun vəziyyəti ( $P_i$ ), digər neyronlar tərəfindən ona verilən həyəcanlanmaların qeyri-xətti funksiyası ( $f$ ) ilə təyin olunur. Yəni,

$$P_i = f\left(\sum_{j=0}^N C_{ij} P_j\right).$$

Burada  $P_j$  - həyəcanlandırıcı neyronun potensialı,  $C_{ij}$  - bütün rabitələrin miqdarıdır. Beləliklə, ən kiçik təbəqə (0) MLP sistemində bilavasitə giriş təsirli  $X$  vektoru ilə həyəcanlandırılır, sonuncu təbəqədən isə nəticə kimi  $Y$  vektoru çıxır.

Hansı məsələnin qoyuluşundan asılı olaraq təsnifatın nəticəsi kimi interpretasiya olunur. Birinci və sonuncu təbəqələr arasında yerləşən təbəqələri adətən gizli təbəqələr adlandırılır. Çoxtəbəqəli sistemlə işlədikdə 1-N neyronlarının vəziyyəti hesablanılır. Nəticədə çıxış parametrlərinin qiyməti müəyyənləşdirilir.

Bizim apardığımız tədqiqatların emal prosesində qismən də olsa neyron dövrələr sistemindən istifadə olunmuşdur. Biz əsasən nəmliyin qiymətləndirilməsinin bu üsulla mümkünlüyü bir daha təsdiq etmişik. Bizim araşdırmalarda CSS işləyib hazırladığı Brain-Marker neyrodövrə paketindən istifadə olunmuşdur. Emal prosesi şəkil 1-də göstərilən sxem üzrə aparılmışdır. Neyrodövrə üzrə aparılan emal prosesində alınmış nəticələr əvvəlki fəsilərdə aparılmış ölçmə nəticələri ilə qarşılıqlı müqayisə əsasında müəyyən fərqlər alınmışdır. Bu fərqlərin əsas səbəbi neyrodövrələr üzrə aparılan ölçmələrin qeyri mükəmməlliyi ilə izah olunmalıdır.

Məlum olduğu kimi, neyron dövrəsi üzrə təlim prosesində rabitə çəkisi adlanan parametrdən istifadə olunur. Bu parametrlərin qiymətindən asılı olaraq axtarılan parametrlərin

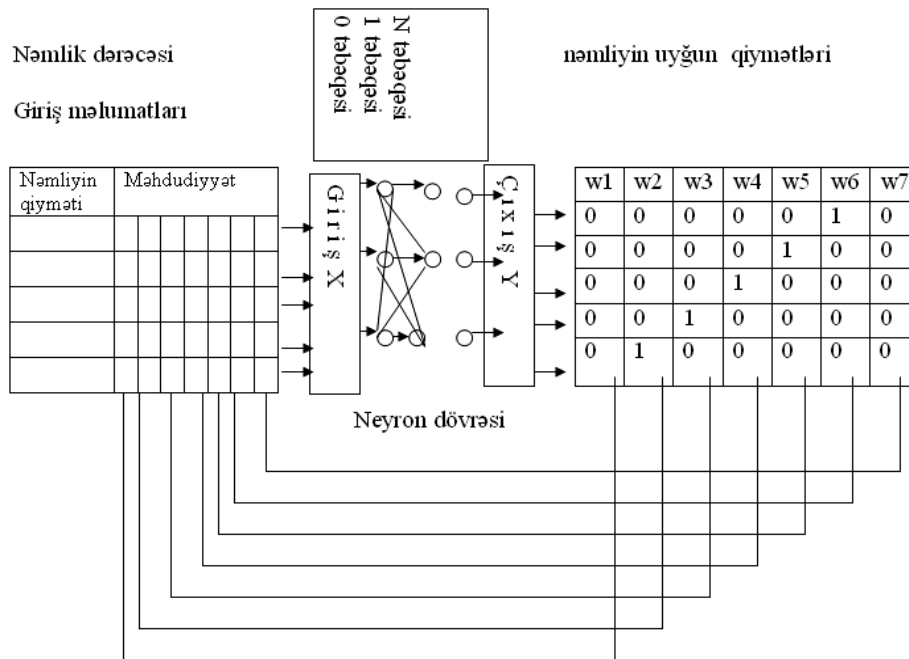
qiymətləndirilməsində alınan xətlər müəyyən hədd daxilində dəyişir. Təlimdən sonra adətən nəticələr nəzarət üçün seçilmiş rejimdə yoxlanılır. Hal-hazırda təlim prosesinin həyata keçirilməsi üçün bir sıra alqoritmlər mövcuddur. Bunlardan ən geniş yayılmışı əks əlaqə üsuludur. Təlim prosesində səviyyələrin sayı, hər bir səviyyədə olan neyronların sayı və  $X$  giriş parametrləri iç,  $Y$  çıxış parametrləri arasındakı əlaqə təminatını yaradan  $C_{ij}$  – rabitə çəkisi müəyyənləşdirilir. Neyron dövrəsində təlim prosesi çoxluqlar üzərində həyata keçirilir. Belə ki, hər bir nöqtə üzrə  $X_i$  giriş vektoruna məlum  $Y_i$  vektoru uyğun gəlir.

Rabitə çəki əmsalının  $C_{ij}$  seçilməsi ən geniş yayılmış üsul kvadratik funksiyanın minimumuna görə qiymətləndirmə üsuludur.

$$E = \sum_i^m \left| Y_i - \bar{Y}_i \right|^2$$

Burada  $m$ - təlim aktında nöqtələrin sayı;  $Y_i$  – aktın  $i$ -ci nöqtəsinin məlum çıxış vektoru;  $\bar{Y}_i$  –  $X_i$  giriş vektoruna MLP-nin reaksiyasıdır.

Neyron dövrəsində təlim prosesinin effektivini artırmaq üçün neyronların sayının seçilməsi və topologiyasının təyin edilməsi əsas şərtlərdən hesab olunur. Adətən bunun üçün müxtəlif topologiyaya malik bir neçə dövrə götürülür və bu dövrlərdən daha yaxşı nəticə verən dövrə seçilir.



## Təlim əlaqələri

Şəkil 1. Neyron dövrlərində təlim prosesinin topoji sxemi

Süni neyron dövrlərin texniki reallaşması iki yolla həyata keçirilir:

1. Xüsusi mikrosxemlərin yaradılması ilə. Bu mikrosxemlərdə neyronların və neyronlar arası rabitə mikrosxeminin xüsusi elementləri tərəfindən həyata keçirilir.
2. Universal kompüterlərdə xüsusi emulsiya vasitəsilə. Bu halda emulsiyanın idarə olunması xüsusi proqram əsasında həyata keçirilir.

Neyron dövrlərinin xüsusi mikrosxemlər əsasında reallaşmasında daha yaxşı nəticələr əldə olunur. Belə ki, bu halda neyronların vəziyyətinin paralel hesablanmasına görə dövrənin işləmə sürəti yüksəlir. Təlim üçün çox vaxt tələb olunan dövrlərdə bu amil daha əhəmiyyətli xarakter daşıyır. Hal-hazırda universal kompüterlərə xüsusi plata yerləşdirməklə süni neyron dövrlərini reallaşdırmaq mümkün olur.

- [1] A.F. Egorov, T.V. Savitskaya. Upravlenie bezopasnostyu khimicheskikh proizvodstv na osnove novikh informatsionnikh tekhnologiy. M. Khimiya «Kolos», 2004.
- [2] A.F. Egorov, T.V. Savitskaya, S.B. Dudarov i dr. Ispolzovanie iskustvennikh neytronnikh setey dlya identifikatsii promishlennikh istochnikov zagryazneniya atmosfernogo vozdukha. Khimicheskaya promishlennost, 2004, № 6.
- [3] Domashnyaya ctranitsa kompanii Softline [Elektronniy resurs]: Informatsionniy portal,

- posvyashonnost razlichnomu programmnomu obespecheniyu - Moskva, 2005. Rejimi dostupa [http://www.softline.ru/product.asp], svobodniy.
- [4] Laboratoriya Base-Group [Elektronniy resurs]: Informatsionniy portal, posvyashonniy tekhnologii analizi dannikh - Ryazan, 2000 Rejimi dostupa: http://www.basegroup.ru. Svobodniy.
- [5] A.S. Abulqasim, S. Gopal. Classification of Asas multi-angle and multispectral measurments using artifikal neural networks Rem.Sens. Environ. 1996. V59. P.79-87.

**R.B. Quliyev, B.M. Azizov, A.A. Abbaszadeh**

**THE USAGE OF ARTIFICIAL NEURAL CIRCUITS FOR PROCESSING OF SATELLITE MEASUREMENT**

The basic concepts of classification of neural circuits and algorithms in the problems of observation about ecological situation of environment are considered.

**Р.Б. Гулиев, Б.М. Азизов, А.А. Аббасзаде**

**ИСПОЛЬЗОВАНИЕ ИСКУССТВЕННЫХ НЕЙРОННЫХ СЕТЕЙ ДЛЯ ОБРАБОТКИ СПУТНИКОВЫХ ИЗМЕРЕНИЙ**

Рассматриваются основные понятия классификации нейронных сетей и алгоритмы в задачах изучения экологического состояния природной среды.

*Received: 08. 07. 08*



## INFLUENCE OF PRELIMINARY ARGON ION BOMBARDMENT OF SILICON AND GERMANIUM SUBSTRATES ON ORIENTATION OF LIQUID CRYSTALLINE MOLECULES

**T.D. IBRAGIMOV, N.J. ISMAILOV, E.A. ALLAHVERDIYEV, I.S. HASANOV**

*Institute of Physics of National Academy of Sciences  
AZ-1143, H. Javid ave., 33, Baku, Azerbaijan*

**G.M. BAYRAMOV, A.R. IMAMALIEV**

*Baku State University  
AZ-1143, Z.Khalilov str. 23, Baku, Azerbaijan*

The possibility of homogenous orientation of liquid crystalline (LC) molecules is studied after bombardment of substrates transparent in infra-red (IR) spectral region (Si, Ge) by argon ions and also after chemical etching. The control of orientation of LC molecules is made by the methods of IR spectroscopy and dielectric measurements..

It has been established that with increasing of ion fluence at preliminary bombardment of substrates by argon ions with energy of 250 eV the LC molecules are oriented planarly while at ion energy of 1.25 keV they are done planarly and then – homeotropically. The preliminary chemical etching of silicon substrates by the solution of KOH in the water and ethylenglycol promotes to planar orientation of LC molecules. The most effect of homeotropic orientation of LC molecules is obtained by preliminary argon ion bombardment of substrates with energy of 250 eV and subsequent etching in the solution of KOH and ethylenglycol.

### 1. Introduction

In order to appreciable an electrooptical effect in liquid crystal (LC), it is absolutely necessary to bring the LC molecules into a certain orientation on the cell bordered walls. Then molecules of the subsequent layers will be arranged to molecules of the surface layer and all volume will represent a single crystal.

One of the methods to obtain a planar configuration of the nematic LC is the substrate rubbing [1-3]. After passing through a micro porous filter (pore diameter  $\sim 0.5 \mu\text{m}$ ), the 3% water solution of the polyvinyl alcohol (PVA) is deposited onto a rotating substrate (400 rev/min) at room temperature. The deposited film is dried up for 30 minutes at 80°C, first, and, then, is rubbed using a piece of textile or the diamond paste.

Using rubbing, homogeneous orientation of LC molecules is obtained for any substrates. Instead of PVA, a solution of the polyamide in N-methylpyrrolidane, diluted in the ratio 1:10 can be used. The polymerization is then achieved in two stages; by 30 minutes annealing at 130°C and 200°C.

The planar orientation of the LC molecules is also obtained by slanting deposition of the oxides onto relevant substrates.

One of the methods to obtain a homeotropically oriented layer is to place a nematic liquid crystal (NLC) between the surfaces covered by lecithin. A solution of the natural egg lecithin in the volatile solvent (alcohol) is used for substrate coating. The concentration of the solution is about 1%. After the coating procedure the substrate is rinsed with solvent and dried up for 30 minutes at 80° C. Another method is to use polymethylsiloxane layer which is easily obtained from dimethyldichlorsilan (10 % solution in toluene) by immersing the plate for 15 minutes at room temperature. Then the covered surface is rinsed by isopropanol and annealing for 30 minutes at 100° C. In order to orientate the molecules of 4-methoxybenzylidene-4-butylaniline (MBBA) and 4-ethoxybenzylidene-4-butylaniline (EBBA) mixture, polymethylsiloxane or the mixture of polymethyl and

polydimethylsiloxane (10 % solution in toluene) are used. Plates are immersed in a solution for 15 minutes at room temperature. The coated surfaces are rinsed in isopropanol and annealed for 30 minutes at temperature 80-100° C LC molecules.

For homogeneous orientation of the LC molecules in some cases it is impossible to apply the above-stated methods. In particular, at manufacturing of photon crystals with the LC stuffing [4-5] it is impossible to apply the method of rubbing. And at using of the LC for special problems of modulation of infra-red light applying of surface-active substances [6] is undesirable. Therefore a search of alternative methods of processing of a surface is an actual problem. In particular, such methods are bombardment of a surface by ions and application of chemically active substances for deep etching.

At bombardment of a surface by ions of neutral gases, the atoms can take off from this surface. This process is called the dispersion. Erosion of a surface leads to structural change of surface layers because of dispersion and is characterized by the dispersion factor defined as an average of the atoms deleted from a solid surface by one particle. Dispersion factors depend on energy of ions, their mass, falling angle, mass of target atoms, crystallite of targets, orientation of crystal axes, and surface energy of bond of target material. Below some threshold energy which is equal to 20-40 eV at normal falling of ions, dispersion practically is absent [7]. Above a threshold the dispersion factor increases with increasing of energy of falling ions and reaches a wide maximum at the energy of 5-50 keV. At high energies the reduction of dispersion factor is connected with increasing of depth of penetration of primary ions in a target and reduction of a part of the energy passed to surface layers by them. Dispersion of a surface material by the accelerated ions of sufficient energy and fluence leads to formation of microscopic deepening which can be the centers of orientation for elongated LC molecules.

It is known that places of crossing of crystal surface by a dislocation are the easiest influence to various solvents. It is connected with that the atom bonds are deformed around of a

dislocation line in the crystal: they are stretched in one places, ones are compressed or broken absolutely off in others. The area of a crystal has superficial surface energy around dislocations. This does it in places of an output of a dislocation on a surface by less steady to the influence of chemical etching. Etching poles, as a result of various rate of etching on a crystal surface, are formed in places of an output of dislocations which can also be the orientation centers for LC molecules.

In the work the possibility of homogenous orientation of LC molecules are studied after argon ion bombardment of substrates transparent in infra-red spectral region (Si, Ge) and also after a method of chemical etching.

## 2. Experimental

Plant was assembled on the base of the VU-1 vacuum device for bombardment of the various semiconductor and dielectric plate surfaces by argon ions (Fig.1). In the order to obtain the homeotropic orientation of LC molecules, high-purity p-type silicon and germanium plates transparent in the mid-IR region were bombarded by argon ions with the fluence defined by the exposition time.

The pairs of plates were fixed on the metal plain base and suspended above a high-voltage electrode on the distance of 40 mm from it. At that case irradiated plates were zero potential. High-purity argon was used as a working gas. A glow discharge was ignited in the chamber at the voltage supply on the electrode. Processing regime was following: ion energy of 250 eV, ion current density of 0.2 mA/cm<sup>2</sup>, and pressure of working gas of 10 Pa. An ion fluence depended from exposition time. It was determined by expression  $D = j t / e$ , where  $j$  – ion current density,  $t$  – exposition time,  $e$  – ion charge. The fluency was  $1.5 \cdot 10^{18}$  cm<sup>-2</sup> at above-indicated conditions and the irradiation time of 20 min. The exposition time varied between 5 and 60 min.

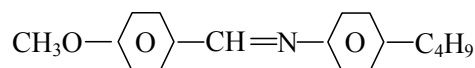


Fig.1. Vacuum plant VU-1 with the system of ionic etching.

With the purpose of effective deepening formation in substrate surfaces, apart the source of Kaufman type was used for increasing of ion argon energy. In order to create the dense plasma, the discharge with the heated cathode was used in a longitudinal magnetic field. Owing to electron oscillations in transverse electromagnetic fields, the high uniformity of plasma was reached. The three-electrode system of ion extraction allows forming the beam with a

diameter of 100 mm and homogenous current. Parameters of the source are following: cathode heating current-12 A; magnet coil current-up to 30 A; discharge current-up to 2 A; discharge voltage-up to 100 V; energy of ions-up to 2 keV; ion beam current-up to 30 mA; ion current density-up to 100  $\mu$ A/cm<sup>2</sup>. The ionic source is installed on the base of the VU-1 device with limiting vacuum of  $5 \cdot 10^{-6}$  Torr.

The idea of the control of LC molecule orientation by the method of infra-red spectroscopy (IR) consists that at concurrence of an electric vector of incident light with the vibration of certain group along a long axis of the LC molecule the corresponding absorption band has maximal intensity. If the direction of an electric vector of incident radiation is perpendicular to one of vibrations along a long axis of a molecule, the corresponding band has the minimal intensity. At application of direct electric field above Fredericksz threshold to the LC cell with negative dielectric anisotropy all molecules are arranged along the cell plane and the corresponding band has the maximal value. Nematic LC 4-methoxybenzilidene - 4' - butylaniline (MBBA) is used for the control of molecule orientation. It has negative optical anisotropy and is described by the structural formula



Thus the group -CH=N- vibrates along a long axis of the MBBA molecules. According to [8] its frequency has value about of 1630 cm<sup>-1</sup>.

IR absorption spectra were carried out on double-beam infra-red spectrophotometer IKS-29 and supervised by double-beam infra-red spectrophotometer Specord - 75 IR in the frequency region of 4200 - 400 cm<sup>-1</sup> and 4000 - 400 cm<sup>-1</sup>, accordingly. The resolution and an accuracy of definition of frequencies were not worse than 2 cm<sup>-1</sup>.

The study of the LC molecule orientation is carried out in so-called "sandwich" cell consisting of two identically processed silicon or germanium parallel plates between which there is liquid crystal MBBA (Fig.2). Thus the processed surfaces of plates adjoin with LC.

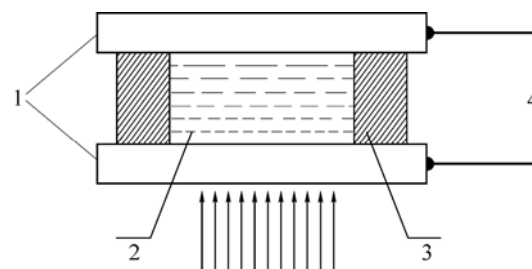


Fig.2. The cell for measurement of IR spectra. 1-silicon or germanium plates; 2-liquid crystal; 3-gaskets; 4- conductive wires.

It is necessary to note that high-purity silicon and germanium are rather transparent in mid-IR region and have only several weak two-phonon bands which are easily compensated in doable-beam spectrophotometer by accommodation of the same plate without LC in the reference window (Рис.3). Both materials equally reflect a lot of light - losses reach to 50 %.

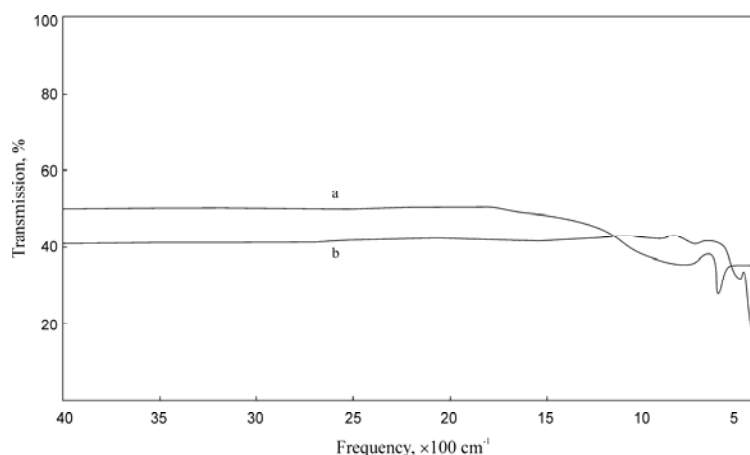


Fig.3. Transmission spectra of silicon (a) and germanium (b) plates with thicknesses of 320  $\mu\text{m}$  and 980  $\mu\text{m}$ , accordingly.

The thickness of LC layer in the cell is regulated by special dielectric gaskets and determined by measurement of capacity of empty cell by formula  $d = \epsilon_0 S/C$ , where  $\epsilon_0 = 8.85$  nF/m electrical constant,  $S$  - the square of working part of electrooptical cell,  $C$  - electrical capacity of the cell. An accuracy of thickness definition is about 0.1  $\mu\text{m}$ . Thickness uniformity is provided by spatial holder allowing to press glass plates to each other from four extreme points and to remove a wedge which is shown as interference bands. The cell is filled by capillary method in vacuum when LC has isotropic phase.

For definition of voltage at which there is Fredericksz' effect the capacity measurement of the same cell versus voltage is used.

Thus the capacity of the cell is changed depending on initial orientation of LC molecules, caused by change of dielectric permeability of LC in the direction perpendicular to the cell. The capacity measurement is carried out on low frequency (up to 1kHz), that creates the certain difficulties of measurements.

In order to measure the value of LC capacity change, the scheme of the differential amplifier with compensation was used. The signal from generator G of sine wave oscillations was applied to the LC cell  $S$  through element R3C2 having on measured frequency of 1 kHz much greater resistance than the cell. A signal on structure through dividing condenser C2 was applied on a high-resistance input of differential amplifier A1. On other input A1 for balance on input from generator G was applied an anaphase signal of the same value. Thus, the signal on output A1 was minimal at absence of voltage on the cell. Voltage on structure was applied from potentiometer R1 and supervised by voltmeter V. At changing of the cell capacity with change of the applied voltage on output A1 there is a signal which was registered on the oscilloscope Os. The value of the changed capacity was determined by the method of compensation of calibrated variable capacity C3 included in parallel with the structure. The structure was located in a warmed cavity  $T$  with the temperature regulator and the measuring device of temperature for carrying out of measurements in the temperature interval 15°-45°C.

### 3. Results and discussion

Study of influence of bombardment of silicon and germanium substrates for homogeneous orientation of LC molecules is carried out on the example of MBBA. IR spectra

of MBBA at different thicknesses are shown on Fig.4. Apparently, a set of strong and weak absorption bands is observed in these spectra.

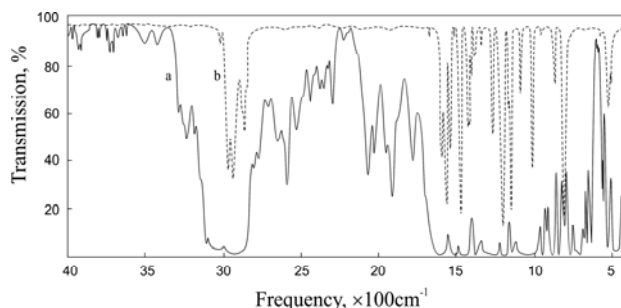


Fig.4. Transmission spectra of the cell with MBBA at different LC layers: a – 205  $\mu\text{m}$ ; b – 10  $\mu\text{m}$ .

Each absorption band corresponds to vibration of the certain group of atoms. In particular, a set of bands between 3050 $\text{cm}^{-1}$  and 2850  $\text{cm}^{-1}$  corresponds to vibrations of  $\text{CH}_2$  and  $\text{CH}_3$  groups. For the orientation control of elongated MBBA molecules we use a band with a maximum of 1630  $\text{cm}^{-1}$  which corresponds to  $-\text{CH}=\text{N}-$  group vibrating along a long axis of the MBBA molecule. This band together nearby ones are represented on Fig.5.

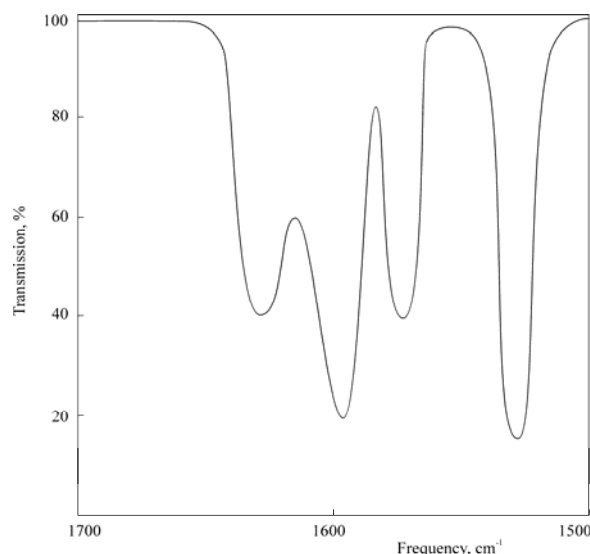


Fig.5. Transmission spectrum of the non processed silicon cell with MBBA with thickness of 10  $\mu\text{m}$  near the band corresponding to vibration of the group  $-\text{CH}=\text{N}-$ .

The intensity of bands changes at increasing of the voltage applied to the cell. The band with a maximum of  $1630\text{ cm}^{-1}$  gradually increases its intensity since the voltage of 3.5 V, reaching the maximal value at some voltage. It is obvious, that at this voltage all MBBA molecules settle down in parallel to relation of a substrate that corresponds to concurrence of the direction of vibration of the group  $-\text{CH}=\text{N}-$  with the direction of an electric field of incident radiation. The measurement of dependences of transmission from voltage on maxima of bands near the above-stated band is carried out for more correct definition of kinetic changes of the band intensity. Corresponding dependences are shown on Fig.6.

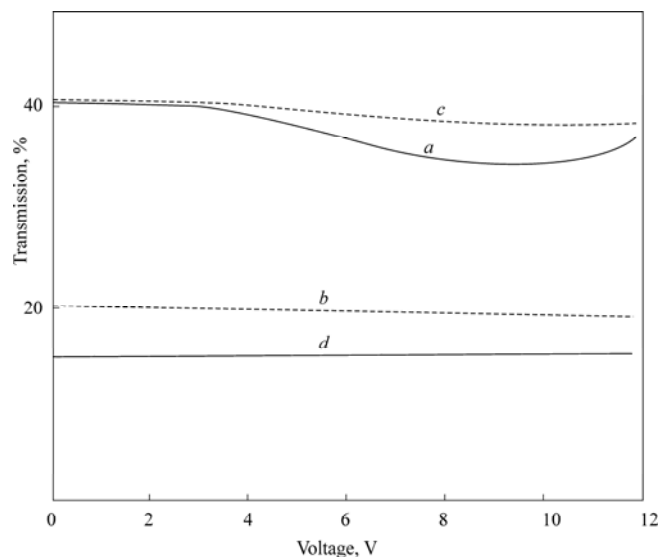


Fig.6. Light transmission of the non processed silicon cell with MBBA depending on the applied voltage at various frequencies: a -  $1630\text{ cm}^{-1}$ ; b -  $1596\text{ cm}^{-1}$ ; c -  $1575\text{ cm}^{-1}$ ; d -  $1512\text{ cm}^{-1}$ .

As seen from this figure, the intensity of light passing through the cell on frequency of  $1630\text{ cm}^{-1}$  gradually increases since 3,6 V, reaching the saturation at 7,5 V then it decreases while it does not almost vary on frequencies corresponding to maxima of other bands. It is interesting to note that the dependence of capacity from voltage similarly behaves (Fig.7).

It is obvious that the beginning of an increase in capacity and absorption on frequency of  $1630\text{ cm}^{-1}$  corresponds to the beginning of reorientation of LC molecules. Saturation corresponds to full orientation of molecules in parallel to the substrate surface and reduction does to origin of turbulence (electrohydrodynamical instability) which is characteristic for liquid crystals with negative anisotropy of dielectric permeability.

If it is primary the LC is not oriented in the cell, the maximal change of capacity at application of voltage makes  $C(U=7.5\text{ V})/C(U=0) = \epsilon_{\perp}/\langle \epsilon \rangle = 1.125$ , where the average value of dielectric permeability is equal to  $\langle \epsilon \rangle = 1/3(2\epsilon_{\perp} + \epsilon_{\parallel})$ ;  $\epsilon_{\perp}$  и  $\epsilon_{\parallel}$  are dielectric permeabilities for orientation of molecules perpendicularly and parallel to the substrate surface, accordingly.

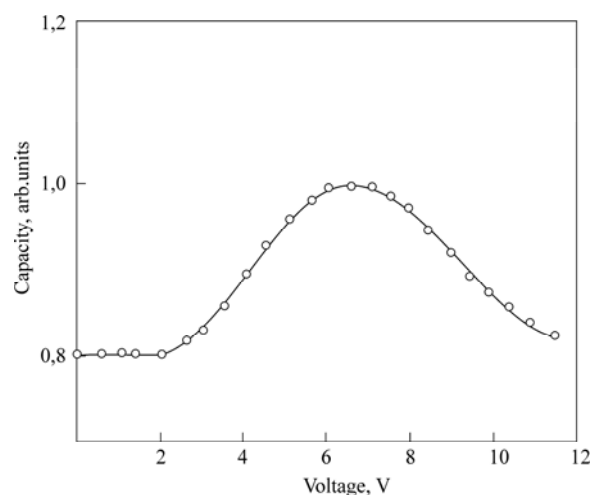


Fig.7. The dependence of capacity of the cell with the non processed silicon electrodes on voltage.

It is known that integrated absorption of a resonant band is proportional to the number of oscillations corresponding to the given optical transition. The dependence of integrated absorption from voltage on the band corresponding vibrations of group  $-\text{CH}=\text{N}-$  is shown for the non processed silicon substrates. It is obvious that the initial part of the graph up to 3.5 V corresponds to non orientated LC molecules while a part of saturation does to full their planar orientation.

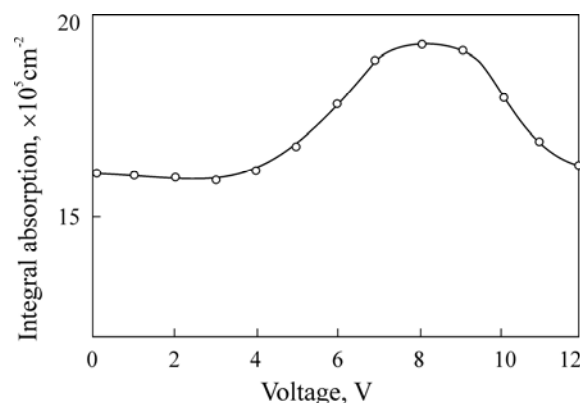


Fig.8. The dependence of integrated absorption from voltage on the band corresponding vibrations of the group- $\text{CH}=\text{N}-$  at the non processed silicon substrates.

It is obvious that to judge about orientation of LC molecules after processing of substrates is possible on an initial part of the graph while the part of saturation coincides for all types of substrate surface processing. If after substrate processing the initial part of the graph is placed above the graph corresponding to the cell with the raw substrates then the molecules aspire to be situated planarly and if below then they do homeotropically. The value of deviation corresponds to a degree of this or that orientation of molecules.

The dependence of integrated absorption from irradiation dose is shown on Fig.11 at preliminary processing of silicon substrates by argon ions with energy of 250 eV.

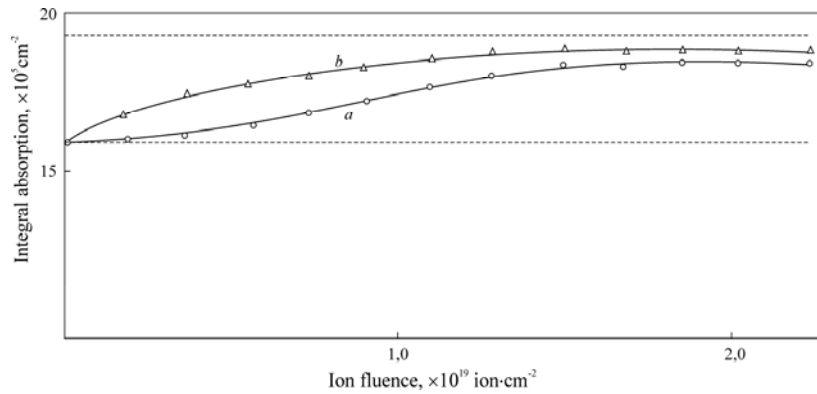


Fig. 9. The dependence of integrated absorption from the ion fluence on the band corresponding vibrations of the group-CH=N- after processing of silicon (a) and germanium (b) substrates by argon ions with energy of 250 eV.

As seen from Fig. 9, the LC molecules aspire to be situated planarly at processing of substrates by argon ions with energy of 250 eV. A decrease of the value of capacity change without and with voltage application confirms initial orientation of LC molecules parallel to the substrate (Fig. 10). At that case, the initial orientation of the LC molecules is arranged on the germanium substrates at less fluences than on

the silicon ones. This fact is explained by more dispersed factors for germanium than for silicon.

At preliminary processing of substrates by argon ions with energy of 1.25 eV the LC molecules are arranged planarly at less fluences and more fluences – homeotropically. At that case, the LC molecules are arranged homeotropically at less fluences of germanium plates than silicon ones (Fig. 11).

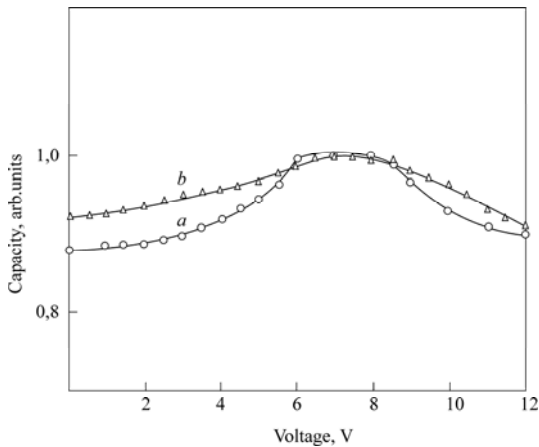


Fig. 10. The dependence of the LC cell capacity with preliminary bombardment of silicon (a) and germanium (b) electrodes by argon ions with energy of 250 eV and an ion fluence of  $7.5 \cdot 10^{18} \text{ ion-cm}^{-2}$ .

At bombardment of crystals by ions of a different fluence there are two effects of opposite character. The smoothing of a surface originally possessing some roughness is occurred at ion fluences in the interval of  $10^{16} \text{ cm}^{-2} - 10^{17} \text{ cm}^{-2}$  [9]. Enough plenty of radiation defects leading development of a relief on the surface is collected inside the crystal at fluences exceeding to  $10^{17} \text{ cm}^{-2}$ . Surface energy of bond can be decreased and the dispersion factor can be increased near the defects because of presence of mechanical pressure. Initial roughness can be increased at badly prepared surface. At this case, crests, cones, flutes and poles can be developed. Similar structures not so strongly differ from what are shown on samples originally well polished. More and more than roughness are appeared on surfaces at increasing of ion fluence. Ones areas are sprayed more quickly than others because of defects of a crystal lattice. Etching poles which are the most typical kinds of the hollows resulting at

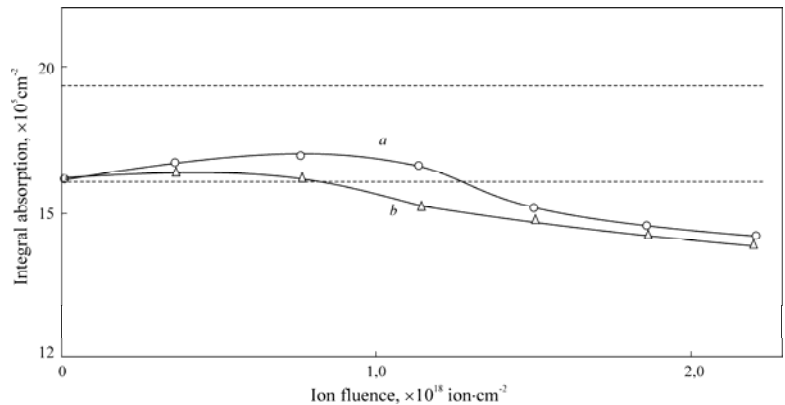


Fig. 11. The dependence of integrated absorption on the band corresponding vibrations of the group-CH=N- from the irradiated doze after processing of silicon (a) and germanium (b) substrates by argon ions with energy of 1.25 keV.

dispersion are formed. They are formed as a result of selective dispersion of places of an output of screw dislocations on the surface. Poles are formed in local areas of the surface where there are those or other dislocations and where the energy of atom bond is lowered. The amount of poles grows with increasing of irradiation doze. They are blocked and increased in dimensions at an increase of an ion fluence. Obviously, at the energy of bombarding ions of 1.25 keV the effect of pole formation predominates and at enough high ion fluences they are the centers of homeotropic orientation of LC molecules.

Micropictures of silicon and germanium surfaces after argon ion bombardment with energy of 1.25 keV and ion fluence of  $1.125 \cdot 10^{18} \text{ ion-cm}^{-2}$  are shown on Fig. 14. As seen, the relief on the surface of plates is different and, one is followed from Fig. 12, corresponds to different types of LC molecule orientation.



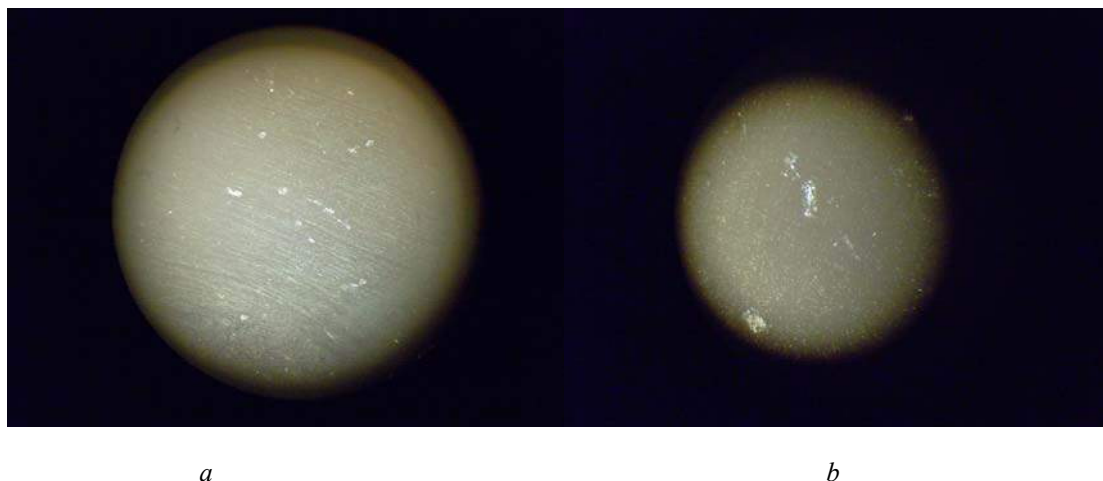


Fig.12. Micropictures of silicon (a) and germanium (b) surfaces after argon ion bombardment with energy of 1.25 keV and ion fluence of  $1.125 \cdot 10^{18} \text{ ion} \cdot \text{cm}^{-2}$

The etchants of simple compound were used for experiments: the solution of KOH in water and ethylenglycol. A set of experiments with the solutions of different percentage compound, at different temperatures, and processing time was carried out for definition of optimal chemical processing regime. Plates of small dimensions were subjected by preliminary cleaning with acetone and spirit then their surfaces were observed under the optical microscope before and after processing operations.

The exact scales were used for preparation of KOH solutions. Preliminary cleared plates became covered on the one side by a layer of chemically proof glue and were maintained before its full hardening. It was done that only internal surfaces of optical cells were exposed to the subsequent etching. Then plates were fallen to the corresponding solution and all system was located in the thermostat with adjustable temperature.

In experiments the contents of alkali in solutions varied from 10 up to 50 %, thermostat temperature was increased up to 60°C.

Observation under the optical microscope has shown that the most appreciable expression of plate surface after chemical etching occurs in the 30 percentage solution of KOH in ethylenglycol.

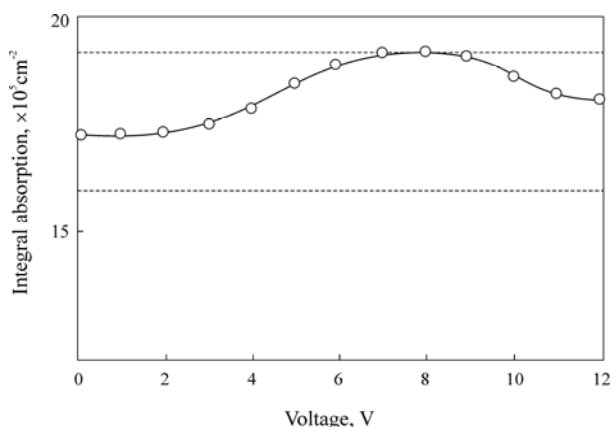


Fig.13. The dependence of integrated absorption from the applied voltage on the band with a maximum of  $1630 \text{ cm}^{-1}$  at preliminary processing of silicon plate by 30 % solution of KOH in ethylenglycol.

The dependence of integrated absorption from applied voltage on the band with a maximum of  $1630 \text{ cm}^{-1}$  at processing silicon plates by the above-stated solution with concentration KOH equaled to 30 % at 60°C is shown on Fig.13.

Apparently from Fig. 13, an initial part of the graph (voltage less than 3 V) situates above a corresponding part for cells with the non processed plates. It indicates that the preliminary etching of plates results in parallel orientation of LC molecules to the plate surface.

The concept of the degree of orientation order is entered for the quantitative description of primary orientation of LC molecules. Frequently [10-11], the degree of orientation order is defined with the help of known ratio  $S = (N-1)/(N+2)$ , where  $N = A_z/A_x$  – dichroic ratio;  $A_z$  and  $A_x$  – peak intensities of the chosen absorption band for two mutually perpendicular directions of light polarization.

In order to analyze our experimental results we shall accept a ratio of a difference between values of integrated absorption on the chosen band of the processed and non processed plates to a difference between values of integrated absorption on same band at the non processed plate without the application of field and at full planar orientation of LC molecules ( $U=7.5\text{V}$ ). The dependence of degree of orientation order from concentration of KOH in water and ethylenglycol is shown on Fig.14.

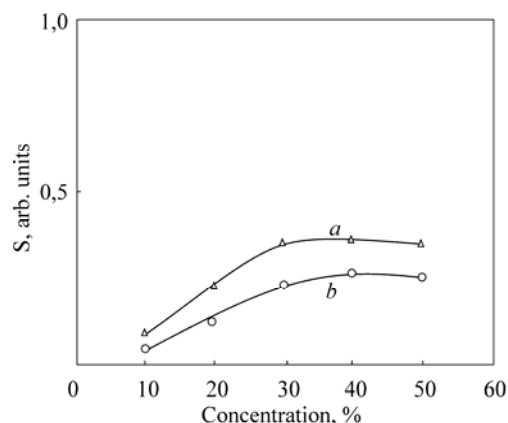


Fig.14. The dependence of degree of orientation order from concentration of KOH in water (a) and ethylenglycol (b).

Apparently, the degree of orientation order reaches the maximal value at concentration of KOH equaled to 30 %. Thus, the degree of orientation order after etching by solution of KOH in ethyleneglycol is higher than one in water.

In order to obtain the maximal effect, both methods of surface processing of silicon are used. In the beginning, the surface of silicon is bombarded by argon ions with energy of 250 eV and ion fluence of  $1.4 \cdot 10^{19} \text{ cm}^{-2}$  then poisoned within 40 minutes in the 30 percentage solution of KOH in ethyleneglycol at 60°C. The dependence of integrated absorption from voltage on the band with a maximum of  $1630 \text{ cm}^{-1}$  is shown on Fig.15.

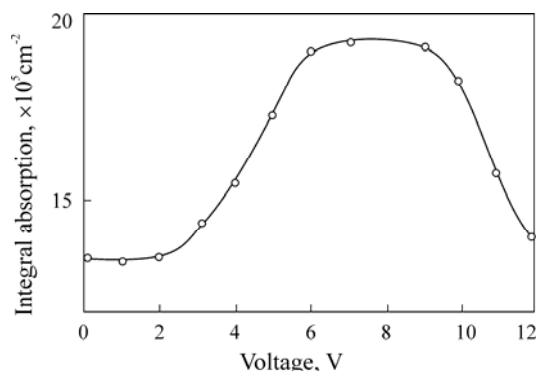


Fig.15. The dependence of integrated absorption from voltage on the band with a maximum of  $1630 \text{ cm}^{-1}$  for the plate processed by both methods.

Surface heterogeneities of nuclear scale arise during dispersion by the action of ionic bombardment. Similar effects can be observed both at falling separate ions and at the ion fluence reaching to  $10^{16} \text{ cm}^{-2}$  [12]. At even greater fluence there are microscopic observable heterogeneities with the sizes of 10-1000 nanometers. Enough high concentration of defects is collected inside the crystal at the ion fluence exceeding  $10^{17} \text{ cm}^{-2}$ . Thus there are local variations of

dispersion factor leading to essential changes of morphology of the surface, namely, etching poles, conic or pyramidal ledges, and also wavy structures. Depth of penetration of ions in depth of a target is small, and dispersion factors are great at argon ion bombardment. It prevents to accumulation of greater concentration of impurities. At the same time, the rate of defect formation should be, apparently, high and the effects connected with defect formation should prevail on the effects caused by accumulation of implanted particles.

Defects are formed on a surface as a result of displacement of atoms and can occur at very small ion fluences. During the occurrence and annihilation of defects, the balance is not established between mechanisms of their formation, transformation and disappearance as there is an erosion of a surface at heavy ion fluences of  $10^{13} \text{ cm}^{-2} - 10^{17} \text{ cm}^{-2}$ . There is a superfluous energy around of dislocations and defects which is connected to distortion of crystalline lattice. It is obvious, that chemical etchants act on these areas more strongly and promote formation of the centers of homeotropic orientation of LC molecules.

#### 4. Conclusion

It is shown that at preliminary bombardment of substrates by argon ions with energy of 250 eV with increasing the ion fluence the LC molecules are oriented planarly while at energy of 1.25 keV with increasing of ion fluence they are done planarly and then - homeotropically. Preliminary chemical etching of substrates by solution of KOH in water and ethyleneglycol only promotes to planar orientation of LC molecules. The greatest effect homeotropic orientation of LC molecules is given with preliminary bombardment of substrates by argon ions with energy of 250 eV at the subsequent etching by solution of KOH in ethyleneglycol.

The work is supported by the European Committees (the STCU grant No 4172).

- [1] L.M. Blinov, V.G. Chiginov, Electrooptic Effects in Liquid Crystal Materials., Springer Verlag, 1994,488p.
- [2] V.A. Belakov, A.S. Sonin, Optics of Cholesteric Liquid Crystals, Nauka, 1982, 360 P. (in Russian)
- [3] J. Konyar, Orientation of Nematic Liquid Crystals and their mixtures, Minsk, 1986, 311 p. (in Russian).
- [4] A.D. Remenuk, Ye.V. Astrova, R.F. Vitman, T.S. Perova, V.A. Tolmachev, D.K. Vij, Investigation of Orientation of Liquid Crystalline Mixture E7 in Composite Photonic Crystals on the Base of Single Crystalline Silicon, Solid State Physics, Vol 48, No 2, 2006, pp.361-367.
- [5] Ye.V. Astrova, T.S. Perova, S.A. Grudinkin, V.A. Tolmachev, Yu.A. Pilugina, V.B. Voronkov, D.K. Vij, Investigation of Orientation of the Molecules of Liquid crystal E7 in Composites on the Base of Split Silicon by Polarized Methods of Infrared Spectroscopy and Raman Scattering, Semiconductors, Vol 39, No 7, 2005, pp.793-801.
- [6] T.D. Ibragimov. Two-mode Modulation of Infrared Light by Small Particles-Liquid Crystal Composite. International Conference on Physics of Optical Materials and Devices. ICOM-2006., 2006, Hotel Plaza, Herceg Novi, Montenegro. p.46.
- [7] R. Behrisch, G. Betz, G. Carter, B. Navinsek, J. Roth, B.M. Scherzer, P.D. Townsend, G.K. Wehner, J.L. Whitton. Sputtering by Particle Bombardment.1983, Springer Verlag, 484 p.
- [8] N. Kirov, P. Simova. Vibrational Spectroscopy of Liquid Crystals. Publishing House of the Bulgarian Academy of Sciences, 1984, 329 p.
- [9] A.N. Kiselev, V.L. Levigunova, V.A. Perevoshikov, V.D. Skupov, Peculiarities of Morphology Change of Silicon Surface at Combination Irradiation of Ions of Various Masses, Surface, No 1, 2004, pp.88-91.
- [10] L.M. Blinov, Electro- and Magneto-optics of Liquid Crystals, Nauka, 1978, 279 p.
- [11] V.N. Matvienko, Ye.A. Kirsanov, Surface Events in Liquid crystals, MSU, 1991, 271 p.
- [12] A.Yu. Didak, M.A. Kozodayev, A. Hofman, V.K. Semina, Yu.N. Cheblukov. Effects of Surface Modification of Silicon at radiation of Fast Hight Ions, Surface, No 4, 2005, pp. 53-55.

**T.D. İbrahimov, N.C. İsmayilov, E.A. Allahverdiyev, İ.S. Həsənov, Q.M. Bayramov, A.R. İmaməliyev**

**SİLİSİUM VƏ GERMANİUM ALTLIQLARININ ƏVVƏLCƏDƏN ARQON İONLARI İLƏ BOMBARDMAN EDİLMƏSİNİN MAYE KRİSTAL MOLEKULLARININ DÜZÜLÜŞÜNƏ TƏSİRİ**

Spektrin infraqırmızı (İQ) oblastında şəffaf Si və Ge altlıqlarının əvvəlcədən arqon ionları ilə bombardman edilməsindən və kimyəvi aşındırmadan sonra maye kristal (MK) molekullarının bircinsli düzülüşü imkanları tədqiq edilmişdir. MK molekullarının düzülüşü İQ – spektroskopiya və dielektrik ölçmələri ilə müəyyənləşdirilmişdir.

Müəyyən edilmişdir ki, altlıqları 250 eV enerjili arqon ionları ilə bombardman edərkən şüalanma dozasının artması ilə MK molekullarının düzülüşü planar olur, ionların enerjisi 1.25 eV olduqda isə, şüalanma dozasının artması ilə düzülüş əvvəlcə planar, sonra isə homeotrop olur. Altlıqların KOH-ın etilenqlikol və su məhlullarında əvvəlcədən kimyəvi aşındırılması MK molekullarının yalnız planar düzülüşünə gətirir. MK molekullarının homeotrop düzülüşünə ən güclü təsir isə altlığın 250 eV enerjili arqon ionları ilə bombardman edilməsi və KOH-ın etilenqlikol məhlulunda sonrakı aşındırılması verir.

**Т.Д. Ибрагимов, Н.Д. Исмаилов, Э.А. Аллахвердиев, И.С. Гасанов, Г.М. Байрамов, А.Р. Имамалиев**

**ВЛИЯНИЕ ПРЕДВАРИТЕЛЬНОЙ БОМБАДИРОВКИ КРЕМНИЕВЫХ И ГЕРМАНИЕВЫХ ПОДЛОЖЕК ИОНАМИ АРГОНА НА ОРИЕНТАЦИЮ ЖИДКОКРИСТАЛЛИЧЕСКИХ МОЛЕКУЛ**

Исследована возможность однородной ориентации молекул жидкого кристалла (ЖК) после предварительной бомбардировки подложек (Si, Ge), прозрачных в инфракрасной (ИК) области спектра, ионами аргона, а также после химического травления. Контроль ориентации молекул ЖК производится методами ИК спектроскопии и диэлектрическими измерениями.

Установлено, что при предварительной бомбардировке подложек ионами аргона с энергией 250 эВ с увеличением дозы облучения молекулы ЖК ориентируются планарно, а при энергии ионов 1,25 эВ с ростом дозы облучения сначала планарно, а затем гомеотропно. Предварительное химическое травление подложек КОН в воде и этиленгликоле способствует только планарной ориентации молекул ЖК. Наибольший эффект гомеотропной ориентации молекул ЖК дает предварительная бомбардировка подложек ионами аргона с энергией 250 эВ с последующим травлением раствором КОН в этиленгликоле.

*Received: 10.07.08*

FeIn<sub>2</sub>S<sub>4</sub>-ÜN DİELEKTRİK XASSƏLƏRİ

N.N. NİFTİYEV

*Azərbaycan Dövlət Pedaqoji Universiteti, Az1000, Bakı, Ü. Hacıbəyov, 34*

O.B. TAĞIYEV

*AMEA Fizika institutu, Az1143, Bakı, H. Cavid pr., 33*

M.B. MURADOV

*Bakı Dövlət Universiteti, Az1145, Z. Xəlilov, 23*

F.M. MƏMMƏDOV

*AMEA Kimya Problemləri İnstitutu, Az1143, H. Cavid pr., 29*

Ü.F. KASUMOV

*AMEA Fizika institutu, Az1143, Bakı, H. Cavid pr., 33*

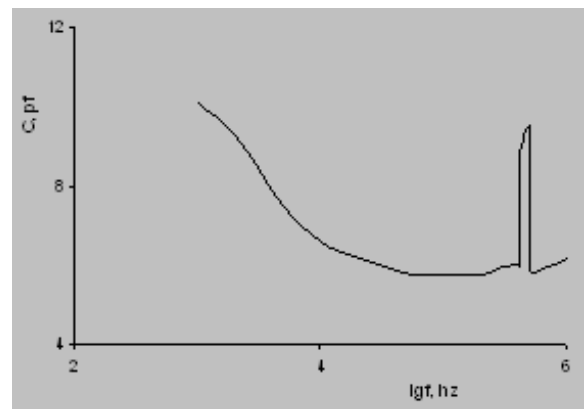
İşdə FeIn<sub>2</sub>S<sub>4</sub> birləşməsinin müxtəlif tezlik və temperaturalarda elektrik tutumu və dielektrik itki bucağının tangensi tədqiq edilmişdir. Kristalın dielektrik nüfuzluğu və yükdaşıyıcıların aktivləşmə enerjisi təyin olunmuşdur.  $C$  və  $tg\delta$  üçün tezliyin müəyyən qiymətlərində rezonans hadisəsi müşahidə edilmişdir. Müəyyən edilmişdir ki, 500kHz və 1MHz tezliklərdə temperatur artdıqca  $tg\delta$  eksponensial qanun üzrə artır.  $2 \cdot 10^3 \div 2,5 \cdot 10^5$  Hz tezlik intervalında  $tg\delta \sim 1/\omega$  tərs mütənəsb asılılığı müşahidə edilir.

Üçlü xalkogenid birləşmələr içərisində AB<sub>2</sub>X<sub>4</sub> (burada A- Mn, Fe, Co, Ni; B- Ga, In; X- S, Se, Te) tipli böyük sinif materiallar özünün mühüm fiziki xassələri sayəsində intensiv olaraq tədqiq edilir [1-9]. Bu birləşmələrin əsasında lazerlər, işıq modulyatorları, fotodedektorlar, termorezistorlar və s. funksional qurğular yaratmaq üçün perspektivlidir. Onlara müxtəlif aşqarlar vurmaqla fiziki xassələrini dəyişmək olar.

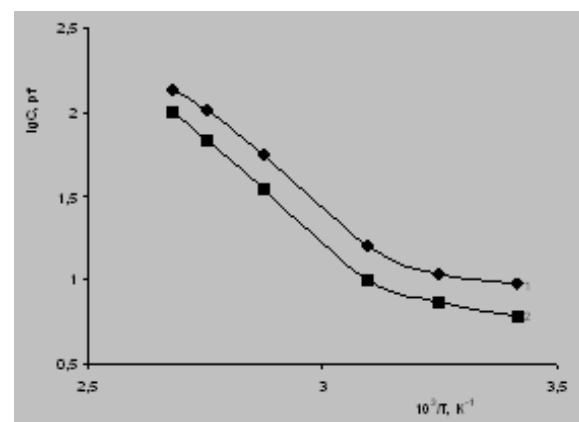
FeIn<sub>2</sub>S<sub>4</sub> kristalı AB<sub>2</sub>X<sub>4</sub> tipli birləşmələr sinfinə aid olub bəzi fiziki xassələri [10-16] işlərində tədqiq edilmişdir. Quruluş və maqnit xassələrinin öyrənilməsi nəticəsində müəyyən edilmişdir ki, FeIn<sub>2</sub>S<sub>4</sub> Neel temperaturundan ( $T_N=4,2K$ ) aşağı temperaturda antiferromaqnit materialdır [10,13]. [14] işində FeIn<sub>2</sub>S<sub>4</sub>-ün statik elektrik sahəsində elektrik xassələri tədqiq edilmiş və çevirmə effekti aşkara çıxarılmışdır. [15-16] işləri isə FeIn<sub>2</sub>S<sub>4</sub> nanokristalının alınmasına və elektrokimyəvi xassələrinin öyrənilməsinə həsr olunmuşdur. Hal-hazırkı işdə FeIn<sub>2</sub>S<sub>4</sub> birləşməsinin dielektrik xassələrinin tədqiqi nəticələri verilmişdir.

FeIn<sub>2</sub>S<sub>4</sub> kristalı stexiometrik miqdarda yüksək təmizlikli (99,999%) elementlər birləşməsindən alınmışdır. Rentgenoqrafik metodla analiz nəticəsində müəyyən edilmişdir ki, FeIn<sub>2</sub>S<sub>4</sub> birləşməsi kristal qəfəs parametrləri  $a=10,62\text{\AA}$  olan şpinel quruluşu malik olur [10,12]. Dielektrik xassələrini öyrənmək üçün qalınlığı  $\sim 0,5\text{mm}$  olan kristal lövhələrə gümüş pastası vuraraq kondensatorlar hazırlanmışdır. Kristallar 293÷400K temperatur intervalında tənzimlənə bilən kriostatda yerləşdirilmişdir. Temperatur ölçmələrinin dəqiqliyi  $\pm 0,5K$  təşkil edir. Elektrik tutumunun və dielektrik itkisinin tangens bucağının ölçülməsi E7-20 ( $25 \div 10^6$  Hz) rəqəmli immetans ölçü cihazının köməyi ilə aparılmışdır. Nümunəyə 1V ölçmə gərginliyi verilmişdir.

Şəkil 1-də 293K temperaturda yarımkeçirici kondensatoru üçün elektrik tutumunun ( $C$ ) cərəyan tezliyindən ( $f$ ) asılılıq qrafiki verilmişdir. Qrafikdən görünür ki, elektrik tutumu 1kHz tezlikdən başlayaraq 100kHz-ə qədər azalır. Sonra isə 400 kHz tezliyə qədər demək olar ki,  $C$  sabit qalır. 420÷500 kHz tezlik intervalında isə rezonans hadisəsi baş verir.



Şəkil 1. FeIn<sub>2</sub>S<sub>4</sub> kristalı üçün 293K temperaturda elektrik tutumunun tezlikdən asılılığı.



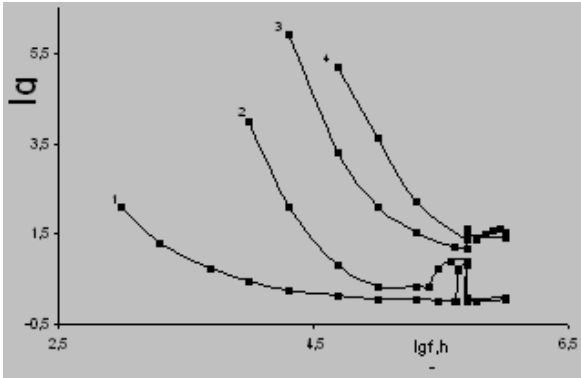
Şəkil 2. FeIn<sub>2</sub>S<sub>4</sub> kristalı üçün müxtəlif tezliklərdə elektrik tutumunun temperaturdan asılılığı: 1 - 500kHz, 2 - 1MHz.

Şəkil 2-də FeIn<sub>2</sub>S<sub>4</sub> birləşməsi üçün 500kHz (1 əyrisi) və 1MHz (2 əyrisi) tezliklərdə elektrik tutumunun temperatur-

dan asılılıq qrafiki verilmişdir. Şəkildən görünür ki, 293÷323K temperatur intervalında  $C$  temperaturdan asılı olaraq zəif artır. 323÷373K temperatur aralığında isə  $C$  bir qədər sürətlə artır. Bu hissə üçün  $\lg C \sim 10^3/T$  asılılığından aktivləşmə enerjisi hesablanmış və  $E = 0,44$  eV qiyməti tapılmışdır.

$$C = \varepsilon \varepsilon_0 S / d$$

düsturundan dielektrik nüfuzluğu ( $\varepsilon$ ) hesablanmış və müəyyən edilmişdir ki, tədqiq olunan temperatur və tezlik intervalında  $\varepsilon$  - nün qiyməti 300 ÷ 2800 intervalında dəyişir. Temperatur artdıqca elektrik tutumunun, həmçinin dielektrik nüfuzluğunun artmasının səbəbi yükdaşıyıcıların konsentrasiyasının artmasıdır.



Şəkil 3. FeIn<sub>2</sub>S<sub>4</sub> kristalı üçün müxtəlif temperaturlarda dielektrik itkisinin tangens bucağının tezlikdən asılılığı: 1 - 293K, 2 - 323K, 3 - 338K, 4 - 363K.

Şəkil 3-də FeIn<sub>2</sub>S<sub>4</sub> kristalı üçün müxtəlif temperaturlarda dielektrik itkisinin tangens bucağının ( $\tan \delta$ ) dəyişən cərəyan tezliyindən asılılıq qrafiki göstərilmişdir.

Şəkildən görünür ki, tədqiq olunan temperaturlarda tezlik artdıqca  $\tan \delta$  -nın qiyməti azalır,  $2,5 \cdot 10^5 \div 5 \cdot 10^5$  Hz tezlik intervalında isə rezonans hadisəsi baş verir.

Temperatur yüksəldikcə rezonans piklərinin maksimumlarının qiyməti azlir. Məlumdur ki, yarımkeçirici və dielektrlərdə itki kristalın quruluşundan və defektlərin təbiətindən asılıdır. Defektlərin konsentrasiyası dielektrik itkisinin qiymətini əhəmiyyətli dərəcədə dəyişə bilər. Dielektrlərdə itki bucağının dəyişən elektrik sahəsinin tezliyindən asılılığını aydınlaşdırmaq üçün fərz edək ki, paralel birləşmə zamanı dielektrik  $C$  tutumuna malik kondensator və  $R$  aktiv müqavimətli naqıl ilə əvəz edilmişdir. Bu zaman itki bucağının tangensini belə ifadə etmək olar:

$$\tan \delta = j_a / j_r = 1 / \omega C R \quad (1)$$

Burada  $j_a$  – aktiv,  $j_r$  – reaktiv cərəyan sıxlığı,  $\omega = 2\pi f$  – tezlikdir.

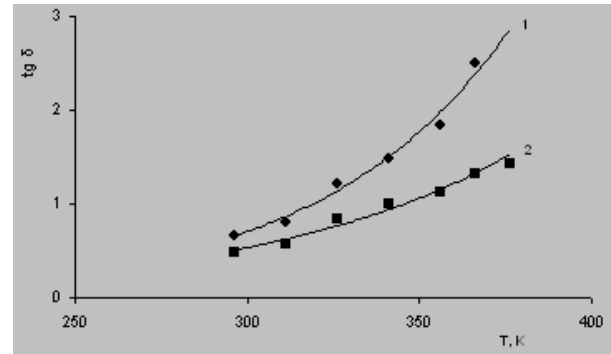
FeIn<sub>2</sub>S<sub>4</sub> kristalı üçün  $2 \cdot 10^3 \div 2,5 \cdot 10^5$  Hz tezlik intervalında  $C$  və  $R$ -in tezlikdən asılı olaraq dəyişməsi az olduğun-

dan, onu nəzərə almasaq, itki bucağının tangensinin tezliklə tərs mütənəsis asılılığının ödənildiyini görürük ( $\sim 1/\omega$ ). Ona görə də şəkil 3-dəki itki bucağının tangensinin tezlikdən asılılıq qrafiki (1) ifadəsinə uyğundur.

Şəkil 1 və 3-dəki  $C$  və  $\tan \delta$ -nın tezlikdən asılılığında müşahidə edilən rezonans hadisəsini baryer modelinin [17] köməyi ilə izah etmək olar. Belə ki, yüksək müqavimətli laylara malik defekt kristallarda lokal baryerə malik müxtəlif qeyri-bircinsliliklərlə (məs: dislokasiya, elektrik domeni) lokallaşmış aşağı müqavimətli bağlayıcı laylar ola bilər. Bağlayıcı layların qalınlığı və birləşmə xüsusiyyətinin elektrik sahəsi gərginliyi və tezliyindən asılılığı onları aktiv element edir.  $\nu$  tezliyi ( $\nu$  – konsentrasiya dalğasında yükdaşıyıcıların rəqs tezliyidir) layın  $d$  qalınlığı və  $v_d$  dreyf sürətindən təyin olunur [17]:

$$2d = v_d / \nu$$

Belə ki, xarici dəyişən elektrik sahəsinin  $f$  tezliyi  $\nu$  tezliyinə bərabər olduğu üçün rezonans hadisəsi baş verir. Rezonans hadisəsinin azalmasının səbəbini belə izah etmək olar ki, temperatur yüksəldikcə  $\nu$  tezliyi yüksəlir və  $f$  xarici sahənin tezliyindən fərqlənir.



Şəkil 4. FeIn<sub>2</sub>S<sub>4</sub> kristalı üçün müxtəlif tezliklərdə dielektrik itkisinin tangens bucağının temperaturdan asılılığı: 1 - 500kHz, 2 - 1MHz.

Şəkil 4 -də FeIn<sub>2</sub>S<sub>4</sub> kristalı üçün  $5 \cdot 10^5$  Hz (1 əyrəsi) və 1MHz (2 əyrəsi) tezliklərdə itki bucağı tangensinin temperaturdan asılılıq qrafiki verilmişdir. Şəkildən görünür ki,  $\tan \delta$  temperatur artdıqca eksponensial qanun üzrə artır.

Beləliklə, işdə FeIn<sub>2</sub>S<sub>4</sub> birləşməsinin müxtəlif temperatur və tezliklərdə elektrik tutumu və dielektrik itki bucağının tangensini tədqiq edilmiş və onların təcrübi qiymətləri hesablanmışdır. FeIn<sub>2</sub>S<sub>4</sub> üçün yükdaşıyıcıların aktivləşmə enerjisi təyin edilmişdir. Müəyyən edilmişdir ki, temperatur artdıqca  $C$  və ya  $\varepsilon$ -nün artmasının səbəbi yükdaşıyıcıların konsentrasiyasının artımıdır.  $C$  və  $\tan \delta$  üçün tezliyin müəyyən qiymətlərində rezonans hadisəsi müşahidə edilmişdir. Müəyyən edilmişdir ki, 500 kHz və 1MHz tezliklərdə temperatur artdıqca  $\tan \delta$  eksponensial qanun üzrə artır.

- [1] K.Z. Rushchanskii, H. Hacusele, D.M. Bercha. J. of Physics and chemistry of Solids. 2002. v.63, p.2019.  
[2] A. Memo, W. Kwarteng – Acheampong, H. Heausele. Mat. Res. Bull. 2003, v.38, n.6, p.1057.

- [3] N. Tsuboi, K. Ogihara, U. Suda, K. Oishi, S. Kobayashi, F. kaneko. Jap. Journal of Applied Physics 2005. v.44, p.725.  
[4] C.Cedeno, C. Diaz de Delgado, J. M. Delgado, L. M. de Chalbaunt, V.Sagredo. J. of Physics and chemistry of solids. 2005. v.66, p.2049.



- [5] *T. Torres, V. Saqredo, L.M. de Chalbaund, G. Attolini, F. Bolzoni.* Physics of Condensed Matter. 2006. v.384, p.100.
- [6] *F.J. Manjon, A. Segura, M. Amboage, J. Pellicer, J.F. Sanchez-Royo and at. al.* Physics Status Solidi ( b ). 2006. v.244, p.229.
- [7] *V. Sagredo, M.C. Moron, L. Betancourt, G.E. Delgado.* J. of Magnetic Materials. 2007. v.312, p.294.
- [8] *N.N. Niftiyev, O.B. Tagiyev.* FTP. 2007. t.41, v.1, s.17 (rusca)
- [9] *N.N. Niftiyev, O.B. Tagiyev, M.B. Muradov.* FTP. 2008. t.42, v.3, s.268 (rusca)
- [10] *T. Kanomata, H. Ido, T. Kaneko.* J. Phys. Soc. Japan. 1973. v.34. № 2, p.554.
- [11] *B.K. Babayeva.* Troynie poluprovodniki i ix primeneniye. Kişinyev: Ştiinça 1976. s.96 (rusca).
- [12] *P.G. Pustamov, B.K. Babayeva, M.R. Allazov.* Jurnal neorqan. ximii. 1979. t.24. № 8, s.2208 (rusca).
- [13] *S. Schlein, W. Aoran.* J. of Solid State chemistry. 1972. v.4, № 2, P.286
- [14] *N.N. Niftiyev, M.A. Alidjanov, O.B. Tagiyev, M.B. Muradov.* Ukr. fiz. Journ. 2002. t.47, № 11. s.1054 (rusca).
- [15] *G. Lu, J. Hu, K. Gian, G. Zhou.* Chem. Lett. 1999. v.6, p.481.
- [16] *C. Xiangyinf, Z. Zhongjie, Z. Xingfa, L. Jianwei, Q. Yitai.* J. of Cristal Growth. 2005. v.277, p.524.
- [17] *P. G. Oreşkin.* Fizika poluprovodnikov i dielektrikov. Vısşaya şkola. 1977, s.448 (rusca).

**N.N. Niftiyev, O.B. Tagiev, M.B. Muradov, F.M. Mamedov, U.F. Kasumov**

#### **DIELECTRIC PROPERTIES OF FeIn<sub>2</sub>S<sub>4</sub>**

The ewlectric capacity and dielectric loss tangent at different frequencies and temperatures for FeIn<sub>2</sub>S<sub>4</sub> compound have been investigated. The crystal dielectric constants and activation energies of electric current carriers have been obtained. The resonance phenomenon  $C$  and  $tg\delta$  is observed at definite frequencies. It is established that  $tg\delta$  increases under exponential law at frequencies 500kHz and 1MHz with temperature increase. The  $tg\delta \sim 1/\omega$  dependence is observed in frequency interval  $2 \cdot 10^3 \div 2,5 \cdot 10^5$  Hz.

**Н.Н. Нифтиев, О.Б. Тагиев, М.Б. Мурадов, Ф.М. Мамедов, У.Ф. Касумов**

#### **ДИЭЛЕКТРИЧЕСКИЕ СВОЙСТВА FeIn<sub>2</sub>S<sub>4</sub>**

Исследованы электрические ёмкости и тангенс угла диэлектрических потерь при различных частотах и температурах для соединения FeIn<sub>2</sub>S<sub>4</sub>. Определены диэлектрические проницаемости кристаллов и энергии активации электрических носителей тока. При определенных частотах наблюдается резонансное явление  $C$  и  $tg\delta$ . Установлено, что с ростом температуры  $tg\delta$  растёт по экспоненциальному закону при частотах 500кГц и 1МГц. В интервале частот  $2 \cdot 10^3 \div 2,5 \cdot 10^5$  Гц наблюдается зависимость  $tg\delta \sim 1/\omega$ .

*Received: 09.07.08*

## SİLİNDRİK GÜZGÜ DAXİL EDİLMİŞ DİFRAKSİYON OPTİK SİSTEMİN AYIRDETMƏ QABİLİYYƏTİNİN EKRAN MƏSAFƏSİNDƏN ASILILIĞI

T.H. DİLBAZOV, N.Y. YAQUBZADƏ, S.A. SÜLEYMANOVA, R.B. ABBASOVA

*Elmi-Tədqiqat Aerokosmik İnformatika İnstitutu, MAKİA*

*AZ 1106, Bakı Azadlıq prospekti, 159*

Silindrik güzgülə daxil edilmiş difraksiyon sistemdə güzgülə ilə çıxış yarığı arasındakı məsafədən asılı olaraq sistemin ayırdetmə qabiliyyətinin dəyişməsi tədqiq edilmişdir.

Spektroskopiyanın tətbiq sahəsinin genişliyi onun üsul və vasitələrinin təkmilləşdirilməsinin, mövcud cihazların texniki parametrlərinin optimallaşdırılmasının daim gündəmdə olmasını tələb edir [1]. Ona görə də cihazların hər bir optik elementinin göstəricilərinin yaxşılaşdırılması tədqiqat obyektinə çevrilə bilər [2, 3].

Spektrometrik cihazların parametrlərinin yaxşılaşdırılması istiqamətində aparılan tədqiqatlar [4] çökük difraksiya qəfəslili klassik optik sistemə silindrik güzgülə daxil etməklə sistemin dispersiyasını və ayırdetmə qabiliyyətini (AQ) əhəmiyyətli dərəcədə artırmanın mümkün olduğunu göstərmişdir.

Bu üsul, [5] -də göstərilədiyi kimi, mövcud üsullardan daha effektiv olmaqla yanaşı konstruktiv cəhətdən də sadə və əlverişlidir: klassik optik sistemin fokus müstəvisində silindrik güzgüləni spektrin səthinə perpendikulyar yerləşdirib əks olunan şüanı istənilən istiqamətə yönəltmək olar. Bu halda cihazın əsas parametrləri olan dispersiya və AQ xeyli yaxşılaşır, ölçü-çəki parametrləri isə demək olar ki, dəyişmir.

Müəyyən edilmişdir ki, silindrik güzgülə daxil edilmiş difraksiyon sistemin AQ, dispersiyaetdirici elementin dispersiyası ilə məhdudlaşmaqla bərabər, sistemin başqa parametrlərindən də asılıdır [5]:

$$\frac{\lambda}{\delta\lambda} = D \cdot \left[ 3 - 2 \frac{S'}{r} \right] \left( \frac{d\varphi}{d\lambda} \right)_q = \frac{A \cdot D \cdot S''}{\cos \psi} \left[ 3 - 2 \frac{S'}{r} \right] \left( \frac{d\varphi}{d\lambda} \right)_q \dots \quad (1)$$

Burada  $\frac{\lambda}{\delta\lambda}$  – sistemin AQ,  $A = \frac{D}{f}$  – nisbi dəşik,  $D$  – di-

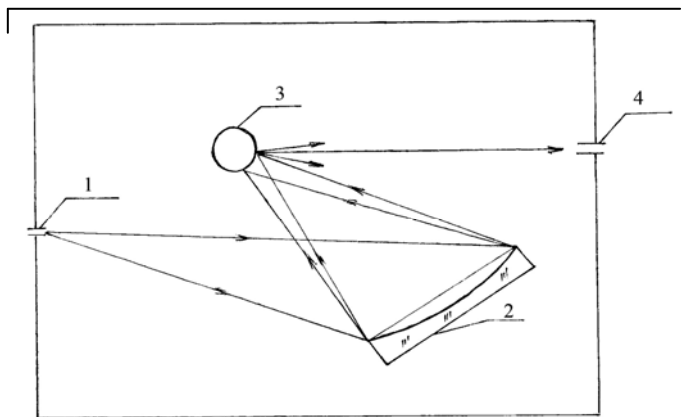
afraqmanın eni,  $f$  – giriş obyektivinin fokus məsafəsi,  $S'$  – qəfəslə güzgülə,  $S''$  – isə güzgülə ilə çıxış yarığı arasındakı məsafədir.  $r$  – güzgülənin radiusu,  $\left( \frac{d\varphi}{d\lambda} \right)_q$  – qəfəsin bucaq dispersiyası,  $\psi$  – spektrin səthinə çəkilən normala işıq dəstəsinin orta şüası arasındakı bucaqdır.

(1) ifadəsindən göründüyü kimi silindrik güzgülə daxil edilmiş sistemin AQ klassik sistemi xarakterizə edən kəmiyyətlərdən ( $A, D, \psi$ ) başqa, qəfəslə güzgülə arasındakı məsafədən, güzgülənin radiusundan və güzgülə ilə çıxış yarığı arasındakı məsafədən – ekran məsafəsindən asılıdır. Qəfəslə güzgülə arasındakı məsafəni çoxaltmaqla sistemin AQ-ni artırmaq məqsəduyğun deyil, çünki qəfəslə güzgülə arasındakı məsafənin artması cihazın ölçülərinin böyüməsinə səbəb olur. Silindrik güzgülə daxil etməklə işləyən ortik sistemlər isə yüksək AQ-li, kiçik ölçülü spektrometrik cihazlar yaradılması məqsədinə xidmət edir.

Silindrik güzgülə daxil edilmiş çökük difraksiya qəfəslili ortik sistemdə güzgülənin diametrini dəyişməklə aparılan tədqiqatların [5, 6] nəticələri göstərir ki, belə sistemlərin köməyi ilə dispersiyaetdirici elementin AQ-nə yaxın AQ olan kiçik ölçülü spektrometrlərin yaradılması mümkündür.

Təqdim olunan işdə silindrik güzgülə daxil edilmiş çökük difraksiya qəfəslili optik sistemin AQ-nin ekran məsafəsindən asılılığının təcrübi nəticələri şərh edilir. Təcrübə aparılan qurğu [6]-də olduğu kimi SbCe fotokatodlu fotoqəbuledicidən, yüksək giriş müqavimətli mikrosxem əsasında yığılmış gücləndiricidən, qeydedici cihaz kimi KСП-4 tipli özuyazan potensiometrədən ibarətdir. Spektrin skanlanması, qəfəsin şaquli ox ətrafında fırlanması ilə aparılır.

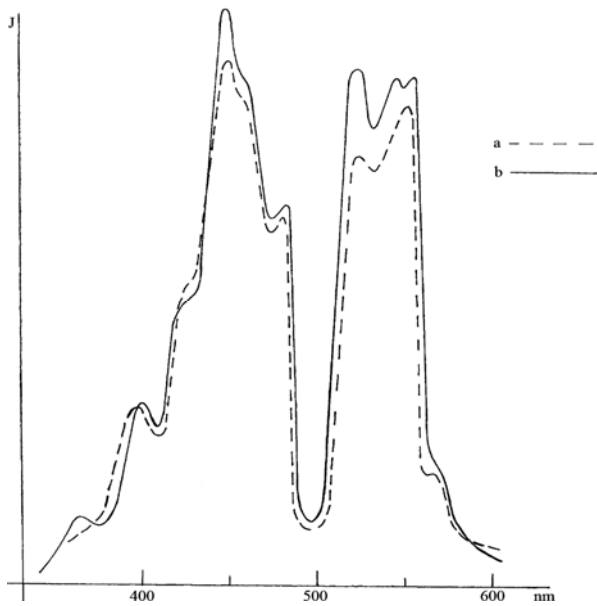
Sistem şəkil 1-də göstərilmişdir.



Şəkil 1. Silindrik güzgülə daxil edilmiş difraksiyon sistem.

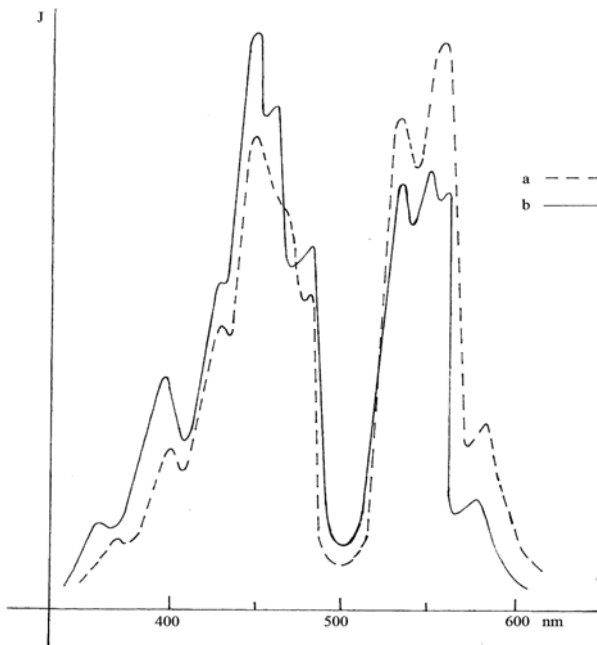
Civə lampasının işığı fokuslayıcı sistemin köməyi ilə 2- çökük difraksiya qəfəsinin fokusunda yerləşən 1- giriş yarığına yönəldilir, qəfəsdən əks olunan spektr qəfəsin fokusunda yerləşən 3- güzgüləsinə düşərək əks olunur. Güzgüdən əks olunan şüalar düşən şüalara nisbətən çox «aralandığından», 4- çıxış yarığından keçən şüaların monoxromatikliyi artır. Katod tərəfdən fotoqəbuledicinin pəncərəsi çıxış yarığına bərkidilmişdir və birlikdə rels üzərində irəliləmə hərəkəti edə bilirlər. Fotoqəbuledicinin həssaslığı spektrin görünən oblastını əhatə etdiyindən cıvənin göy ( $\lambda_{max}=404-407$ ; 435,8nm) və yaşıl ( $\lambda_{max}=546,1nm$ ) xətləri tədqiq edilmişdir. Diametri 10 mm və 5 mm olan güzgülərdən, ekran məsafələri 40 mm və 50 mm olan hallarda çıxış yarığından keçən cıvə xətlərinin görünən oblastdakı spektrləri araşdırılır.

Şəkil 2-də cıvə lampasının diametri 10 mm olan silindrik güzgülədən əks olunmuş spektri göstərilmişdir.



Şəkil 2. Diametri 10 mm olan güzgüdən əks olunmuş spektrlər :  
a-ekran məsafəsi 40 mm; b- ekran məsafəsi 50 mm

Güzgü ilə çıxış yarığı arasındakı məsafə 40 mm (a) və 50 mm (b) olduqda  $\lambda_{max}=404-435,8$  nm oblastındakı göy xəttin spektrində ciddi dəyişikliklər müşahidə olunur,  $\lambda_{max}=546,1$  nm olan yaşıl xəttin dəyişikliyi isə hiss olunacaq qədərdir: güzgü ilə çıxış yarığı arasındakı məsafə 40 mm olan halda bu xəttin 2 maksimumu aydın göründüyü halda, məsafə 50 mm olduqda daha bir xəttin maksimumu seçilir. Güzgü ilə çıxış yarığı arasındakı məsafə 30 mm olduqda ümumi mənzərə məsafə 40 mm olan haldan az fərqlənir.



Şəkil 3. Diametri 5 mm olan güzgüdən əks olunmuş spektrlər:  
a-ekran məsafəsi 40 mm ; b- ekran məsafəsi 50 mm.

Şəkil 3-də cıvə lampasının göy və yaşıl xətlərinin diametri 5 mm olan güzgüdən əks olunmuş spektri göstərilmişdir.

Güzgü ilə çıxış yarığı arasındakı məsafə 40 mm (a) olduqda göy xəttin maksimumunda simmetrikinin pozulması, bu oblastda başqa xəttin də olmasını deməyə əsas verir. Güzgü ilə çıxış yarığı arasındakı məsafə 50 mm (b) olan halda spektrdə əhəmiyyətli dəyişiklər müşahidə olunur:  $\lambda_{max}=435,8$  nm zolağı «parçalanaraq» bir-birinə yaxın 2 xəttə ayrılır. Cıvə lampasının spektrində bu oblastda  $\lambda_{max}=433,9$  nm və  $\lambda_{max}=434,4$  nm xətlərinin olması [6]-da qeyd edilmişdir. Burada həmin xətlərdən birinin, bəlkə də ikisinin birlikdə əmələ gətirdiyi zolağın maksimumunun vəziyyəti dəqiq qeyd olunur.  $\lambda_{max}=546,1$  nm olan xəttin də spektrdə 3 maksimumun vəziyyəti ayırd edilir.

Yüksək AQ-li spektral cihazların köməyi ilə aparılan tədqiqatlar [7] nəticəsində cıvənin yaşıl xəttinin  $6^3P_2 - 7^3S_1$  keçidi ilə bağlı olduğu və bu xəttin incə strukturunda cıvənin izotoplarına məxsus müxtəlif intensivlikli 14 xəttin olduğu müəyyən edilmişdir. Bunlardan cıvənin  $H_q^{198}, H_q^{200}, H_q^{202}, H_q^{204}$  izotoplarının əmələ gətirdiyi xətlərin intensivliyi nisbətən böyük olub  $\lambda_{max}=546,1$  nm xətti ilə müqayisə oluna bilirlər.

Silindrik güzgü daxil edilmiş difraksiyon sistemdə güzgü ilə çıxış yarığı arasındakı məsafəni dəyişdikdə spektrdə vəziyyətləri qeyd oluna bilən «yeni» xətlərin cıvənin izotoplarına məxsus olduğu şübhə doğurmur.

Beləliklə, silindrik cüzcü daxil edilmiş difraksiyon sistemdə güzgü ilə çıxış yarığı arasındakı məsafəni çoxaltmaqla aparılan tədqiqatlar sistemin AQ-ni artırmağın mümkünlüyü ilə yanaşı, (1) - ifadəsindəki AQ ilə ekran məsafəsi arasındakı asılılığı təsdiq edir.

Müxtəlif diametrli güzgülərlə aparılan təcrübələrin nəticələri [6], belə sistemin AQ-nin (1) ifadəsində olduğu kimi güzgünün diametri ilə tərs mütənasib olaraq dəyişdiyini nəzərə alsaq, kiçik ölçülü, yüksək AQ-li spektrometrik cihazların işlənməsi zamanı hər iki asılılıqdan həm ayrı-ayrılıqda, həm də hər ikisindən eyni zamanda istifadə etmək olar. Bunun təsdiqi kimi bir faktı qeyd etmək olar: başqa parametrlər eyni olduqda diametri 10 mm olan güzgüdən əks olunaraq 50 mm məsafədə yerləşən çıxış yarığından keçən spektrlə, diametri 5 mm olan güzgüdən əks olunaraq 35 mm məsafədə yerləşən çıxış yarığından keçən spektr, demək olar ki, eynidir.

Silindrik güzgü daxil edilmiş difraksiyon sistemin AQ-nin güzgünün ölçüsündən və ekran məsafəsindən asılılığından istifadə etməklə texniki göstəriciləri müasir analoqlarından üstün olan spektrometrik cihazlar yaratmaq mümkündür.

Silindrik güzgü daxil edilmiş çökük qəfəslili difraksiyon sistemin bəzi üstünlüklərini qeyd edək :

-difraksiya qəfəsinin və güzgünün vəziyyətlərinin seçilməsindən asılı olaraq çıxış yarığını cihazın gövdəsində ölçmələrin aparılması üçün münasib olan istənilən istiqamətdə yerləşdirmək olar;

-müxtəlif diametrli güzgülərdən, yaxud xüsusi formalı hazırlanmış bir güzgüdən istifadə etməklə AQ iş prosesində dəyişdirilə bilən müşahidə cihazları işləmək mümkündür ;

-müasir texnologiya çox yüksək AQ-li, aberrasiyaları azaldılmış, ştrixləri arasındakı məsafələr müxtəlif olan qoloqrafik çökük difraksiya qəfəsləri hazırlamağa imkan verir [8]. Belə dispersiyaetdirici elementdən silindrik güzgü daxil edilmiş difraksiyon sistemlərdə istifadə etməklə spektrdə incə strukturları belə tədqiq etməyə imkan verə biləcək kiçik ölçüçəki parametrlili cihazlar işləmək olar .

Slindrik güzgülə daxil edilmiş çökük difraksiya qəfəsləri difraksiya optik sistemin köməyi ilə çoxkanallı spektrometrlərin işlənməsi də məqsəduyğundur. Slindrik güzgülədən əks olunan spektrın dispersiyası (həm də AQ) güzgülədən çıxış yarığına qədər olan məsafədən asılı olduğundan, müxtəlif ka-

nallarda spektrın müxtəlif  $\Delta\lambda$  oblastını ayırmaq olar. Belə spektrometrlərdə işıq ötürücü vasitələrin və interferensiya filtrlərin istifadə edilməsinə ehtiyac olmadığından, faydalı siqnalın itgisi əhəmiyyətli dərəcədə azalır.

- |   |   |
|---|---|
| [1] Yu.B. Bajanov, L.K. Timergazeev. Opticheskiy jurnal. 2004, t.71, №1, s.17-22. (rusca)   | [5] T.H. Dilbazov, N.Y. Yaqubzadə. Fizika, 2006, c. 12, №4, s. 71-73.                               |
| [2] L.L. Doskolovich, S.I. Kharitonov. Opticheskiy jurnal. 2005, t.72, №4, s.34-38. (rusca) | [6] N.Y. Yaqubzadə, R.B. Abbasova, T.H. Dilbazov. MAKА-nın xəbərləri. 2007, c.7, № 1-2, s. 108-112. |
| [3] A.B. Гринкович. Opticheskiy jurnal. 2006, t.73, №5, s. 48-51. (rusca)                   | [7] F.A. Korolyov, V.I. Odintsov. Optika i spektroskopiya. 1956, t.1, №1, s.17-21.                  |
| [4] N.Y. Yaqubzadə, T.H. Dilbazov. MAKА-nın xəbərləri. 2006, № 3-4, s. 83-88.               | [8] N.K. Pavlicheva. Opticheskiy jurnal. 2002, t.69, №4, s.69-75.                                   |

**T.G. Dilbazov, N.Y. Yagubzade, S.A. Suleymanova, R.B. Abbasova**

**THE DEPENDENCE OF THE RESOLUTION OF DIFFRACTION SYSTEMS  
ON THE SCREEN DISTANCE**

The dependence of the resolution of spectrometer systems on the distance between cylindrical mirror and output slit is investigated. The experiment results show that the resolution of the system increases at the increase of the distance between mirror and output slit.

**Т.Г. Дилбазов, Н.Я. Ягубзаде, С.А. Сулейманова, Р.Б. Аббасова**

**ЗАВИСИМОСТЬ РАЗРЕШАЮЩЕЙ СПОСОБНОСТИ ДИФРАКЦИОННОЙ СИСТЕМЫ  
ОТ ЭКРАННОГО РАССТОЯНИЯ**

Исследована зависимость разрешающей способности спектрометрической системы от расстояния между цилиндрическим зеркалом и выходной щелью.

Результаты эксперимента показывают, что с увеличением расстояния между зеркалом и выходной щелью повышается разрешающая способность системы.

*Received: 11.03.08*

## ETİLPROPIONATIN ÖZLÜ AXINININ AKTİVLƏŞMƏ PARAMETRLƏRİ VƏ TERMİK XASSƏLƏRİ

E.Ə. MƏSİMOV, B.G. PAŞAYEV, H.Ş. HƏSƏNOV

*Bakı Dövlət Universiteti, Az-1148, Z. Xəlilov, 23*

K.D. HÜSEYNOV

*Azərbaycan Dövlət Pedaqoji Universiteti, Az1000, Bakı, Ü. Hacıbəyov, 34*

İşdə etilpropionatın 300-500 K temperatur və 5-50 MPa təzyiq intervalında özlü axının aktivləşmə parametrləri, istidən həcm genişlənmə əmsalı və izotermik sıxılma əmsalı hesablanmış, bu parametrlərin temperaturdan və təzyiqdən asılı olaraq dəyişmələri təhlil edilmişdir. Alınan nəticələr göstərir ki,  $\Delta H_{\eta}^* = f(T)_p$ ,  $\Delta S_{\eta}^* = f(T)_p$ ,  $\alpha_p = f(T)_p$  və  $\beta_T = f(T)_p$  asılılıqlarında izobarlar,  $\Delta H_{\eta}^* = f(P)_T$ ,  $\Delta S_{\eta}^* = f(P)_T$ ,  $\alpha_p = f(P)_T$  və  $\beta_T = f(P)_T$  asılılıqlarında isə izotermaların uzantıları bir nöqtədə kəsişirlər.

Etilpropionat propion turşusunun mürəkkəb efiridir, adi halda şəffafdır, kimya texnologiyasının bir çox sahələrində tətbiq olunur və fərdi mayelər qrupuna aiddir. Bu mayenin sıxlığı və dinamik özlülüğü təəffüzdən geniş temperatur və

təzyiq intervalında ətraflı şəkildə tədqiq edilmişdir [1] və həmin nəticələr hal parametrlərinin uyğun qiymətlərində 1 və 2 sayılı cədvəllərdə verilmişdir.

Cədvəl 1

Müxtəlif təzyiq və temperaturlarda etilpropionatın dinamik özlülüğü ( $\eta$ , mPa·san).

T, K	5 MPa	10 MPa	20 MPa	30 MPa	40 MPa	50 MPa
300	0,504	0,533	0,573	0,612	0,651	0,690
325	0,394	0,413	0,445	0,477	0,509	0,538
350	0,313	0,331	0,360	0,389	0,416	0,441
375	0,255	0,271	0,294	0,317	0,341	0,364
400	0,209	0,224	0,243	0,264	0,287	0,309
425	0,172	0,184	0,202	0,222	0,242	0,261
450	0,141	0,152	0,169	0,187	0,206	0,225
475	0,115	0,125	0,141	0,159	0,178	0,196
500	0,092	0,103	0,118	0,134	0,152	0,169

Cədvəl 2

Müxtəlif təzyiq və temperaturlarda etilpropionatın sıxlığı ( $\rho$ , kg/m<sup>3</sup>).

T, K	5 MPa	10 MPa	20 MPa	30 MPa	40 MPa	50 MPa
300	886,4	891,2	900,3	908,5	915,8	923,2
325	861,9	867,2	876,1	884,2	892,3	900,4
350	834,1	839,8	850,6	860,7	869,7	878,1
375	805,9	813,2	825,7	836,8	847,2	855,0
400	776,2	785,8	799,7	813,2	824,9	836,0
425	744,0	753,7	772,7	788,8	802,8	815,1
450	708,0	721,6	745,0	764,4	780,6	794,6
475	669,5	687,9	716,5	738,8	757,0	773,8
500	624,0	653,9	689,2	714,2	734,6	751,8

Təcrübənin xətası dinamik özlülük əmsalı ( $\eta$ ) üçün 1-2%, sıxlıq ( $\rho$ ) üçün isə 0.05-0.07% olmuşdur. Cədvəllərdən görünür ki, maye etilpropionatın fiziki xassələri hal parametrlərindən ciddi şəkildə asılıdır.

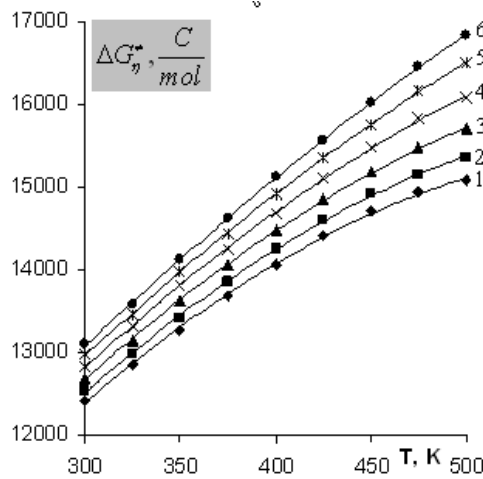
İşdə qarşıya qoyulan məqsəd geniş təzyiq və temperatur intervalında etilpropionatın ( $C_2H_5COOC_2H_5$ ) özlü axının aktivləşmə parametrlərini ( $\Delta G_{\eta}^*$ ,  $\Delta H_{\eta}^*$ ,  $\Delta S_{\eta}^*$ ), istidən həcm genişlənmə əmsalını ( $\alpha_p$ ) və izotermik sıxılma əmsalını ( $\beta_T$ ) təyin etmək, bu parametrlərin təzyiq və temperatur asılılıqlarında müşahidə olunan qanunauyğunluqları müəyyənəlmək olmuşdur. Bu məqsədlə 5-50 MPa təzyiq və 300-500K

temperatur intervalında etilpropionatın dinamik özlülüğünün və sıxlığının qiymətlərindən istifadə edərək, baxılan təzyiq və temperaturlarda özlü axının aktivləşmə parametrləri, istidən həcm genişlənmə və izotermik sıxılma əmsalları təyin edilmiş və bunlara əsasən baxılan mayədə yaranan struktur xüsusiyyətləri təhlil edilmişdir.

Özlü axının aktivləşmə parametrlərinin təyini üsulu [2, 3] işlərində ətraflı verilmişdir.

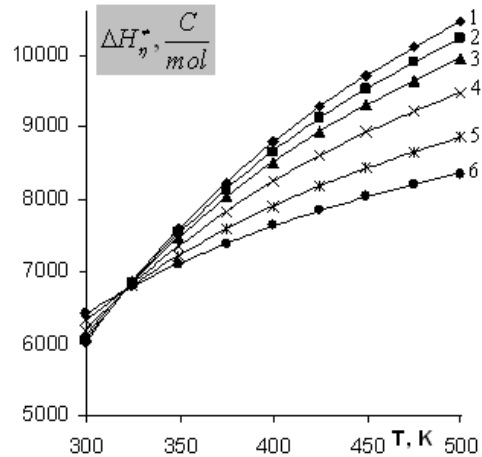
Etilpropionatın özlü axınının aktivləşmə parametrlərinin müxtəlif izobarlarının temperaturdan asılılıqları 1-3 sayılı şəkillərdə göstərilmişdir.



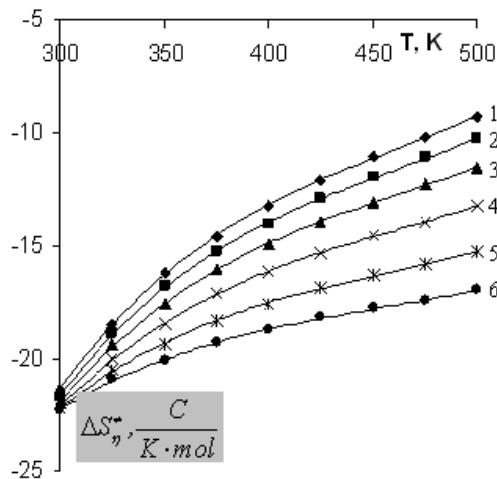


Şəkil 1. Etilpropionatın müxtəlif təzyiqlərdə özlü axınının aktivləşmə Gibbs enerjisinin temperaturdan asılılığı.

1-5 MPa, 2-10 MPa, 3-20 MPa, 4-30 MPa, 5-40 MPa, 6-50 MPa.



Şəkil 2. Etilpropionatın müxtəlif təzyiqlərdə özlü axınının aktivləşmə entalpiyasının temperaturdan asılılığı.



Şəkil 3. Etilpropionatın müxtəlif təzyiqlərdə özlü axınının aktivləşmə entropiyasının temperaturdan asılılığı.

1-5 MPa, 2-10 MPa, 3-20 MPa, 4-30 MPa, 5-40 MPa, 6-50 MPa.

1 sayılı şəkildən görünür ki, etilpropionat üçün təzyiqin və temperaturun artması ilə  $\Delta G_{\eta}^{\ddagger}$  artır. Özlü axının Eyrinq [4] və Frenkel [5] nəzəriyyələrinə görə  $\Delta G_{\eta}^{\ddagger}$  molekulun potensial çəpəri keçməsi üçün görülən işdir. Ehtimal etmək olar ki, temperaturun artması ilə tədqiq olunan mayedə potensial çəpəri aşmaq istəyən molekulların sayı artır. Həmçinin, təzyiqin artması ilə potensial çəpərin hündürlüyü, temperaturun artması ilə isə potensial çəpərin eni artır. Bu da maye molekullarının potensial çəpəri keçməsinə çətinləşdirir. Nəticədə  $\Delta G_{\eta}^{\ddagger}$  təzyiqdən və temperaturdan asılı olaraq artır.

Qeyd edək ki, özlü axının aktivləşmə entalpiyası ( $\Delta H_{\eta}^{\ddagger}$ ) mayedə yaranan dəyişmələri enerji baxımından, özlü axının aktivləşmə entropiyası ( $\Delta S_{\eta}^{\ddagger}$ ) isə struktur baxımından xarakterizə edir. Tədqiq olunan mayedə təzyiqdən və temperaturdan asılı olaraq enerji və struktur xarakteristikalarını müəyyənəlmək üçün  $\Delta H_{\eta}^{\ddagger} = f(T)_P$ ,  $\Delta S_{\eta}^{\ddagger} = f(T)_P$  və

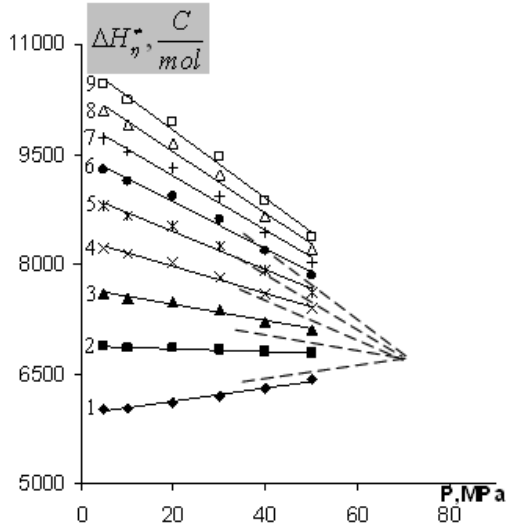
$\Delta H_{\eta}^{\ddagger} = f(P)_T$ ,  $\Delta S_{\eta}^{\ddagger} = f(P)_T$  asılılıqları təhlil edilmişdir (şəkil 2-5).

Şəkil 2-dən görünür ki, hər bir izobar üçün temperatur artdıqca  $\Delta H_{\eta}^{\ddagger}$  artır, həmçinin  $\Delta H_{\eta}^{\ddagger} = f(T)_P$  asılılığında hər bir izobarı xarakterizə edən xətləri bir nöqtədə kəsişirlər.

Deməli, kəsişmə nöqtəsində  $\left( \frac{\partial \Delta H_{\eta}^{\ddagger}}{\partial P} \right)_T = 0$  olur. Etilpropio-

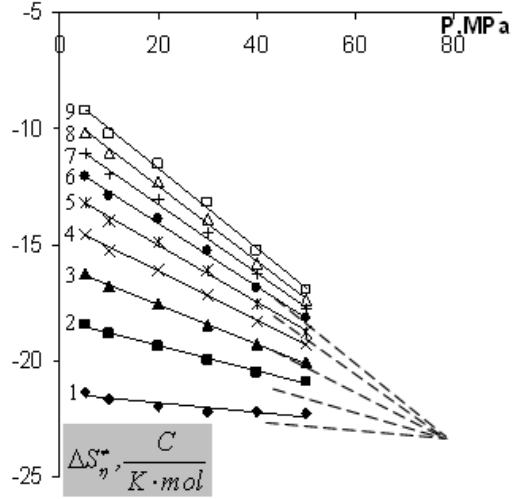
nat üçün bu nöqtə  $T_k^{\Delta H_{\eta}^{\ddagger}} \approx 320 K$  qiymətinə uyğun gəlir. Həmçinin müəyyən olunmuşdur ki, etilpropionat üçün təzyiqin elə qiyməti var ki,  $\left( \frac{\partial \Delta H_{\eta}^{\ddagger}}{\partial T} \right)_P = 0$  olur (şəkil 4). Bunu

$\Delta H_{\eta}^{\ddagger} = f(P)_T$  asılılığında hər bir izotermi xarakterizə edən xətləri ekstrapolyasiya etməklə tapmaq olar. Etilpropionat üçün bu nöqtə  $P_k^{\Delta H_{\eta}^{\ddagger}} \approx 86 MPa$  qiymətinə uyğun gəlir.



Şəkil 4. Etilpropionatın müxtəlif temperaturalarda özlü axınının aktivləşmə entalpiyasının təzyiqdən asılılığı.

1-300 K, 2-325 K, 3-350 K, 4-375 K, 5-400 K, 6-425 K, 7-450 K, 8-475 K, 9-500 K.



Şəkil 5. Etilpropionatın müxtəlif temperaturalarda özlü axınının aktivləşmə entropiyasının təzyiqdən asılılığı.

Tədqiqatlar nəticəsində müəyyən olunmuşdur ki,  $\Delta H_\eta^\# = f(T)_P$  və  $\Delta H_\eta^\# = f(P)_T$  asılılıqlarında müşahidə olunan qanunauyğunluqlar  $\Delta S_\eta^\# = f(T)_P$  və  $\Delta S_\eta^\# = f(P)_T$  asılılıqlarında da müşahidə olunur (şəkil 3 və 5). Belə ki, hər tədqiq olunan maye üçün  $\Delta S_\eta^\# = f(T)_P$  asılılığında hər bir izobarı xarakterizə edən xətlər  $T_{k.}^{\Delta S_\eta^\#} \approx 300 K$  nöqtəsində kəsişirlər.  $\Delta S_\eta^\# = f(P)_T$  asılılığında hər bir izotermi xarakterizə edən xətlər isə etilpropionat üçün  $P_{k.}^{\Delta S_\eta^\#} \approx 86 MPa$  nöqtəsində kəsişirlər. Göründüyü kimi, baxılan maye üçün  $P_{k.}^{\Delta H_\eta^\#} = P_{k.}^{\Delta S_\eta^\#}$  olur.

İşdə etilpropionatın istidən həcmi genişlənmə və izotermik sıxılma əmsallarının təzyiqdən və temperaturdan asılılıqları da tədqiq olunmuş, həmçinin özlü axının aktivləşmə parametrləri ilə müqayisə edilmişdir. Termodinamikadan məlumdur ki, istidən həcmi genişlənmə və izotermik sıxılma əmsalları

$$\alpha_p = \frac{1}{V} \left( \frac{\partial V}{\partial T} \right)_P = - \frac{1}{\rho} \left( \frac{\partial \rho}{\partial T} \right)_P \quad (1)$$

$$\beta_T = - \frac{1}{V} \left( \frac{\partial V}{\partial P} \right)_T = \frac{1}{\rho} \left( \frac{\partial \rho}{\partial P} \right)_T \quad (2)$$

(1) və (2) düsturları ilə hesablanır [6]. Bu düsturlarla  $\alpha_p$  və  $\beta_T$ -ni hesablamaq üçün, uyğun olaraq, hər bir izobar üçün  $\rho(T) = a_0 + a_1 T + a_2 T^2$  və hər bir izoterm üçün isə  $\rho(P) = b_0 + b_1 P + b_2 P^2$  asılılığı qurulmuşdur. Yazılmış

polinom tənliklərə daxil olan  $a_0, a_1, a_2, b_0, b_1, b_2$  sabitləri riyazi optimallaşma metodu ilə təyin edilmişdir. Bu polinomları yuxarıdakı tənliklərdə nəzərə alsaq,  $\alpha_p$  və  $\beta_T$ -ni hesablamaq üçün aşağıdakı ifadələri alırıq:

$$\alpha_p = - \frac{1}{\rho} (a_1 + 2a_2 T) \quad (4)$$

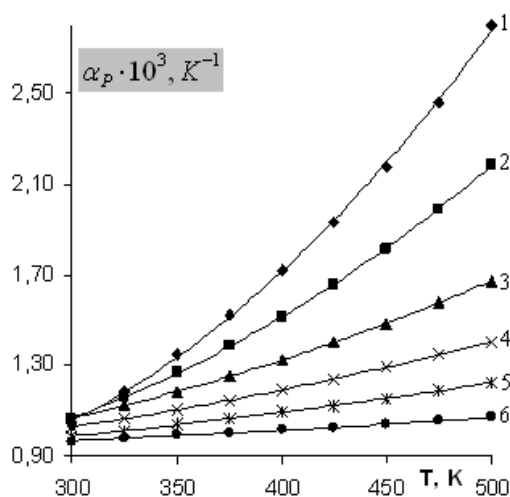
$$\beta_p = \frac{1}{\rho} (b_1 + 2b_2 P) \quad (5)$$

Etilpropionatın istidən həcmi genişlənmə və izotermik sıxılma əmsallarının müxtəlif izobarlarının temperaturdan asılılıqları 6-7 sayılı şəkillərdə, müxtəlif izotermliyinin təzyiqdən asılılığı isə 8-9 sayılı şəkillərdə göstərilmişdir.

Şəkil 6 və 7-dən görünür ki,  $\Delta S_\eta^\# = f(T)_P$  asılılığında olduğu kimi,  $\alpha_p = f(T)_P$  və  $\beta_T = f(T)_P$  asılılığında temperaturun elə qiyməti var ki, həm  $\left( \frac{\partial \alpha_p}{\partial P} \right)_T = 0$  və həm də

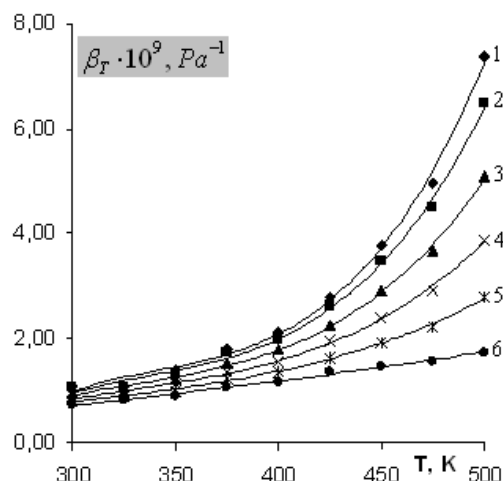
$\left( \frac{\partial \beta_T}{\partial P} \right)_T = 0$  olur. Tədqiqatlarımız nəticəsində müəyyən olun-

muşdur ki, temperaturun bu qiyməti  $T_{k.}^{\Delta S_\eta^\#} \approx T_{k.}^{\alpha_p} \approx T_{k.}^{\beta_T} \approx 300 K$  -dir. Şəkil 8 və 9 əsasən ehtimal etmək olar ki,  $\Delta H_\eta^\# = f(P)_T$  və  $\Delta S_\eta^\# = f(P)_T$  asılılıqlarında olduğu kimi,  $\alpha_p = f(P)_T$  və  $\beta_T = f(P)_T$  asılılıqlarında da müxtəlif izotermliyinin uzantıları bir nöqtədə kəsişirlər. Görünür etilpropionatın maye fazasının özlü axınının aktivləşmə parametrlərinin və termik xassələrinin belə səciyyəvi xarakteri ümumi bir əsas malikdir, bu isə bir çox məsələlərdə özünü göstərir.

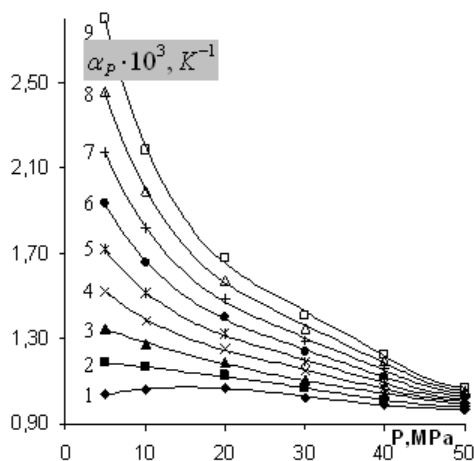


Şəkil 6. Etilpropionatın müxtəlif təzyiqlərdə istidən həcmnin genişlənmə əmsalının temperaturdan asılılığı.

1-5 MPa, 2-10 MPa, 3-20 MPa, 4-30 MPa, 5-40 MPa, 6-50 MPa.

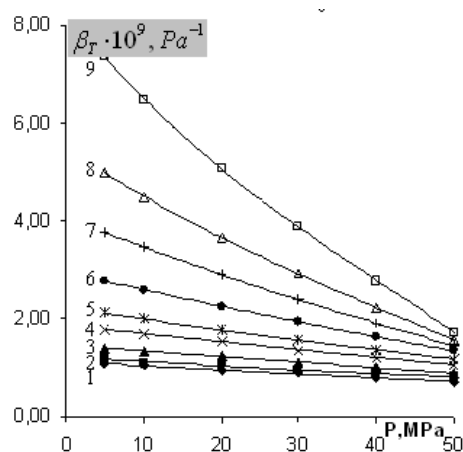


Şəkil 7. Etilpropionatın müxtəlif təzyiqlərdə izotermik sıxılma əmsalının temperaturdan asılılığı.



Şəkil 8. Etilpropionatın müxtəlif temperaturalarda istidən həcmnin genişlənmə əmsalının təzyiqdən asılılığı.

1-300 K, 2-325 K, 3-350 K, 4-375 K, 5-400 K, 6-425 K, 7-450 K, 8-475 K, 9-500 K.



Şəkil 9. Etilpropionatın müxtəlif temperaturalarda izotermik sıxılma əmsalının təzyiqdən asılılığı.

- [1] К.Д. Гусейнов. Докторская диссертация. Баку-1979.
- [2] Е.Ə. Мəсимов, Н.Ş. Нəсəнов, В.Г. Пəşəєєв, Н.Н. Нəсəнова. Özlü axının aktivləsmə parametrlərinin təyini üsulları. Bakı Universitetinin Xəbərləri, fizika-riyaziyyat elmləri seriyası, 2005, № 2, s.138-150.
- [3] К.Д. Hüseєнов, В.Г. Пəşəєєв, Ə.М. Quliyєв. Metilpropionatın özlü axınının aktivləsmə parametrləri və struktur xüsusiyyətləri. АМЕА-nın Xəbərləri, fizika-riyaziyyat və texnika elmləri seriyası, fizika və astro-nomiya 2008, № 2, s.117-120.

- [4] С. Глессон, К. Лейдлер, Г. Эйринг. Теория абсолютных скоростей. М.: Изд-во иностр. лит., 1948. 600 с.
- [5] Я.И. Френкель. Кинетическая теория жидкостей. Издательство «Наука» Ленинградское отделение. Ленинград 1975, с.221-235.
- [6] Б.П. Никольский, Н.А. Смирнова, М.Ю. Панов, Н.В. Лутугина, В.В. Пальчевский, А.А. Пендин, Ф.А. Белинская, О.К. Первухин, А.К. Чарыков. Физическая химия. Ленинград издательство «Химия», 1987., 880 с.

Е.А. Masimov, K.D. Huseynov, B.G. Pashayev, H.Sh. Hasanov

## THE ACTIVATION PARAMETERS OF VISCOUS FLOW AND THERMAL PROPERTIES IN ETILPROPIONAT

The dynamic viscosity and density of etilpropionate has been studied at the temperature interval from 300 K to 500 K and pressure range from 5 MPa to 50 MPa. The activation parameters and thermal coefficients of viscous flow are calculated on the basis of obtained date. The obtained results show that isobars in dependences  $\Delta H_{\eta}^{\#} = f(T)_p$ ,  $\Delta S_{\eta}^{\#} = f(T)_p$ ,  $\alpha_p = f(T)_p$  and  $\beta_T = f(T)_p$  and isotherms in dependences  $\Delta H_{\eta}^{\#} = f(P)_T$ ,  $\Delta S_{\eta}^{\#} = f(P)_T$ ,  $\alpha_p = f(P)_T$  and  $\beta_T = f(P)_T$  intersect each other at some points.

**АКТИВАЦИОННЫЕ ПАРАМЕТРЫ ВЯЗКОГО ТЕЧЕНИЯ И ТЕРМИЧЕСКИЕ СВОЙСТВА  
ЭТИЛПРОПИОНАТА**

В работе изучено динамическая вязкость и плотность этилпропионата в интервале температур 300-500 К и давлении 5-50 МПа. На основе полученных данных были вычислены активационные параметры вязкого течения и термические коэффициенты. Полученные результаты показывают, что на зависимостях  $\Delta H_{\eta}^{\ddagger} = f(T)_p$ ,  $\Delta S_{\eta}^{\ddagger} = f(T)_p$ ,  $\alpha_p = f(T)_p$  и  $\beta_T = f(T)_p$  изобары, а на зависимостях  $\Delta H_{\eta}^{\ddagger} = f(P)_T$ ,  $\Delta S_{\eta}^{\ddagger} = f(P)_T$ ,  $\alpha_p = f(P)_T$  и  $\beta_T = f(P)_T$  изотермы пересекаются в определенных точках.

*Received: 02.07.08*

# THE INFLUENCE OF THE SUBSTITUTION OF CALCIUM BY ZINC ON THERMAL CONDUCTIVITY AND THERMAL POWER OF $\text{Bi}_2\text{Sr}_2\text{Ca}_2\text{Cu}_3\text{O}_x$

V.M. ALIEV, S.S. RAGIMOV, R.I. SELIM-ZADE, A.N. MAMMADOVA

*H.M. Abdullayev Institute of Physics NAS of Azerbaijan,*

*Baku-1143, H. Javid av., 33*

It was investigated the influence of Ca substitution by Zn on the thermal conductivity, thermal power, specific resistivity of  $\text{Bi}_2\text{Sr}_2\text{Ca}_2\text{Cu}_3\text{O}_x$  in the 70-300K temperature interval. It was established that the Ca substitution by Zn leads to increase of lattice thermal conductivity and conductivity type from (+) to (-). It was shown, that these changes are stipulated by improvement of quality of  $\text{Bi}_2\text{Sr}_2\text{Zn}_2\text{Cu}_3\text{O}_x$  ceramics.

Despite of the reached successes in research of HTSC, search of materials though in what that, surpassing existing still proceeds. One of ways of reception of new materials is replacement of one of complex component HTSC, other analogue. Therefore, in the presented work in  $\text{Bi}_2\text{Sr}_2\text{Zn}_2\text{Cu}_3\text{O}_x$  system full replacement of atoms Ca by atoms Zn is made.

With the purpose of finding-out of efficiency of replacement of atoms Ca by Zn in Bi-based HTSC system it was carried out research of factor of thermal conductivity and electric properties of new structure 2223 with initial system.

Thermal conductivity is one of the most sensitive physical properties not only to structural changes of a crystal, but also for various types of defects in them. As defects in HTSC there can be deviations from stoichiometry, borders of grains, dispositions isotopes and others of heterogeneity. Is known also that in HTSC materials, especially in ceramics, in view of absence in them of strict crystal structure and presence of high concentration of defects, free length of phonons is slightly change in wide temperature interval.

The thermal conductivity was measured by a stationary method in cryostat, allowing to spend measurement in an interval 2-300K.

As in the 150-300K interval the thermal conductivity in HTSC possesses rather low value it is necessary to enter the amendment on the losses of heat radiated from a surface of the sample and the heater, and also bringing assembly wires. The technique of the account losses on radiation is based on the theory of thermal radiation of an absolute black body. The given technique is developed in work [1] for bodies of grey color and approved in [2]. According to it the thermal conductivity  $k$  was calculated by:

$$k = \frac{W - \varepsilon}{\Delta T} \cdot \frac{l}{S}$$

where  $W=IU$ -capacity of a heater,  $S$ -cross-section of the sample,  $l$ -distance between thermocouples,  $\Delta T$  is a difference of temperatures between the top and bottom thermocouples,  $\varepsilon = Q_{\text{rad}} + Q_{\text{wire}}$  warmly, radiated by a lateral surface of the sample and a heater, and also outflow by bringing wires.  $Q_{\text{rad}}$  is calculated under the formula:

$$Q_{\text{rad}} = \{S_{\text{sam}}(T_{\text{av}}^4 - T_e^4) + S_{\text{heat}}(T_{\text{heat}}^4 - T_e^4) \cdot \sigma\}$$

Where  $S_{\text{sam}}$ -is the area of lateral surface of sample,  $S_{\text{heat}}$  is area of a surface of a heater,  $T = (T_1 + T_2) / 2$  - is an average temperature of the sample,  $T_1$  is temperature of a casing of the device,  $T_2$  - is temperature of a heater,  $\sigma=A\sigma_0$  - is factor of

emission of the sample for a grey body  $\sigma_0=3,45 \cdot 10^{-10} \text{ W/cm}^2 \cdot \text{K}^{-4}$  - of Stephan-Bolsmann constant.

Outflow of heat from bringing wires takes place at all temperatures and is defined by the formula:  $\Delta Q = kS\Delta T/l$ , where  $k$ -thermal conductivity of thermocouples, the  $S$ -area of cross-section,  $l$ -length of wires from the sample up to the top part of volume of a casing,  $\Delta T$ -difference temperature between the sample and a casing of the device.

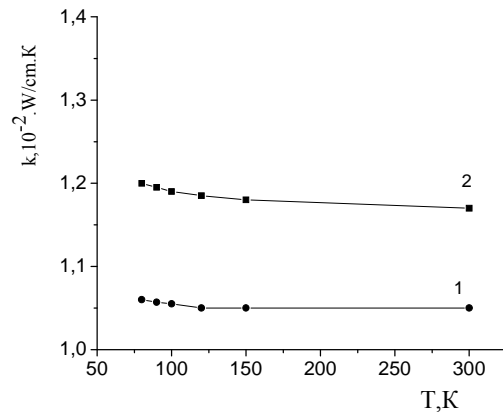


Fig.1. The temperature dependences of thermal conductivity: 1-  $\text{Bi}_2\text{Sr}_2\text{Ca}_2\text{Cu}_3\text{O}_x$ , 2-  $\text{Bi}_2\text{Sr}_2\text{Zn}_2\text{Cu}_3\text{O}_x$ .

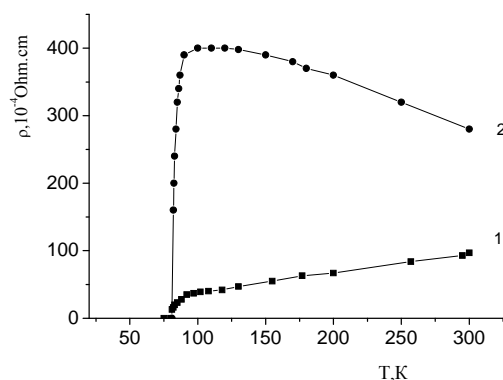


Fig.2. The temperature dependences of specific resistivity: 1 -  $\text{Bi}_2\text{Sr}_2\text{Ca}_2\text{Cu}_3\text{O}_x$ , 2-  $\text{Bi}_2\text{Sr}_2\text{Zn}_2\text{Cu}_3\text{O}_x$

The calculations have shown, that the maximal losses connected with radiation at  $T=300\text{K}$  for the investigated sample reaches 15-20 %, and outflow on wires does not exceed 3-4 %. The Fig.1 show the temperature dependences of lattice  $k$  above described amendments, and the fig.2 show specific resistance of the investigated samples respectively.

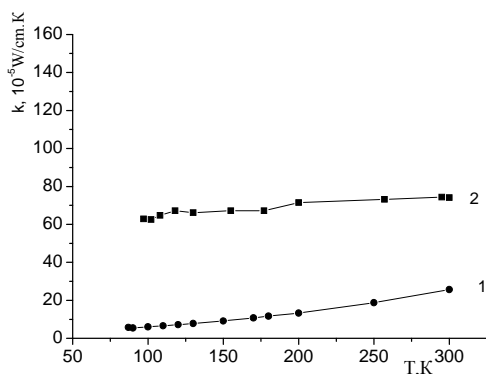


Fig. 3. The temperature dependences of electronic thermal conductivity: 1 -  $\text{Bi}_2\text{Sr}_2\text{Ca}_2\text{Cu}_3\text{O}_x$ , 2-  $\text{Bi}_2\text{Sr}_2\text{Zn}_2\text{Cu}_3\text{O}_x$

The electronic part of thermal conductivity  $k_e$  has been estimated according to Wiedemann-Frants relation ( $k = LT/\rho$ ) by the account of a degree degeneration and the electron scattering mechanism at which Lorenz's number accepted value 1,8.10 Ohm.K. The calculations have shown, that  $k_e$  in  $\text{Bi}_2\text{Sr}_2\text{CaCu}_3\text{O}_x$  does not exceed 4 %, and in  $\text{Bi}_2\text{Sr}_2\text{Zn}_2\text{Cu}_3\text{O}_x$ , it is insignificant is small (fig.3). These data give the basis to accept  $k(T)$  for temperature dependence lattice thermal conductivities. From fig.3 it is visible, that in bismuth HTSC with Ca  $k(T)$  slightly depends on temperature, whereas it should decrease proportionally  $k \sim T$ .

The temperature dependences of thermal power of  $\text{Bi}_2\text{Sr}_2\text{CaCu}_3\text{O}_x$  and  $\text{Bi}_2\text{Sr}_2\text{Zn}_2\text{Cu}_3\text{O}_x$  is presented in fig.4. As seen, in  $\text{Bi}_2\text{Sr}_2\text{Zn}_2\text{Cu}_3\text{O}_x$  the thermal power  $S$  has a positive sign and has small value, with decrease of  $T$  it slightly increases and at phase transition (PT) sharply falls up to  $S=0$ . In the sample with Zn value  $S$  is more, than in the sample with Ca, also has  $n$ -type of conductivity, with decrease of  $T$  the  $S$  decreases and at PT also falls up to  $S=0$ . These data indicated on strong degeneration of holes in  $\text{Bi}_2\text{Sr}_2\text{Zn}_2\text{Cu}_3\text{O}_x$ , it leads to metal temperature course of  $S(T)$ .

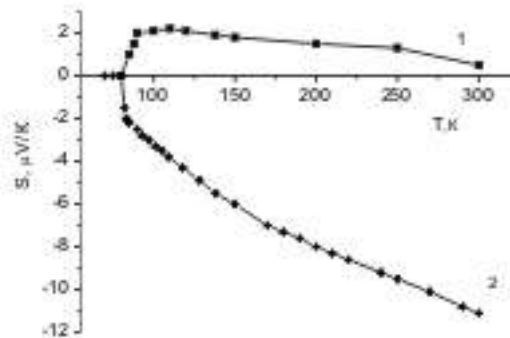


Fig.4. The temperature dependences of thermal power: 1 -  $\text{Bi}_2\text{Sr}_2\text{Ca}_2\text{Cu}_3\text{O}_x$ , 2-  $\text{Bi}_2\text{Sr}_2\text{Zn}_2\text{Cu}_3\text{O}_x$ .

The increasing of lattice thermal conductivity of  $\text{Bi}_2\text{Sr}_2\text{Zn}_2\text{Cu}_3\text{O}_x$  gives the basis to conclude, that full replacement of atoms Ca by Zn reduces concentration of defects and improves quality of Bi-based HTSC. It testify also the fact of change of a sign of  $S$  from hole conductivity on electronic and removal of degeneration of charge carriers.

It is necessary to note, that in the literature exists different representations about value and a sign of thermal power in the Y-, Ta-, Bi and Hg-based cuprates [3]. In particular it is indicated, that negatively charged CuO-planes cause hole conductivity, and positively charged BiO-planes cause electronic one [3]. In [4] the authors consider, that the value and sign of  $S$  are defined, basically, not number of CuO-planes, and concentration of charge carriers in these planes also. Our data give the basis to consider, that the replacement Ca on Zn leads to a formation of donor levels. Certainly, it is difficult to indicate on a concrete element creating such levels, but it is possible to believe, that it is caused by some deviation from stoichiometry such complex structure of Bi-based HTSC.

Authors acknowledges to prof. S.A.Aliev for interest to work and useful discussions.

- [1] E.D. Devyatkov, A.V. Petrov, I.A.Smirnov, B.J.Mojzhes FTT, (1960), т.11, №4, p.733.  
[2] S.A. Aliev, U.H. Suyunov, M.I. Aliev. FTP, (1973), №7, p.2024.

- [3] I. Tot, G.H.Panova, V.D. Gorobchenko, A.V. Irodova, O.A.Lavrova, A.A.Shikov, SFXT, (1990), т.3, №8, p.1821-1830.  
[4] H.J.Trodahl, Phys. Rev. B., (1996), v.51, №9, p.6175.

V.M. Əliyev, S.S. Rəhimov, R.İ. Səlimzadə, A.N. Məmmədova

### KALSİUMUN SİNKİLƏ ƏVƏZ EDİLMƏSİNİN $\text{Bi}_2\text{Sr}_2\text{Ca}_2\text{Cu}_3\text{O}_x$ -DƏ İSTİLİKKEÇİRMƏYƏ VƏ TERMÖE.H.Q. TƏSİRİ

70-300K temperatur intervalında kalsiumun sinklə əvəz edilməsinin  $\text{Bi}_2\text{Sr}_2\text{Ca}_2\text{Cu}_3\text{O}_x$ -də istilikkeçirməyə, termoe.h.q.-nə və xüsusi müqavimətə təsiri öyrənilmişdir. Göstərilmişdir ki, Ca-un Zn ilə əvəz edilməsi nəticəsində materialın istilikkeçiriciliyi artır və keçiriciliyin işarəsi (+)-dən (-)-ə keçir. Təyin edilmişdir ki, alınan nəticələr  $\text{Bi}_2\text{Sr}_2\text{Zn}_2\text{Cu}_3\text{O}_x$  keramikasının keyfiyyətinin yaxşılaşması ilə əlaqədardır.

В.М. Алиев, С.С. Рагимов, Р.И. Селим-заде, А.Н. Мамедова

### ВЛИЯНИЕ ЗАМЕЩЕНИЯ КАЛЬЦИЯ ЦИНКОМ НА ТЕПЛОПРОВОДНОСТЬ И ТЕРМОЭДС В $\text{Bi}_2\text{Sr}_2\text{Ca}_2\text{Cu}_3\text{O}_x$

Проведено исследование влияния замещения кальция цинком в  $\text{Bi}_2\text{Sr}_2\text{Ca}_2\text{Cu}_3\text{O}_x$  на теплопроводность, термоэдс и удельное сопротивление в интервале температур 70-300K Установлено, что замещение Са на Zn приводит к повышению решеточной теплопроводности и к смене знака проводимости от (+) на (-). Показано, что эти изменения обусловлены улучшением качества висмутовых керамик  $\text{Bi}_2\text{Sr}_2\text{Zn}_2\text{Cu}_3\text{O}_x$ .

Received: 08.07.08

# HALL EFFECT AND CONDUCTIVITY IN POROUS SILICON WITH LOW POROSITY ON THE BASE OF Si<As>

H.A. HASANOV

*H. Aliev Academy of Ministry of National Safety*

The investigation results of temperature dependences of specific resistance and Hall coefficient of mesoporous silicon with low porosity, formed on the base of Si<As> are given in the present article. The formulas of double-layer Petritz model are used at calculations. The obtained results are analyzed in the framework of theory of effective medium, which allows us to consider the materials with foreign inclusions in matrix.

## Introduction

Hall effect is the classic method for data accessing about concentration of charge carriers in the semiconductors [1] and that's why its use for investigation of porous silicon (PS) is reasonable. There are only two works, in which the measurement of Hall effect in porous silicon [2, 3] is mentioned, are known in World. The detail description of experimental data is absent in these two works and that's why it is hard to agree with some conclusions of authors. The main difficulties at Hall effect measurement in PS are connected with its high specific resistance and necessity to take into consideration the substrate short-circuiting effect, especially that's why this method has not found such wide application for the investigation of porous structures. However, as our investigations show, Hall effect can be effectively used for the investigation of low-resistance layers of porous silicon. The aim of the given paper is the investigation of Hall effect and electrical conduction of mesoporous silicon with low porosity (5-30%) on the base of Si<As>.

## Experimental part

The measurements of Hall effect and conductivity are carried out by potentiometer on double-layer PS/silicon substrate structures (fig. 1) on direct current with the use of commutation of electric and magnetic fields at the value of magnetic field  $0.3 \div 0.5$  T in temperature interval 290-380K. PS, formed on substrates KES-0.01 with electron concentration  $n=10^{18} \text{ cm}^{-3}$  of orientation (111) is used for investigations. The anodizing is carried out in 46% water solution HF at current density  $10 \div 20 \text{ mA/cm}^2$ .

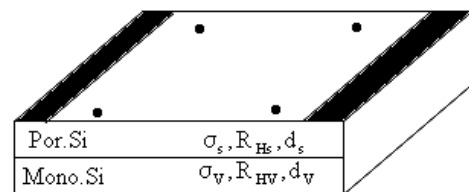


Fig. 1. The image of double-layer PS/silicon structure for measurement of Hall effect [3].

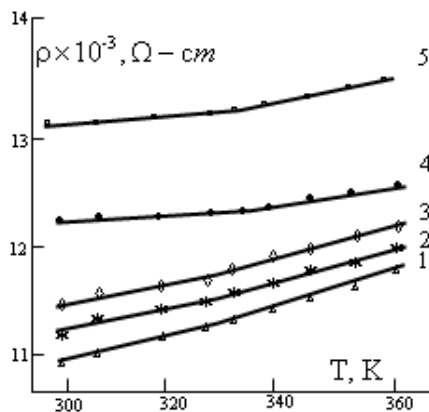
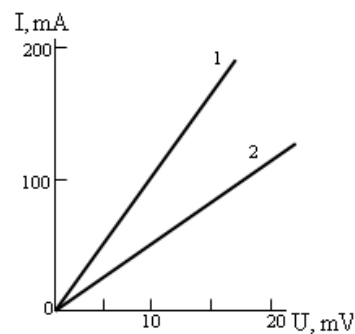


Fig. 2. a – temperature dependences of specific resistance for initial silicon (1) and double-layer structures (2-5), obtained at  $j=10 \text{ mA/cm}^2$  for  $t_a$ : 2 - 20, 3- 30, 4 - 40, 5 – 60 min.; b – linear volt-ampere characteristics of contacts: 1-  $j=10 \text{ mA/cm}^2$ ,  $t_a=10 \text{ min.}$ , 2 -  $j=10 \text{ mA/cm}^2$ ,  $t_a=50 \text{ min.}$



The time of anodic treatment varies in the limits  $20 \div 60$  min. The practically linear dependencies of layer thickness of PS on treatment time and weight porosity on thickness of porous layer are observed under these conditions. PS layers have the thickness  $10 \div 90 \text{ mcm}$  and weight porosity 5-30%. The plasmachemical elimination of surface amorphized film is carried out for improvement of contact ohmicity and decrease of value of transient resistance. The indium test contacts for measurement of Hall effect and specific resistance are covered on PS surface by mask. The contact

ohmicity is proved by Koh-Streck method, the values of transient resistances are  $0.7 \div 2.1 \Omega \cdot \text{mm}$ .

The typical dependencies of specific resistance  $\rho$  of double-layer structures in temperature interval 290-380K are given on the fig.2,a; the temperature dependence of specific resistance for initial silicon is also given here. As it is seen from this figure, the similar temperature variations  $\rho(T)$  for investigated samples and monocrystalline silicon is observed and increase of specific resistance values of double-layer structure at increase of anodic treatment time takes place. The



temperature change of Hall coefficient  $R_H$  for investigated structures is shown on the fig.3,a. Moreover, temperature dependences  $R_H(T)$  for double-layer samples have similar change character in the comparison with monocrystalline silicon; the values of Hall coefficient for all samples are in narrow band of values  $(1.1 \div 1.7) \cdot 10^{-6} \text{ m}^3/\text{C}$ , shown on the

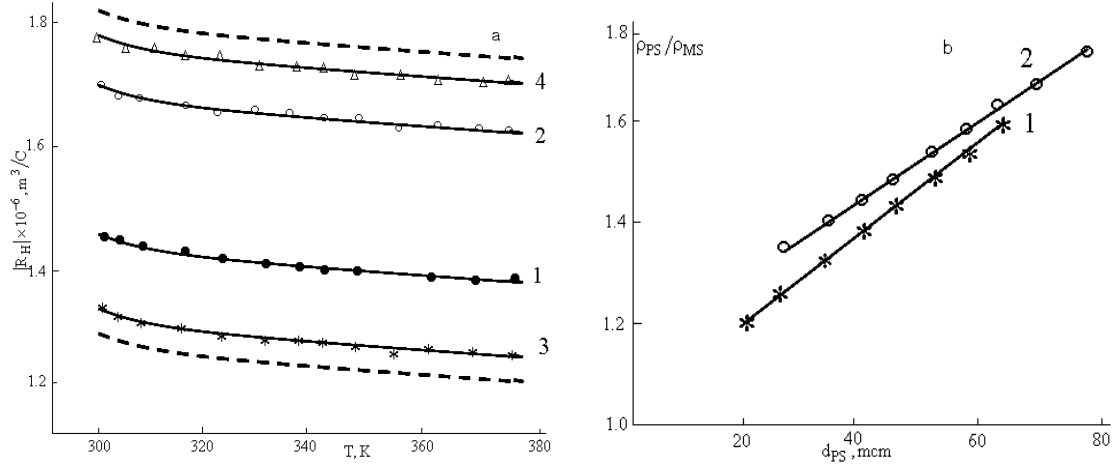


Fig. 3. *a* – typical temperature dependences of Hall coefficient for initial silicon (1) and double-layer structures (2-4), obtained at: 2-  $j=10 \text{ mA/cm}^2$ ,  $t_a=40 \text{ min.}$ ; 3-  $j=10 \text{ mA/cm}^2$ ,  $t_a=30 \text{ min.}$ ; 4-  $j=10 \text{ mA/cm}^2$ ,  $t_a=60 \text{ min.}$ ; *b* – dependence of ratio  $\rho_{PS}/\rho_{MS}$  on PS film thickness for different  $j$ : 1 -  $10 \text{ mA/cm}^2$ , 2 -  $20 \text{ mA/cm}^2$ .

### Discussion of obtained results

The traditional calculation methods of layer electrophysical parameters, consisting in double-layer structure [1] are used for treatment of obtained results. The experiment cycle on layerwise elimination of substrate material simultaneously with Hall measurements is carried out in order to more reliably eliminate the influence of silicon substrate. It is established, that the changes of concentration and mobility of charge carriers in the comparison with initial silicon don't take place in the volume of substrate KES-0.01 itself at given treatment regimes. That's why the parameters of one layer (silicon substrate) in double-layer structure are taken as equal ones for initial silicon at following calculations. It is known, that porous silicon, obtained in close regimes on silicon, strongly doped by arsenic, has the columnar structure [4, 5] with pore diameter of 5nm order. That's why the two-phase model of porous silicon layer, consisting of monocrystalline matrix-frame (phase 1) and cylindrical empty places, perpendicular to surface (phase 2) is put in calculation formulas.

The formulas of double-layer Petritz model [1] are used at calculations:

$$\sigma = \frac{\sigma_s d_s + \sigma_v d_v}{d}, \quad (1)$$

$$R_H = \frac{\sigma_s^2 d_s R_{Hs} + \sigma_v^2 d_v R_{Hv}}{(\sigma_s d_s + \sigma_v d_v)^2}, \quad (2)$$

where  $R_{Hs}$  is Hall coefficient for upper layer (porous silicon),  $\sigma_s$  is electrical conduction of upper layer (PS),  $R_{Hv}$  is Hall coefficient for lower layer (silicon substrate),  $\sigma_v$  is electrical conduction of lower layer;  $d_s$ ,  $d_v$ ,  $d$  are thicknesses of upper, lower layers and whole structure, correspondingly. In formulas (1) and (2)  $R_H$  and  $\sigma$  are Hall coefficient and

fig.3,a. Any change regularity of Hall coefficient in the dependence of regimes of electrochemical working is absent inside this band. Moreover, the experimental values  $R_H$  also fill the given band of values for double-layer samples, obtained in similar technological conditions and for samples of monocrystalline silicon from different plates.

conductivity correspondingly for whole double-layer structure. The measurement results on silicon substrates, crude in electrolyte are used in the capacity of data for the layer of monocrystalline silicon.

The calculations show that PS specific resistance value is bigger in  $1.1 \div 1.6$  times than specific resistance of initial silicon substrates in measured double-layer structures. This is shown on the fig.3,b, where the ratios of specific resistances of PS and monocrystalline silicon ( $\rho_{PS}/\rho_{MS}$ ) are given for two densities of anodizing current for investigated interval of PS thicknesses. As it is mentioned above, the porosity of investigated samples is almost proportional to PS thickness, so the ratio of specific resistances should increase with increase of porosity value by the law, which is close to linear one. The obtained results are analyzed in the framework of theory of effective medium, which allows us to consider the materials with foreign inclusions in matrix. If PS is considered as monocrystalline frame (with conductivity  $\sigma_{MS}$ , value of Hall coefficient  $R_{HMS}$  and mobility of carriers  $\mu_{MS}$ ), penetrated by cylindrical non-conducting empty places, then conductivity  $\sigma_{PSv}$ , Hall coefficient  $R_{HPS}$  and mobility  $\mu_{PS}$  of such heterogeneous system depend on porosity value. We have the following relations:

$$\sigma_{PS} = \frac{\sigma_{MS}(1-P)}{1+P}, \quad (3)$$

$$R_{HPS} = R_{HMS}, \quad (4)$$

$$\mu_{PS} = \frac{\mu_{MS}(1-P)}{1+P}. \quad (5)$$

at cylindrical spaces of arbitrary cross-section, the axes of which are perpendicular to electric field and parallel to magnetic one in the framework of theory of effective medium [1].

The analysis of experimental results with the help of formula (3) shows, that experimentally observed law of the increase of PS specific resistance on the increase of porosity value enough well corresponds to theoretical statements of theory of effective medium. This is shown on the fig.4, where theoretical and experimental data in the porosity interval 5-30% are presented.

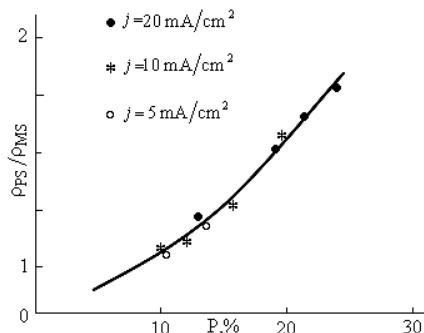


Fig. 4. The theoretical and experimental dependencies  $\rho_{PS}/\rho_{MS}=f(P)$  for investigated samples. The points are experimental values; line is theoretical dependence in the framework of theory of effective medium.

Thus, analysis of experimental results on measurement of Hall effect and specific resistance of structures with porous layers shows that all changes of specific resistance of double-layer structures on the base of KES-0.01 can be explained by the formation of unconducting empty places in silicon

without formation of depletion regions round pores and without concentration change of charge carriers in silicon frame. The calculations of Hall coefficient for double-layer structures (f.2) at the condition of concentration constancy of charge carriers in PS matrix at observable increase of resistance of porous layer in 1.1÷1.6 times prove about the fact that changes of Hall coefficient shouldn't exceed the value of measurement experimental error  $R_H$ , that explains the observable effects (fig.3) at carrying out of Hall measurements. Note, that absence of depletion in PS, obtained on strongly doped substrates of n-type, is also mentioned by Andersen [6] on the base of capacitance measurements at the use of substrates, doped by phosphorus ( $0.003 \pm 0.005 \Omega\text{-cm}$ ).

### Conclusion

1. The value of PS specific resistance in measured double-layer structures is bigger in 1.1-1.6 times, than the specific resistance of initial silicon substrates.
2. The ratio of specific resistances of porous structure and substrate increases with the increase of porosity value on the law, closed to linear one.
3. Hall coefficient value for all investigated samples are in small interval of values  $(1.1 - 1.7) \cdot 10^{-6} \text{ m}^3/\text{C}$ .
4. Any regularity of the change of Hall coefficient is absent in the dependence on the regimes of electrochemical treatment.

- [1] E.V. Kuchis. 1990 Galvanomagnitnie effekti i metodi ikh issledovaniya. (Moscow, Radio I svyaz) s. 264. (In Russian).
- [2] M.N. Preobrajenskiy, S.P. Zimin, D.S. Zimin. 1998. Vozmozhnosti metoda akusticheskoy mikroskopii pri izuchenii kristallicheskogo stroeniya tonkikh plyonok. Sb. "Visokii tekhnologii v promishlennosti Rossii". (Moscow, MAI) s. 168 (in Russian).
- [3] S.P. Zimin, D.S. Zimin. 2000. Variety of aluminium – porous silicon contacts electrical parameters. Materials

for Advanced Metallization :Materials of European Workshop. ( Streza, Italy) p.138.

- [4] H.Ə. Həsənov, R.Ş. Rəhimov. Bakı. Bakı Universitetinin Xəbərləri, fizika-riyaziyyat elmlər seriyası, 2008, №1, səh. 134-140.
- [5] H.Ə. Həsənov. Bakı, "Elm", "Fizika", XIII cild, 2007, №5, səh. 88-92.
- [6] R.C. Anderson, R.S. Muller, C.W. Tobias. 1991 Investigations of the electrical properties of porous silicon J. Electrochem. Soc., V.138, P.3406-3411.

H.Ə. Həsənov

### AZMƏSAMƏLİ Si <As> ƏSASINDA FORMALAŞDIRILMIŞ MEZOMƏSAMƏLİ SİLİSIUMDA HOLL EFFEKTİ VƏ ELEKTRİK KEÇİRİCİLİYİ

Təqdim olunmuş işdə azməsəmali Si <As> əsasında formalaşdırılmış mezoməsəmali silisiumda Holl effekti və elektrik keçiriciliyinin temperatur asılılıqlarının tədqiqinin nəticələri verilmişdir. Hesablamalar Petrits düsturlarının köməyi ilə aparılmışdır. Alınmış nəticələr materialı matrisdə yad qoşmalar olan materiallardakı prosesləri izah edə bilən effektiv mühitlər nəzəriyyəsi çərçivəsində təhlil edilmişdir.

Г.А. Гасанов

### ЭФФЕКТ ХОЛЛА И ПРОВОДИМОСТЬ В МЕЗОПОРИСТОМ КРЕМНИИ С НИЗКОЙ ПОРИСТОСТЬЮ НА ОСНОВЕ Si<As>

В представленной работе приведены результаты исследований температурных зависимостей удельного сопротивления и коэффициента Холла мезопористого кремния с низкой пористостью, сформированного на основе Si<As>. Вычисления проведены на основе двухслойной модели Петрица. Полученные результаты проанализированы в рамках теории эффективной среды, которая позволяет нам рассматривать исследуемые объекты как материалы с инородными включениями в матрице.

Received: 10.09.08

## DEVELOPMENT OF HIGH – ACCURACY GROUND SYSTEM FOR REGISTRATION OF AIRGLOW

**H.H. ASADOV**

*Head of Department of Atmospheric Research of National Aerospace Agency (Azerbaijan)*

**T.M. ALIYEVA**

*Head of Sector of Atmospheric Research of National Aerospace Agency (Azerbaijan)*

**I.M. MIRZABALAYEV, I.G. CHOBAN-ZADEH**

*Atmospheric Research of National Aerospace Agency (Azerbaijan)*

In the paper “Development of high - accuracy ground system for registration of airglow” features of measurement of intensity of airglow with compensation of background signals are considered.

The method of emission delta spectroscopy allowing full separate compensation of effects of fine – and coarse fractions of aerosol to the results of held measurements is proposed. The possibility of high accuracy ground measurements of anormal emission of atmosphere in fixed wavelengths is also considered. The method of differential optical emission spectroscopy, realization of which allows to carry out such measurements is described.

### 1. Introduction

Natural or artificial illumination of atmosphere, i.e. gases, existing in upper layers of atmosphere at heights more than 70 – 80 km is important component of total radiation of the sky at night. The night radiation of atmosphere besides continual spectrum also contain the emission lines of oxygen, hydrogen, natrium, and molecular lines of hydroxyl, oxygen, monoxide of carbon, ozone, water, nitrogen oxides.

The illumination of atmosphere is only one part of existing atmospheric light energy, because there are also illuminations of stars, zodiac light and scattering day light of the Sun. The spectrum of atmospheric illumination includes wavelengths beginning from  $1000\text{\AA}$  as far as 22,5 mcm. The main line of emission of atmosphere – on wavelength -  $\lambda$   $5577\text{\AA}$ , appears at heights 90 – 100 km, within layer having width 30 – 40 km. Generation of such illumination is conditioned with Chapman mechanism, based on recombination of oxygen atoms. Emission lines at wavelength  $6300\text{\AA}$  appear in the case of dissociating recombination of  $O_2^+$ . There are also illumination of nitrogen at wavelengths  $5198/5201\text{\AA}$  and  $5890/5896\text{\AA}$ . In general, all indications of natural anormal radiation of atmosphere linked with processes of energy transfer and magneto – ionospheric disturbances, being reaction to non – equal entry of energy from top (solar radiation, particles, etc.).

At low and equatorial latitudes the strong electro dynamically related events happen due to unique geometry of magnetic force lines. At upper latitudes the upper atmosphere is electrically linked with magnetospheric currents.

During magnetic storms, links between different latitude sided becomes more indicative and during this period a significant part of energy and moments transfer from upper latitudes to the lower latitudes by the help of moving ionospheric disturbances, gravitation waves, etc. take place [1].

One of important and useful methods for research of dynamics of upper atmosphere is measurement of airglow and auroral illumination of atmosphere. Intensity of emission at various latitudes and heights depends on volume depth of different factors causing these illuminations. In its turn, these factors are situated in dynamic processes effected by such factors as gravitation waves, winds, temperature, etc.

### 2. Formulation of problem

During last decades a large number of satellite and ground measurements of night illumination of atmosphere was carried out.

As it is noted in [2], the accurate comparison of data, obtained from various platforms frequently may be fulfilled only in cases, if these data is linked with general coordinate system. This task mat be solved using geographic coordinates. Possibility of accurate registration of atmospheric airglow using ground and satellite methods and calculation on this basis the location of source of radiation is of fundamental importance from view – point of general scientific usefulness of data on optical anormal radiation of different origin.

As it is noted in [2], commonly almost half of results of airglow measurements have low quality due to partly or full cloudiness. The direct lunar radiation leads to insignificant losses of information, bit if aerosol exists, the scattered lunar light way cause serious problems, especially during registration of weak illuminations.

But during research of illumination of airglow at coastal regions is should be taken into account, that coarse fractional part of aerosol acting more effectively in UV and visible spectral bands may significantly decrease authenticity and reproducibility of results of triangulation carried on the basis of ground measurements data. Therefore, removal of effect to results of ground measurements of anormal atmospheric radiation is most important and actual task from view – point of global research of airglow.

#### 2.1. Method of emission delta spectroscopy

Now we describe basic principles of suggested method of emission delta spectroscopy for measurements of anormal atmospheric illumination at coastal regions.

Let is consider the case of anormal atmospheric illumination at wavelength  $\lambda_2$  (fig. 1). At the considered wavelength band (UV or visible part of Solar spectrum) the total optical depth of atmosphere consist of such components as molecular scattering, molecular absorption, and aerosol

absorption. As it was shown above, the temporal non – stability of coastal aerosol leads to non – accuracy and losses of reproducibility of measurements results, which in its turn leads to errors of spatial localization of illuminated zones, and also places of reasons caused them both on the Earth and Atmosphere. We can show, that when estimating the intermediate parameter  $\ln Z$ , where  $Z$  - conditional dimensionless value of ratio of three signals, determined on following formula, the appropriate choosing of wavelength  $\lambda_1$  may lead to compensation of effect of non – stability of aerosol to accuracy of localization.

$$\ln Z = \ln I(\lambda_2) - \frac{\ln I(\lambda_1) + \ln I(\lambda_3)}{k}. \quad (1)$$

It should be noted, that  $I(\lambda_2), I(\lambda_1), I(\lambda_3)$  are to be determined on the basis of Bouguer – Beer law as follows:

$$I(\lambda_i) = I_0(\lambda_i) \cdot e^{-m\tau_{\Sigma}(\lambda_i)}, \quad i = \overline{1,3}, \quad (2)$$

where  $I_0(\lambda_i)$  - value of Solar constant at wavelengths  $(\lambda_i), i = \overline{1,3}$ ;  $m$  - optical mass;  $\tau_{\Sigma}(\lambda_i)$  - total optical depth of atmosphere, determined as follows:

$$\tau_{\Sigma} = \tau_{\Sigma}^* + \tau_c + \tau_f, \quad (3)$$

where  $\tau_{\Sigma}^*$  - partial optical depth of atmosphere, indicating such effects as molecular scattering, molecular absorption and aerosol scattering;  $\tau_c$  - optical depth of coarse component of atmospheric aerosol;  $\tau_f$  - optical depth of fine component of atmospheric aerosol.

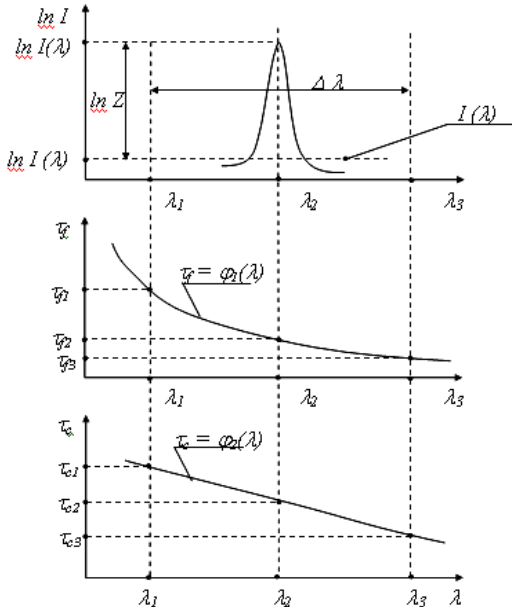


Fig. 1. Main parameters effected to accuracy of measurements of illuminations at wavelength  $\lambda_1, \lambda_2$  and  $\lambda_3$ .

Functions  $\tau_f = \varphi_1(\lambda)$  and  $\tau_c = \varphi_2(\lambda)$  are conditionally shown in fig. 1. In this case the task of research may be formulated as follows: Upon given functions  $\tau_f = \varphi_1(\lambda)$ ;  $\tau_c = \varphi_2(\lambda)$ , and known values of  $\lambda_2$  and  $\lambda_3$  we should find

out such a value of  $\lambda_1$ , upon which the value of  $z$  would not depend from parameters  $\tau_f$  and  $\tau_c$ , i.e. full compensation of aerosol error were achieved.

To solve the above formulated task, first of all we should transform the formula (1) as follows:

$$Z = \frac{I(\lambda_2)}{\sqrt[k]{I_f(\lambda_1) \cdot I_f(\lambda_3)}}. \quad (4)$$

Taking into consideration of equations (2), (3) and (4) we can find out the condition of full separate compensation of  $\tau_c$  and  $\tau_f$ .

$$\frac{\tau_f(\lambda_1) + \tau_f(\lambda_3)}{k} = \tau_f(\lambda_2), \quad (5)$$

$$\frac{\tau_c(\lambda_1) + \tau_c(\lambda_3)}{k} = \tau_c(\lambda_2). \quad (6)$$

Here we note, that the basic principle of aerosol's physics used as basis for formulas (5) and (6) is that fine and coarse fractions of aerosol have different origins and practically zero inters fractional correlation.

Using formulas (5) and (6) we can obtain following equation:

$$\frac{\tau_f(\lambda_1) + \tau_f(\lambda_3)}{\tau_c(\lambda_1) + \tau_c(\lambda_3)} = \frac{\tau_f(\lambda_2)}{\tau_c(\lambda_2)}. \quad (7)$$

From equation (7) we can find out the formula calculation value of  $\tau_c(\lambda_1)$ , which would provide full separate parametric compensation:

$$\tau_{cal}(\lambda_1) = \frac{\tau_c(\lambda_2)[\tau_f(\lambda_1) + \tau_f(\lambda_3)]}{\tau_f(\lambda_2)} - \tau_c(\lambda_3). \quad (8)$$

Therefore, the formula (8) makes it possible to calculate  $\tau_{cal}(\lambda_1)$ , which would provide compensation of aerosol errors. But in real case the coarse fraction has its own real function  $\tau_{cre}(\lambda)$  and within context of this article this function cannot be changed. As a result, the value of wavelength  $\lambda_1$  may be calculated using following equation:

$$\tau_{cal}(\lambda) = \tau_{cre}(\lambda). \quad (9)$$

Solution of equation (9) in regard of  $\lambda_1$  is illustrated in fig. 2. Results of experimental measurements of  $\tau_{fre}$  and  $\tau_{cre}$  are given in Table 1.

Table 1

	$\tau_{fre}$	$\tau_{cre}$
$\lambda_1$	0,85	0,31
$\lambda_2$	0,44	0,23
$\lambda_3$	0,3	0,21
$\lambda_4$	0,53	0,27

Taking into consideration the data given in table 1, the equation (8) allows to carry out following calculations

$$\tau_{cal}(\lambda_1) = \frac{0,23[\tau_f(\lambda_1) + 0,3]}{0,44} - 0,21 = 0,523[\tau_f(\lambda_1) + 0,3] - 0,21.$$

If  $\tau_f(\lambda_1) = 0,85$  we have  $\tau_{cal}(\lambda_1) = 0,39$ .

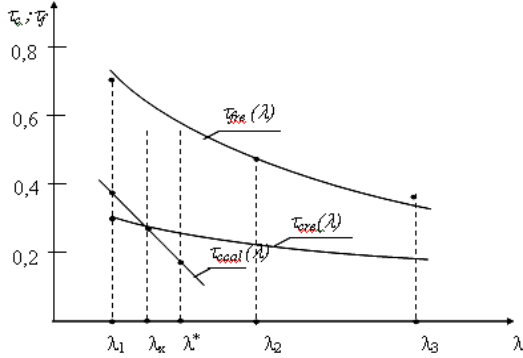


Fig. 2. Solution of equations (9).

Similar calculation may be carried out for wavelength  $\lambda^*$  determined as

$$\lambda^* = \frac{\lambda_1 + \lambda_2}{2}.$$

As a result of calculations we have

$$\tau_{cal}(\lambda^*) = 0,21.$$

Approximating the function  $\tau_{cal} = \tau_{cal}(\lambda)$  with a line function using calculated values at the points  $\lambda_1$  and  $\lambda^*$  we can find out the point of crossing of curves of functions  $\tau_{cal} = \tau_{cal}(\lambda)$  and  $\tau_{cre} = \tau_{cre}(\lambda)$ . The searched for crossing point is  $\lambda_1$  (fig. 1). As a result, we obtain possibility to calculate accurately such a value of  $\lambda_1 = \lambda_x$ , upon which the full separate compensation of two fractions of aerosol may be achieved.

## 2.2 Method of differential emission spectroscopy

The non – stability of optical depth of atmosphere in UV band is mainly caused by temporal variability of optical depths of ozone, atmospheric aerosol and Rayleigh scattering. Next in this paper we shall describe an original method making it possible to carry out the accurate measurements of intensity of anormal illumination of atmosphere with full statistical compensation of non – stability of separate components of total optical depth of atmosphere.

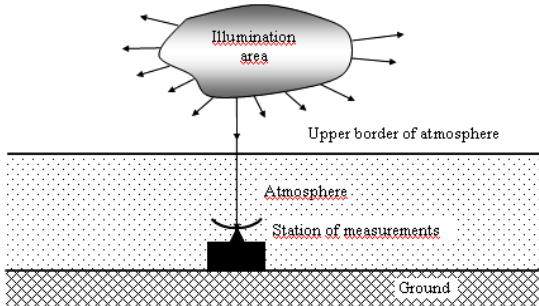


Fig. 3. Schematic illustration of procedure of measurement of intensity of anormal illumination.

Procedure of one station measurements of intensity of anormal illumination of atmosphere is given in fig. 3.

The general conception of suggested method of differential emission spectroscopy is as follows. Assume that illumination of atmosphere at wavelength  $\lambda_2$  exists (fig. 4). We should determine the intensity of illumination at the external border of atmosphere assuming that values of intensities of normal illumination at the border of atmosphere at wavelengths  $\lambda_1$  and  $\lambda_3$  i.e.  $I_0(\lambda_1)$  and  $I(\lambda_3)$  are known. The main condition of held measurements is ensuring statistical fullness of compensation of random changes of atmospheric optical depth. Briefly, this requirement may be explained as follows. The total optical depth of atmosphere  $\tau_\Sigma$  is determined as a sum of separate components  $\tau_i$ , i.e.

$$\tau_\Sigma = \sum_{i=1}^n \tau_i.$$

Measurements are held at wavelengths  $\lambda_j$ ,  $j = \overline{1, n}$ .

Here we should take into account, that coefficients of correlation of components of optical depth  $\tau_i$  are significantly different. It is well known, that some components of optical depth of atmosphere is characterized with more strong correlation on wavelength than between these components in fixed value of wavelength [4]. From another side, as it is known [5], for any two random parameters, the variance of sum or difference of these random parameters may be determined as follows:

$$D(x_1 \pm x_2) = \sigma_1^2 + \sigma_2^2 \pm 2\rho_{12}\sigma_1\sigma_2,$$

where  $\sigma_1, \sigma_2, \rho_{12}$  - is root – mean – square deviations and coefficient of mutual correlation of  $x_1$  and  $x_2$ , Therefore, if  $\rho_{1,2} \approx 1$  we have

$$\sigma(x_1 + x_2) = \sigma_1 \pm \sigma_2,$$

if  $\rho_{1,2} \approx 0$ , we have

$$\sigma(x_1 + x_2) = \sqrt{\sigma_1^2 + \sigma_2^2}.$$

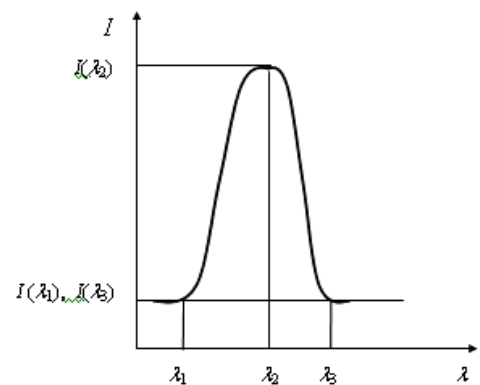


Fig. 4. For explanation of method of differential spectroscopy.

Now we can conclude, that mutual compensation of random parameters  $x_1$  and  $x_2$  is possible only upon

presence of strong correlation between them. On the basis of this condition of correlation theory it may be concluded, that the statistically full compensation of effects of components of  $\tau_{\Sigma}$  is possible by separate homogenic compensation of latter's. Now we should find out the mathematical condition for such a compensation and deduce the main equation of suggested method of DOAS. Let us consider two – component model of optical depth of atmosphere and measurements held at three wavelengths  $\lambda_1, \lambda_2$  and  $\lambda_3$ . As a result of held measurements we shall have following system of equations:

$$I(\lambda_1) = I_0(\lambda_1) \cdot e^{-m\tau_{\Sigma}(\lambda_1)} \quad (10)$$

$$I(\lambda_2) = I_0(\lambda_2) \cdot e^{-m\tau_{\Sigma}(\lambda_2)} \quad (11)$$

$$I(\lambda_3) = I_0(\lambda_3) \cdot e^{-m\tau_{\Sigma}(\lambda_3)} \quad (12)$$

Taking logarithms from both sides of (10) – (12), we have

$$\ln \frac{I_0(\lambda_1)}{I(\lambda_1)} = m\tau_{\Sigma}(\lambda_1) \quad (13)$$

$$\ln \frac{I_0(\lambda_2)}{I(\lambda_2)} = m\tau_{\Sigma}(\lambda_2) \quad (14)$$

$$\ln \frac{I_0(\lambda_3)}{I(\lambda_3)} = m\tau_{\Sigma}(\lambda_3). \quad (15)$$

Multiplying both sides of equations (13) – (15) accordingly to variable coefficients  $k_1$  and  $k_3$ , we carry out following operation:

formula (13) + formula (15) – formula (14).

As a result of aforesaid transformations we can obtain following equation:

$$k_1 m\tau_{\Sigma}(\lambda_1) + k_3 m\tau_{\Sigma}(\lambda_3) - m\tau_{\Sigma}(\lambda_2) = k_1 \ln \frac{I_0(\lambda_1)}{I(\lambda_1)} + k_3 \ln \frac{I_0(\lambda_3)}{I(\lambda_3)} - \ln \frac{I_0(\lambda_2)}{I(\lambda_2)}. \quad (16)$$

Representing the total optical depth  $\tau_{\Sigma}$  as a following sum of two components,

$$\tau_{\Sigma} = \alpha + \beta,$$

From equation (16) we can deduce following system of equations, describing the condition of full separate compensation of components  $\alpha$  and  $\beta$

$$\begin{cases} k_1 m\alpha(\lambda_1) + k_3 m\alpha(\lambda_3) - m\alpha(\lambda_2) = 0 \\ k_1 m\beta(\lambda_1) + k_3 m\beta(\lambda_3) - m\beta(\lambda_2) = 0 \end{cases} \quad (17)$$

Solution of the system (17) using classic Kramer's method gives us searched for values  $k_{10}, k_{30}$ .

In this case, from right side of equation (16) we can obtain following main equation of suggested method of differential optical emission spectroscopy (DOES)

$$\frac{I_0(\lambda_2)}{I(\lambda_2)} = \left[ \frac{I_0(\lambda_1)}{I(\lambda_1)} \right]^{k_{10}} \cdot \left[ \frac{I_0(\lambda_3)}{I(\lambda_3)} \right]^{k_{30}}. \quad (18)$$

As a result, the obtained equation (18) allows to find out the accurate value of intensity of atmospheric illumination using results of measurements of intensity at wavelength  $\lambda_2$  at the Earth surface, multiplied to following correcting coefficient

$$\left[ \frac{I_0(\lambda_1)}{I(\lambda_1)} \right]^{k_{10}} \cdot \left[ \frac{I_0(\lambda_3)}{I(\lambda_3)} \right]^{k_{30}}.$$

It should be noted, that two – component model of total optical depth is characteristic for UV band. If the measurement are held out of UV band, then three – and more

component model of optical depth of atmosphere should be considered. The number of fixed wavelengths of measurements in this case should be more than number of components by one. Naturally, there would be necessary to find out appropriate number of coefficients  $k_i$  by solving system of linear equations by order more than that system (10).

### Conclusion

It should be noted that combination of suggested multi – wavelengths method with well – known triangulation procedures may lead to increase of effectiveness of triangulation procedures, used for detection of source of illumination.

In this case the relevant methods of multi wave triangulation, taking into consideration different optical masses of beams trajectory should be developed.

It should be noted, that such a compensated methods of measurements have an universal feature and after some modifications may be easily used for solution of tasks of localization of absorbing medium.

The method described here may be used both in district stations designated for monitoring of anormal illumination of atmosphere and in multi station networks. In the second case, the procedure of calculation described here should be repeated for each station separately, because one cannot expect equality of mean values of optical parameters relevant for various places installation of such stations.

In conclusion we should stress out the utmost importance of proper solution of accurate localization task of illumination area of atmosphere, because solution of it commonly link with task of localization of reason of such an illumination, which may exists both on the surface or inside the Earth.

[1] D.Pallamrayn. Cedarweb.hao.ucar.edu/community/passive\_optical/pallamrayrev.pdf. Applications of optical spectrographs for Passive Remote Sensing of Upper Atmosphere.

[2] Brion J. Jackol, Fokke Creutzberg, Eric F. Donovan, and Leroy L. Cogger. Triangulation of Auroral Red – Line Emission Heights. Sodankula Geophysical Observatoty Publications. 2003, No. 92, p. 97-100.

- [3] *N.T. O'Neill, T.F. Eck, B.N. Holben, A. Smirnov and O. Dubovik. Journal of Geophysical Research. v. 106, No. D9. p. 9787-9806, May 16, 2001.*
- [4] *M.V. Kabanov, M.V. Panchenko, Y.A. Pkhalov. Optical features of atmospheric haze of coastal regions. Novosibirsk: Nauka, Sib. branch, 1988, 201 p.*
- [5] *Handbook on mathematics, M. Nauka, 1968.*

**H.H. Əsədov, T.M. Əliyeva, İ.M. Mirzəbalayev, İ.G. Çoban-zadə**

**ATMOSFERİN ANOMAL İŞIQLANMASINI QEYD ETMƏK ÜÇÜN YÜKSƏK DƏQİQLİKLİ YERÜSTÜ  
SİSTEMLƏRİNİN İŞLƏNİB HAZIRLANMASI**

Məqalədə atmosferin anomal işıqlanma intensivliyinin fon siqnallarının kompensasiyası ilə ölçülməsi xüsusiyyətləri nəzərdən keçirilmişdir. Emission delta spektroskopiya metodu təklif edilmişdir ki, bu metod xırda dispers və iri dispers aerosolun aparılan ölçmələrin nəticələrinə təsirini ayrı-ayrılıqda tam kompensasiya etməyə imkan verir. Həmçinin, atmosferdəki anomal işıqlanmaların fiksə edilmiş dalğa uzunluqlarında yüksək dəqiqlikli yerüstü ölçmələrinin aparılması imkanı nəzərdən keçirilmişdir. Bu cür ölçmələrə imkan verən differensial optik emission spektroskopiya metodu təsvir edilmişdir.

**Х.Г. Асадов, Т.М. Алиева, И.М. Мирзабалаев, И.Г. Чобан-заде**

**РАЗРАБОТКА НАЗЕМНОЙ ВЫСОКОТОЧНОЙ СИСТЕМЫ ДЛЯ РЕГИСТРАЦИИ АНОМАЛЬНОГО  
СВЕЧЕНИЯ АТМОСФЕРЫ**

В статье рассмотрены особенности измерения интенсивности аномального свечения атмосферы с компенсацией фоновых сигналов.

Предложен метод эмиссионной дельта спектроскопии, позволяющий полную раздельную компенсацию эффекта мелкодисперсионного и грубодисперсионного аэрозоля на результат проводимых измерений. Также рассмотрена возможность проведения высокоточных наземных измерений аномального излучения атмосферы на фиксированных длинах волн. Изложен предлагаемый метод дифференциальной оптической эмиссионной спектроскопии, реализация которого позволяет проводить такие измерения.

*Received: 18.09.08*



## HAMILTONIAN REDUCTION FOR NON-ABELIAN CONFORMAL AFFINE TODA THEORIES

**M.A. MUKHTAROV**

*Institute of Mathematics and Mechanics  
370602, Baku, F.Agaev str. 9, Azerbaijan*

The discrete symmetry transformation method has been applied for non-abelian conformal affine Toda models.

1. Within the integrable models in 1+1 dimensions, the investigation of the different Toda Field Theories has recently received a lot of attention. According to their underlying algebraic structure, they can be divided into three categories; each one exhibiting nice characteristic properties. First, associated to the finite simple Lie algebras, there are the Conformal Toda models, which are conformally invariant 1+1 field theories. Even more, they permit the construction of extensions of the Virasoro algebra including higher spin generators, namely W-algebras. The second class of theories are the Affine Toda models, based on loop algebras, which can be regarded as a perturbed Conformal Toda model where the conformal symmetry is broken by the perturbation while the integrability is preserved [1]. One of their main properties is that they possess soliton solutions. These two classes of models are called abelian or non-abelian referring to whether their fields live on an abelian or non-abelian group [2, 3, 4, 5]. Finally, the conformal symmetry can be restored in the abelian Affine Toda models just by adding two extra fields which do not modify the dynamics of the original model; one of these fields is a connection whose only role is to implement the conformal invariance. These are the so called Conformal Affine Toda models [6, 7], and they are based on a full Kac-Moody algebra; moreover, they are integrable [8], and have soliton solutions [9]. In fact, many properties of the Affine Toda models can be more easily understood by considering them as the Conformal Affine Toda models with the conformal symmetry spontaneously broken.

At the same time the problem of constructing of the solutions of self-dual Yang-Mills (SDYM) model and its dimensional reductions, the one dimensional WZNW model in our case, in the explicit form for arbitrary semisimple Lie algebra, rank of which is greater than two, remains important for the present time. The interest arises from the fact that almost all integrable models in one, two and (1+2)-dimensions are symmetry reductions of SDYM or they can be obtained from it by imposing the constraints on Yang-Mills potentials [10-27].

Two effective methods of generating of the exact solu-

tions, the Riemann Hilbert Problem formalism [20] and the discrete symmetry transformation method [22], have been applied to Toda like systems. This work is devoted to construct a group theoretical background of earlier considerations.

The two-loop WZNW model was introduced in [6] as the generalization of the ordinary WZNW model to the affine case. Its equations of motion are given by

$$\partial_+ (\partial_- \hat{g} \hat{g}^{-1}) = 0 \quad ; \quad \partial_- (\partial_+ \hat{g} \hat{g}^{-1}) = 0 \quad ,$$

where  $\partial_{\pm}$  are derivatives with respect to the light-cone variables  $x_{\pm} = x \pm t$ , and  $\hat{g}$  is an element of the group  $G$  formed by exponentiating an untwisted affine (real) Kac-Moody (KM) algebra  $\hat{G}$ . Its generators  $T_a^m$ ,  $D$  and  $C$  satisfy the commutation relations

$$[T_a^m, T_b^n] = f_{ab}^c T_c^{m+n} + m C g_{ab} \delta_{m+n,0} \quad (2.2)$$

$$[D, T_a^m] = m T_a^m, \quad [C, D] = [C, T_a^m] = 0 \quad (2.3)$$

where  $f_{ab}^c$  are the structure constants of a finite (real) semisimple Lie algebra  $G$ ,  $n$  and  $m$  are integers, and  $g_{ab}$  is the Killing form of  $G$ , i.e.,  $g_{ab} = \text{Tr}(T_a T_b)$ ,  $T_a$  being the generators of  $G$ . The non-degenerate bilinear form of  $\hat{G}$  is defined as

$$\text{Tr}(T_a^m T_b^n) = \delta_{m+n,0} \text{Tr}(T_a T_b), \quad \text{Tr}(C, D) = 1$$

$$\text{Tr}(C, T_a^m) = \text{Tr}(D, T_a^m) = 0 \quad (2.4)$$

and we will use the same notation,  $\text{Tr}$ , for both the Killing form of  $G$  and the bilinear form of  $\hat{G}$ .

2. The two-loop WZNW model is invariant under left and right translations

$$\hat{g}(x_+, x_-) \rightarrow \hat{g}_L(x_-) \hat{g}(x_+, x_-), \quad \hat{g}(x_+, x_-) \rightarrow \hat{g}(x_+, x_-) \hat{g}_R(x_+) \quad (2.5)$$

The corresponding Noether currents are the components of  $\partial_- \hat{g} \hat{g}^{-1}$  and  $\hat{g}^{-1} \partial_+ \hat{g}$ , and they generate two commuting copies of the so called two-loop Kac-Moody algebra, defined by the relations

$$\begin{aligned} [J_a^m(x), J_b^n(y)] &= f_{ab}^c J_c^{m+n}(x) \delta(x-y) + g_{ab} \delta_{m+n} (k \partial_x \delta(x-y) + m J^C(x) \delta(x-y)) \\ [J^D(x), J_a^m(y)] &= m J_a^m(y) \delta(x-y) \\ [J^C(x), J^D(y)] &= k \partial_x \delta(x-y) \\ [J^C(x), J_a^m(y)] &= 0 \end{aligned} \quad (26)$$

The left and right currents satisfying the above relations are related to the group element  $\hat{g}$  in eq.(2.1) by

$$F_R(x_+) = k\hat{g}^{-1}\partial_+\hat{g} = \sum_{ab} \sum_{n=-\infty}^{\infty} g^{ab} J_{R,a}^{-n}(x_+) T_b^n + J_R^D(x_+)C + J_D^C(x_+)D \quad (2.10)$$

$$F_L(x_-) = -k\partial_-\hat{g}\hat{g}^{-1} = \sum_{ab} \sum_{n=-\infty}^{\infty} g^{ab} J_{L,a}^{-n}(x_-) T_b^n + J_L^D(x_-)C + J_D^C(x_-)D \quad (2.11)$$

where  $g^{gl}$  is the inverse of the Killing form  $g_{ab}$  defined above. The different meaning of the two central extensions in eqs.(2.6)-(2.9) algebra is clarified by expressing the algebra as

$$[Tr(UF(x), Tr(VF(y))] = Tr([U, V]F(x))\partial(x-y) + kTr(UV)\partial_x\partial(x-y) \quad (2.12)$$

where  $U, V$  are two elements of the Kac-Moody algebra  $\hat{G}$ ,  $F$  is either  $F_R$  or  $F_L$ , and  $Tr$  is the invariant bilinear form of  $\hat{G}$ .

Consider now a gradation of the Kac-Moody algebra  $\hat{G}$

$$\hat{G} = \bigoplus_s \hat{G}_s \quad (2.13)$$

with

$$[\hat{G}_s, \hat{G}_r] \subset \hat{G}_{s+r} \quad (2.14)$$

The reduction presented in this section does not require that this gradation is integer; it just needs that the grades  $s$  take zero, positive and negative values, i.e.,

$$\hat{G} = \hat{G}_+ \oplus \hat{G}_0 \oplus \hat{G}_- \quad (2.15)$$

with

$$\hat{G}_+ = \bigoplus_{s>0} \hat{G}_s, \quad \hat{G}_- = \bigoplus_{s<0} \hat{G}_s \quad (2.16)$$

We now consider those group elements that can be written in a ‘‘Gauss decomposition’’ form

$$\hat{g} = NBM \in G \quad (2.17)$$

where  $N, B$  and  $M$  are group elements formed by exponentiating elements of  $\hat{G}_+, \hat{G}_0$  and  $\hat{G}_-$  respectively.

Using eq.(2.17), we can write the equations of motion (2.1) as

$$\partial_- K_R = [K_R, \partial_- MM^{-1}] \quad (2.18)$$

$$\partial_+ K_L = [K_L, N^{-1} \partial_+ N] \quad (2.19)$$

where we have introduced

$$K_L = N^{-1} \partial_- \hat{g} \hat{g}^{-1} N = N^{-1} \partial_- N + \partial_- BB^{-1} + B \partial_- MM^{-1} B^{-1} \quad (2.20)$$

$$K_R = M \hat{g}^{-1} \partial_+ \hat{g} M^{-1} = B^{-1} N^{-1} \partial_+ NB + B^{-1} \partial_+ B + \partial_+ MM^{-1} \quad (2.21)$$

Although the quantities  $K_{L/R}$  are not chiral, they have a simpler structure than the currents and will be very useful in what follows. We will reduce the two-loop WZNW model by imposing constraints not directly on the currents but on  $K_{L/R}$ . We impose the constraints

$$B^{-1} (N^{-1} \partial_+ N) B = \Lambda_l \quad (2.22)$$

$$B (\partial_- M) M^{-1} B^{-1} = \Lambda_{-l} \quad (2.23)$$

where  $\Lambda_{\pm l}$  are constant elements of  $\hat{G}_{\pm l}$ . These constraints reduce the two-loop WZNW model to a theory containing only the fields corresponding to the components of  $B$  and to the components of  $N$  and  $M$  associated to the generators whose grade is  $< l$  and  $> l$  respectively.

To obtain the equations of motion for such model one notices that the constraints (2.22) and (2.23) imply that

$$N^{-1} \partial_+ N \in \hat{G}_l \quad (2.24)$$

$$(\partial_- M) M^{-1} \in \hat{G}_{-l} \quad (2.25)$$

Therefore the only terms of zero grade on the right hand side of (2.19) are coming from  $[\Lambda_{-l}, N^{-1} \partial_+ N] = [\Lambda_{-l}, B \Lambda_l B^{-1}]$ . So we get

$$\partial_+ (\partial_- BB^{-1}) = [\Lambda_{-l}, B \Lambda_l B^{-1}] \quad (2.26)$$

which can also be written as

$$\partial_- (B^{-1} \partial_+ B) = -[\Lambda_l, B^{-1} \Lambda_{-l} B] \quad (2.27)$$

These are the equations of motion of what we call the generalized non-abelian conformal affine Toda models.

3. The one dimensional reduction of self duality equations obtained in [20] are the equations for the element  $f$ , taking values in the semisimple algebra,

$$\frac{\partial^2 f}{\partial r^2} + 2 \frac{\partial f}{\partial r} - [H, [H, f]] - 2[X^-, [X^+, f]] - 2[X^+, [X^-, f]] + 2[[\frac{\partial}{\partial r} - H, f], [X^+, f]] = 0 \quad (3.1)$$

Here  $H, X^\pm$  are generators of  $A_1(SL(2, C))$  algebra

$$[X_M^+, X^-] = H, [H, X^\pm] = \pm 2X^\pm$$

embedded to gauge algebra in the half-integer way.

Let's rewrite (3.1) in the equivalent form:

$$\begin{aligned} & \left[ \frac{1}{2} \left( \frac{\partial}{\partial r} + H \right) - [X^+, f], -\frac{1}{2} \left( \frac{\partial}{\partial r} - H, f \right) + X^- \right] - \\ & - \frac{1}{2} \left( \frac{\partial}{\partial r} - H, f \right) + X^- = 0 \end{aligned}$$

This equation after changing the variable  $t = \ln r$  has the following form

$$\begin{aligned} & \left[ \frac{\partial}{\partial t} + \frac{1}{2} H - [X^+, f], -\frac{\partial f}{\partial t} + \frac{1}{2} [H, f] + X^- \right] - \\ & - \frac{\partial f}{\partial t} + \frac{1}{2} [H, f] + X^- = 0 \end{aligned} \quad (3.2)$$

Introducing the notation

$$\tilde{F} = e^{\frac{1}{2}Ht} \left( -\frac{\partial f}{\partial t} + \frac{1}{2} [H, f] + X^- \right) e^{-\frac{1}{2}Ht}, \quad (3.3)$$

multiplying (2) from the left side by  $e^{\frac{1}{2}Ht}$  and from the right side by  $e^{-\frac{1}{2}Ht}$ , we obtain

$$\frac{\partial \tilde{F}}{\partial t} - \left[ \left( e^{\frac{1}{2}Ht} X^+ e^{-\frac{1}{2}Ht}, e^{\frac{1}{2}Ht} f e^{-\frac{1}{2}Ht} \right), \tilde{F} \right] + \tilde{F} = 0$$

Due to the evident equality

$$e^{\frac{1}{2}Ht} X^+ e^{-\frac{1}{2}Ht} = e^t X^+$$

the last equation can be rewritten in a form

$$\frac{\partial \tilde{F}}{\partial t} - e^t [[X^+, \tilde{f}], \tilde{F}] + \tilde{F} = 0, \quad (3.4)$$

where

$$\tilde{f} = e^{\frac{1}{2}Ht} f e^{-\frac{1}{2}Ht}.$$

In terms of these notations we have from (3.3) the following expression

$$\tilde{F} = -\frac{\partial \tilde{f}}{\partial t} + [H, \tilde{f}] + X^- e^{-t} = 0$$

Let's introduce the notation

$$F = e^t \tilde{F} = -e^t \frac{\partial \tilde{f}}{\partial t} + e^t [H, \tilde{f}] + X^- = 0$$

Then (3.4) has a form

$$\frac{\partial F}{\partial t} + [A, F] = 0, \quad (3.5)$$

where  $A = -e^t [X^+, \tilde{f}]$ .

The equation (5) is one-dimensional evolution equation defined by Lax pair operators and it is one of the principal criteria of equations integrability.

From the presentation (3.5) it is followed that

$$\frac{\partial}{\partial t} sp F^n = 0, \text{ for } \forall n$$

and solution of the equations can be found in a form

$$F = \varphi F_0 \varphi^{-1}, \quad (3.6)$$

where  $\varphi(t)$  takes values in the corresponding Lie group and  $F_0 = F|_{t=0}$ .

From equation (5) and presentation (6) it is directly followed the expression for the operator  $A$ :

$$A = \varphi' \varphi^{-1} \quad (\varphi' = \frac{\partial \varphi}{\partial t}) \quad (3.7)$$

Let's consider the commutator of  $F$  with  $X^+$ :

$$\begin{aligned} [X^+, F] &= [X^+, X^-] - e^t \frac{\partial}{\partial t} [X^+, \tilde{f}] + e^t [X^+, [H, \tilde{f}]] = \\ &= H - e^t \frac{\partial}{\partial t} [X^+, \tilde{f}] - 2e^t [X^+, \tilde{f}] + e^t [X^+, [H, \tilde{f}]] = \\ &= H - \frac{\partial}{\partial t} (e^t [X^+, \tilde{f}]) - e^t [X^+, \tilde{f}] + [H, e^t [X^+, \tilde{f}]]. \end{aligned}$$

Taking into account (3.6) and (3.7) the last expression can be rewritten in a form

$$[X^+, \varphi F_0 \varphi^{-1}] = H - (\varphi' \varphi^{-1})' - \varphi' \varphi^{-1} + [H, \varphi' \varphi^{-1}].$$

Making the substitution  $\varphi = e^{Ht} q$  and introducing a new variable  $\tau = e^{-t}$ , we have

$$\frac{\partial}{\partial \tau} \left( \frac{\partial q}{\partial \tau} q^{-1} \right) = [q F_0 q^{-1}, X^+] \quad (3.7)$$

Equation (3.8) is one-dimensional generalized non-abelian conformal affine Toda model as it is obviously seen from eq. (2.26).

The next question how to obtain from this solution new solutions using the discrete symmetry transformation:

$$\begin{aligned}
 F^- &= \frac{1}{f^+} \\
 \frac{\partial F^0}{\partial z} &= (f^0 - F^0 + z) \frac{\partial \ln f^+}{\partial z} - \frac{\partial f^0}{\partial z} \\
 \frac{\partial F^0}{\partial \bar{z}} &= (f^0 - F^0 + \bar{z}) \frac{\partial \ln f^+}{\partial \bar{z}} - \frac{\partial f^0}{\partial \bar{z}} \\
 \frac{\partial F^+}{\partial z} &= (f^0 - F^0 + z)^2 \frac{\partial \ln f^+}{\partial z} - 2f^+(f^0 - F^0 + z) \frac{\partial f^0}{\partial z} - (f^+)^2 \frac{\partial f^-}{\partial z} \\
 \frac{\partial F^+}{\partial \bar{z}} &= (f^0 - F^0 + \bar{z})^2 \frac{\partial \ln f^+}{\partial \bar{z}} - 2f^+(f^0 - F^0 + \bar{z}) \frac{\partial f^0}{\partial \bar{z}} - (f^+)^2 \frac{\partial f^-}{\partial \bar{z}}
 \end{aligned} \tag{3.8}$$

Here  $f(f^+, f^0, f^-)$  is considered to be a known solution of equation (3.7) and  $F(F^+, F^0, F^-)$  is one to be determined. The discrete symmetry transformation is to apply at

first to two-dimensional generalization of equation (3.7) and then one-dimensional solution is to obtain by reduction. The concrete realization of the solution will be derived in next publications.

- |   |   |
|---|---|
| <p>[1] T.Eguchi and S-K.Yang, Phys. Lett. 224B, 1989, 373-378; T.J. Hollowood and P. Mansfield, Phys. Lett. 226B, 1989, 73-79.</p> <p>[2] A.N. Leznov and M.V. Saveliev, Commun. Math. Phys. 89, 1983, 59-75; Theor. Mat. Phys. 54, 1983, 209-217.</p> <p>[3] A.N. Leznov and M.V. Saveliev, Group Theoretical Methods for Integration of Non Linear Dynamical Systems; Progress in Physics 15 (Birkhauser, Basel, 1992).</p> <p>[4] J.L. Gervais and M.V. Saveliev, Phys. Lett. 286B, 1992, 271.</p> <p>[5] J. Underwood, Aspects of non abelian Toda theories, hep-th/9304156.</p> <p>[6] H. Aratyn, L.A. Ferreira, J.F. Gomes and A.H. Zimerman, Phys. Lett. 254B, 1991, 372-380</p> <p>[7] O. Babelon and L. Bonora, Phys. Lett. 244B (1990)220-226.</p> <p>[8] A. Aratyn, L.A. Ferreira, J.F. Gomes and A.H. Zimerman, Phys. Lett. A, hep-th/9308086.</p> <p>[9] H. Aratyn, C.P. Constantinidis, L.A. Ferreira, J.F. Gomes and A.H. Zimerman, Nucl. Phys. B406 [FS](1993)727-770</p> <p>[10] R.S. Ward, Phil. Trans. R. Soc. Lond. A315, 451 (1985); Lect. Notes Phys., 1987, 280, 106; Lond. Math. Soc. Lect. Notes Ser., 1990, 156, 246.</p> <p>[11] L.J. Mason and G.A. J.Sparling, Phys. Lett., 1989, A137, 29; J. Geom. and Phys., 1992, 8, 243.</p> <p>[12] S. Chakravarty, M.J. Ablowitz and P.A. Clarkson, Phys. Rev. Lett., 1990, 1085.</p> | <p>[13] I. Bakas and D.A. Depireux, Mod. Phys. Lett., 1991, A6, 399.</p> <p>[14] M.J. Ablowitz, S. Chakravarty and L.A. Takhtajan, Comm. Math. Phys., 1993, 158, 1289.</p> <p>[15] T.A. Ivanova and A.D. Popov, Phys. Lett., 1992, A170, 293.</p> <p>[16] L.J. Mason and N.M.J. Woodhouse, Nonlinearity 1, 1988, 73; 1993, 6, 569.</p> <p>[17] M. Kovalyov, M. Legare and L. Gagnon, J. Math. Phys., 1993, 34, 3425.</p> <p>[18] M. Legare and A.D. Popov, Pis'ma Zh. Eksp. Teor. Fiz., 1994, 59, 845.</p> <p>[19] A.A. Belavin and V.E. Zakharov, Phys. Lett., 1978, B73, 53.</p> <p>[20] A.N. Leznov and M.A. Mukhtarov, J. Math. Phys., 1987, 28 (11), 2574; Prepr. IHEP, 1987, 87-90. Prepr. ICTP 163, Trieste, Italy, 1990; J. Sov. Lazer Research, 13 (4), 284, 1992.</p> <p>[21] A.N. Leznov, IHEP preprint-92/87, 1990.</p> <p>[22] A.N. Leznov, M.A. Mukhtarov and W.J. Zakrzewski, Tr. J. of Physics 1995, 19, 416.</p> <p>[23] M.A. Mukhtarov, Fizika, 2002, v. 5, N 2, 38</p> <p>[24] M.A. Mukhtarov, Fizika, 2002, v. 5, N 3, 3</p> <p>[25] V.G. Knizhnik and A.B. Zamolodchikov, Nucl. Phys. B247, 1984, 83.</p> <p>[26] F. Bastianelli, Nucl. Phys. B361, 1991, 555.</p> <p>[27] A.A. Tseytlin, Nucl. Phys. B411, 1994, 509.</p> |
|---|---|

M.A. Muxtarov

## TODUN QEYRİ-ABEL KONFORM AFFİN MODELİNİN HAMILTON REDUKSİYASI

Todun qeyri-abel konform Affin modeli üçün diskret simmetriyanın dəyişmə metodu tətbiq edilmişdir.

M.A. Мухтаров

## ГАМИЛЬТОВА РЕДУКЦИЯ НЕАБЕЛЕВЫХ КОНФОРМНЫХ АФФИННЫХ МОДЕЛЕЙ ТОДА

Метод преобразований дискретной симметрии применен для неабелевых конформных аффинных моделей Тода.

Received: 18.09.08

## ROENTGENOGRAPHIC INVESTIGATION OF $\text{Bi}_2\text{Te}_3\text{-Bi}_2\text{Se}_3\text{<Tb>}$ AND $\text{Bi}_2\text{Te}_3\text{-Bi}_2\text{Se}_3\text{<Cl>}$ FILMS

N.M. ABDULLAYEV

*H.M. Abdullayev Institute of Physics of NAS of Azerbaijan  
H. Javid ave., 33, Baku, AZ-1143, Azerbaijan*

The real accretion of microparticle sizes, any structural reconstructions, formation of new phases don't take place at annealing of  $\text{Bi}_2\text{Te}_3\text{-Bi}_2\text{Se}_3\text{<Tb>}$  and  $\text{Bi}_2\text{Te}_3\text{-Bi}_2\text{Se}_3$  up to  $\sim 600\text{K}$ , the polycrystalline structure is observed on X-ray pattern. The calculations of interplanar spacings show that structure becomes more strength at film annealing at temperature  $\sim 600\text{K}$ .

### Introduction

Nowadays the alternative power engineering shows the interest in film thermo-electric generators, and also the demand to infra-red radiation detectors has increased. The thermoelements or thermobatteries, covered on the substrates by the method of vacuum condensation with the use of masks and photolithography [1].

It is known, that monocrystalline films with complex technology of their preparation loose their quality during exploitation in time. The change of scattering parameter clearly reveals in small-grained films  $\text{Bi}_2\text{Te}_{2.1}\text{Se}_{0.9}$  evaporated on amorphous substrate [1] in comparison with scattering which is character for these compositions in volume crystals  $r=0$  (scattering on acoustic photons). The amorphous films have some understated characteristics than polycrystalline ones.

The substrate temperature should be in optimal limits for obtaining of qualitative film. Roentgenographic investigation of thin films had been carrying out by Frankombe and Semiletov. The temperature of (glass) substrate at which the film is formed corresponding to the composition  $\text{Bi}_2\text{Te}_3$ , has been defined at film investigation. The strong fluctuation from  $\text{Bi}_2\text{Te}_3$  composition begins at increase  $t_{\text{sub}}$  higher than  $200^\circ\text{C}$  [2]. Too low substrate temperature opposes to uniform distribution of adsorbed atoms; they group into "islands" of different thicknesses. Vice versa, too high substrate temperature leads to the separation of already settled atoms, their re-evaporation [3].

The task of X-ray investigation of system of polycrystalline films  $\text{Bi}_2\text{Te}_3\text{-Bi}_2\text{Se}_3\text{<Tb>}$  and  $\text{Bi}_2\text{Te}_3\text{-Bi}_2\text{Se}_3\text{<Cl>}$  obtained by thermal spraying in vacuum by the method of hot wall, has been proposed by us with the aim of improvement of physical thermoelement characteristics because of decrease of their geometric sizes, with transition on polycrystalline films, evaporated on amorphous substrate.

The given work is dedicated to X-ray investigation method of obtained polycrystalline films of bismuth telluride with terbium and chlorine up to and after annealing.

### Investigation method

The investigated films  $\text{Bi}_2\text{Te}_3$ ,  $\text{Bi}_2\text{Te}_3\text{-Bi}_2\text{Se}_3\text{<Tb>}$  and  $\text{Bi}_2\text{Te}_3\text{-Bi}_2\text{Se}_3\text{<Cl>}$  with optimal thickness 0,30 mcm prepared by evaporation of synthesized substances in installation BYII-4 in vacuum  $\sim 10^{-4}\text{Pa}$  on preliminarily pre-heated NaCl crystals and glass, had been grown by the method of hot wall [1,4]. The more success conditions for steam condensation are formed on substrate, the partial steam condensation on cap walls is led to the minimum by additionally pre-heated wall, where wall temperature at spraying is  $800\text{K}$ , substrate temperature is  $\sim 600\text{K}$  at precipitation rate of thin layers is  $\sim 2\text{nm/sec}$  [5].

The obtained polycrystalline films  $\text{Bi}_2\text{Te}_3\text{-Bi}_2\text{Se}_3\text{<Tb>}$  and  $\text{Bi}_2\text{Te}_3\text{-Bi}_2\text{Se}_3\text{<Cl>}$  given below have been investigated by roentgenography method.

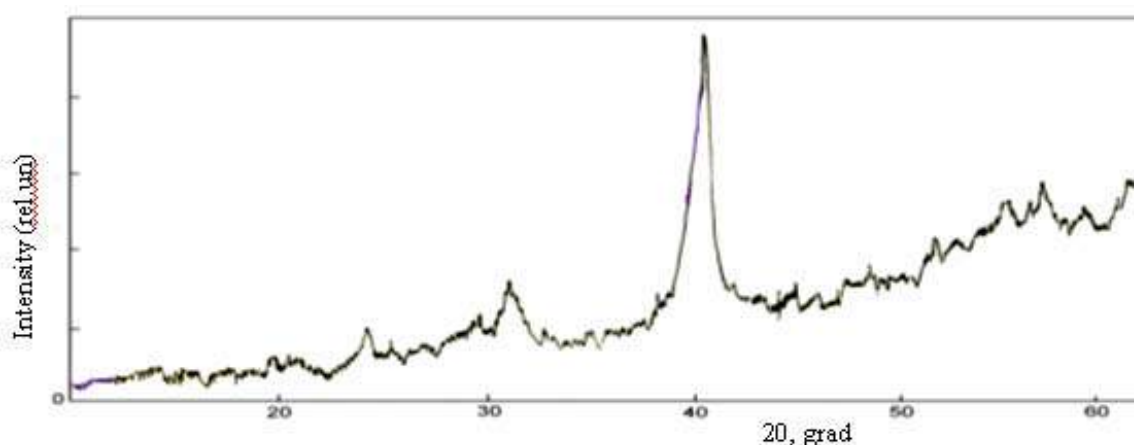


Fig.1. Roentgenogram of unannealed  $\text{Bi}_2\text{Te}_3\text{-Bi}_2\text{Se}_3\text{<Tb>}$  film.

The film samples suitable for roentgenographic investigations by thickness 30 nm are prepared by sublimation of synthesized compound of  $\text{Bi}_2\text{Te}_3$  and

$\text{Bi}_2\text{Te}_3\text{-Bi}_2\text{Se}_3\text{<Tb>}$  composition, i.e.  $(\text{Bi}_2\text{Te}_3\text{-Bi}_2\text{Se}_3)_{1-x}\text{Tb}_x$  ( $x=0,15$ ) and  $\text{Bi}_2\text{Te}_3\text{-Bi}_2\text{Se}_3\text{<Cl>}$  on freshly cleaved bounds of haloid crystal NaCl and glass substrates.

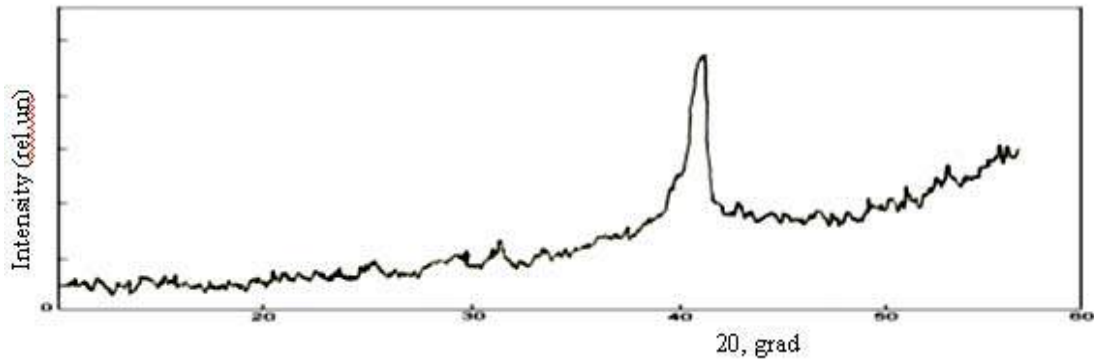


Fig. 2. Roentgenogram of unannealed  $\text{Bi}_2\text{Te}_3\text{-Bi}_2\text{Se}_3\langle\text{Cl}\rangle$  film.

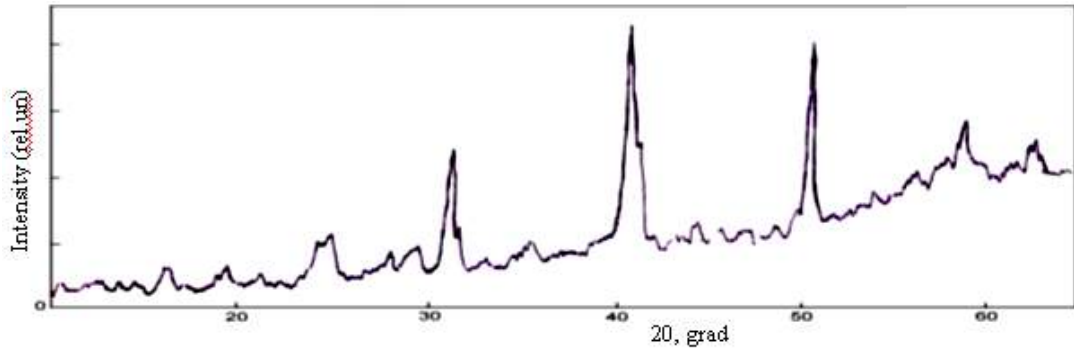


Fig. 3. Roentgenogram of annealed  $\text{Bi}_2\text{Te}_3\text{-Bi}_2\text{Se}_3\langle\text{Tb}\rangle$  film.

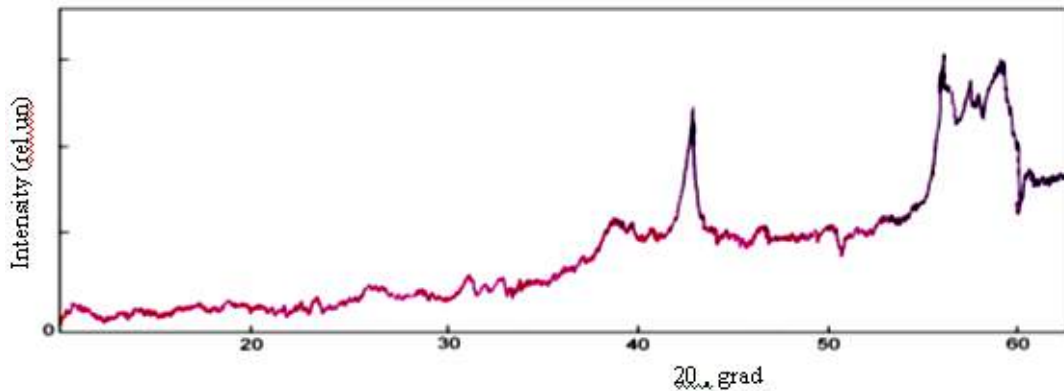


Fig. 4. Roentgenogram of annealed  $\text{Bi}_2\text{Te}_3\text{-Bi}_2\text{Se}_3\langle\text{Cl}\rangle$  film.

The obtained samples are treated by roentgenographic analysis on DRON-2,0 ( $\text{CuK}_\alpha$  is radiation, Ni is filter) at the mode 35kV, 10mA. 10, 13, 15, 16 clear diffraction reflections for  $\text{Bi}_2\text{Te}_3$  analogues have been fixed in the limits  $5^\circ \leq 2\theta \leq 70^\circ$  correspondingly. The obtained diffraction patterns are almost identical ones with small difference of reflex intensity and angles of reflection. The film roentgenogram of  $\text{Bi}_2\text{Te}_3\text{-Bi}_2\text{Se}_3\langle\text{Tb}\rangle$  and  $\text{Bi}_2\text{Te}_3\text{-Bi}_2\text{Se}_3\langle\text{Cl}\rangle$  polycrystals before and after annealing are well indicated on the base of  $\text{Bi}_2\text{Te}_3$  hexagonal lattice [6].

## Results

The thermo-annealing influence at  $\sim 600$  on the film structure and properties, precipitated on the glass has been investigated. The films, precipitated on the glass, are treated by annealing in the vacuum for the elimination of elastic stress fields. The annealing with duration 24 hours with temperature decrease in 25 grad/min is carried out in vacuum  $\sim 10^{-4}\text{Pa}$ .

Table 1.

Roentgenographic investigation of  $\text{Bi}_2\text{Te}_3\text{-Bi}_2\text{Se}_3\langle\text{Tb}\rangle$  and  $\text{Bi}_2\text{Te}_3\text{-Bi}_2\text{Se}_3\langle\text{Cl}\rangle$  films.

Nº	$d_{sc},$ p-tip	$d_{exp},$ p-tip	$I/I_0$	Hkl	$d_{exp},$ n-tip	$I/I_0$
1	5,050	5,415	2	222	5,523	1
2	3,770	3,849	10	110	3,889	5
3	3,210	3,292	1	221	3,366	1
4	-	2,716	10	332	3,029	10
5	-	2,593	10	444	2,869	7
6	2,370	2,450	20	433	2,629	10
7	2,230	2,344	2	443	2,469	7
8	2,190	2,215	6	011	2,230	5
9	2,030	2,110	9	555; 231; 544	-	-
10	1,996	2,007	5	554; 11 1; 200	-	-
11	1,809	1,868	2	220; 342; 311	1,926	10
12	-	1,802	17	331	1,819	10
13	1,696	1,755	15	665; 442	-	-
14	1,608	1,611	20	453	1,637	10
15	1,486	1,526	20	665 442	1,551	10
16	1,450	1,458	10	533	1,492	5

The roentgenogram obtained at the radiation of polycrystalline films  $\text{Bi}_2\text{Te}_3\text{-Bi}_2\text{Se}_3$  <Tb> and  $\text{Bi}_2\text{Te}_3\text{-Bi}_2\text{Se}_3$  <Cl> are well indicated on the base of hexagonal lattice of  $\text{Bi}_2\text{Te}_3$  polycrystal ( $a=0,43835$ ,  $c=3,0487\text{nm}$ ; sp.gr.  $D_{3d}^5$ ,  $R_{3m}$ ,  $Z=3$ ) and satisfies data [7]. The all reflexes having strong and average intensities which are character for the given structure are observed on roentgenogram. The results of calculated  $hkl$ ,  $I/I_0$  and experimental interplanar spacings  $d_{exp}$  in the films  $\text{Bi}_2\text{Te}_3\text{-Bi}_2\text{Se}_3$  <Tb> of  $p$ -type and  $\text{Bi}_2\text{Te}_3\text{-Bi}_2\text{Se}_3$  <Cl> of  $n$ -type in comparison with science data  $d_{sc}$  are given in the table 1 [7-8].

The analysis of obtained data and calculated values show on the fact that compositions of annealed films  $\text{Bi}_2\text{Te}_3\text{-Bi}_2\text{Se}_3$  <Tb> and  $\text{Bi}_2\text{Te}_3\text{-Bi}_2\text{Se}_3$  <Cl> form the isostructure on the base of hexagonal structure of bismuth telluride chalcogenide.

### Conclusion

On the base of X-ray investigation of the thin film structures obtained by thermal spraying on the glass, it has been established that polycrystalline films of  $\text{Bi}_2\text{Te}_3\text{-Bi}_2\text{Se}_3$  <Tb> and  $\text{Bi}_2\text{Te}_3\text{-Bi}_2\text{Se}_3$  <Cl> compositions by thickness 0,30 mcm form at substrate temperature  $\sim 600\text{K}$ . Therefore, the real increase of microparticle sizes, any structural reconstructions, formations of new phases aren't observed at annealing of  $\text{Bi}_2\text{Te}_3\text{-Bi}_2\text{Se}_3$  <Tb> and  $\text{Bi}_2\text{Te}_3\text{-Bi}_2\text{Se}_3$  <Cl> up to  $\sim 600\text{K}$ , the polycrystalline structure are observed on roentgenogram. The calculations of interplanar spacings show that structure becomes more strength at film annealing at temperature  $\sim 600\text{K}$ .

The author is thankful to G.G. Huseynov for help in the carrying out of investigations.

- 
- [1] N.S. Lidorenko. Plyonochkiye termoelementi: fizika i primeneniye. M., Nauka, 1985, 3, 7, 179, 199. (in Russian)
- [2] B.M. Golcman, V.A. Kudinov, I.A. Smirnov. Poluprovodnikoviy termoelektricheskiye materialy na osnove  $\text{Bi}_2\text{Te}_3$ . M., Nauka, 1972, 18, 302. (in Russian)
- [3] S.I. Mehdiyeva, N.Z. Jalilov, N.M. Abdullayev, N.R. Memmedov, M.I. Veliyev, V.Z. Zeynalov. TPE-06, 3-<sup>rd</sup> Intern. Conf. on Techn. & Phys. Probl. in Pow. Engin., Ankara, Turkey, May 29-31, 2006, 695.
- [4] S.I. Mekhtiyeva, N.Z. Dzhalilov, N.M. Abdullayev, N.R. Memmedov, V.Z. Zeynalov. Mikrostruktura plyonok  $\text{Bi}_2\text{Te}_3\text{-Bi}_2\text{Se}_3$  legirovannikh. AMEA, Xeberler, XXVII, № 2, Bakı, 2007, 148. (in Russian)
- [5] A.G. Abdullayev, E.I. Veliyulin, S.Sh. Kakhramanov. Vliyaniye legirovaniya i interkalirovaniya na svoystva khalkogenidov vismuta. Baku, 1991. (in Russian)
- [6] D.I. Ismailov, G.M. Akhmedov, R.Sh. Shafizade. Dokl. AN Azerb. SSR, 45, №4, 1998, 6-8. (in Russian)
- [7] Spravochnik. Minerali. T. I, Izd. AN SSSR, M. 1960, 573. (in Russian)
- [8] S.S. Tolkachev. Tablici mejploskostnykh rasstoyaniy. Izd. «Khimiya» Leningradskoye otd.. 1968, 78.

**N.M. Abdullayev**

### **$\text{Bi}_2\text{Te}_3\text{-Bi}_2\text{Se}_3$ <Tb> və $\text{Bi}_2\text{Te}_3\text{-Bi}_2\text{Se}_3$ <Cl> TƏBƏQƏLƏRİN RENTGENOGRAFİK TƏDQİQİ**

$\text{Bi}_2\text{Te}_3\text{-Bi}_2\text{Se}_3$  <Tb> və  $\text{Bi}_2\text{Te}_3\text{-Bi}_2\text{Se}_3$  <Cl> nazik təbəqələri  $\sim 600\text{K}$ -dək qızdırdıqda yeni fazaların əmələ gəlməsi və hər hansı bir struktur dəyişikliyi, mikrohissəciklərin ölçülərində real böyüməsi baş vermir.

**Н.М. Абдуллаев**

### **РЕНГЕНОГРАФИЧЕСКОЕ ИССЛЕДОВАНИЕ ПЛЁНОК $\text{Bi}_2\text{Te}_3\text{-Bi}_2\text{Se}_3$ <Tb> и $\text{Bi}_2\text{Te}_3\text{-Bi}_2\text{Se}_3$ <Cl>**

При отжиге плёнок  $\text{Bi}_2\text{Te}_3\text{-Bi}_2\text{Se}_3$  <Tb> и  $\text{Bi}_2\text{Te}_3\text{-Bi}_2\text{Se}_3$  <Cl> до  $\sim 600\text{K}$  не происходит реального увеличения размера микрочастиц, каких либо структурных перестроек, образование новых фаз: на рентгенограмме наблюдается поликристаллическая структура. Расчёты межплоскостных расстояний показывают, что при отжиге плёнок структура упрочняется.

*Received: 01.07.08*



## ATOM RADIAL DISTRIBUTION IN AMORPHOUS FILMS

 $\text{Yb}_{1-x}\text{Sm}_x\text{As}_2\text{Te}_4$ 

E.Sh.GADJIYEV, S.Z. JAFAROVA

*Institute of Physics of National Academy of Sciences**AZ-1143, H. Javid ave., 33, Baku, Azerbaijan*

I.Kh. MAMEDOV

*National Aircraft Academy,**Az-1104, Baku*

Electron scattering intensity curve from amorphous  $\text{Yb}_{1-x}\text{Sm}_x\text{As}_2\text{Te}_4$  films has been obtained by electron diffraction method depending on the scattering angle to  $S_{\max}=120\text{nm}^{-1}$ .

Atom radial distribution curve has been plotted. The radii of coordination spheres have been determined in  $\text{Yb}_{1-x}\text{Sm}_x\text{As}_2\text{Te}_4$ .

The use of complex compounds of rare-earth elements under pressure of chalcogenide saturated vapors allows obtaining by thermal spraying of the films which are perspective ones for formation of planar light guide [1].

The amorphous films of compounds of  $\text{Yb}_{1-x}\text{Sm}_x\text{As}_2\text{Te}_4$  system containing glass chalcogenides (GCh) and rare-earth elements obtained by thermal evaporation have been investigated in refs [2-3].

The atom radial distribution in amorphous films  $\text{Yb}_{1-x}\text{Sm}_x\text{As}_2\text{Te}_4$  ( $x=0,02\%$ ) has been studied in the present work.

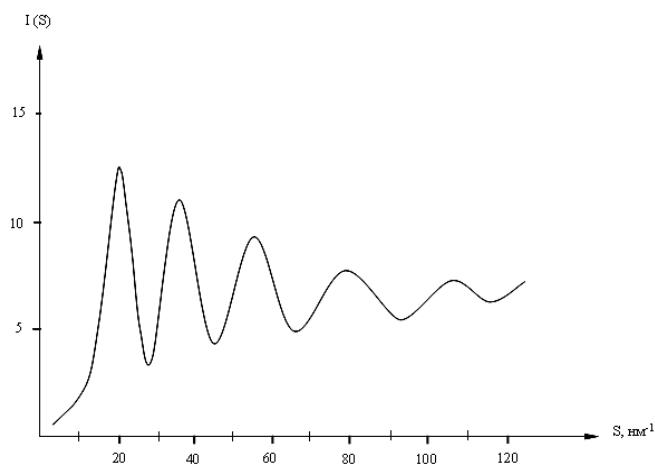


Fig.1. The intensity curves of electron scattering for  $\text{Yb}_{1-x}\text{Sm}_x\text{As}_2\text{Te}_4$  amorphous films.

The amorphous films  $\text{Yb}_{1-x}\text{Sm}_x\text{As}_2\text{Te}_4$  with thickness  $\sim 30$  nm are obtained by thermal evaporation of monocrystalline  $\text{Yb}_{1-x}\text{Sm}_x\text{As}_2\text{Te}_4$  from specially made furnaces from wolfram-rhenium alloy in vacuum  $\sim 10^{-5}\text{Pa}$ . The dosed content of Sm impurity in compounds is 0.02%. The freshly cleaved faces of NaCl, KCl crystal and amorphous celluloid being at room temperature are used as substrates. The deposition rate of films is  $\sim 10$  nm/sec. The obtained amorphous films are stable at room temperature and crystallize at temperature  $T=503\text{K}$ .  $\text{Yb}_{1-x}\text{Sm}_x\text{As}_2\text{Te}_4$  in crystalline state has rhombic lattice with parameters:  $a=1,148$ ,  $b=1,410$ ,  $c=1,410$ ,  $c=0,407\text{nm}$  sp.gr.  $P_{\text{man}}$ .

The crystallization of amorphous films shows the identity of the compositions of amorphous and crystalline films. The structure of short range ordering in  $\text{Yb}_{1-x}\text{Sm}_x\text{As}_2\text{Te}_4$  films is studied by diffraction method of fast electrons ( $U_{\text{acc}}=74\text{kV}$ ) with the use of rotating sector that allows revealing the maximums of diffraction reflection in far-angular region. The intensity curve of electron scattering the maximal value of “S” for which is equal to  $S_{\max}=120\text{nm}^{-1}$  (fig.1) has been constructed after electron-diffraction pattern microphotomentering. The five maximums at  $S_1=21,0\text{nm}^{-1}$ ;  $S_2=36,0\text{nm}^{-1}$ ;  $S_3=56,0\text{nm}^{-1}$ ;  $S_4=79,0\text{nm}^{-1}$ ;  $S_5=106,0\text{nm}^{-1}$  are observed on intensity curve of electron scattering in the dependence on scattering angle.

The method of atom radial distribution is used for definition of amorphous film structures. The curves of atom radial distribution (CARD) for amorphous compounds are constructed by us on the base of known formula [4]:

$$4\pi r^2 \sum_i \sum_j c_i k_i k_j \rho_{ij}(r) = 4\pi r^2 \rho_0 \left( \sum_i c_i k_i \right)^2 + \frac{2r}{\pi} \alpha \int_0^s s [\alpha(s) - 1] \sin sr ds \quad (1)$$

Here  $\rho_{ij}(r)$  is partial function of radial distribution of atomic density of  $j$ -type atoms round  $i$ -type ones,  $\alpha$  is normalizing constant,  $\alpha(s)$  is structural factor,  $S=4\pi s \sin \theta / \lambda$ , where  $\theta$  is scattering angle. The “ $c$ ” coefficients in formula (1) take into consideration the relative content of element atoms including in chemical formula of investigated compound. The relative atom scattering abilities of each chemical element “ $k$ ” are defined by the formula:

$$k_i = \frac{k(s)}{\sqrt{\sum_{i=1}^3 c_i f_i^2(s)}} \quad (2)$$

where  $f_i(s)$  is atom scattering factor of  $i$ -type element. The average atomic density  $\rho_0$  of investigated amorphous films is calculated by the following formula:

$$\rho_0 = \frac{\rho N_A}{\sum_i c_i A_i} \quad (3)$$

where  $\rho$  is density of crystalline substance in  $\text{g}/\text{cm}^3$ ,  $A_i$  are element atomic masses including into chemical formula,  $N_A$  is Avogadro constant which is equal to  $6 \cdot 10^{23} \text{mol}^{-1}$ . The normalizing constant “ $\alpha$ ” for transition from relative intensity units to absolute ones defined by us on average atomic density is equal to  $\alpha=0,09$  for  $\text{Yb}_{1-x}\text{Sm}_x\text{As}_2\text{Te}_4$ . The average atomic density  $\rho_0$  calculated on (3) is equal to  $\rho_0=0,426 \text{nm}^{-1}$ .  $K_{\text{Yb}}=1,319$ ;  $K_{\text{As}}=0,714$ ;  $K_{\text{Te}}=1,031$  are obtained for scattering abilities of ytterbium, arsenic and tellurium. CARD (fig.2) is calculated and constructed on the base of obtained experimental intensity on formula (1). The radii of first and second coordination spheres which are equal to 0,245nm and 0,372nm correspondingly are defined from CARD. The radius decrease of coordination spheres in  $\text{Yb}_{1-x}\text{Sm}_x\text{As}_2\text{Te}_4$  in comparison with amorphous  $\text{YbAs}_2\text{Te}_4$  is connected with impurity influence of Sm atoms [5]. The first coordination maximum on CARD of amorphous  $\text{Yb}_{1-x}\text{Sm}_x\text{As}_2\text{Te}_4$  corresponds to As – Te distance, but atoms of tellurium and arsenic are connected with each other by the covalent bond. It follows from the fact that sum of covalent radii of arsenic and tellurium is equal to  $r_{\text{As}}^{\text{cov}} + r_{\text{Te}}^{\text{cov}} = 0,121 \text{nm} + 0,117 \text{nm} = 0,238 \text{nm}$  that is close to the radius value of first coordination sphere ( $r_1=0,245$ ). The  $\text{Yb}^{2+}$  ions in the structure of amorphous  $\text{Yb}_{1-x}\text{Sm}_x\text{As}_2\text{Te}_4$  are in the second coordination

sphere of arsenic atoms and are nearest neighbors of tellurium atoms. The sum of radii of first coordination sphere and  $\text{Yb}^{2+}$  ion ( $r_1 + r_{\text{Yb}} = 0,245 + 0,107 = 0,352 \text{nm}$ ) evidences about this fact that is close to the radius value of second coordination sphere  $r_2=0,352 \text{nm}$ ).

Thus, it is established that the obtained films are amorphous ones at vacuum deposition of monocrystalline  $\text{Yb}_{1-x}\text{Sm}_x\text{As}_2\text{Te}_4$  on NaCl, KCl substrates and on amorphous celluloid being at room temperature.

$$4\pi r^2 \sum_i \sum_j c_i k_i k_j \rho_y(r)$$

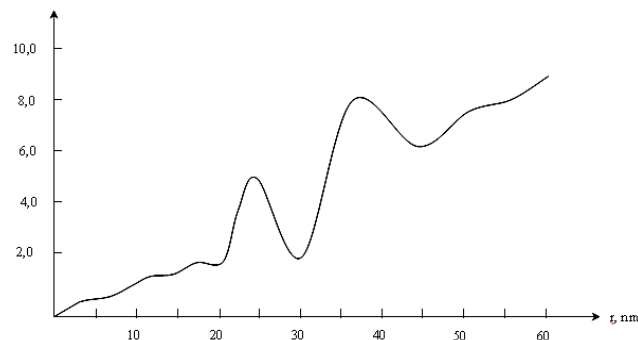


Fig.2. The curve of atom radial distribution  $\text{Yb}_{1-x}\text{Sm}_x\text{As}_2\text{Te}_4$ .

It is shown that impurities of Sm atoms influence on radius values of coordination spheres of  $\text{YbAs}_2\text{Te}_4$ , i.e. I and II radii of coordination spheres of  $\text{Yb}_{1-x}\text{Sm}_x\text{As}_2\text{Te}_4$  decrease in comparison with  $\text{YbAs}_2\text{Te}_4$ .

- [1] S.A. Kozyukhin, A.R. Fayrulin, E.N. Voronkov. FTP, 2005, t. 39, vip. 8, s. 1012. (in Russian).  
[2] E.Sh. Gadjiyev. Azerbaijan National Transaction of Azerbaijan Academy of Sciences, Series of Physical-mathematical and Technical sciences, Physics and Astronomy, XXVII №5, 2007, 121.

- [3] E.Sh. Gadjiyev. XXVII №2, 2008, 99. (in Russian)  
[4] A.F. Skrishevsky. Strukturniy analiz jidkostey i amorfnykh tel. M.: Visshaya shkola, 1980. s. 328. (in Russian)

E.Ş. Hacıyev, S.Z. Cəfərova, İ.X. Məmmədov

#### $\text{Yb}_{1-x}\text{Sm}_x\text{As}_2\text{Te}_4$ NAZİK TƏBƏQƏLƏRİNDƏ ATOMLARIN RADIAL PAYLANMASI

$\text{Yb}_{1-x}\text{Sm}_x\text{As}_2\text{Te}_4$  nazik təbəqələrindən elektronların səpilməsinin intensivlik ayrıləri səpilmə bucağından ( $C_{\text{max}}=120 \text{nm}^{-1}$ ) asılı olaraq alınmışdır.  $\text{Yb}_{1-x}\text{Sm}_x\text{As}_2\text{Te}_4$  nazik təbəqələrində atomların radial paylanma əyrisi qurulmuş və koordinasiya sferalarının radiusları təyin edilmişdir.

Э. Ш. Гаджиев, С.З. Джафарова, И.Х. Мамедов

#### РАДИАЛЬНОЕ РАСПРЕДЕЛЕНИЕ АТОМОВ В АМОРФНЫХ ПЛЕНКАХ $\text{Yb}_{1-x}\text{Sm}_x\text{As}_2\text{Te}_4$

Получена кривая интенсивности рассеяния электронов в зависимости от угла рассеяния до  $S_{\text{max}}=120 \text{nm}^{-1}$  для аморфных пленок  $\text{Yb}_{1-x}\text{Sm}_x\text{As}_2\text{Te}_4$ .

Построена кривая радиального распределения атомов. Определены радиусы координационных сфер в  $\text{Yb}_{1-x}\text{Sm}_x\text{As}_2\text{Te}_4$ .

Received: 02.07.08

## WAVE DIFFRACTION ON PLANE BELT WITH DIFFERENT SURFACE IMPEDANCE

T.M. AHMEDOV

*Institute of Mathematics and Mechanics of Azerbaijan NAS  
AZ-1141, Baku, Azerbaijan, F.Agayev str., 9*

The multiple articles [1-3] are dedicated to task solution of wave diffraction on plane belt with ideal boundary conditions (BC). BC of Dirichlet and Neumann types correspond to ideal BC. Such BC appear when it is supposed that belt has ideal electric or magnetic conductivity [1,4]. However, in practice the plane metallic belt has the finite conductivity. In this case the boundary is described by BC of impedance type [4]. From mathematics point of view, BC of third kind corresponds to this boundary [5]. The article [6] is devoted to strong problem solution of wave diffraction on belt with impedance BC. In work [6] the belt surface is described from both sides is described by the one and the same impedance. In the given paper we'll solve the task of E-polarized wave diffraction on the belt the surface of which is described from both sides by the different impedance. By other words the belt is described by two-sided BC. The approach which generalizes the work results for strong solution of this problem is proposed. The proposed method allows constructing the effective numerical algorithms on the base of which the plane dispersion characteristics are calculated.

## 1. Problem definition

Let's the plane wave falls on plane belt of  $2a$  dimension situated in XOZ plane in the center of coordinate system XOY from  $y>0$  side.

$$V^i(x, y) = e^{-ik(x \cos \theta + y \sin \theta)} = e^{-ik(x \alpha_0 + y \sqrt{1 - \alpha_0^2})} \quad (1)$$

Here  $\alpha_0 = \cos \theta$ ,  $\theta$  is wave incidence angle,  $k = \frac{2\pi}{\lambda}$  is wave number.

The complete field is presented in the form of sum of incident and scattered fields, i.e.

$$e_z(x, y) = V^i(x, y) + e_z^s(x, y) \quad (2)$$

The complete field should correspond to following conditions:

- everywhere out of belt surface to Helmholtz equation

$$\left( \frac{\partial^2}{\partial x^2} + \frac{\partial^2}{\partial y^2} + k^2 \right) e_z(x, y) = 0 \quad (3)$$

- on belt surface to impedance BC of [4] type

$$\frac{\partial e_z}{\partial y} + \frac{ik}{\eta_1} e_z \Big|_{y=+0} = 0, \quad \frac{\partial e_z}{\partial y} - \frac{ik}{\eta_2} e_z \Big|_{y=-0} = 0, \quad |x| < a, \quad (4)$$

where  $\eta_1, \eta_2$  correspond to impedance on belt surface from  $y > 0$  and  $y < 0$  sides correspondingly.

-to Meixner condition on edges [1,7]

-Scattered field  $e_z^s(x, y)$  should correspond to condition of Sommerfeld radiation on infinity which has the form [1]

$$\lim_{r \rightarrow \infty} \sqrt{r} \left( \frac{\partial}{\partial r} + ik \right) e_z^s(x, y) = 0, \quad (5)$$

## 2. Task solution

Let's write the conception of following type [1,5] for scattered field  $e_z^s(x, y)$  on the base of potential theory

$$e_z^s(x, y) = -\frac{i}{4} \int_{-a}^a \{f_1(x') + f_2(x')\} \frac{\partial}{\partial y} \{H_0^{(1)}(k \sqrt{(x-x')^2 + y^2})\} dx', \quad (6)$$

here  $H_0^{(1)}(x)$  is Hankel function of zero order which corresponds to bivariate Green function of free product. The unknown functions  $f_1(x')$  and  $f_2(x')$  are potential densities of simple and double layers which correspond to density functions of surface currents and are defined as component jump of complete field on belt surface ( $y=\pm 0$ ), i.e.

$$f_1(x) = \left[ \frac{\partial E_z}{\partial y} \right]_{-}^{+} \Big|_{y=0}, \quad f_2(x) = [E_z]_{-}^{+} \Big|_{y=0} \quad |x| < a \quad (7)$$

It is seen that perception for scattered field (6) corresponds to Helmholtz equation and condition of radiation on infinity (5).

Let's obey the complete field  $e_z(x, y)$  to boundary condition (4) at  $y=\pm 0$  for definition of unknown current

densities  $f_1(x')$  and  $f_2(x')$ . Taking into consideration (7), we obtain:

$$\begin{aligned} f_1(x') + ik \left( \frac{E_z^+}{\eta_1} + \frac{E_z^-}{\eta_2} \right) &= 0, \quad |x| < a \\ f_2(x') + \frac{1}{ik} \left( \eta_1 \frac{\partial E_z^+}{\partial y} + \eta_2 \frac{\partial E_z^-}{\partial y} \right) &= 0, \quad |x| < a. \end{aligned} \quad (8)$$

Further we obtain the integral equation (IE) of following type with taking into consideration of (2) and (6) perceptions for definition of  $f_1(x)$  and  $f_2(x')$  functions:

$$-\frac{1}{k} \frac{2\eta_1\eta_2}{\eta_1+\eta_2} f_1 + i \frac{\eta_1-\eta_2}{\eta_1+\eta_2} f_2 = 2iV^i + \frac{1}{2} \int_{-a}^a f_1(x') H_0^{(1)}(k|(x-x')|) dx', \quad |x| < a \quad (9)$$

$$\begin{aligned} & -i \frac{\eta_1-\eta_2}{\eta_1+\eta_2} f_1 + \frac{2k}{\eta_1+\eta_2} f_2 = \\ & = 2i \frac{\partial V^i}{\partial y} \Big|_{y=0} + \frac{1}{2} \lim_{y \rightarrow 0} \frac{\partial^2}{\partial y^2} \int_{-a}^a f_2(x') H_0^{(1)}(k\sqrt{(x-x')^2 + y^2}) dx'. \end{aligned} \quad (10)$$

The equations (9) and (10) are Fredholm's IE of second kind with the help of which  $f_1(x)$  and  $f_2(x')$  functions will be defined. Let's rewrite the given IE in images of Fourier

$f_1(x)$  and  $f_2(x')$  functions. With this aim we continue this function by the zero out of  $|x| < a$ . Then we can write:

$$\left. \begin{aligned} F_1(\alpha) &= \int_{-1}^1 f_1(a\xi') e^{-i\varepsilon\xi'\alpha} d\xi' = \int_{-1}^1 \tilde{f}_1(\xi') e^{-i\varepsilon\alpha\xi'} d\xi', \quad \tilde{f}_1(\xi') = af_1(a\xi'), \\ F_2(\alpha) &= \int_{-1}^1 f_2(a\xi') e^{-i\varepsilon\xi'\alpha} d\xi' = \int_{-1}^1 \tilde{f}_2(\xi') e^{-i\varepsilon\alpha\xi'} d\xi', \quad \tilde{f}_2(\xi') = f_2(a\xi'), \\ \tilde{f}_1(\xi') &= \frac{\varepsilon}{2\pi} \int_{-\infty}^{+\infty} F_1(\alpha) e^{i\varepsilon\alpha\xi'} d\alpha, \quad \tilde{f}_2(\xi') = \frac{\varepsilon}{2\pi} \int_{-\infty}^{+\infty} F_2(\alpha) e^{i\varepsilon\alpha\xi'} d\alpha, \end{aligned} \right\} \quad (11)$$

where  $F_1(\alpha)$  and  $F_2(\alpha)$  functions are images of Fourier  $f_1(x)$  and  $f_2(x)$  functions correspondingly and  $\varepsilon$ ,  $\xi$  parameters are defined as  $\varepsilon = ka$ ,  $x = a\xi$ .

Then take into consideration that spectral perception [1,7] takes place for Hankel function  $H_0^{(1)}(x)$ .

$$H_0^{(1)}(k\sqrt{(x-x')^2 + y^2}) = \frac{1}{\pi} \int_{-\infty}^{\infty} e^{ik(\alpha(x-x') + |y|\sqrt{1-\alpha^2})} \frac{1}{\sqrt{1-\alpha^2}} d\alpha \quad (12)$$

where that function branch  $\sqrt{1-\alpha^2}$  for which  $\text{Im}\sqrt{1-\alpha^2} \geq 0$  at  $|\alpha| \rightarrow \infty$  along real line. This is followed from radiation condition (5).

Substituting (11) and (12) in IE (9) and (10) for Fourier images we obtain IE of following type:

$$Z_1 f_1(a\xi) + Z_2 f_2(a\xi) = 2ie^{-i\varepsilon\xi\alpha_0} + \frac{1}{2\pi} \int_{-\infty}^{\infty} F_1(\alpha) e^{i\varepsilon\xi\alpha} \frac{1}{\sqrt{1-\alpha^2}} d\alpha, \quad |\xi| < 1. \quad (13)$$

$$-Z_2 f_1(a\xi) + \tilde{Z}_1 f_2(a\xi) = 2k\sqrt{1-\alpha_0^2} e^{-i\varepsilon\xi\alpha_0} - \frac{\varepsilon k}{2\pi} \int_{-\infty}^{\infty} F_2(\alpha) e^{i\varepsilon\xi\alpha} \sqrt{1-\alpha^2} d\alpha, \quad |\xi| < 1. \quad (14)$$

Here  $Z_1$ ,  $Z_2$ ,  $\tilde{Z}_1$  parameters which are defined as

$$Z_1 = -\frac{1}{k} \frac{2\eta_1\eta_2}{\eta_1+\eta_2}, \quad Z_2 = i \frac{\eta_1-\eta_2}{\eta_1+\eta_2}, \quad \tilde{Z}_1 = \frac{2k}{\eta_1+\eta_2}. \quad (15)$$

for simplification.

Further multiplying IE (13) and (14) both sides on  $e^{i\varepsilon\beta\xi}$  function and integrating on variable  $\xi$  in limits  $[-1,1]$ , we obtain IE of following type:

$$\begin{aligned} & \frac{Z_1}{a} F_1(\beta) + Z_2 F_2(\beta) = \\ & = 4i \frac{\sin \varepsilon(\alpha_0 + \beta)}{\varepsilon(\alpha_0 + \beta)} + \frac{1}{\pi} \int_{-\infty}^{\infty} F_1(\alpha) \frac{\sin \varepsilon(\alpha - \beta)}{\varepsilon(\alpha - \beta)} \frac{d\alpha}{\sqrt{1-\alpha^2}}, \end{aligned} \quad (16)$$

$$\begin{aligned} & -\frac{Z_2}{\varepsilon} F_1(\beta) + \frac{\tilde{Z}_1}{k} F_2(\beta) = 4\sqrt{1-\alpha_0^2} \frac{\sin \varepsilon(\alpha_0 + \beta)}{\varepsilon(\alpha_0 + \beta)} - \\ & - \frac{1}{\pi} \int_{-\infty}^{\infty} F_2(\alpha) \frac{\sin \varepsilon(\alpha - \beta)}{(\alpha - \beta)} \sqrt{1-\alpha^2} d\alpha. \end{aligned} \quad (17)$$

Now let's construct the algorithm of IE solution (16) and (17). As a rule, the desired functions of current density  $\tilde{f}_1(\xi)$  and  $\tilde{f}_2(\xi)$  should correspond to the condition [1,6] in order to scattered field  $e_z^s(x, y)$  will correspond to Meixner condition on edges.

$$\tilde{f}_j(\xi) \underset{\xi \rightarrow \pm 1}{\approx} (1-\xi^2)^{\nu_j}, \quad -\frac{1}{2} \leq \nu_j \leq \frac{1}{2}, \quad j=1,2; \quad \nu_1 = -1/2, \nu_2 = 1/2. \quad (18)$$

The value selection of  $\nu_j$  parameter from interval  $[-1/2, 1/2]$  depends on physical nature of considered task. In the given case  $\tilde{f}_j(\xi)$  function describes the surface current density for which  $\nu_j$  parameter is equal to  $\nu_1 = -1/2$ . Let's develop  $\tilde{f}_j(\xi)$  function in uniformly convergent series on Gegenbauer polynomials of following type for correspondence with condition (18):

$$\tilde{f}_j(\xi) = (1-\xi^2)^{\nu_j} \sum_{n=0}^{\infty} f_n^j C_n^{\nu_j+1/2}(\xi), \quad (19)$$

where  $f_n^j$  are unknown coefficients, and  $C_n^{\nu_j+1/2}(\xi)$  are Gegenbauer polynomials.

We can obtain the following perception on the base of perception (19) for image of Fourier function  $\tilde{f}_j(\xi)$ :

$$F_j(\alpha) = \frac{2\pi}{\Gamma(\nu_j+1/2)} \sum_{n=0}^{\infty} (-i)^n f_n^j \beta_n^{\nu_j} \frac{J_{n+\nu_j+1/2}(\varepsilon\alpha)}{(2\varepsilon\alpha)^{\nu_j+1/2}}, \quad (20)$$

Here  $J_n(x)$  is Bessel function  $\beta_n^{\nu_j} = \frac{\Gamma(n+2\nu_j+1)}{\Gamma(n+1)} \approx n^{2\nu_j}$  at  $n \rightarrow \infty$ .

Let's substitute the perception for Fourier image (20) in IE (16) and (17) and take into consideration that the following relations [1, 8, 10] take place for values of  $\mu_j = \nu_j + 1/2 \geq 0$  parameter.

$$\frac{1}{\pi} \int_{-\infty}^{\infty} \frac{J_{m+\mu_j}(\varepsilon\beta)}{\beta^{\mu_j}} \frac{\sin \varepsilon(\alpha-\beta)}{\alpha-\beta} d\beta = \frac{J_{m+\mu_j}(\varepsilon\alpha)}{\alpha^{\mu_j}}. \quad (21)$$

Then we obtain infinite system of linear algebraic equations (ISLAE) of second kind of following type for obtaining unknown  $f_n^1$  and  $f_n^2$ :

$$\sum_{n=0}^{\infty} x_n^1 [Z_1 d_{mn}^{\mu_1 0} - c_{mn}^{\mu_1}] + Z_2 \sum_{n=0}^{\infty} x_n^2 d_{mn}^{\mu_1 1} = 4i\gamma_m^{\mu_1}, \quad m = 0, 1, 2, \dots \quad (22)$$

$$\sum_{n=0}^{\infty} x_n^1 [-Z_2 d_{mn}^{\mu_2 0}] + \sum_{n=0}^{\infty} x_n^2 [Z_1 d_{mn}^{\mu_2 1} + b_{mn}^{\mu_2}] = 4\sqrt{1-\alpha_0^2} \gamma_m^{\mu_2}. \quad (23)$$

Here the designations are introduced:

$$x_n^1 = \begin{cases} f_{0,n=0}^1, & x_n^2 = (-i)^n (n+1) f_n^2, \\ 2(-i)^n \frac{f_n^1}{n}, & n > 0 \end{cases}$$

$$\gamma_m^{\mu_j} = (-1)^m \frac{J_{m+\mu_j}(\varepsilon\alpha)}{\alpha^{\mu_j}}, \quad (24)$$

$$d_{mn}^{\mu_1 0} = d_{mn}^{00} = \int_{-\infty}^{\infty} \frac{J_n(\varepsilon\beta) J_{m+\mu_1}(\varepsilon\beta)}{\beta^{\mu_1}} d\beta,$$

$$d_{mn}^{\mu_2 1} = d_{mn}^{11} = \int_{-\infty}^{\infty} \frac{J_{n+1}(\varepsilon\beta) J_{m+\mu_2}(\varepsilon\beta)}{\beta^{\mu_2+1}} d\beta,$$

$$c_{mn}^{\mu_1 0} = c_{mn}^{00} = \int_{-\infty}^{\infty} \frac{J_n(\varepsilon\beta) J_{m+\mu_1}(\varepsilon\beta)}{\beta^{\mu_1} \sqrt{1-\beta^2}} d\beta$$

$$b_{mn}^{\mu_2 1} = b_{mn}^{11} = \int_{-\infty}^{\infty} J_{n+1}(\varepsilon\beta) J_{m+\mu_2}(\varepsilon\beta) \frac{\sqrt{1-\beta^2}}{\beta^{\mu_2+1}} d\beta.$$

Note that in all these formulas the parameter  $\mu_j = \nu_j + 1/2 \geq 0$  has the following values  $\mu_1 = \nu_1 + 1/2 = 0$ ,  $\mu_2 = \nu_2 + 1/2 = 1$ .

ISLAE (22) and (23) is related to equation class, which have investigated in detail in work [10]. There it is shown that the reduction method is applied to solution of ISLAE (22) and (23). This means that unknown coefficients  $f_n^j$  can be defined with any accuracy. The unknown functions  $\tilde{f}_j(\xi)$  characterizing the surface current densities, on which the scattered field  $e_z^s(x, y)$  (6) is defined, can be defined on found coefficients  $f_n^j$  on the base of formula (19).

### 3. Integral calculation in matrix elements

The calculation of matrix elements  $d_{mn}^{\mu_j 0}$ ,  $d_{mn}^{\mu_j 1}$ ,  $c_{mn}^{\mu_j 0}$  which are presented by integrals on compositions of Bessel functions, is the main moment at ISLAE solution (22) and (23). The subintegral function becomes quick oscillating one that makes calculation process difficult at increase of  $\varepsilon$  parameter values. The matrix elements  $d_{mn}^{\mu_j 0}$  and  $d_{mn}^{\mu_j 1}$  can be calculated in analytic form on the base of table integrals [8]. They have the following form:

$$d_{mn}^{\mu_1 0} = \{1 + (-1)^{m+n}\} \frac{1}{\varepsilon} \left(\frac{\varepsilon}{2}\right)^{\mu_1} \frac{\Gamma(\mu_1) \Gamma(\frac{n+m+1}{2})}{\Gamma(\frac{n-m+1}{2}) \Gamma(\frac{n+m+2\mu_1+1}{2}) \Gamma(\frac{m-n+2\mu_1+1}{2})}, \quad (25)$$

$$d_{mn}^{\mu_2 1} = \{1 + (-1)^{m+n}\} \frac{1}{2} \left(\frac{\varepsilon}{2}\right)^{\mu_2} \frac{\Gamma(\mu_2+1) \Gamma(\frac{n+m+1}{2})}{\Gamma(\frac{n-m+3}{2}) \Gamma(\frac{n+m+2\mu_2+3}{2}) \Gamma(\frac{m-n+2\mu_2+1}{2})}. \quad (26)$$

Further the integral calculation in matrix elements  $c_{mn}^{\mu j 0}$  and  $b_{mn}^{\mu j 1}$  can be carried out on the base of algorithms proposed in works [6,12]:

$$c_{mn}^{\mu 1 0} = \{1 + (-1)^{n+m}\} I_{mn}^E(0,0),$$

$$I_{mn}^E(\lambda, \mu) = I_{mn}^{E,1}(\lambda, \mu) - i I_{mn}^{E,2}(\lambda, \mu). \quad (28)$$

The values  $I_{mn}^{E,1}(\lambda, \mu)$  and  $I_{mn}^{E,2}(\lambda, \mu)$  are defined in [6,12] and they have the form:

$$I_{mn}^{E,1}(0,0) = \frac{\varepsilon^{m+n}}{2} \sum_{k=0}^{\infty} d_{kmn}^{00} \varepsilon^{2k} \frac{\Gamma(\frac{m+n}{2} + k + \frac{1}{2})}{\Gamma(\frac{m+n}{2} + k + 1)} \quad (29)$$

$$d_{kmn}^{00} = \frac{(-1)^k}{\Gamma(k+1)} \frac{\Gamma(k + \frac{m+n+1}{2}) \Gamma(k + \frac{m+n+2}{2})}{\Gamma(k+m+n+1) \Gamma(k+m+1) \Gamma(k+n+1)}$$

Here  $\Gamma(\lambda)$  is gamma function.

$$I_{mn}^{E,2}(0,0) = \left[ \sum_{k=0}^{N-1} \frac{1}{2\pi} \Gamma(-k+N) \Gamma(k + \frac{1}{2}) \Gamma(k + \frac{1}{2}) \Gamma(k+1) \varepsilon^{2k} \right] /$$

$$/ \{ \Gamma(k+1) \Gamma(k-N+m+1) \Gamma(k-N+n+1) \Gamma(k+N+1) \} +$$

$$+ \sum_{k=0}^{\infty} \frac{1}{2\pi} \frac{\Gamma(k+N+\frac{1}{2})}{\Gamma(k+N+1)} d_{kmn}^{00} \varepsilon^{2k+m+n} \{ 2 \ln \varepsilon + 2\Psi(k+N+\frac{1}{2}) -$$

$$- \Psi(k+1) - \Psi(k+m+1) - \Psi(k+n+1) - \Psi(k+m+n+1) \}].$$

$$N = \frac{m+n}{2}. \quad (30)$$

The corresponding integrals for index values  $m=n=0$  have the form:

$$I_{00}^{E,2}(0,0) = \sum_{k=0}^{\infty} \frac{1}{2\pi} \frac{\Gamma(k+\frac{1}{2})}{\Gamma(k+1)} d_{k00}^{00} \varepsilon^{2k} \{ 2 \ln \varepsilon + \Psi(k+\frac{1}{2}) + \Psi(k+\frac{1}{2}) - 4\Psi(k+1) \} \quad (31)$$

The integrals in matrix elements  $b_{mn}^{\mu j 1}$  are calculated on analogous procedure. Let's write the representations for them in the form of rapid-convergent series which have the form:

$$b_{mn}^{\mu 1 1} = b_{mn}^{11} = \{1 + (-1)^{n+m}\} I_{mn}^H(1,1), \quad (32)$$

$$I_{mn}^H(1,1) = I_{mn}^{H,1}(1,1) + i I_{mn}^{H,2}(1,1), \quad (33)$$

$$I_{mn}^{H,1}(1,1) = \frac{\varepsilon^{m+n+2}}{4} \sum_{k=0}^{\infty} d_{kmn}^{11} \varepsilon^{2k} \frac{\Gamma(\frac{m+n}{2} + k + \frac{1}{2})}{\Gamma(\frac{m+n}{2} + k + 2)}, \quad (34)$$

$$d_{kmn}^{11} = \frac{(-1)^k}{\Gamma(k+1)} \frac{\Gamma(k+1 + \frac{m+n+1}{2}) \Gamma(k+2 + \frac{m+n}{2})}{\Gamma(k+m+n+3) \Gamma(k+m+2) \Gamma(k+n+2)}, \quad (35)$$

$$I_{mn}^{H,2}(1,1) = \left[ - \sum_{k=0}^{N-1} \frac{1}{4\pi} \Gamma(-k+N) \Gamma(k + \frac{1}{2}) \Gamma(k + \frac{3}{2}) \Gamma(k+2) \varepsilon^{2k+2} \right] /$$

$$/ \{ \Gamma(k+2) \Gamma(k-N+m+2) \Gamma(k-N+n+2) \Gamma(k+N+3) \} +$$

$$+ \sum_{k=0}^{\infty} \frac{1}{4\pi} \frac{\Gamma(k+N+\frac{1}{2})}{\Gamma(k+N+2)} d_{kmn}^{11} \varepsilon^{2k+m+n+2} \{ 2 \ln \varepsilon + \Psi(k+N+\frac{1}{2}) +$$

$$+ \Psi(k + \frac{k+m+n+3}{2}) + \Psi(k + \frac{k+m+n}{2} + 2) - \Psi(k+1) - \Psi(k+m+2) -$$

$$- \Psi(k+N+2) - \Psi(k+n+2) - \Psi(k+m+n+3) \}]. \quad (36)$$

The suggested approach allows forming the high-performance computational algorithms for solution connected with ISLAE (22), (23) on the base of which the calculations of scattering characteristics of plane belt are carried out.

The system of connected ISLAE (22), (23) come undone in one particular case just when the  $\eta_1$  and  $\eta_2$  impedance values coincide with each other on low and upper surfaces of belt. Really, parameters  $Z_1$ ,  $\tilde{Z}_1$ ,  $Z_2$  take the following values at  $\eta_1 = \eta_2 = \eta$ :

$$Z_2 = 0, \quad Z_1 = -\frac{\eta}{k}, \quad \tilde{Z}_1 = \frac{k}{\eta}$$

In that case ISLAE (22) and (23) decompose on two independent equation with respect to  $x_n^1$  and  $x_n^2$ . These equations coincide with results of work [6].

#### 4. Physical characteristics.

The following parameters: directional diagram (DD), diameters of complete diffusion and backscattering [1,4] are considered in the capacity of physical values characterizing the belt scattering properties. Let's give the definition of these values.

DD characterizes the scattered field behavior in long-distance band which will be written in cylindrical coordinate system in the following form:

$$e_z^s(r, \varphi) \approx A(kr) \phi_E(\varphi), \quad kr = k\sqrt{x^2 + y^2} \rightarrow \infty, \quad (37)$$

$$A(kr) = \sqrt{\frac{2}{\pi kr}} e^{i(kr - \pi/4)}, \quad \phi_E(\varphi) = \phi_E^1(\varphi) + \phi_E^2(\varphi), \quad (38)$$

$$\phi_E^1(\varphi) = -\frac{i}{4} F_1(\cos \varphi) = -\frac{i\pi}{4} \sum_{n=0}^{\infty} x_n^1 J_n(\varepsilon \cos \varphi), \quad (39)$$

$$\phi_E^2(\varphi) = \frac{\varepsilon}{4} \sin \varphi F_2(\cos \varphi) = \frac{\pi}{4} \tan \varphi \sum_{n=0}^{\infty} x_n^2 J_{n+1}(\varepsilon \cos \varphi). \quad (40)$$

$$\phi_E(\varphi) = \phi_E^1(\varphi) + \phi_E^2(\varphi) \text{ function describes DD.}$$

The diameters of complete diffusion  $\sigma_s^E$  and backscattering  $\sigma^E$  are defined by the following [1,4]:

$$\frac{\sigma_s^E}{4a} = -\frac{1}{\varepsilon} \operatorname{Re} \phi_E(\theta), \quad \frac{\sigma^E}{\lambda} = \frac{2}{\pi} |\phi_E(\varphi)|^2. \quad (41)$$

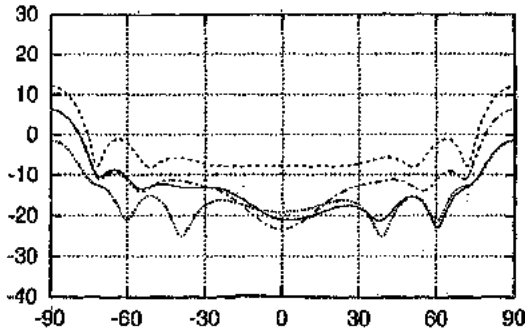


Fig. 1.

The calculation results of diameters of complete diffusion and backscattering on the base of developed efficient computational algorithms are presented on fig.1-4. The dependences of inverse dispersion diameter on angle of incidence for values of frequency parameter  $\varepsilon = ka$  (Fig.1  $\varepsilon=5$ ; Fig.2  $\varepsilon=15$ ) are shown on fig.1,2. On these figures the dotted curves correspond to impedance values  $\eta_1 = \eta_2 = 0$  that corresponds to ideal conducting belt. The curves with dots and dots with line dotted correspond to impedance value  $\eta_1 = \eta_2 = 1.5$  and  $\eta_1 = \eta_2 = 3.0$  correspondingly. The block curves on these figures correspond to impedance value  $\eta_1 = 3.0$  and  $\eta_2 = 1.5$ .

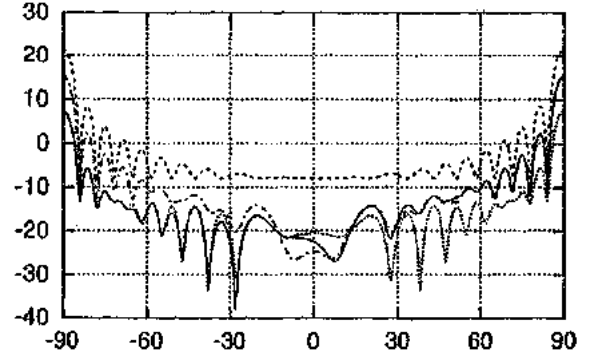


Fig. 2.

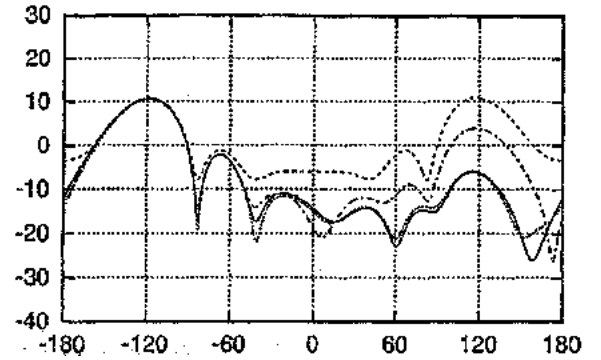


Fig. 3.

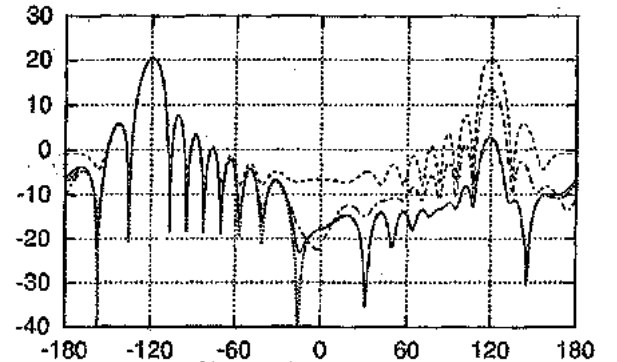


Fig. 4.

DD for values of angle of incidence  $\theta=60^\circ$  and  $\varepsilon=ka$  (Fig.3  $\varepsilon=5$ , Fig.4- $\varepsilon=15$ ) are presented on the figures 3,4. The order of curve position on impedance values  $\eta_1$ ,  $\eta_2$  is the same as on fig.1,2.



- [1] *Kh. Khenl, A. Maye, K. Vestpfal.* Teoriya difraktsii. Moskva: Mir. 1964, -428s.
- [2] *E.I. Nefedov, A.T. Fialkovskiy.* Asimptoticheskaya teoriya difraktsii elektromagnitnikh voln na konechnikh strukturakh. M.: Nauka. 1972, -247s.
- [3] *L.N. Litvinenko, S.L. Prosvirnin.* Spektralnie operatori rasseyaniya v zadachakh difraktsii voln na ploskikh ekranakh. Kiev: Nauk. Dumka, 1984, -240s.
- [4] *T.V. Senior and J. Volakis.* Approximate Boundary Conditions in Electromagnetics. The Institution of Electrical Engineers, London, United Kingdom, 1995.
- [5] *R.M. Mors, G. Feshbakh.* Metodi teoreticheskoy fiziki. T.1.M. – IL. 1958, -930s.
- [6] *T. Ikiz, S. Koshikawa, K. Kobayashi, E.I. Veliev and A.H. Serbest.* Journal of electromagnetic waves and applications. 2001, V.15, n.3, 315-340.
- [7] *R. Mittra, S. Li.* Analiticheskie metodi teorii volnovodov. M.-Mir, 1974, -327s.
- [8] *A.P. Prudnikov, Yu.A. Brichkov, O.I. Marichev.* Integrali i ryadi (spetsialnie funktsii). M.: Nauka, 1983, -752s.
- [9] *I.M. Braver, P.Sh. Fridberg and I.M.Yakovlev.* The behavior of the electromagnetic field near the edge of a resistive half-plane. IEEE Trans. Antennas and Propagat., Vol.AP-36, pp.1760-1768. 1988
- [10] *E. Veliev and V.P. Shestopalov.* Sov. Physics dokl., 1988, v.33, n.6, 411-413.
- [11] *D.N. Watson.* Teoriya Besselevikh funktsiy. T.1. M.: IL, 1949, -1000s.
- [12] *T.M. Akhmedov.* Fizika, cild 14, №2, s. 75-79.

**T.M. Əhmədov**

### **MÜXTƏLİF SƏTHLİ İMPEDANSLA MÜSTƏVİ LENT ÜZƏRİNDƏ DALĞALARIN DİFRAKSİYASI**

İdeal sərhəd şərtləri ilə müstəvi lentdə dalğaların difraksiya probleminə çoxlu sayda məqalələr [1-3] həsr olunmuşdur. İdeal SŞ-ə Dirixle və Neyman tipli SŞ uyğun gəlir. Belə SŞ-lər ideal elektrik və ya maqnit keçiriciliyinin olduğu güman edildiyi halda yaranır [1-4]. Ancaq praktiki olaraq müstəvi metallik lentlər sonlu keçiriciliyə malikdir. Bu halda sərhədlər SŞ impedans tipinə uyğundur [4]. Riyazi nöqtəyi nəzərdən bu sərhədə üçüncü tip SŞ uyğundur. İmpedans SŞ-li lent üzərində difraksiya dalğalarının məsələsinin ciddi həllinə [6] məqalə həsr olunmuşdur. [6] işində lentin səthi hər iki tərəfdən eyni impedansla göstərilmişdir. Bu işdə biz difraksiya məsələsini müstəvi E-polyarizasiyalı dalğa üçün həll edəcəyik. Bu hal impedans SŞ-in xüsusi halıdır. Başqa sözlə lent ikitərəfli SŞ ilə göstərilmişdir. Bu məsələnin ciddi həlli üçün [6] işinin nəticələrini ümumiləşdirən yanaşma təklif olunur.

**T.M. Ахмедов**

### **ДИФРАКЦИЯ ВОЛН НА ПЛОСКОЙ ЛЕНТЕ С РАЗЛИЧНЫМ ПОВЕРХНОСТНЫМ ИМПЕДАНСОМ**

Проблема дифракции волн на плоской ленте с идеальными граничными условиями (ГУ) посвящены многочисленные статьи [1-3]. Идеальным ГУ соответствуют ГУ типа Дирихле или Неймана. Такие ГУ возникают, когда предполагается, что лента имеет идеально электрическую, либо магнитную проводимость [1,4]. Однако, на практике плоская металлическая лента имеет конечную проводимость. В этом случае граница описывается ГУ импедансного типа [4]. С математической точки зрения этой границе соответствует ГУ третьего рода [5]. Строгому решению задачи дифракции волн на ленте с импедансными ГУ посвящена статья [6]. В [6] поверхность ленты с двух сторон описывается одним и тем же импедансом. В данной работе мы построим решение задачи дифракции плоской E- поляризованной волны на ленте, поверхность которой с двух сторон описывается различным импедансом. Иными словами, лента описывается двусторонними ГУ. Для строгого решения этой задачи предлагается подход, который обобщает результаты работы [6].

*Received: 04.03.08*

# EXACT SOLVABLE NONLINEAR PARTIAL DIFFERENTIAL EQUATIONS AND THEIR NEW SOLUTIONS

E.A. AKHUNDOVA

*H.M. Abdullayev Institute of Physics of NAS of Azerbaijan  
H. Javid ave., 33, Baku, AZ-1143, Azerbaijan*

We consider three types of nonlinear partial differential equation of polynomial form. Using the method of motion integrals the exact solutions of its equations are found.

## Introduction.

There are many methods of obtaining exact solutions of nonlinear equations: see [1-3]. The nonlinear forms of some linear partial differential equation are considered in work [4]. We were found explicit substitutions of dependent variables which transform the equation under study to linear equations. In this paper which is continuation of paper [4] we investigate five types of two variable nonlinear partial differential equations of third order which reduce to linear equations by substitutions of dependent variables. We obtain the exact solutions of one of types of presented equations. We confine ourselves to equations of polynomial type.

## Classes of nonlinear equations.

Let us consider a general linear partial equation of the second order:

$$a\psi_t + b\psi_{xt} + c\psi_{tt} + d\psi_{xx} = 0 \quad (1)$$

Making the substitutions of the following form:

$$\psi = \exp(\gamma\varphi + \delta\varphi_x + \beta\varphi_t) \quad (2)$$

(other substitutions lead to non-polynomial equation) we obtain five different partial differential equations which are linear with respect to the derivatives of the third order and nonlinear with respect to of the second and first orders in the dependence of relations between coefficients  $a, b, c, d, \gamma, \delta, \beta$ :

$$\text{I. } \alpha(\gamma\varphi_t + \delta\varphi_{xt}) + d(\gamma^2\varphi_{xx}^2 + 2\gamma\delta\varphi_{xx}\varphi_x + \gamma\varphi_{xx} + \delta\varphi_{xxx}) = 0 \\ b = c = \beta = 0.$$

$$\text{II. } \alpha(\gamma\varphi_t + \delta\varphi_{xt}) + b(\gamma^2\varphi_t\varphi_x + \gamma\delta\varphi_{xt} + \varphi_x + \gamma\delta\varphi_x\varphi_{xx} + \delta^2\varphi_{xt}\varphi_{xx} + \gamma\varphi_{xt} + \delta\varphi_{xxx}) = 0 \\ c = d = \beta = 0.$$

$$\text{III. } \alpha(\gamma\varphi_e + \delta_{ue}) + c[\gamma^2\varphi_t^2 + \delta^2\varphi_{xt}^2 + \gamma\varphi_{tt} + 2\gamma\delta\varphi_{xt}\varphi_t + \gamma^2\varphi_x^2 + \delta^2\varphi_{xx}^2 + \gamma\varphi_{xx} + 2\gamma\delta\varphi_{xx}\varphi_x \\ + \delta(\varphi_{xxx} + \varphi_{xtt})] = 0 \\ c = d; \beta = b = 0.$$

$$\text{IV. } \alpha(\gamma\varphi_t + \beta\varphi_{tt}) + d(\gamma^2\varphi_x^2 + \beta_{tx}^2 + 2\gamma\beta\varphi_{tx}\varphi_x + \gamma\varphi_{xx} + \beta\varphi_{txx}) = 0. \\ b = c = \delta = 0.$$

$$\text{V. } \alpha[\gamma\varphi_t + \beta(i\varphi_{xt} + \varphi_{tt})] + d[\gamma^2(\varphi_t\varphi_x + \varphi_x^2) + 2\gamma(i\varphi_{tt}\varphi_x - \varphi_t\varphi_{xx} + i\varphi_t\varphi_{xt} + 2i\varphi_{xx}\varphi_x + 2\varphi_{tx}\varphi_x) \\ + \gamma^2(-i\varphi_{xt} - \varphi_{tt}\varphi_{xx} + i\varphi_{tt} - \varphi_{xt} - \varphi_{xx}^2 + \varphi_{tx}^2 + 2i\varphi_{xx}\varphi_{tx}) + \alpha(i\varphi_{xt} + \varphi_{xx}) + \gamma(i\varphi_{xtt} - \varphi_{xxt} + i\varphi_{xxx} + \varphi_{txx})] = 0. \\ c = 0; b = id; \beta = i\gamma.$$

Other equations of this class are reduced to shown equations by substitutions of independent variables (particularly  $x \leftrightarrow t$ ).

Let us obtain the exact solution of equation II. This equation is reduced to following linear equation:

$$\alpha\psi_t + d\psi_{xx} = 0 \quad (3)$$

by the replacement

$$\psi = \exp(\gamma\varphi + \beta\varphi_t) \quad (4)$$

Among solutions of equation (3) the coherent-state functions exists (we propose  $a, d = \text{const}$ ):

$$\psi_{\alpha} = (\pi)^{\frac{1}{4}} \exp \left\{ -|\alpha|^2 / 2 - \alpha^2 (2dt / 2a + 1) + \alpha x (2)^{\frac{1}{2}} \right\} x (dt / 2a + 1)^{\frac{1}{2}} \exp \left\{ -[x - \alpha (2)^{\frac{1}{2}} (dt / 2a - 1)]^2 / 2(dt / 2a + 1) \right\} \quad (5)$$

Substituting (5) in (3) we obtain the exact solution of equation II:

$$\psi_{\alpha}(x, t) = \gamma^{-1} [\ln(\pi^{\frac{1}{4}}) - |\alpha|^2 / 2 - \alpha^2 (dt / 2a + 1 - \beta \gamma^{-1}) / 2 - \ln(dt / 2a + 1) / 2] - (\beta d)^{-1} a^{-1} [(-\beta d / 2a \gamma + x^2) - 4dx / \sqrt{2} + \alpha^2 \exp(-\gamma / \beta + d\gamma / 2a\beta) E_i(2a\gamma(dt / 2a + 1) / d\beta)] \quad (6)$$

where  $E_i(ax) = \int [exp(ax) / x] dx$ .

Knowing that  $\psi_{\alpha}$  is generating function of Hermitian polynomials one can obtain others solutions of following form:

$$\psi_n(x, t) = \gamma^{-1} [\ln(\pi^{\frac{1}{4}}) - |\alpha|^2 / 2 - \ln(dt / 2a + 1) / 2] - 2a\beta^{-1} (-\beta / \gamma + x^2) \exp(d\gamma / 2a\beta - \gamma / \beta) E_i(2a\gamma(dt / 2a + 1) / d\beta) + \exp(-\gamma / \beta) \int \ln[Hn(\sqrt{2}(-d^2 t^2 / 4a^2 - 1) / 4x)] \exp(\gamma / \beta) dt \quad (7)$$

If the integrals of motion of equation (3), i.e. operators  $\hat{I}_{\alpha}$  satisfying the following relation:

$$[\hat{I}_{\alpha}, a\delta / dt + d\delta^2 / d\alpha^2] \psi = 0. \quad (8)$$

then from arbitrary solution  $\varphi_{(x,t)}$  of equation (3) one can obtain new solutions by following rule [5]:

$$\tilde{\psi} = f(\hat{I}_1, \hat{I}_2, \dots, \hat{I}_n) \psi \quad (9)$$

where  $f$  is arbitrary function.

Therefore if  $\varphi$  is solution of equation II then the following arbitrary functions are solutions of this equation:

$$\tilde{\varphi} = \hat{L} \tilde{\psi} = \hat{L} f(\hat{I}_1, \hat{I}_2, \dots, \hat{I}_n) L^{-1} \varphi \quad (10)$$

where  $\hat{L}$  is transformation operator from  $\psi$  to  $\varphi$ .

Integrals of motion for equation (3) are:

$$I_1 = \partial / \partial t; I_2 = \partial / \partial x; I_3 = x - 2tda^{-1} \partial / \partial x \quad (11)$$

One can obtain new exact solutions of equation II from known solutions (for example (5) and (6)):

$$\tilde{\varphi} = (\gamma + \beta \delta / \partial t)^{-1} \ln f(\hat{I}_1, \hat{I}_2, \hat{I}_3) \exp(\gamma \varphi + \beta \frac{\delta \varphi}{\partial t}) \quad (12)$$

The solutions of rest equations I – V can be obtained by analogical way.

- [1] K. Takenura, Jour. of phys.A, 2002, v.356 №41, p.8867.  
[2] J. Dziarmage, Phys.Rev.Lett, 1998, vol.81, №8, p 1551.  
[3] V.V. Dubrovskiy, A.N. Tupko. UMN, 2001, vol.56, №3.

- [4] E.A. Akhundova. Fizika, 2005, cild.XI, №1-2.  
[5] E.B. Aronson, I.A. Malkin, V.I. Manko. EChAYa, 1974, t.5, s.122.(in Russian).

E.A. Axundova

## XÜSUSİ TÖRƏMƏLƏRDƏ DƏQİQ HƏLL OLUNAN QEYRİ-XƏTTİ DİFERENSİAL TƏNLİKLƏR VƏ ONLARIN YENİ HƏLLƏRİ

Xüsusi törəmələrdə polinomial şəkilli qeyri-xətti diferensial tənliklərin üç tipi nəzərdən keçirilmişdir. Hərəkət integralları metodundan istifadə edərək, bu tənliklərin dəqiq həlləri tapılmışdır.

E.A. Ахундова

## ТОЧНО РЕШАЕМЫЕ НЕЛИНЕЙНЫЕ ДИФФЕРЕНЦИАЛЬНЫЕ УРАВНЕНИЯ В ЧАСТНЫХ ПРОИЗВОДНЫХ И ИХ НОВЫЕ РЕШЕНИЯ

Рассмотрены три типа нелинейных дифференциальных уравнений в частных производных полиномиального вида. Используя метод интегралов движения, найдены точные решения этих уравнений.

Received: 24.10.08

# THE MEASUREMENTS OF THERMAL-EXPANSION COEFFICIENT IN $\text{Cu}_{2-x}\text{Te}$ CRYSTALS ( $x=0; 0,10; 0,15; 0,20; 0,25$ ) BY X-RAY METHOD

Yu.G. ASADOV, A.G. BABAYEV, Yu.I. ALIYEV, D.I. ISMAYLOV, R.D. ALIYEVA

*H.M. Abdullayev Institute of Physics of NAS of Azerbaijan*

*H. Javid ave., 33, Baku, AZ-1143, Azerbaijan*

The measurements of thermal-expansion coefficient in crystals by the method of high-temperature roentgenography are described in detail. The thermal-expansion coefficients are calculated from temperature dependence of crystal lattice parameters of existing modifications in  $\text{Cu}_{2-x}\text{Te}$  ( $x=0; 0,10; 0,15; 0,20; 0,25$ ) and surfaces of thermal-expansion coefficients are shown in each case.

The study of thermal-expansion coefficient (TEC) of crystals by the method of high-temperature roentgenography is seemed enough trivial task as the same questions with less experimental difficulties and with bigger accuracy are solved with application of dilatometric method [1-3]. However, the possibility of investigation carrying out on micro-samples is the advantage of the method of high-temperature roentgenography. The study of TEC anisotropy (tensor of thermal expansion in common case) on one-phase crystals and also TEC measurement in phase mixture can be carried out with the help of method of high-temperature roentgenography. TEC definition is led to equation differentiation for temperature dependence of crystal lattice parameters.

As the interplanar spacing  $d$  of system of reflecting crystalline planes is connected with glancing angle  $\theta$  and wave length  $\lambda$  of X rays by the equation  $d = \frac{\lambda}{2 \sin \theta}$  so increase of distance  $d$  is fixed on variation of value  $\theta$  with temperature increase.

Differentiating the given equation over  $\theta$  we obtain:

$$\frac{\partial d}{\partial \theta} = -\frac{\lambda}{2} \sin \theta \operatorname{ctg} \theta = -d \operatorname{ctg} \theta \quad \text{or} \quad \frac{\partial d}{d} = \operatorname{ctg} \theta \partial \theta.$$

From this equation it is seen that  $\partial \theta$  value for the given change of  $\partial d$  increases from the finite value up to infinitely bigger one on  $\theta$  approximation to  $90^\circ$ . Therefore,  $\theta$  and  $\theta - \Delta \theta$  will be at reflection of monochromatic beam of X rays falling on crystal at two different temperatures.

If  $d_1$  and  $d_2$  are interplanar spacings of the given system of crystal planes at  $T_1$  and  $T_2$  temperatures so

$$d_1 = \frac{\lambda}{2 \sin \theta_1} \quad \text{and} \quad d_2 = \frac{\lambda}{2 \sin \theta_2}.$$

Let's obtain TEC from the equation

$$d_2 = d_1 [1 + \alpha (T_2 - T_1)]$$

or

$$\alpha = \frac{d_2 - d_1}{d_1 (T_2 - T_1)}.$$

Substituting  $d_1$  and  $d_2$  value, we obtain:

$$\alpha = \frac{\frac{\lambda}{2} \left( \frac{1}{\sin \theta_2} - \frac{1}{\sin \theta_1} \right)}{\frac{\lambda}{2 \sin \theta_1} (T_2 - T_1)} = \frac{\sin \theta_1 - \sin \theta_2}{\sin \theta_2 (T_2 - T_1)}.$$

This exact expression is necessary to use if the change of  $\theta$  angle at crystal expansion is comparable with  $(\pi - 2\theta)$  on the value. The formula for  $\alpha$  obtained by differentiation of  $d = \frac{\lambda}{2 \sin \theta}$  equation is correct only at the condition that change of  $\theta$  angle is less in comparison with  $(\pi - 2\theta)$ .

The number of independent linear expansion coefficients is different for crystals of different crystal systems. The linear expansion tensor for cubic crystals "degenerates" in scalar; the two independent coefficients are for tetragonal, hexagonal and trigonal crystals; the three independent coefficients are for orthorhombic ones; the four independent coefficients are for monoclinic ones and six independent coefficients are for triclinic ones.

The homogeneous deformation at the change of crystal temperature is described by symmetric second-rank tensor

$$\alpha_{ik} = \begin{vmatrix} \alpha_{11} & \alpha_{12} & \alpha_{13} \\ \alpha_{12} & \alpha_{22} & \alpha_{23} \\ \alpha_{13} & \alpha_{23} & \alpha_{33} \end{vmatrix}. \quad (1)$$

$i$  is defined by the following formula on arbitrary direction:

$$\Delta_i = c_{1i}^2 \alpha_{11} + c_{2i}^2 \alpha_{22} + c_{3i}^2 \alpha_{33} + 2c_{1i}c_{2i}\alpha_{12} + 2c_{1i}c_{3i}\alpha_{13} + 2c_{2i}c_{3i}\alpha_{23}. \quad (2)$$

Here,  $c_1, c_2, c_{3i}$  are direction cosines of  $i$  direction with X, Y, Z axes. One can find such coordinate system X', Y', Z' in which equation (2) has the form:

$$\Delta_i = \alpha_{11} c_{1i}^2 + \alpha_{22} c_{2i}^2 + \alpha_{33} c_{3i}^2 \quad (3)$$

and  $(\alpha_{ik})$  tensor transform into diagonal tensor  $(\alpha_{ii})$ . The axes of X', Y', Z' coordinate system are the main directions of thermal-expansion tensor.

$$\alpha_{ii} = \begin{vmatrix} \alpha_{11} & 0 & 0 \\ 0 & \alpha_{22} & 0 \\ 0 & 0 & \alpha_{33} \end{vmatrix}.$$

The position of the main axes of thermal-expansion tensor in crystals of higher crystal systems is described by crystal symmetry uniquely. The tensor definition in these cases is lead to measurement of TEC value along the one (cubic crystal system), two (hexagonal and trigonal ones) or three (orthorhombic one) crystallographic axes.

In crystals of low crystal systems the task of thermal-expansion tensor finding is difficult by the fact that position of their main axes isn't defined by crystallographic coordinate system uniquely. Only one of main tensor axes ( $\alpha_{ik}$ ) in monoclinic crystals coincides with axis [010]. The tensor can have the different orientation with respect of this axis and therefore, this tensor has the four independent components. For their definition it is necessary to measure any four interplanar spacing  $d_{hkl}$  as temperature functions. For calculations it is comfortable to measure  $d_{010}$  and three values  $d_{h0k}$ . In triclinic crystals the tensor ( $\alpha_{ik}$ ) can has any orientation with respect of crystallographic axes and has six components. For their definition it is necessary to measure any six  $d_{hkl}$ . For calculation it is comfortable to measure six following values:  $d_{100}, d_{010}, d_{001}, d_{110}, d_{101}, d_{011}$ .

The orientation finding of main directions of thermal-expansion tensor and the definition of TEC main values is mathematically are reduced to definition of quadratic form (2) and to sum of squares (3).

The thermal expansion of  $\text{Cu}_{2-x}\text{Te}$  ( $x=0; 0,10; 0,15; 0,20; 0,25$ ) crystals in the given work is calculated from temperature dependence of elementary cell parameters in temperature interval involving all possible structural changes. The parameters of crystal elementary cell change at decrease of its temperature on  $\Delta T$ . Let's designate the parameter values of crystal elementary cell by primed letters at the change of its temperature on  $\Delta T$ , then:

$$a' = a(1 + \alpha_1 \Delta T)$$

$$b' = b(1 + \alpha_2 \Delta T)$$

$$c' = c(1 + \alpha_3 \Delta T)$$

From these equations TEC on main crystallographic equations will be:

$$\alpha_{[100]} = \frac{a' - a}{a(T_2 - T_1)}, \quad \alpha_{[010]} = \frac{b' - b}{b(T_2 - T_1)},$$

$$\alpha_{[001]} = \frac{c' - c}{c(T_2 - T_1)}, \quad \text{where } T_2 > T_1.$$

The technique of roentgenographic thermal-expansion tensor definition in low-symmetrical crystals is described in detail in [4-8]. In the cases of higher and average crystal systems the thermal-expansion tensor can be led to main axes coinciding with main crystallographic directions:

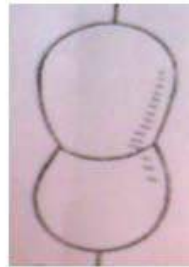
$$\varepsilon_{[100]} = \alpha_{[100]} \Delta T; \quad \varepsilon_{[010]} = \alpha_{[010]} \Delta T;$$

$$\varepsilon_{[001]} = \alpha_{[001]} \Delta T$$

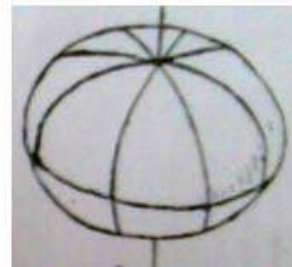
As it is mentioned above the topology of CTR surfaces is investigated in [5] and it is shown that surface of thermal-expansion coefficients in the case of cubic crystals (isotropic distribution) has the form of sphere (fig.1, a) having the higher symmetry  $\frac{\infty}{\infty m}$ .



a) CTR surfaces  
 $\alpha'_{[100]} = \alpha'_{[010]} = \alpha'_{[001]} > 0$



b) CTR surfaces  
 $\alpha' = \alpha'_{[100]}(c_1^2 + c_2^2) + \alpha'_{[001]}c_3^2$   
 $\alpha'_{[100]}, \alpha'_{[001]} > 0; \alpha'_{[001]} > \alpha'_{[100]}$



c) CTR surfaces  
 $\alpha' = \alpha'_{[100]}(c_1^2 + c_2^2) + \alpha'_{[001]}c_3^2$   
 $\alpha'_{[100]}, \alpha'_{[001]} > 0; \alpha'_{[100]} > \alpha'_{[001]}$



d) CTR surfaces  
 $\alpha' = \alpha'_{[100]}(c_1^2 + c_2^2) + \alpha'_{[001]}c_3^2$   
 $\alpha'_{[001]} > 0; \alpha'_{[100]} < 0; \alpha'_{[001]} > 0$



e) CTR surfaces  
 $\alpha' = \alpha'_{[100]}c_1^2 + \alpha'_{[010]}c_2^2 + \alpha'_{[001]}c_3^2$   
 $\alpha'_{[100]}, \alpha'_{[010]}, \alpha'_{[001]} > 0$



f) CTR surfaces  
 $\alpha' = \alpha'_{[100]}c_1^2 + \alpha'_{[010]}c_2^2 + \alpha'_{[001]}c_3^2$   
 $\alpha'_{[100]}, \alpha'_{[010]} > 0; \alpha'_{[001]} < 0$

The two independent coefficients are for tetragonal, hexagonal and trigonal crystals. The surface of thermal=expansion coefficients for these crystals which have  $\alpha_{[100]} \neq \alpha_{[010]} \neq \alpha_{[001]}$  becomes the oval-like and oblong at  $\alpha_{[001]} > \alpha_{[100]}$  (fig.1, b) or flattened at  $\alpha_{[100]} > \alpha_{[001]}$  along [001] axis (fig.1, c), surface symmetry is  $\frac{\infty}{\infty m}$ . If  $\alpha_{[001]} > 0$ ,  $\alpha_{[100]} < 0$

for the same crystal systems, so CTR surfaces consists of two positive (white) egg-shaped regions and one toroidal negative region (black region (fig.1,d).

The coefficient surfaces have the form of ellipsoid (fig.1,e) for orthorhombic crystals which have  $\alpha_{[100]} \neq \alpha_{[010]} \neq \alpha_{[001]}$ , the one prolonged positive region and two negative egg-shaped regions (fig.1,f) exist at the one negative coefficient (for example  $\alpha_{[001]}$ ).

The listed six types of TEC surfaces describe all possible cases of crystal thermal expansion.

The coefficient ( $\alpha_v$ ) of volumetric expansion is equal to the sum of three main linear expansion coefficients, i.e.  $\alpha_v = \alpha_{[100]} + \alpha_{[010]} + \alpha_{[001]}$ .

TEC is the one of few thermodynamical values which are accessible to direct measurement (including roentgenographic one). Being the second derivative over

thermodynamical potentials, TEC characterizes the system behavior especially in points of polymorphous transforms.

### 1. Crystal thermal-expansion coefficients of existing Cu<sub>2</sub>Te phases

In work [12] it is shown that Cu<sub>2</sub>Te crystals at room temperature are two-phased ones and consist of hexagonal and its superstructural orthorhombic modification independently on growth conditions. At 453K the second hexagonal modification forms. At 450K  $a$  and  $c$  parameters of hexagonal modification increase by jump and  $a$  and  $b$  parameters of orthorhombic modifications decrease by jump. At 590K first hexagonal and orthorhombic modifications transform into second hexagonal modification and the crystal becomes one-phased one in temperature interval 590-660K. At 660K the reflections relating to orthorhombic modification recondition with appearance of (111) reflection of high-temperature HCC modification. The orthorhombic and second hexagonal modifications at 821K transform into high-temperature HCC modification. TEC are calculated on main crystallographic directions from temperature dependence of lattice parameters of existing modification which are given in table 1.

Table 1.

Thermal-expansion of existing modifications of Cu <sub>2</sub> Te ( $\cdot 10^{-6}K^{-1}$ )					
Modification	Temperature, K	$\alpha_{[100]}$	$\alpha_{[010]}$	$\alpha_{[001]}$	$\bar{\alpha} = \frac{\alpha_{[100]} + \alpha_{[010]} + \alpha_{[001]}}{3}$
Hexagonal-I	290-373	16,27		17,78	16,77
	290-473	29,38		29,82	29,53
	290-573	44,89		45,13	44,97
Hexagonal-II	473-573	37,89		37,99	37,92
	473-673	39,49		39,52	39,50
	473-821	45,80		45,76	45,79
Orthorhombic	290-373	17,12	37,39	30,73	28,41
	290-473	32,13	32,02	-94,32	-10,04
	290-573	-09,66	11,14	-20,18	-6,03
	290-821	4,45	1,16	5,45	3,69
HCC	821-873	26,11			26,11
	821-973	36,37			36,37
	821-1073	38,49			38,49

As it is seen from the table 1 the anisotropy of thermal-expansion coefficient is almost absent in both hexagonal modifications, i.e.  $\alpha_{[100]} \leq \alpha_{[001]} > 0$ . TEC surface for these modifications becomes the oval-like one as it is shown on the fig.1,b. TEC surfaces have symmetry  $\frac{m \cdot 2}{m}$  for orthorhombic

modification which has  $\alpha_{[100]} \neq \alpha_{[010]} \neq \alpha_{[001]}$ . The one elongated positive region and two negative egg-shaped regions (fig.1,f) are at the one negative coefficient.

In the case of cubic modification TEC surface has the form of sphere (fig.1,a) having the highest symmetry  $\frac{\infty}{\infty m}$ .

### II. Thermal-expansion coefficients of Cu<sub>1,90</sub>Te crystal

Single crystals Cu<sub>1,90</sub>Te at room temperature as Cu<sub>2</sub>Te ones are two-phased ones and consist of hexagonal and orthorhombic modifications [12]. At 673K orthorhombic modification transforms into hexagonal one and the crystal becomes the one-phased one in temperature interval

673-773K and  $c$  parameter of hexagonal modification decreased by the jump and  $a$  parameter increases by the jump with appearance of reflections from high-temperature HCC modifications. At 873K the hexagonal modification transforms into HCC modification. These anomalous changes of hexagonal modification parameters also influence on thermal expansions which are given in table 2.

As it is seen from table 2 the surface of thermal-expansion coefficients becomes the oval-like one, oblate one at  $\alpha_{[100]} > \alpha_{[001]}$  along [001] axis (fig.1,c) surface symmetry is  $\frac{\infty}{\infty m}$ .

TEC surfaces have symmetry  $\frac{m \cdot 2}{m}$  for orthorhombic modifications which have  $\alpha_{[100]} \neq \alpha_{[010]} \neq \alpha_{[001]}$ . The surface has the ellipsoid form (fig.1,e) at all positive coefficients.

TEC surface has the sphere form (fig.1,a) at cubic modifications and has the highest symmetry  $\frac{\infty}{\infty m}$ .

Table 2.

Thermal-expansion coefficients of existing modifications of $\text{Cu}_{1,90}\text{Te}$ ( $\cdot 10^{-6}\text{K}^{-1}$ )					
Modification	Temperature, K	$\alpha_{[100]}$	$\alpha_{[010]}$	$\alpha_{[001]}$	$\bar{\alpha} = \frac{\alpha_{[100]} + \alpha_{[010]} + \alpha_{[001]}}{3}$
Hexagonal	293-373	27,48		29,51	28,16
	293-473	77,92		28,70	61,51
	293-573	65,07		33,72	54,62
	293-673	59,07		31,14	49,76
	293-773	103,81		-19,49	62,71
Orthorhombic	293-873	117,39		52,27	95,68
	293-373	21,34	95,69	197,17	104,73
	293-473	36,42	57,17	114,35	69,31
	293-573	25,66	47,93	93,89	55,83
	293-673	40,22	44,23	72,84	52,43
HCC	773-873	41,83			41,83
	773-973	41,83			41,83
	773-1073	41,83			41,83

### III. Thermal-expansion coefficient $\text{Cu}_{1,85}\text{Te}$ crystal

Single crystals  $\text{Cu}_{1,85}\text{Te}$  [11] crystallize at room temperature in hexagonal crystal system and at 707K

hexagonal modification transforms into high-temperature HCC modification. TEC are calculated from temperature dependence of crystal lattice parameters which are given in the table 3.

Table 3.

Thermal-expansion coefficients of existing modifications of $\text{Cu}_{1,85}\text{Te}$ ( $\cdot 10^{-6}\text{K}^{-1}$ )				
Modification	Temperature, K	$\alpha_{[100]}$	$\alpha_{[001]}$	$\bar{\alpha} = \frac{2\alpha_{[100]} + \alpha_{[001]}}{3}$
Hexagonal	293-373	13,15	37,93	21,41
	293-473	27,95	40,45	32,12
	293-573	35,43	39,58	36,81
	293-673	32,30	29,21	31,27
HCC	673-726	37,10		37,10
	673-773	34,90		34,90
	673-873	36,29		36,29

The surface of linear-expansion coefficients of hexagonal modification satisfies to condition  $\alpha_{[100]}, \alpha_{[001]} > 0$ ;  $\alpha_{[001]} > \alpha_{[100]}$  and that's why has the form shown on fig.1,b and TEC surface of HCC crystals (isotropic expansion) has the sphere form (fig.1,a).

### IV. TEC of crystal modifications $\text{Cu}_{1,80}\text{Te}$

Single crystals  $\text{Cu}_{1,80}\text{Te}$  as  $\text{Cu}_{1,85}\text{Te}$  ones crystallize in hexagonal crystal system at room temperature and at 730K

the hexagonal modification transforms into HCC modification [9]. TEC for hexagonal and HCC modifications which are given in table 4, are calculated from temperature dependence of crystal lattice parameters.

TEC surface of hexagonal modification satisfies to condition  $\alpha_{[100]}, \alpha_{[001]} > 0$ ;  $\alpha_{[001]} > \alpha_{[100]}$  and that's why has the form shown on fig.1,b and TEC surface of HCC crystals (isotropic expansion) has the sphere form (fig.1,a).

Table 4.

Thermal-expansion coefficients of existing modifications $\text{Cu}_{1,90}\text{Te}$ ( $\cdot 10^{-6}\text{K}^{-1}$ )				
Modification	Temperature, K	$\alpha_{[100]}$	$\alpha_{[001]}$	$\bar{\alpha} = \frac{2\alpha_{[100]} + \alpha_{[001]}}{3}$
Hexagonal	290-373	22,48	69,72	38,23
	290-473	19,73	44,52	27,99
	290-573	37,02	36,81	36,95
	290-673	32,66	35,29	33,54
HCC	773-873	19,89		19,89
	773-973	19,89		19,89
	773-1073	19,89		19,89

### V. TEC of $\text{Cu}_{1,75}\text{Te}$ crystal modifications.

Single crystals  $\text{Cu}_{1,75}\text{Te}$  [10] has the hexagonal structure at room temperature. This modification at 698K transforms into HCC modification. TEC is calculated from temperature

dependence of lattice parameters of both modifications the results of which are given in table 5.

As it is seen from table 5 the condition  $\alpha_{[100]}, \alpha_{[001]} > 0$ ;  $\alpha_{[001]} > \alpha_{[100]}$  are fulfilled and that's why TEC surface shown

on the fig.1,b. TEC surface has the sphere form (fig.1,a) in HCC modification.

The cations in  $\text{Cu}_{2-x}\text{Te}$  ( $x=0; 0,10; 0,15; 0,20; 0,25$ ) gradually decrease from stoichiometric composition ( $\text{Cu}_2\text{Te}$ ) up to non-stoichiometric one ( $\text{Cu}_{1,75}\text{Te}$ ) and the influence of cation lack on crystalline structure, mechanism of structural transformations, phase formation, temperature and also number of phase transformations has revealed. It is established that perfection and fact that phases one-phase

grown crystals mainly depend on cation lack, i.e. the crystals become one-phase ones with lack increase of cuprum cations.

The strong anisotropy of thermal expansion on the main crystallographic directions in all considered crystals leads to weakening of chemical bond in the structure and by this reason all low-temperature structures transform in HCC modification in which the atom thermal oscillations in crystalline lattice at definite temperature.

Table 5.

Thermal-expansion coefficients of existing modifications of  $\text{Cu}_{1,90}\text{Te}$  ( $\cdot 10^{-6}\text{K}^{-1}$ )

Modification	Temperature, K	$\alpha_{[100]}$	$\alpha_{[001]}$	$\bar{\alpha} = \frac{2\alpha_{[100]} + \alpha_{[001]}}{3}$
Hexagonal	290-373	22,48	69,72	38,23
	290-473	19,73	44,52	27,99
	290-573	37,02	36,81	36,95
	290-673	32,66	35,29	33,54
HCC	773-873	19,89		19,89
	773-973	19,89		19,89
	773-1073	19,89		19,89

- [1] A.N. Zisman, V.N. Kachinskiy. PTE, 1982, №5, s.172 (in Russian).
- [2] P.G. Strelkov, S.I. Novikova. PTE, 1975, №5, s.105 (in Russian).
- [3] I.I. Myakin, I.I. Lifanov, V.I. Ivanov i dr. Izmer. tekhnika, 1971, №1, s.19 (in Russian).
- [4] A.K. Shubnikov. 1956, t.1, s.95 (in Russian).
- [5] Z.I. Ejnova, G.S. Jdanov, M.M. Umanskiy. Kristallografiya, 1959, t.4, №5, s.723 (in Russian).
- [6] V.V. Zibkov, M.M. Umanskiy. Kristallografiya, 1957, t.2, №4, s.508 (in Russian).
- [7] A.K. Shubnikov. Kristallografiya, 1956, t.1, s. 95 (in Russian).
- [8] J. Nay. Fizicheskie svoystva kristallov. Izd-vo In. Lit., Moskva, 1960, s.385 (in Russian).
- [9] Yu.G. Asadov, G.B. Gasimov, L.V. Rustamova. Dokl. AN Az. SSR, 1989, t.14, s.22 (in Russian).
- [10] Yu.G. Asadov, L.V. Rustamova. Kristallografiya, 1991, t.36, v.1, s.147 (in Russian).
- [11] L.V. Rustamova, G.B. Gasimov, K.M. Jafarov, Yu.G. Asadov. Neorg. Mat., 1991, t.26, s.2065 (in Russian).
- [12] Yu.G. Asadov, L.V. Rustamova, K.M. Jafarov, A.G. Babayev. Phase Transitions, 1992, v.38, p.247.

Y.Q. Əsədov, Ə.Q. Babayev, Y.İ. Aliyev, C.İ. İsmayıllov, R.C. Aliyeva

## **$\text{Cu}_{2-x}\text{Te}$ ( $x=0; 0,10; 0,15; 0,20; 0,25$ ) KRİSTALLARINDA İSTİDƏN GENİŞLƏNMƏ ƏMSALLARININ RENTGEN METODU İLƏ TƏYİNİ**

Tədqiq olunan kristallarda yüksəktemperatur rentgen metodu ilə istidən genişlənmə əmsallarının təyini verilmişdir.  $\text{Cu}_{2-x}\text{Te}$  ( $x=0; 0,10; 0,15; 0,20; 0,25$ ) kristallarındakı modifikasiyaların qəfəs parametrlərinin temperaturdan asılılığından istidən genişlənmə əmsalları təyin edilmiş və hər hal üçün istidən genişlənmə əmsallarının səthi göstərilmişdir.

Ю.Г. Асадов, А.Г. Бабаев, Ю.И. Алыев, Д.И. Исмаилов, Р.Д. Алыева

## **ИЗМЕРЕНИЯ КОЭФФИЦИЕНТОВ ТЕПЛОВОГО РАСШИРЕНИЯ В КРИСТАЛЛАХ $\text{Cu}_{2-x}\text{Te}$ ( $x=0; 0,10; 0,15; 0,20; 0,25$ ) РЕНТГЕНОВСКИМ МЕТОДОМ**

Подробно изложено измерения коэффициента теплового расширения в кристаллах методом высокотемпературной рентгенографии. Из температурной зависимости параметров кристаллической решетки существующих модификаций в  $\text{Cu}_{2-x}\text{Te}$  ( $x=0; 0,10; 0,15; 0,20; 0,25$ ) рассчитаны коэффициенты теплового расширения и в каждом случае показаны поверхности коэффициентов теплового расширения.

Received: 02.07.08



## DETERMINATION OF INCOHERENT NEUTRON SCATTERING CROSS SECTION IN ZIRCONIUM ELEMENT BY MCNP4C CODE

D. MASTI

*Baku State University,  
AZ -1148, Z. Khalilov, 23 Baku, Azerbaijan*

Neutron crystallography is an efficient investigation method for determination the structure of materials, but neutron sources are very rare and expensive to build and to maintain. The strongest neutron source is nuclear reactor, but its expense is billions of dollars to build and operate. High cost was a major factor in the cancellation of the advanced neutron source project. For obviation this difficulty, have been designed computer methods. These methods have been employed for determination of materials characteristics, but very limitations exist for neutron crystallography in methods of computer based. In this paper shown, neutron diffraction and neutron scattering with a proper design method of computer based can be used for overcome some of these limitations. In this context, is studied the feasibility of computer method by MCNP4C code for determination of coherent and incoherent neutron scattering cross section for natural zirconium and also, neutrons diffraction.

### 1. Introduction

The thermal neutron scattering cross section is usually divided into three different parts:

-Inelastic: Important for all materials and described by the scattering law  $S(\alpha, \beta)$ .

-Coherent elastic: Important for crystalline solids like graphite, beryllium or  $\text{UO}_2$ .

-Incoherent elastic: Important for hydrogenous solids like polyethylene or light water and zirconium.

Thus, for research of incoherent neutron scattering cross section, we select zirconium element. In nuclear reactors one of the most practical elements is zirconium. Zirconium is widely used in core reactor. All channels, spacer grids, and clad materials (as fuel rod cladding), are made up of zirconium alloy in order to save neutron economy [7].

In this paper simulated Pressurized Water Reactor (PWR) and neutron diffraction in crystallography section. Finally,

coherent and incoherent cross sections of zirconium element by thermal neutrons are obtained, by means of MCNP4C code.

MCNP is a general-purpose Monte Carlo N-Particle code that can be used for neutron, photon, electron, or coupled neutron/photon/electron transport, including the capability to calculate eigenvalues for critical systems.

The code treats an arbitrary three-dimensional configuration of materials in geometric cells bounded by first- and second-degree surfaces and fourth-degree elliptical tori. In MCNP4C code, the neutron energy regime is from  $10^{-11}$  MeV to 20 MeV, consequently (existence of thermal neutrons in these limits) it is possible to simulate neutron diffraction and Bragg's law [1-4].

### 2. The model preparation for calculation of MCNP4C code

We can employ two designs for our investigation. A schematic diagram of the equipment used in studying neutron diffraction effects is given in figure 1 (A, B).

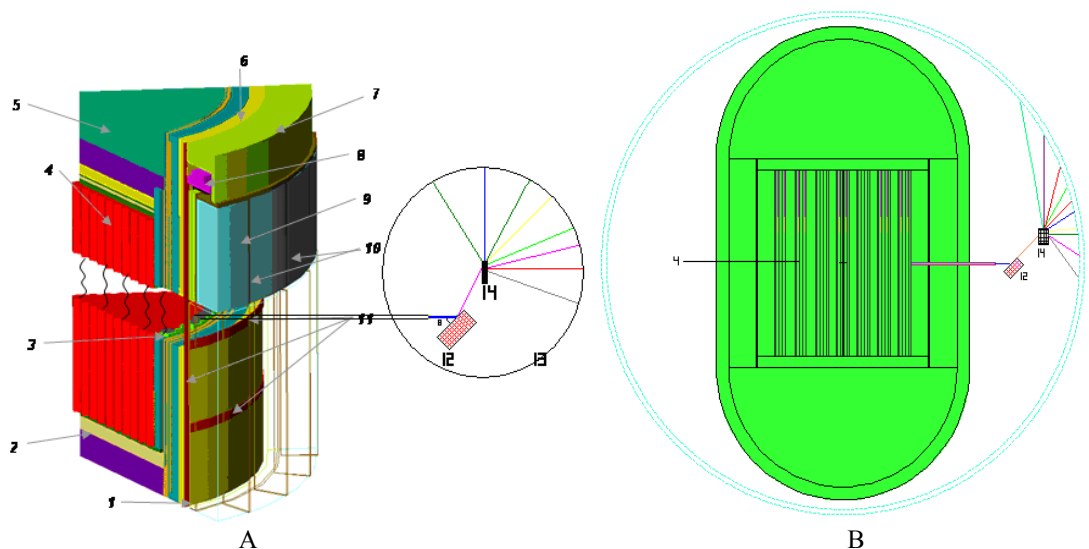


Fig.1: Two designs for investigation of neutron scattering and neutron diffraction.

1-Thermal insulation; 2-down reflector; 3- Core baffle; 4- Reactor core; 5- Up reflector; 6-Reactor pressure vessel; 7- Shielding; 8- Thrust truss; 9- Water tank; 10- Tank edge; 11- Registration areas; 12- Crystal monochromator; 13- Metallic sphere; 14- Zirconium.

Reactor core consists of 163 hexagonal fuel assemblies with  $U^{235}$  enrichment between 1.6 and 4.02 %. Fuel assemblies are in hexagonal shape and consist of 311 pin-type fuel rods. Fuel rods are arranged in a triangular array with 12.75 mm pitch. Every fuel rod is constrained in the correct position by the presence of 15 spacer grids made up of Zr + %1Nb. There are 20 special channels in the fuel assemblies. The central channel serves as a structural element of the fuel assembly framework. One channel shifted with respect to the center is used to house the in-core instrumentation systems. Eighteen channels are the guide ones wherein the control rods are moving and the burnable absorber rods are installed as well. All channels and spacer grids are made up of zirconium alloy in order to save neutron economy. Arrangements of fuel rods over the sections of the fuel assembly types are shown in figure 2.

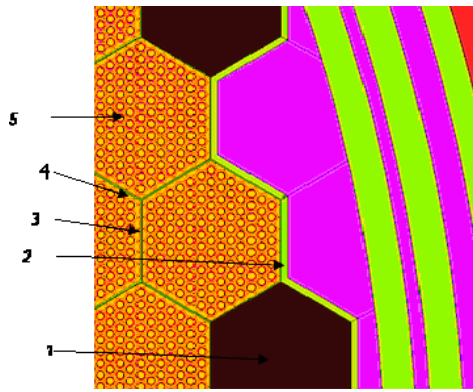


Fig.2: Reactor core configuration. 1- Measurement tube 2- Core baffle 3- Cladding fuel Assembly 4-Water in reactor core. 5- Fuel rod.

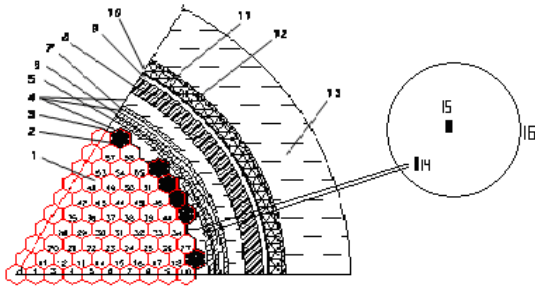


Fig.3: Configuration of reactor core and crystallography section. 1- Reactor core; 2- Cladding fuel Assembly; 3- Core baffle; 4- Water; 5- Basket; 6- Core barrel; 7- Shield; 8- Pressure vessel; 9- air gap; 10- Cladding; 11-Thermal insulation; 12- Tank wall; 13- Biological shield; 14- Crystal monochromator; 15- Metallic sphere.

A collimated beam of thermal neutrons is passed out through the radiation shielding in reactor and falls upon a single crystal monochromator of sodium given in figure 3. This crystal is oriented so as to Bragg-reflect neutrons of wavelength 1.08 Å (energy 0.069 eV). After collimation through slits of size 1 cm by 3.5 cm, the monochromatic beam strikes a flat plate of the crystalline solid of zirconium under study that

zirconium located inside metallic sphere in near of reactor pressure vessel (the diffracted neutrons count-rate is measured in a detector that here accomplished by this metallic sphere, figures 1,3). The neutron current in the primary monochromatic beam is about 200000 neutrons and in the diffraction peaks about 155000 neutrons [5, 7-16].

### 3. The results of calculations and their analysis

Relation of total scattering cross section ( $\sigma_{tot}$ ) with coherent scattering cross section ( $\sigma_{coh}$ ) and incoherent scattering cross section ( $\sigma_{inc}$ ) are:

$$\sigma_{inc} = \sigma_{tot} - \sigma_{coh} \quad (1)$$

Therefore, at first we obtain coherent scattering cross section ( $\sigma_{coh}$ ), thereafter total scattering cross section ( $\sigma_{tot}$ ) and finally incoherent scattering cross section ( $\sigma_{inc}$ ).

#### A) Method of calculation of coherent scattering cross section ( $\sigma_{coh}$ )

We now calculate by MCNP4C code the intensity of the Bragg peak of standard method, originally devised for the scattering of neutrons, namely rotating and oscillating crystal method (rotation of crystal) [6,21]. in this method of measuring a Bragg peak, a monochromatic beam of neutrons is incident on a crystal that can be rotated.

From the intensity of the diffraction peaks, it is possible to calculate coherent cross section by use of equation [11]:

$$F_{hkl}^2 = \frac{P_{hkl}}{P_0} \cdot \frac{4\pi}{\lambda^3 \cdot L \cdot h} \cdot \frac{\sin^2 2\theta}{e^{-\mu h \sec \theta}} \cdot \frac{1}{j_{hkl} \cdot M^2} \quad (2)$$

where  $F_{hkl}$  structure factor;  $P_{hkl}$  and  $P_0$  are the peak and incident beam intensities;  $\lambda$  the neutron wavelength;  $L$  and  $h$  the width and thickness of the specimen;  $M$  the number of molecules per cubic centimeter;  $\mu$  the absorption (linear) coefficient;  $j$  the multiplicity factor for the planes in question;  $r$  distance of specimen from outlet thermal neutrons of gap; and  $\theta$  the angle between the plane and beam.

In case of single-atom samples, like natural zirconium (Zr), scattering amplitude ( $f_0$ ) is determined by use of formula [18]:

$$F_{hkl} = R_{hkl} \cdot f_0 \quad (3)$$

where  $R_{hkl}$  is geometrical part of structure factor.

With use of  $f_0$ , it is possible to calculate coherent cross section by use of equation:

$$\sigma_{coh} = 4\pi (f_0)^2 \quad (4)$$

In figure 4 is shown neutron diffraction pattern taken for a crystal sample of natural zirconium (Zr) [17-20].

After calculations, value of coherent neutron scattering cross section ( $\sigma_{coh}$ ) of natural zirconium obtained 6.41 barns.

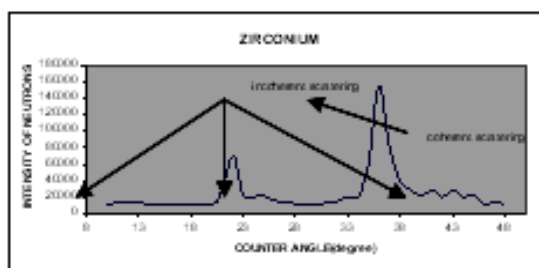


Fig. 4. Neutron diffraction pattern taken for natural zirconium.

## B) Method of calculation of total scattering cross section ( $\sigma_{tot}$ )

For calculation of total scattering cross section ( $\sigma_{tot}$ ), we can use of elements cross sections in MCNP code. MCNP has plotting capabilities. MCNPLOT command, plots tally results produced by MCNP and cross section data used by MCNP.

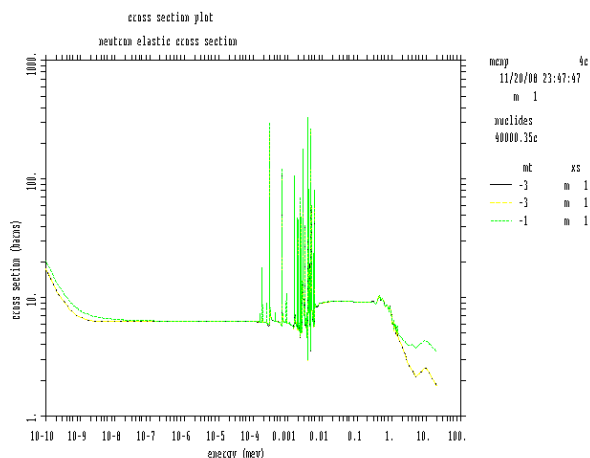


Fig. 5. Neutron total cross section and total scattering cross section for natural zirconium.

It can draw ordinary two-dimensional x-y plots, contour tally plots, More than one curve can be plotted on a single x-y plot. For natural zirconium, neutron total cross section and elastic scattering cross section are shown in fig.5. The neutron energy regime is from  $10^{-10}$  MeV to 20 MeV. From this figure and use of effective scattering cross section in the laboratory system for neutrons in MCNP code, value of total neutron scattering cross section ( $\sigma_{tot}$ ) in range of thermal neutrons for natural zirconium obtained 6.47 barns [1-4].

## C) Definition of incoherent scattering cross section ( $\sigma_{inc}$ )

We now calculate value of incoherent neutron scattering cross section ( $\sigma_{inc}$ ) by use of formula:  $\sigma_{inc} = \sigma_{tot} - \sigma_{coh}$ , which has obtained 0.06 barns.

In table.1 is shown comparison of obtained results with experiment results [18, 22].

Table 1

Cross section (b)	Coherent scattering	Incoherent scattering	Total scattering
Laboratory	6.44	0.02	6.46
MCNP4C	6.41	0.06	6.47

## 4. Conclusion.

As one can see from this discussion, the computer simulation technique as MCNP4C code has enabled the determination of coherent and incoherent neutron scattering cross section. The power of this method can be further will be enhanced by proper combination of several methods from several computer simulation techniques to eliminate the ambiguities in complex crystals structure.

- [1] J.F. Briesmeister. 2000. MCNP-A General Monte Carlo N-Particle Transport code, Version 4C, Los Alamos National Laboratory Report LA-13709-M.
- [2] Members of Cross-Section Evaluating Working Group, Melane, 2001. ENDF-102, Data Formats and Procedures for the Evaluated Nuclear Data File, ENDF-6, National Nuclear Data Center, Brookhaven National Laboratory.
- [3] Reactor Physics Constants, Second Edition, ANL-5800, chap 7, section 7.2.
- [4] RSICC COMPUTER CODE COLLECTION MCNP4C Monte Carlo N-Particle Transport Code System Contributed by: Los Alamos National Laboratory, OAK RIDGE NATIONAL LABORATORY, managed by: UT-BATTELLE, LLC for the U.S. DEPARTMENT OF ENERGY - April 2000.
- [5] P.G. Borodkin. Yadernaya i radiacionnaya bezopasnost, № 1, 2008 г. (in Russian).
- [6] G.L.Squters, Introduction to the theory of thermal neutron scattering, Cambridge University press 1978.
- [7] Lamarsh. John. Introduction to Nuclear Engineering, Addison-Wesley Company, 1977.
- [8] M. Zarkesh. Principles of design, equipment assembly and operating of NPP. Tehran - Iran 2004. ISBN: 964-8171-13-0.
- [9] A. Davarzani. Nuclear reactors applied physics. Tehran - Iran 2004. ISBN: 964-8171-50-5.
- [10] R. Mahmoodi. Reactor VVER - 1000 (V- 320), Tehran - Iran 2004. ISBN: 964-8171-25-4.
- [11] E.O. Wollan, C.G. Shull. The diffraction of neutrons by crystalline powders. Tennessee AEC, Oak Ridge, Tenn, 4-11-49-850-A1462.
- [12] E.O. Wollan, C.G. Shull, M.C. Marney. Neutron diffraction studies, Tennessee AEC, Oak Ridge, Clinton Laboratories, AECD - 2359.
- [13] E.O. Wollan, C.G. Shull, G.A. Morton, W.L. Davidson. Neutron diffraction analysis of NaH and NaD. Technical Information Branch, Oak Ridge, Tennessee AEC, MDDC 842.
- [14] D. Masti. Definition of differential and integral reactivity worth of control rods for WVER-1000 by MCNP Code, Amrikabir Technical University, Teheran, Iran, Thesis (M.S.), 2001.

#### **D. MASTI**

- [15] *D. Masti*. MCNP a general Monte Carlo N-particle transport code, Baku State University. 2008. № 4.
- [16] *T. Margulova*. Nuclear power stations. Mir Publishers, Moscow 1978.
- [17] *J. Beykon*. Difraksiya neytronov. 1963 g. Oktyabr, t. LXXXI, vip. 2, Uspekhi fizicheskikh nauk. (in Russian).
- [18] *R.P. Ozerov*. Uspekhi fizicheskikh nauk 1951 g. Dekabr, t. XLV, vip 4.
- [19] *Yu. L. Izyumov*. Teoriya rasseyaniya medlennikh neytronov v magnitnikh kristallakh. 1963 g. May, t. XXX, vip. 1. Uspekhi fizicheskikh nauk. (in Russian).
- [20] *P.A. Androsenko, M.P. Malkov*. Precizionnoye modelirovaniye rasseyaniya teplovikh neytronov PK brand. ISBN 5-7262-0559-6. IV Konferenciya «Nauchno-innovacionnoye sodrudnichestvo». Fiziko-energeticheskiy institut, Obninsk. (in Russian).
- [21] *I. Noorbehesht*. A introduction to crystallography (geometry), third Edition, Esfahan University 2004. ISBN: 964-6478-38-7.
- [22] *R. E. Rundle, C. G. Shull, E. o. Wollan*. the crystal structure of thorium and zirconium dihydrides by x-ray and neutron diffraction, 1951, Ames Laboratory. AECU-1275.

#### **D. Masti**

### **MCNP4S KODU VASITƏSİLƏ NEYTRONLARIN SİR KONİUM ELEMENTİNDƏN QEYRİ-KOHERENT SƏPİLMƏSİNİN EFFEKTİV KƏSİYİNİN TƏYİNİ**

Materialların strukturlarının təyində neytron kristalloqrafiyası effektiv metodlardan biridir. Lakin neytron mənbələrinin qurulub və istismarı olduqca bəla başa gəlir. Ən güclü neytron mənbəyi reaktordur ki, onun da qiyməti milyard dollardır. Bütün bunlar materialların xarakteristikalarının təyini üçün kompüter metodlarının işlənilib hazırlanmasına səbəb olmuşdur. Kompüter metodlarında da neytron kristalloqrafiyası üçün müəyyən məhdudiyyətlər vardır. Baxılan işdə müvafiq kompüter metodları və MCNP4S kodu vasitəsilə neytronların difraksiya səpilmələrinin tədqiqindəki məhdudiyyətlərin aradan qaldırılması göstərilmişdir. MCNP4S kodu vasitəsilə neytronların sirkoniumdan qeyri-koherent səpilməsinin effektiv kəsiyi təyin edilmişdir.

#### **Д. Масти**

### **ОПРЕДЕЛЕНИЕ СЕЧЕНИЯ НЕКОГЕРЕНТНОГО РАССЕЙАНИЯ НЕЙТРОНОВ НА ЦИРКОНИИ КОДОМ MCNP4C**

Нейтронная кристаллография является эффективным методом для определения структуры материалов. Но строительство и содержание нейтронных источников очень дорогие. Самый мощный нейтронный источник - ядерный реактор, но его расходы составляют миллиарды долларов. Высокая стоимость была главным фактором для разработки компьютерных методов для определения характеристики материалов. В компьютерных методах тоже существуют ограничения для нейтронной кристаллографии. В данной работе показано, что с помощью компьютерного метода и кода MCNP4C можно устранить эти ограничения для исследования дифракционного рассеяния нейтронов. Кодом MCNP4C определяются сечения некогерентного рассеяния нейтронов на цирконии.

*Received: 24.10.08*

## OZON QAZI SİNTEZİNİN ELEKTRON TEXNOLOGİYASI

A.M. HƏŞİMOV, K.B. QURBANOV, H.C. HÜSEYNOV

AMEA H.M. Abdullayev adına Fizika İnstitutu, Az-1143, Bakı, H.Cavid, 33

Məqalədə müxtəlif istehsal sahələrinin inkişaf etdirilməsində, hazırlanan məhsulun üstün keyfiyyət göstəricilərinə malik olmasında elektron texnologiyalarının tətbiq olunmasının effektivliyi əsaslandırılmışdır. Xüsusi halda ozon qazının istehsalı üzrə yüksək məhsuldarlığa malik ozonatorun hesabı üzrə nəticələr təqdim olunmuşdur.

Xalq təsərrüfatının müxtəlif sahələrində elektron texnologiyasının tətbiqi effektiv üsul hesab olunur və bu bir sıra proseslərdə istifadə olunaraq müsbət nəticələrlə özünü təsdiq etmişdir. Elektron texnologiyası üsulları güclü elektrik sahələrinin və elektrik qaz boşalmalarının texnoloji proseslərə təsirinə əsaslanır.

Elektrik sahəsi atom və molekulara, hətta ölçüləri kiçik olan maddə hissəciklərinə təsir edərək onlara istiqamətlənmiş hərəkət verərək elektrosepasiya, elektroqarışdırma, elektroorientasiya, elektriki yüklənmə, elektrosüzgəc, elektrotəmizləmə və sairə bu kimi proseslərin həyata keçirilməsini təmin edir. Elektrik qazboşalmalarının təsirləri maddənin fiziki və kimyəvi xassələrini dəyişməyə səbəb olur ki, bu da materiallara arzu olunan xüsusiyyətlərin aşılmasına imkanlar yaradır. Yuxarıda göstərilən proseslərdə materiallardan əsasən qazlarda elektrik cərəyanının keçməsi müşahidə olunur. Qazlarda elektrik cərəyanının öyrənilməsi qaz elektronikasında olduğu səbəbindən yuxarıda şərh olunan texnologiyalar elektron texnologiyası adı almışdır. Elektron texnologiyasında elektrik enerjisinin proseslərə birbaşa təsirlərindən istifadə edildiyindən onun digər enerji növlərinə çevrilməsinə ehtiyac olmur, bu da öz növbəsində istehsal sürətinin yüksək olmasını və istehsalın iqtisadi səmərəliliyini təmin edir.

Qeyd etmək lazımdır ki, elektrik enerjisinin tətbiqinin ətalətsiz idarə olunması elektron texnologiyasının texnoloji proseslərin avtomatlaşdırılmasının sadələşdirilməsinə imkan yaradır.

Elektron texnologiyası eyni həcmdə elektrik, mexaniki, istilik, kimyəvi və bir sıra digər təsirlərin eyni zamanda tətbiq olunmasına yol verdiyindən istilik mühadiləsi, kimyəvi reaksiyalar və bu kimi fiziki-kimyəvi proseslərin effektivliyinin yüksəlməsinə səbəb olur.

Yuxarıda qeyd olunanlar elektron texnologiyasının yeni sxemlərinin işlənilməsinin, yeni aparat və qurğuların hazırlanmasının və onların xalq təsərrüfatının müxtəlif sahələrində tətbiqinin günün aktual problemləri sırasına daxil olduğunu əsaslandırır.

Elektron texnologiyasında istifadə olunan ozon qazının tətbiq oblası geniş və müxtəlifdir [1-5]:

- ozon qazı sənaye tullantı suların effektiv təmizlənməsini;
- tullantı suların tərkibində fenol, radon, sionid maddələrini parçalayaraq suyun bu maddələrdən effektiv təmizlənməsini;
- suyun şəffaflığını, canlı orqanizmə zərərli virus və mikrobların zərərsizləşdirilməsini təmin edir. Ozon qazı bəzi kimyəvi reaksiyalarda katalizator kimi istifadə olunur.
- Ozon qazı vastəsilə bir sıra oksidləşmə proseslərini asanlıqla həyata keçirmək olur:
  - formaldehidin və qarışqa turşusu almaqla metan qazının oksidləşməsi;
  - etilenin etilenoksidə çevrilməsi;

- ozonun təsirlə karbohidrogenlərin oksidləşməsi və nəticədə kimya sənayesinin məhsulu olan spirtlərin aldehidlərin alınması və sairə bu kimi prosesləri misal göstərmək olar.

Yuxarıda ozon qazının kimya sənayesində tətbiqinin nəticələrinə əsaslanaraq qazboşalmalarının, başqa sözlə elektron texnologiyasının təsirlərinin kimya sənayesində geniş oblasın inkişaf etməsinə səbəb olduğu aydın olur.

Təqdim olunan məqalədə ozon üzrə yüksək məhsuldarlığa malik elektron texnologiyasına daxil olan qurğunun layihələndirilməsi və müvafiq hesabı verilmişdir.

Təklif olunan ozonator qurğusunun layihəsi aşağıdakı elementləri tərkibinə daxil edir.

Ozonator qurğusunun ümumi sxemi 3 ədəd elektrik qazboşalması elementi, vahid soyutma sistemi, vahid elektrik təchizatı sistemi, qaz daxil olma və ozon-oksigen çıxış sistemindən təşkil olunmuşdur. Hər bir qazboşalması elementi vastəsilə 0,5 kq/saat məhsuldarlıqla ozon istehsal olunması nəzərdə tutulmuşdur. Bu halda çıxışda 2% ozonun ayrılması gözlənilməlidir. İş rejimini dəyişməklə çıxışda ozonun miqdarın 7%-ə çatdırmaq olar.

Qazboşalması elementlərinin hər biri eyni oxlu  $l$  uzunluğa malik metal borulardan ibarət olaraq, daxili kiçik diametrlı borunun bir çıxışı qapanmış halda, xarici səthində  $d_q$  qalınlıqda şüşə emal çəkilir. Boruların arasında qazboşalması əmələqələn  $d_q$  qalınlıqlı silindrik şəkilli qaz aralığı mövcud olur ki, bu aralıqda ozonator işə salındıqda ozon qazının sintezi müşahidə olunur. Ozonatorun hər iki borusunun su axını ilə soyudulması nəzərdə tutulur. Ozonatorun daxili borusu yüksək potensiallı olduğundan soyutma suyunun qurğuya daxil olması və çıxması dövrəsinə  $8 MqOm$  qiymətində müqavimət daxil edilir ki, bu müqavimətin hesabına sızma cərəyanlarının gücü 25 Vt, sızma cərəyanlarının qiyməti isə 2 mA-dən çox olmasın.

Ozonator qurğusuna daxil olan digər elementlər yüksək gərginliklər texnikasının qaydalarına müvafiqliyi təmin edilərək hazırlanmışdır. Qurğuda  $d_q=1,2m$  qazboşalması aralığı  $d_q=1,2mm$ , qaz kütləsi olaraq 1 atm təzyiqdə deşilmə gərginliyi  $E_d=35kv/sm$  və dielektrik nüfuzluğ  $\epsilon=7-9$  olan oksigen qazından istifadə edilmişdir. Hər bir boru ozonator generatoru olaraq ozon üzrə  $m=0,5kq/saat$  məhsuldarlığa malikdir.

Ozon generatorlarının geometrik parametrlərini təyin edək. Qəbul edək ki, 2500-5000 Hz tezlikli gərginlik tətbiq etdikdə  $k=5kq/saat$  olur.

$m=k \cdot s_a$ , burada  $s_a$  -dielektrik arakəsmənin işçi sahəsidir:

$$s_a = m / k = 0,5 / 5 = 0,1 m^2$$

olar.

Bu halda borunun  $l$  uzunluğunun diametrə hasili üçün:

$$l \cdot D_a = 0,1 / \pi m^2$$

alarıq.

Əgər  $D_a=60\text{mm}$  olarsa, onda  $l=0,5\text{m}=500\text{mm}$  olar. Bu halda xarici borunun daxili diametri  $D_a + 2d_q$ , daxili borunun xarici diametri isə  $D_a - 2d_q$ , müvafiq olaraq  $62,4\text{ mm}$  və  $57,4\text{ mm}$  təşkil edir.

Qaz kütləsinin parametrləri aşağıdakı münasibətdən təyin edilir:

$$m = cV = c\omega S_0$$

Burada  $c\text{-}kq/m^3$  -konsentrasiya,  $V\text{-}m^3/saat$  qaz sərfi,  $\omega\text{-}m/saat$  -la xətti sürət,  $S_0\text{-}dairəvi$  aralığın en kəsiyinin sahəsidir.

$$S_0 = \pi D_a \cdot d_q = 226 \cdot 10^{-6} \text{ m}^2$$

$m=0,5kq/saat$  olduğundan,  $c=0,04kq/m^3$  qiymətləri konsentrasiyanın təqribən  $\sim 2\%$ -ə uyğun gəlir.

$$V = 12,9 \text{ m}^3 / saat$$

$$\omega = 15,3 \text{ m/san}$$

qiymətləri alınır.

Bu sürətlər qaz kütləsinin reaktorun aktiv zonasında  $0,03$  saniyə müddətində qalmasına qətiir. Bu halda reaktorun daxilində təzyiq artımı,

$$\Delta p = \frac{\rho \omega^2}{2} = 250 \text{ Pa} = 0,0025$$

atmosfer təşkil edir.

Qazboşalmasının başlanğıc gərginliyi

$$u_z = E \cdot d_q = 35 \text{ kV/sm} \cdot 0,12 \text{ sm} = 4,2 \text{ kV}$$

təşkil edir.

Ozonatorun işçi gərginliyi  $u_{işçi}=12\text{kV}$ , dielektrik arakəsməyə düşən gərginlik  $u_d=7,8\text{kV}$  olduqda

$$E_d = \frac{u_d}{d_d} = 6,5 \text{ kV/mm} \text{ olur.}$$

Ozonatorda ayrılan aktiv güc aşağıdakı münasibətlə müəyyənəşdirilir:

$$P_0 = 4 f u_z (u_d c_d - u_z c_q)$$

burada  $c_d, c_q$  - dielektrik arakəsmənin və qaz aralığının tutumudur və aşağıdakı kimi təyin edilir.

$$c_d = \frac{\epsilon \epsilon_0 S_a}{d_d} \approx 600 \cdot 10^{-12} \text{ F}$$

$$c_q = \frac{\epsilon \epsilon_0 S_0}{d_q} = 740 \cdot 10^{-12} \text{ F}$$

Bu halda  $P_0 = 3,6 \text{ kVt}$  qiymətini alır. Ozonator qurğusunun 3 elementinin ümumi gücü  $10,8\text{kVt}$  təşkil edir. Yüksək təzyiqlərdə ( $1,5 \text{ atm}$ ) izolyasiya üzrə sızma və tutum cərəyanlarını nəzərə alsaq  $5000 \text{ Hz}$  tezliklərdə mənbənin gücü  $15 \text{ kVt}$ -dan az olmamalıdır. Bu halda qurğunun aktiv gücü və məhsuldarlığı azalmış olar.

Beləliklə məqalədə şərh olunan layihə və hesabat ozon qazı üzrə müxtəlif məhsuldarlığa malik ozonatorların layihələndirilməsində baza sənədi kimi istifadə oluna bilər.

- [1] V.F. Kojinov. Ozonirovanie vodi. Stroyizdat, M., 1974.  
[2] V.A. Orlov. Tekhnologiya ozonirovaniya vod., M., 1996.  
[3] Yu.V. Philipov, V.A. Voblikovi, V.I. Panteleeva. Elektrosintez ozona. M. Izd-vo MGU, 1987.

- [4] N.A. Mamedov, B.B. Davidov, K.M. Dashdamirov, G.M. Sadikhzade, J.N. Jabbarov, Sh.Sh. Alekberov. Problemi energetiki, №3, 2004, s.66-69.  
[5] V.V. Linin, M.P. Ponovich, S.N. Tkachenko. Fizicheskaya khimiya ozona. M. Izd-vo MGU, 1998, s.480.

**A.M. Gashimov, K.B. Gurbanov, G.J. Guseinov**

## **ELECTRONIC TECHNOLOGY OF OZONE SYNTHESIS**

The application efficiency of electronic technology in the development of different industries is established in this paper. The calculations of ozone device of high efficiency are given.

**А.М. Гашимов, К.Б. Гурбанов, Г.Дж. Гусейнов**

## **ЭЛЕКТРОННАЯ ТЕХНОЛОГИЯ СИНТЕЗА ОЗОНА**

В статье обосновывается эффективность применения электронной технологии в развитии различных промышленных отраслей, в частности представлены расчеты озонаторной установки высокой производительности.

*Received: 17.09.08*

TiGaSe<sub>2</sub> IS PEIERLS DIELECTRICM.Yu. SEYIDOV<sup>1,2</sup>, R.A. SULEYMANOV<sup>1,2</sup>, T.G. MAMEDOV<sup>2</sup>, R.A. KHAMOYEV<sup>2</sup><sup>1</sup>*Department of Physics, Gebze Institute of Technology,  
41400, Kocaeli, Turkey*<sup>2</sup>*G.M.Abdullayev Institute of Physics of National Academy of Sciences of Azerbaijan,  
AZ-1143 Baku, Azerbaijan*

The investigation results of temperature dependences of dielectric constants ( $\varepsilon$ ), dark and pyroelectric currents and also VAC and dark current time evolutions of layered ferroelectric-semiconductor TiGaSe<sub>2</sub>, obtained at fixed temperatures in 77K÷ 300K interval are presented in the present work. The pronounced anomaly in the “pit” form with visually noticeable temperature boundaries ~150K and ~200K is firstly revealed on  $\varepsilon(T)$  curve measured in the direction which perpendicular to the layers in the region of low frequencies. Also the development of electric instabilities revealing in the form of low-frequency current quasiperiodic vibrations on sample VAC in strongly limited temperature interval 145K – 205K is firstly experimentally fixed. The time character of current instabilities is established. It is shown that it is important for observance of the given instabilities that electric field should be given to the sample by the means of contact-free master potential electrodes prepared in the form of thin mica separator. The instability nature and its influence on the different physical parameters of layered crystal TiGaSe<sub>2</sub> are discussed.

## 1. Introduction

Thallium-gallium diselenide (TiGaSe<sub>2</sub>) relating to the family of low-dimension (layered and open-chain) triple chalcogenide semiconductor compounds with general formula  $\text{TI}^+(\text{M}^{3+}\text{X}_2)^-$  where M = In, Ga; X = Se, S, Te is the interest example of ferroelectric-semiconductor in the scientific relation and important in the practical one the properties of which are actively investigated during long time. The significant volume of experimental material dedicated to systematic study of structural properties and physicochemical peculiarities TiGaSe<sub>2</sub>, synthesis condition development of these compounds and preparation technology of high-qualitative single crystals [1-7] has accumulated in the scientific works in the result of long-term investigations. Thus, for example, by rentgenodiffraction investigations it is established that TiGaSe<sub>2</sub> layered crystals have the monoclinic type of crystal structure with  $C_{2h}^6$  symmetry space group and  $a = 10,77\text{\AA}$ ,  $b = 10,771\text{\AA}$ ,  $c = 15,636\text{\AA}$  and  $\beta = 100,06^\circ$  lattice spacings. The two-dimensional-periodic double layer alternating parallel to crystallographic plane (001) (or perpendicular to c axis) is the main structural crystal unit. Each “sublayer” consists of group consistency of Ga<sub>4</sub>Se<sub>10</sub>-pyramids being the main structural reason which are constructed from combination of four elementary gallium-selenium GaSe<sub>4</sub> tetrahedrons. Two layers access to each other by vertexes of pyramids and are relatively shifted by such way that trigonal pyramids form in which TI atoms locate. The elementary cell contains 16 formula units (64 atoms) [1-7].

The interest to TiGaSe<sub>2</sub> is caused by the presence of temperature phase transition (PhT) consistency at atmosphere pressure in its structure. The three structural PhT: two in the volume and the one on the surface are explicitly identified by the structural [5,8], heat [9-14], acoustic [15-18], optical [19-22], dielectric [23-32], pyroelectric [33], NMR [34,35], EPR [36] and other investigations in TiGaSe<sub>2</sub> crystals. PhT realize in crystal volume: near  $T_f \sim 120\text{K}$  from high-temperature paraelectric phase into incommensurable (INC) phase and near  $T_c \sim 110\text{K}$  from INC-phase into improper, modulated, commensurable (C) ferroelectric phase with the spontaneous polarization vector lying in the layer plane. Note that PhT temperatures for TiGaSe<sub>2</sub> samples chosen from different technological sets can differ from above mentioned

ones on few degrees up or down on temperature scale. PhT in INC-phase is connected with stability loss of layered crystal lattice with respect to some degree of freedom corresponding to wave vector  $\vec{k}_i = (\delta; \delta; 0.25)$ , where  $\delta = 0.02$  is incommensurability parameter [5,8]. The parameter  $\delta$  at transforms into zero by the jump at  $T = T_c$  so ferroelectric properties of low-temperature C-phase are connected with “blocking” of modulation wave vector on rational value  $\vec{k}_i = (0; 0; 0.25)$  (soft mode on the boundary of Brillouin band). The symmetry space group of low-temperature polar phase and also temperature behavior of  $\delta$  incommensurability parameter haven't been revealed yet in spite of many attempts. PhT on the surface is observed near  $T \sim 135\text{K}$  according to [33,37]. The significant improvement in the understanding of surface PhT nature in TiGaSe<sub>2</sub> is absent in the present scientific works.

Meanwhile, enough many experimental facts obtained on the base of CSL and IR [19, 38-42] investigations and also by the methods of micro-wave and submillimetric dielectric spectroscopy [43, 44] which don't agree with above mentioned data and show on the TiGaSe<sub>2</sub> relation to the class of eigen ferroelectrics with intermediate INC-phase on temperature as the softening of some phonons in the middle of Brillouin band in commensurable ferroelectric phase is observed near PhT temperature. Nowadays the inconsistency reasons of above mentioned results can't be considered as finally determined ones in spite of the fact that there are several models [23-28, 45-47] in the scientific works which explain them.

Note that TiGaSe<sub>2</sub> crystals usually have the composition differing from stoichiometric one [48,49] because of the difference in steam tension of initial components. The stoichiometry failure in growing process or high-temperature thermal annealing of TiGaSe<sub>2</sub> samples leads to appearance of increased structural defect concentration in the form of Se volume inclusions the concentration and charge state of which significantly influence on semiconductor properties of TiGaSe<sub>2</sub> (double carrier injection, residual photoconductivity [48, 49] and etc.).

Besides regions close to temperatures of structural PhT, TiGaSe<sub>2</sub> single crystals reveal the series of unusual properties which don't have the proper explanation. Firts of all, it is



necessary to note the works [43,44] in which the dynamics non-trivial behavior of  $\text{TlGaSe}_2$  crystal lattice consisting in splitting of soft ferroelectric mode on two components: low-frequency branch behaves itself normally and high-frequency one behaves itself anomalously with temperature change. Firstly its frequency monotonously decreases with temperature decrease, goes through minimum near  $\sim 180\text{K}$  and then it increases. The tractability of this singularity is given in [50] on the base of model of toroidal PhT. In [20,21] it is established that under study of temperature dependences of transmission spectrums of  $\text{TlGaSe}_2$  samples chosen from different technologies sets and investigated in the direction perpendicular to layers, the intensity oscillations of monochromatic light (see fig.7, b) passing through the crystal are observed in  $\text{TlGaSe}_2$  some samples aren't observed in the white light and their period doesn't depend on thickness of  $\text{TlGaSe}_2$  investigated plates, they are defined only by sample temperature. With the help of control investigations authors establish that oscillations observable in the experiment aren't connected with multipath light interference in  $\text{TlGaSe}_2$  parallel-sided plates and thermoluminescence of crystal impurity centers. By authors opinion [20, 21, 51] the above mentioned oscillations are connected with diffraction of monochromatic light on soliton lattice presenting itself the region alternation corresponding to commensurable ferroelectric phase on the structure and narrow domain-like walls which are phase solitons. By other words authors suppose that PhT into INS-phase in  $\text{TlGaSe}_2$  takes place near  $\sim T_f \sim 247\text{ K}$  and into ferroelectric C-phase takes place near  $T_c \sim 140\text{ K}$ , i.e. near temperatures not designated by structural investigations. It is need to note that theoretic estimations carried out in refs [52-55] make the realization in the experiment of above mentioned oscillation mechanism of transmission intensity in  $\text{TlGaSe}_2$  unclear.

Besides the above mentioned unusual peculiarities, the one more is observed in the ref [22] at temperature investigations of conoscopic figures of  $\text{TlGaSe}_2$  thin plates consisting in return of  $\text{TlGaSe}_2$  optical axes beginning from the temperatures  $\sim 180\text{K}$ . The authors of ref [22] specially emphasize that observable phenomena can't be explained by even supposed PhT in  $\text{TlGaSe}_2$  structure and is connected with appearance the internal electric fields directed perpendicular to  $\text{TlGaSe}_2$  layers (the nature of which by the opinion of ref [22] authors is still unclear) and their influence on crystal refraction coefficients in the given temperature region in the crystal.

Finally let's mention the refs [10, 11, 16] in which the unusual temperature behavior of thermal-expansion coefficient and Yung module of  $\text{TlGaSe}_2$  are observed in temperature interval  $\sim 140\text{K} \div \sim 200\text{K}$ .

Taking into consideration the above mentioned the detail study of resistive and dielectric properties of  $\text{TlGaSe}_2$  single crystal samples in temperature interval  $140\text{K} \div 200\text{K}$  with the aim of search and establishing of correlations between above represented unusual physical properties  $\text{TlGaSe}_2$  in the given temperature region and measurements of dielectric and transport properties is the task of present paper. The experimental evidences of the fact that the given peculiarities present themselves the different forms of electric instability revealing realizing in the form of nonequilibrium PhT in  $\text{TlGaSe}_2$  electronic subsystem are given in the work. Let's note that the data about similar investigations in the scientific work are absent in the moment of present work carrying out.

## 2. Sample preparation and measurement technique.

The specially chosed high-resistive samples  $\text{TlGaSe}_2$  cutted from grown single crystal ingots modified by method Bridgmen-Stockbarger are used for investigations. X-ray micro-analysis carried out by the means of EDX (energy dispersive X-ray) attachment to scanning electron microscope proves the sample formula composition. According to EDX-analysis data the percent relation of initial components in the investigated sample differs from stoichiometric one to the side of tallium atom deficit and it is equal to (22,58 at %)Tl, (26,58 at %)Ga and (50,84 at %)Se. Let's also note that the control tests on  $\text{TlGaSe}_2$  samples sawed out from other technological sets the stoichiometric composition of which either almost corresponds to above mentioned one or absolutely differs from it to the side of thallium atom excess and selenium atom deficit are carried by us with the aim of confirmation of obtained results.

The following electro-physical properties: VAC, dark current in the dependence on constant electric voltage applied to the sample and light intensity by the which the sample radiation is carried out up to measurements; the frequency dependence of complex dielectric constant; the current of short circuit passing through the sample (pyroelectric current near ferroelectric PhT) are studied in the prepared samples in wide temperature interval.

The samples for electric measurements in constant electric field present themselves the rectangular plates with typical dimensions: thickness  $\sim 1,5\text{mm}$  and surface area  $\sim 8\text{mm}^2$ . The two by two current-conducting contacts from silver paste, to which the thin copper wires are applied, are evaporated on basic mirror surfaces of  $\text{TlGaSe}_2$  plates for the obtaining of low-resistance electric contacts with the sample. The width of interstice between contacts on each sample is  $\sim 2\text{mm}$ . Besides, the control measurements on the samples with electrodes from aurum evaporated on sample surfaces by the method of high-temperature thermal evaporation in vacuum are carried by us. The results obtained by the using of these electrodes are identical ones. From this it is followed that  $\text{TlGaSe}_2$  sample contacts with electrodes have the resistance which is essentially less than the crystal volume resistance.

The nitric cryostat with optical windows and automatic regulation and temperature stabilization is used for investigations. The control of temperature and the rate of its change is carried with the help of Lake Shore 340 Temperature Controller. The measurements are carried in dynamic regime with different rates of linear temperature change in interval from  $0,1\text{K/min}$  up to  $20\text{K/min}$ . The sample temperature is measured by platinum resistance thermometer Pt-100 at the temperature stabilization level not less  $0,01\text{K}$ . The sample radiation is carried by the light of quartz-halogen bulb with power  $100\text{W}$ .

The current measurements are carried out with the help of peak-ampere-meter Keithley 485 to the input of which the sample is connected off in resistance mode. The sensitivity lower limit of measured installation is  $0,1\text{pA}$  with measurement error of current through crystal not more than  $\pm 0,01\text{pA}$ .

The pyrocurrent measurements are carried out by the common method of short-circuit sample at its uniform heating. The peak-ampere-meter Keithley-485 is used in the capacity of registering device. The contacts from silver pasta



are coated on mirror surfaces TlGaSe<sub>2</sub> sample layers as along polar direction so perpendicular to one. The measurement procedure contains the following operations: firstly the sample is cooled up to melting point of liquid nitrogen in the darkness at the presence of external polarized current electric field the strength 400V/cm (which is essentially less than the coercive field one). Further the sample is heated up to room temperature in the dynamic regime with linear rate of temperature change 20K/min. Parallel to it the short-circuit current ( $i_p(T)$ ) passing through the sample (pyroelectric current near ferroelectric PhT) is registered in the regime of short-circuit sample.

VAC measurements are carried out with the help of electrometer Keithley 614 in isothermal conditions in the test current scanning regime. The current amplitude registered by the electrometer is  $\sim 0,1\text{pA}$ , the voltage applied to the sample is in interval  $-100\text{ V} \div +100\text{ V}$ .

The special investigations at which the electric contacts are removed from sample surface and electric field is applied by the means of non-contact, potential-retarding electrodes carried out in the form of thin mica separator (by thickness  $\sim 300\text{ }\mu\text{m}$ ) hold on the sample surface with the help of vacuum lubrication are carried out with the aim of exclusion of electric contacts on TlGaSe<sub>2</sub> electrophysical properties. By other words the cycle of electric measurements is repeated on the sample putted between condenser armatures connected to closed circuit consisting of the direct current source, condenser and electrometer.

The investigations of complex dielectric constant are carried out in quazi-static temperature regime by the method of impedance spectroscopy in frequency range 50Hz – 13MHz with the help of HP 4192A LCR-meter. The measurements are carried out on TlGaSe<sub>2</sub> sample having the form of rectangular parallelepiped with parallel-sided ends with area  $12\text{mm}^2$  and  $10\text{mm}^2$  correspondingly in both perpendicular to the layers and along polar direction one. The sample surfaces which one perpendicular to polar direction are mechanically polished and burnished up to optical quality. The electric contact to the electrode formed by the evaporation of gold films on sample surface is carried out with the help of current contact devices. The sample during measurements is in thermostatically controlled chamber inside thin-walled glass Dewar. The temperature is controlled by cuprum-constant thermocouple. The accuracy of temperature maintenance is not less than 0,5K and sensitivity of its measurement is not less than 0,1K.

### 3. Experimental results.

The temperature dependences of dielectric constant real part ( $\epsilon'$ ) of TlGaSe<sub>2</sub> measured in heating regime at different fixed frequencies (200 Hz  $\div$  13 MHz) of measurement field in direction perpendicular to layers are presented on the fig.1. As it is seen from fig.1 the spectrums of dielectric constant real part show the significant frequency dispersion in the frequency range 200Hz $\div$ 10kHz (at frequencies bigger than 100kHz dielectric constant spectrum approbation and  $ac$  conductivity of TlGaSe<sub>2</sub> significantly becomes worse and corresponding curves on the fig.1 and 2 aren't shown in order to not fill the figure). The visually seen anomalies of  $\epsilon'(T)$  dependence in the form of small maximum near  $T \sim 120\text{K}$  and superficial hole in temperature interval  $\sim 150\text{K} \div \sim 200\text{K}$  with enough sleep low-temperature and tail high-temperature

slopes. The low-frequency anomalies in behavior  $\epsilon'(T)$  are gradually suppressed and practically aren't observed at frequency of measurement field 10KHz with alternative field frequency growth (see the inclusion on fig.1). The region of enough intensive  $\epsilon'(T)$  increase close to exponential one on the background of which the small bend is registered is observed at  $T > 190\text{K}$  in whole investigated frequency range 200Hz $\div$ 13 MHz.

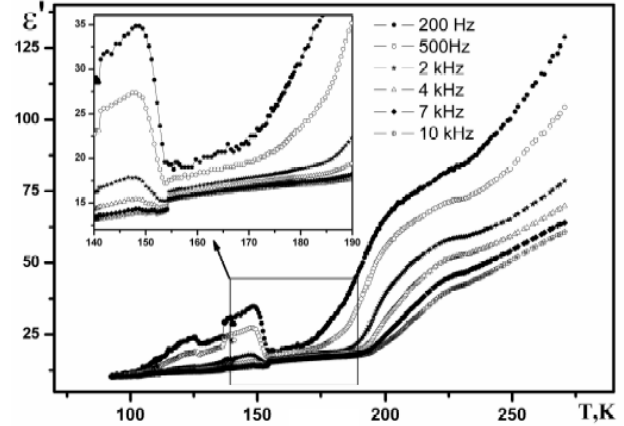


Fig.1. Temperature dependences of dielectric constant real component of TlGaSe<sub>2</sub> measured in heating regime in the direction perpendicular to layers at different frequencies. The anomalous behavior of  $\epsilon'(T)$  TlGaSe<sub>2</sub> in temperature interval 150 K  $\div$  200 K is shown on the attachment.

The spectrum temperature dependences of  $ac$  conductivity ( $\sigma$ ) of layered crystal TlGaSe<sub>2</sub> measured in the regime of sample heating in the direction perpendicular to the layers in frequency range 200Hz $\div$ 13 MHz are presented on the fig.2. From fig.2 it is seen that qualitatively temperature step of whole  $\sigma$  curves measured on different frequencies coincides with data of fig.1, moreover, the clearly expressed anomaly having “hole” form in temperature interval  $\sim 150\text{K} \div \sim 200\text{K}$  is also the main peculiarity of each from curves  $\sigma(T)$  in the investigated frequency range.

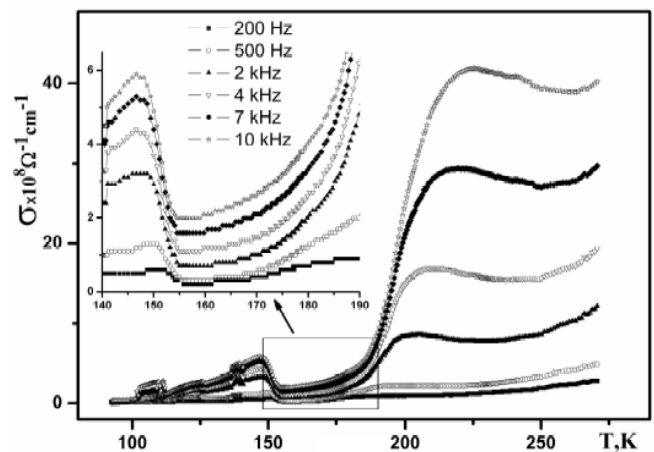


Fig.2. Spectrum temperature dependences of  $ac$  conductivity of TlGaSe<sub>2</sub> measured in the direction perpendicular to layers at different frequencies. The anomalous behavior of  $\epsilon'(T)$  TlGaSe<sub>2</sub> in temperature interval 150 K  $\div$  200 K is shown on the attachment.

The typical temperature dependences of complex dielectric constant real part of TlGaSe<sub>2</sub> measured in the

direction parallel to layer plane in frequency range 200Hz÷13MHz are shown on the fig.3. As it is seen from the fig.3 the curves  $\varepsilon'(T)$  are essentially differed from the observable ones in the direction perpendicular to the layers. The measurements of  $\varepsilon'(T)$  at different frequencies show that ferroelectric PhT in TlGaSe<sub>2</sub> takes place at  $T_c \sim 110$  K and has all peculiarities character for relaxation processes of Debye type: the peak  $\varepsilon'(T)$  connected with ferroelectric PhT washes

out with decrease of dielectric constant maximum value and insignificant increase of PhT temperature with increase of frequency of alternative measurement field. Let's note that anomaly in the form of strong maximum character for ferroelectric PhT which is also suppressed with measurement field frequency increase (fig.3,b) is observed near  $T_c \sim 110$  K on temperature dependence  $\varepsilon''$  (conductivity) studied in the direction parallel to TlGaSe<sub>2</sub> layers.

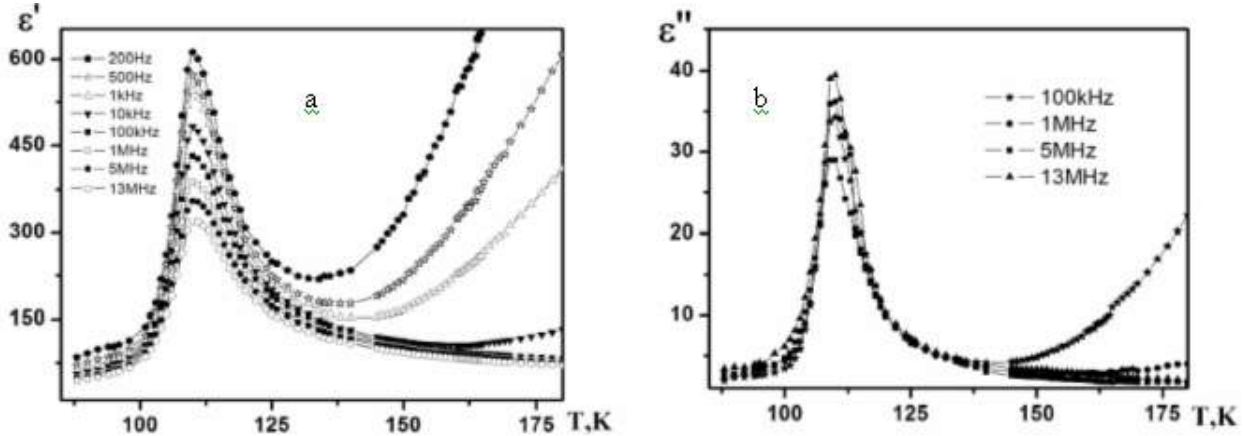


Fig.3. Temperature dependences of real (a) and imaginary (b) components of dielectric constants of TlGaSe<sub>2</sub> measured in heating regime in the direction perpendicular to layers at different frequencies.

As it has been mentioned, the layered crystals TlGaSe<sub>2</sub> at normal conditions are semiconductors of p-type with width of forbidden band varying in the limits  $\Delta E \sim 2.03 \div 2.1$  eV ( $\Delta E$  values obtained by different authors can differ from each other as they significantly depend on the conditions and the method of sample growth, crude purity for growth, crystal high-temperature annealing in other mediums and other factors as other physical properties of TlGaSe<sub>2</sub> [23, 24, 56, 57]) and good sensitivity. TlGaSe<sub>2</sub> samples investigated in the present work have the specific resistance  $\sim 1.5 \cdot 10^7 \Omega \text{ cm}$  and higher at temperatures close to room ones in the dependence on type and concentration of uncontrolled deep impurity. Their VAC obtained with the help of metallic contacts (silver pasta, aurum) are practically linear at room temperature, the polarity change of applied voltage doesn't almost change the contact resistance, temporary delay between applied voltage and electric current isn't also observed. Thus, the used electric contacts can be considered as ohmic ones.

The temperature dependence of electric current ( $i$ ) passing through TlGaSe<sub>2</sub> sample perpendicular to the layers at application to the crystal of constant external voltage 7V is shown on the fig.4. The curve  $i(T)$  is obtained in the heating regime at the rate of sample temperature scanning 1K/min. As it is seen from the fig.4 the dependence  $i(T)$  has semiconductor character moreover, beginning from  $T \sim 180$  K the current value strongly increases with temperature increase. The plot region  $i(T)$  is well described by activation law of arrenius type in temperature interval bigger than  $\sim 180$  K, moreover, activation energy of deep impurity defined on inclination of  $\ln i(T)$  dependence region on  $10^3/T$  is 0.31 eV. The oscillating character of  $i(T)$  curve in temperature interval 117÷180 K is shown in larger scale on the addition to fig.4. It is seen that  $i(T)$  curve after small increase in temperature interval 90 K ÷ 117 K on law close to exponential

one "drops" in quasi-periodic oscillation process the character of which changes at 138 K and 168 K at the achievement of temperature point 117 K. The oscillation isn't observed in  $i(T)$  behavior at temperature than higher temperature 180 K. The specially carried out investigations  $i(T)$  in interval 117 K ÷ 180 K in temperature stabilization regime show that current oscillations have temporary character with quasi-period  $\sim 1$  min.

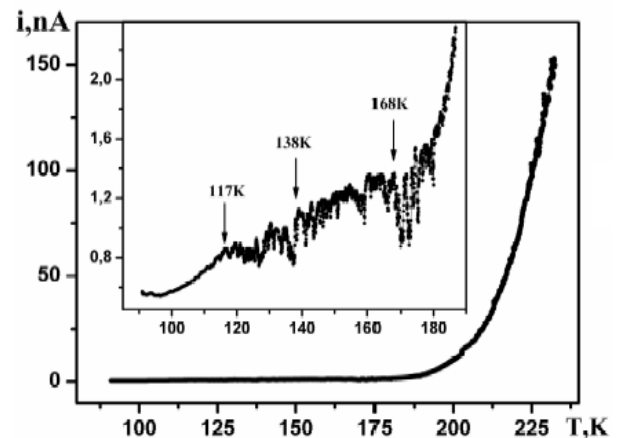


Fig.4. Temperature dependence of dark current passing through sample TlGaSe<sub>2</sub> perpendicular to layers at the application of external potential 7V. The curve  $i(T)$  is obtained in heating regime at sample temperature scanning rate 1K/min.

The curves on the figures 5, 6 and 7 give the visual illustration of  $i(T)$  dependence character changes of initial TlGaSe<sub>2</sub> at variation of experiment external conditions: rate change of sample temperature heating ( $dT/dt$ ) and applied to sample of constant voltage ( $U$ ).

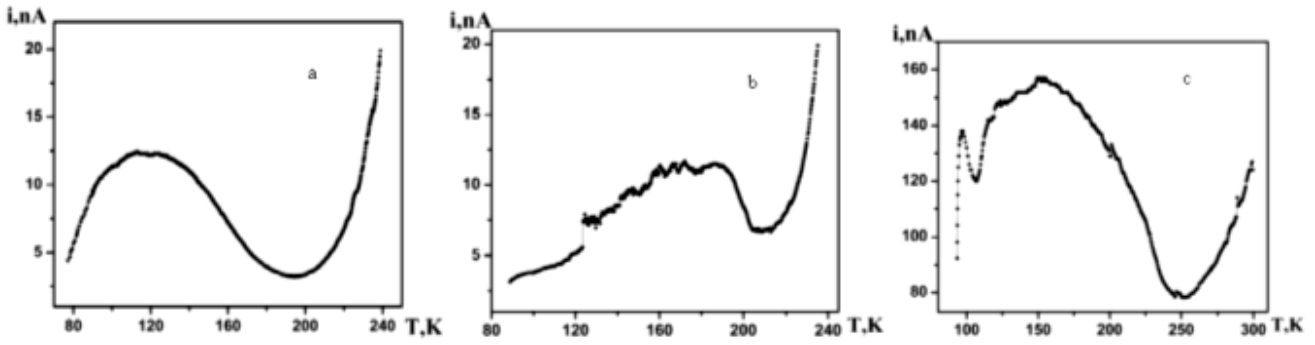


Fig.5. The same as on fig.4. Experimental dependences  $i(T)$  are obtained under following experiment conditions: a is  $dT/dt = 5$  K/min,

$U = 5$  V; b is  $dT/dt = 5$  K/min,  $U = 7$  V; c is  $dT/dt = 10$  K/min,  $U = 4$  V.

The curve  $i(T)$  obtained at the rate of sample temperature scanning 5K/min and external voltage 5V is presented on the fig.5a. It is seen that  $i(T)$  dependence in temperature interval 77K ÷ 200K has bell-shaped character with maximum corresponding to ~117K moreover beginning from ~117K up to ~200K the semiconductor sample resistance increases with temperature increase. The similar experimental dependences  $i(T)$  are obtained by us at other experiment conditions

(fig.5, b:  $dT/dt = 5$  K/min,  $U = 7$  V, fig.5 c:  $dT/dt = 10$  K/min,  $U = 4$  V). As it is seen from fig.5 the increase of temperature heating rate is accompanied: by essential increase of current value passing through the sample and expansion of bell form temperature interval in  $i(T)$  behavior which takes place up to ~250K at heating rate 10K/min.

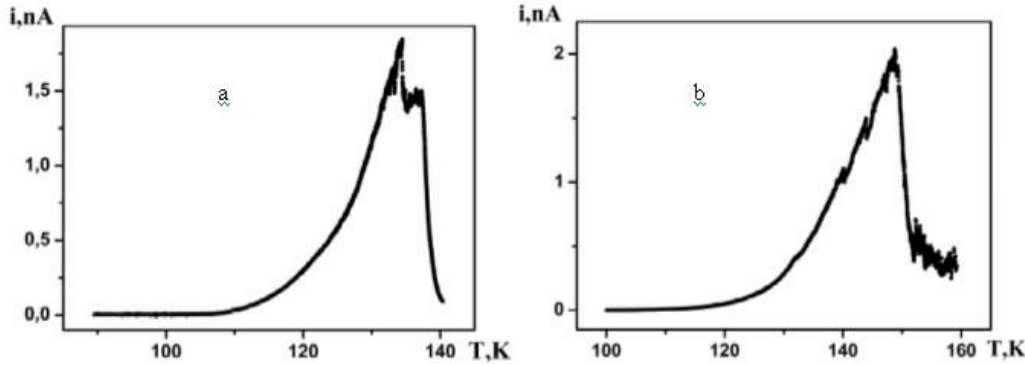


Fig.6. The same as on fig.4. Experimental curves  $i(T)$  curves are obtained at slow heating of initial sample with rates 0.1 K/min (a) and 0.2 K/min (b) at application of constant external potential 10V to the crystal.

The given experimental fact evidences about the fact that electro-transfer in TlGaSe<sub>2</sub> in the given “sensitive” temperature interval is defined not only by equilibrium electronic component, i.e. by carriers thermally activated from local levels in forbidden bands but by nonequilibrium component connected with formation of polarized state in crystal volume.

The experimental curves  $i(T)$  given on the fig.6 demonstrate the existence of relaxation effects more visually (of volume-charged polarization) in summary conductivity of TlGaSe<sub>2</sub>. From data of this figure it is seen that temperature dependences of current transfer in direction perpendicular to layers measured at super slow heating of initial sample with rates 0.1K/min and 0.2K/min endure the significant modifications in comparing with early presented data. The exponential growth of both curves of  $i(T)$  shown on the fig.6,a,b replaces by strong decrease of current value at achievement of temperature ~139K (fig.6,a) and ~148K (fig.6,b) that probably is caused by polarization processes (disappearance and/or formation of polarization charges) in the sample and their application on corresponding conductivity currents.

The current temperature dependence in the direction perpendicular to layers measured at initial crystal heating with rate 1K/min and application of small constant voltage

0,8V to the sample is presented on the fig.7,a. The intensity temperature dependence of monochromatic light passing through TlGaSe<sub>2</sub> crystal taken from publications [20, 21] is shown on the fig.7,b in the capacity of illustrations. The comparable analysis of these figures shows that  $i(T)$  curve up to small details makes the temperature dependence of transmission intensity. The detail consideration of fig.7,a allows us to emphasize some consistent temperature regions on  $i(T)$  curve: if current value in the interval ~ 80K ÷ 165K passing through the sample practically doesn't depend on temperature then interval ~ 165 K ÷ 200 K is characterized by the current value increase on the background of which the specific oscillations in  $i(T)$  behavior with quasi-period which is also equal to ~1min, are observed. The oscillating character  $i(T)$  is especially revealed in interval ~200K ÷ 220K which is characterized by the strong increase of amplitude of quasi-periodic current oscillations. The oscillating process isn't observed at temperatures higher than ~220K. The curve  $i(T)$  passes through maximum in this temperature interval, moreover maximal temperature corresponds to the point  $T \sim 242$ K.

The typical low-temperature VAC of initial sample obtained at direct (with increase of applied constant voltage) and reverse steps (with voltage decrease) with application of electric field along  $c$  axis is presented on the fig.8. It is seen

that the VAC ohmic region shifts to the region of lower voltages ( $\sim 10V$ ) with temperature decrease, moreover VAC curve is almost parallel to voltage axis in the region of critical voltage  $\sim 10V \div 30V$ , i.e it. has the form of *N*-shaped curve with the region of negative differential resistance (NDR). The

*N*-shaped characteristics are reversible ones, however the region of critical voltages at reverse step is less than at direct one. The current of VAC reverse branch is accompanied by hysteresis. VAC extrapolation to value  $i = 0$  gives the value of residual voltage  $\sim 30V$  on the sample.

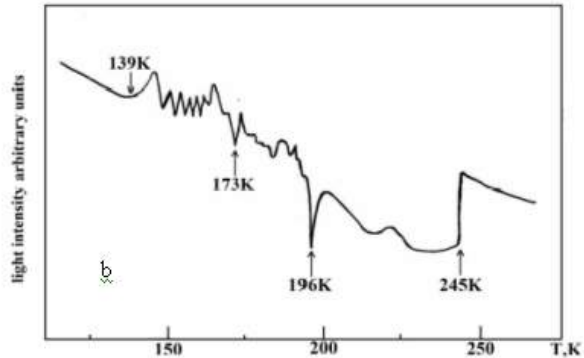
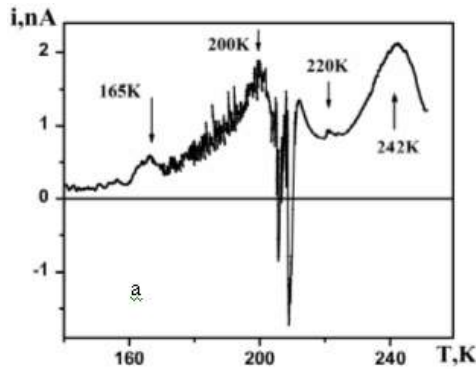


Fig.7. a: the same as on fig.4. Experimental curve  $i(T)$  is obtained at heating of initial sample with rate 0.1 K/min at application of small constant potential 8V to the crystal, b: intensity temperature dependence of monochromatic light passing through  $TlGaSe_2$  crystal taken from publications [20, 21]

Besides the current value have the tendency not to transform into zero at reverse step in the region of small voltages. VAC hysteretic peculiarity connected probably with formation and kinetic changes of nonequilibrium processes (internal electric fields connected with polarized state) in the investigated sample reminds the ferroelectric hysteretic curves of polarization dependence on applied voltage if the net current passing through the sample is taken as the displacement current.

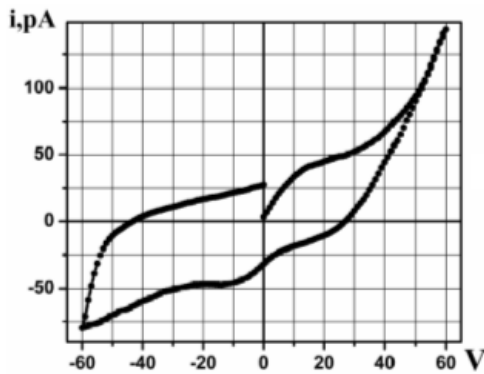


Fig.8. VAC obtained on initial sample with metallic contacts at temperature 113K. The change range of electric voltage  $-60V \div +60V$  applied to the sample changing with the step 1V for 1 second.

As it is known [58, 59] the relaxation effects in high-ohmic semiconductors connected with the presence of polarized charges in the crystal significantly depend on the influence of external effects of different types on the sample, sample pre-history before the measurements, temperature boundaries of sample heating in the previous measurement, cooling regime and etc. We carry out the investigation of dark current of  $TlGaSe_2$  initial sample previously cooled by the lighting (the light of quartz-halogen bulb with power 100W) from room temperature up to 77K (see fig.9). As it is seen from this figure, the form of  $i(T)$  curve endures the significant modifications in "sensitive" temperature interval  $\sim 160K \div 220K$  that is also caused by the polarization processes in the sample and their application on the corresponding currents of equilibrium conductivity.

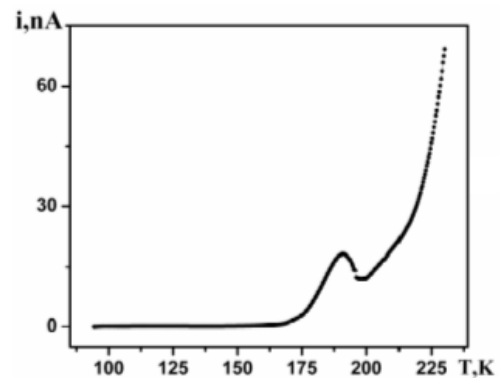


Fig.9. The same as on the fig.4. The curve  $i(T)$  is obtained in heating regime with rate 7K/min of initial sample  $TlGaSe_2$  preliminary cooled under light (the light of halogen bulb by power 100W) from room temperature up to 77K at application of external constant potential 7V.

Let's note that initial characteristics of the investigated crystal are totally restored after its short temporary keeping at room temperature during 10÷20 min.

It is known that [60] transport properties of high-ohmic semiconductors are defined not only by material volume, but by its near-electrode regions. We try to reveal the connection of above mentioned resistometric investigation results of  $TlGaSe_2$  processes with the ones on electrodes.

The curve form of dark current written in geometry which is perpendicular to the layers in the conditions when the external electric field on the sample is applied through block artificially created dielectric interstice carried out in the form of thin mica separator is shown on the fig.10. The given method allows us to avoid the undesirable surface and contact phenomenon presenting at conductivity measurements on usual technique with electrode application.

From the fig.10 it is seen that displacement current curve ( $i_{dis}(T)$ ) in the region of low temperatures reminds the temperature dependence of static dielectric constant of  $TlGaSe_2$  given in [24-28]: the small anomaly is observed in the bend form near  $\sim 98K$  and further the curve passes through maximum moreover the biggest value  $i_{dis}(T)$  is

achieved at temperature  $\sim 117\text{K}$  in PhT point into INC phase. Besides, the anomaly on  $i_{dis}(T)$  curve in the spiked peak form is observed near  $177\text{K}$  through “sandwich” mica – ample – mica, monotonously increases with temperature increase higher than  $\sim 180\text{K}$  that is probably caused by consistent inclusion of carriers from the corresponding deep levels in electric transition processes.

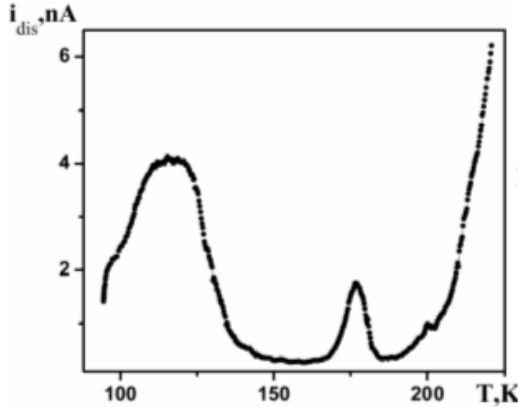


Fig.10. Temperature dependence of displacement current measured in the direction perpendicular to the layers of TlGaSe<sub>2</sub> sample with application of blocking mica separators. The data are obtained at temperature heating rate  $5\text{K/min}$  and external potential  $10\text{V}$  applied to crystal.

VAC are investigated on initial sample TlGaSe<sub>2</sub> isolated by mica separators in wide temperature interval (fig.11). We show many experimental data obtained by us (in spite of their variety) on the fig.11 as they are observed at first time.

Let's mention that there are the evidences of the fact that observable phenomena doesn't connect with any instrument phenomenon in measurement process.

VAC series obtained at two potential polarities in temperature interval  $80\text{K} \div 140\text{K}$  is shown on the fig.11. It is seen that linear VAC curve and symmetric in relation to polarity of applied electric static voltage one measured at  $T=80\text{K}$  (VAC saves the same form up to  $\sim 106\text{K}$ ) deforms at approximation to  $T_c$  and inside INC-phase. The position significantly changes in temperature interval  $145\text{K} \div 205\text{K}$  (fig. 11 b, c, d): VAC has the form of specific oscillations with multiple increase of current amplitude and becomes even in respect to applied electric field (i.e. the polarity change of external voltage isn't accompanied by the change current direction). The oscillation process isn't observed higher the temperature  $205\text{K}$  and at too high level of sample light (see fig.12,a).

Beginning from  $210\text{K}$  the current amplitude values on VAC curves strongly decrease; VAC form begins to take the linearity contours; the reverse branch appears on VAC curve. VAC at  $220\text{K}$  practically doesn't differ from VAC measured at  $80\text{K}$ . During experiments we reveal that current oscillations observable in the given temperature interval have the temporary character with quasi-period  $\sim 1\text{min}$ . The example of compatible record of current oscillations and time is shown on the fig.12,b.

Finally, the temperature dependence of pyroelectric current ( $i_p$ ) measured at in heating regime on investigated sample TlGaSe<sub>2</sub> isolated by mica separators in the direction perpendicular to layers.

It is seen that there are two clearly expressed maximums on  $(i_p)T$  curve: the one near temperature  $\sim 98\text{K}$ , the second one at temperature  $\sim 150\text{K}$ , moreover the extreme value of  $(i_p)T$  in the given points differ from each other in more than 1,5 times that is probably evidences about their different nature. The measurements  $(i_p)T$  carried out on TlGaSe<sub>2</sub> crystals lead to the results which significantly differ from data of figure 13 with application of usual electric contacts in the directions both perpendicular to the layers and along plane layers. In particular, only one clearly expressed peak near  $T_c$  [33] is observed on  $(i_p)T$  curve.

#### 4. The discussion of obtained results.

Thus, the obtained experimental facts during of present investigations can be summed by the following way:

1. The current transfer differs by unique contribution combinations from equilibrium conductivity component (mobile carriers of band type) and nonequilibrium processes connected with formation and change of polarized state (the conductivity from nonmobile or localized charge carriers) in the direction perpendicular to TlGaSe<sub>2</sub> sample layers in temperature interval  $120\text{K} \div 205\text{K}$ . The higher/lower the rate of sample temperature scanning or the less value of external electric field applied to the sample the stronger the deposit of volume-charged polarization in crystal sum electric conductivity reveals. Probably, the balance of the given contributions into kinetics electric charge transfer in TlGaSe<sub>2</sub> samples chosen from technological sets is very delicate and as the consequence the unusual form variety of temperature dependence resistivity curve [61-63] and its high sensitivity to the temperature change rate and value of external electric field are observed in practices instead expected Drude behavior.

2. The one more result obtained in the present work and enough rarely observed among different known semiconductor compounds [64] is connected with registration in TlGaSe<sub>2</sub> of current oscillations appearing probably because of electric instability taking place in crystal electron subsystem in temperature region  $140\text{K} \div 205\text{K}$ . The direct experimental evidence of the fact that the given oscillations aren't connected with carrier injections through contacts but are caused by crystal volume properties is given by the method of blocking electrode. The joint analysis of the figures 1, 2, 5, 7, 11 and 13 and also data presented in [10, 11, 16, 20-22, 43, 44] allows us to make the conclusion that observable peculiarities in temperature interval  $140\text{K} \div 205\text{K}$  have the one and the same nature and evidence the sample electric heterogeneity (conductivity heterogeneity in the volume) moreover the heterogeneity formation micro-mechanism and their topology are connected with nature of these layered compounds.

3. The data comparison of figures 1, 2, 4  $\div$  10 and 13 shows that direction of internal electric field of volume-charged polarization appearing in TlGaSe<sub>2</sub> samples in the direction perpendicular to layers is always reverse one to the external electric field applied to the crystal in the measurement process.

It is necessary to divide whole temperature interval of observable effects on three character regions for perception integrity of current transfer kinetics physical picture in the direction perpendicular to layers of layered crystals TlGaSe<sub>2</sub>:



the region of low temperatures up to  $\sim 140\text{K}$ , transition region  $\sim 140\text{K} < T < \sim 205\text{K}$  and high-temperature region  $T > \sim 205\text{K}$ .

The origin of current oscillations in temperature interval  $\sim 117\text{K} \div \sim 140\text{K}$  (see fig.4) can be connected with electron-thermal switching, i.e. with reverse sample switching from low-ohmic state into high-ohmic one the mechanism of which is considered in detail in [65, 66]. According to this theoretical model, any process accompanying by the conductivity decrease of semiconductor material with temperature increase should lead to non-linear VAC (of S- or N-type) and can cause the current instability.

Joule heating mechanism of semiconductor being near PhT on conductivity is considered in works [65, 66], however, it isn't excluded that increase of volume-charged polarization contribute into crystal electroconductivity (see fig. 5  $\div$  10) can be the alternative mechanism of NDR. The presence of strong electric field applied to semiconductor is the key point for realization of the given mechanism. Taking

into consideration the fact that current oscillations in the given temperature interval are observed only on  $\text{TiGaSe}_2$  sample with electric contacts from metal, then one can confirm that strong electric field concentrates in thin near-contact layer of investigated material. Such volume near-contact layer with significant distribution of near-electronic potential (more clearly with non-linear dependence of voltage drop along sample length) should influence on measurements of crystal capacity and electroconductivity (see fig.4-8).

Nowadays the detail quantitative analysis of instabilities (current oscillations on VAC) revealed by us in paraelectric temperature region far from PhT points  $\sim 140\text{K} < T < \sim 205\text{K}$  is difficult to carry out. By our opinion our results are the first experimental observation of such type effect in  $\text{TiGaSe}_2$ . Thus, here we give only some initial thoughts for future analysis of this phenomenon.

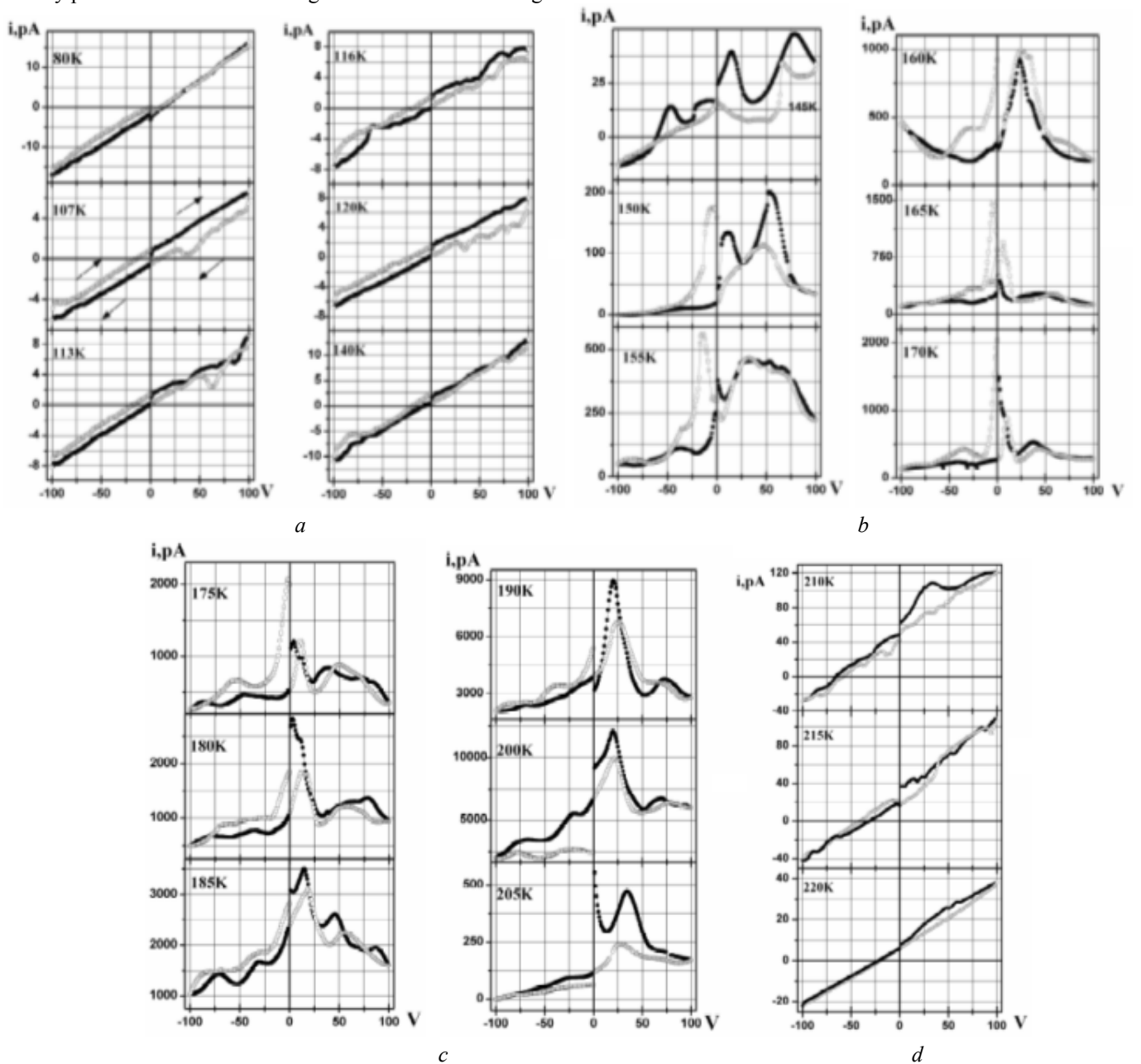


Fig. 11. VAC series obtained on  $\text{TiGaSe}_2$  sample isolated by mica separators in the direction perpendicular to the layers in temperature interval  $80\text{ K} \div 140\text{ K}$ . The change range of electric voltage applied to the sample is  $100\text{ V} \div +100\text{ V}$ , the step is  $1\text{ V}$  for  $1\text{ s}$ . The dark circles are  $0\text{ V} \div +100\text{ V}$ , light ones are  $+100\text{ V} \div 0\text{ V}$ , dark squares are  $0\text{ V} \div -100\text{ V}$ , light ones are  $100\text{ V} \div 0\text{ V}$ .

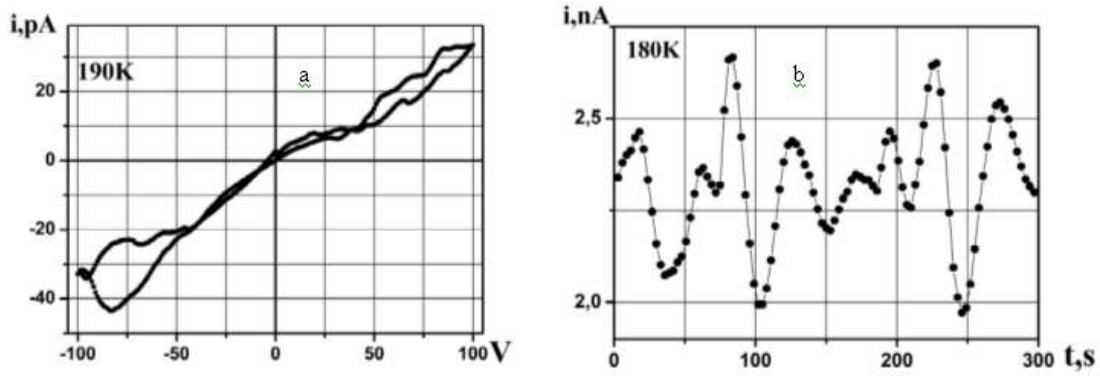


Fig.12. a) is VAC curve measured at sample light by the halogen bulb light by power 100W at temperature 190K; b) is example of recording of current oscillations in time. The curve is obtained at temperature 180K at constant potential 20V applied to sample.

The hypothesis of electronic PhT is the more logical one for interpretation of experimental data obtained by us. The investigated crystals TlGaSe<sub>2</sub> are resistively instable in the above mentioned temperature interval, probably because of change (or dominance) of one conductivity regime by other one (or under other one). By this reason it is profitable that the system transits into electrically heterogeneous state, i.e. “splits” on macroscopic regions – electric domains periodically alternating in the direction perpendicular to layers [64]. In our case, i.e. in the system having the layered structure the domains present themselves the plane condensators on opposite plane of which (domain walls) the charge carriers of opposite signs concentrate. The voltage between domain walls in such condensator domain model is defined by surface charge density on domain walls and the current is defined by charge quantity forming on walls in time unit. The bias current registered by non-contact method through the sample surface presents itself the algebraic sum of currents in domains. It isn’t excluded that directions of displacement currents in domains of different dimensions and geometries can differ in external electric field by both the value and direction. The displacement current dependence on voltage, i.e. VAC (see fig.11) at change of external electric field applied to the sample is caused by temporary bursts of volume charge on microcondensator plates.

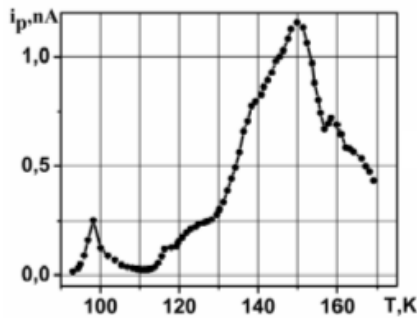


Fig.13. Temperature dependence of pyroelectric current measured in heating regime on investigated sample TlGaSe<sub>2</sub> isolated by mica separators in the direction perpendicular to layers.

The singular “dielectrization” of semiconductor system described above causes the many questions such as: the question about heterogeneity dimensions and typology of heterogeneous state; about nature and mechanisms leading

to heterogeneous state formation; about the role and interconnection of such state with low temperature structural PhT. However, it is important to note that electrically heterogeneous state or phase-splitting medium doesn’t lead to sample trivial chemical dividing of sample on phases. Under the phase we understand the homogeneous macroscopic regions (clusters) differing by carrier concentrations in the result of freezing (localization) of charge carrier part on distributed on impurity ions or defect accumulations. For example, according to [48] the peculiarity of technology of TlGaSe<sub>2</sub> layered crystal growth is the fact that there are always the defect accumulations in the form of volume inclusions of Se in their structure. In the case of investigated crystal the specific part of chargedly enriched phase (semiconductor) in the respect of chargedly depleted (dielectric) one depends on temperature and other external influences, that’s why current oscillations on VAC (see fig.11) have the strong temperature boundaries. It is obvious that the behavior of frequency dependences of dielectric constant and conductivity of TlGaSe<sub>2</sub> sample in temperature interval  $\sim 140K < T < \sim 205K$  ( see fig. 1 and 2) is the important argument for the benefit of the fact that the effect observed on fig.11 is caused by especially such scenario of electronic PhT semiconductor – dielectric type.

The consistent “switching” in electric transition processes of corresponding deep levels at  $T > \sim 205K$  is accompanied by destroy of electrically heterogeneous state in TlGaSe<sub>2</sub>. In the given temperature interval the contribution into sample electroconductivity gives only equilibrium impurity component and consequently, sample conductivity will have clear semiconductor behavior.

Let’s also note that similar fact on above mentioned process of phase splitting in TlGaSe<sub>2</sub> layered crystal in temperature interval  $\sim 150K > T > \sim 205K$  takes place in layered metal-oxide high-temperature supersemiconductors. As it is known, the superstructure and corresponding charge density modulation which is named charge density wave (CDW) [67, 68] form in many quasi-one-dimension supersemiconductors at temperature decrease in the result of Peierls instability in initial lattice. It is established that CDW fix on impurities and defects in real compounds, and conductivity in weak electric field is defined by electron-hole excitations through Peierls track. CDW influence on many thermodynamic parameters of superconducting materials in particular on thermal-expansion coefficient, heat capacity and etc because of strong electron-phonon bond (anomaly). In the next chapter it is shown that

temperature region  $\sim 140 \text{ K} < T < \sim 205 \text{ K}$  also characterizes by anomalous behavior of thermodynamic properties in  $\text{TiGaSe}_2$  layered crystal that is the evidence of electrically heterogeneous state deposit on crystal thermodynamic parameters.

### 5. The anomalies of thermal-expansion coefficients and elastic properties of $\text{TiGaSe}_2$ caused by nonequilibrium PhT in electron subsystem.

The temperature dependences of thermal-expansion coefficients in both directions perpendicular ( $\alpha_{\perp}$ ) and parallel to layer plane ( $\alpha_{\parallel}$ ) [10, 11] are investigated on crystals of triple compounds  $\text{TiGaSe}_2$  in wide temperature interval including the points of structural PhT. The investigations are carried out on optical interferometer (more detail see [10,11]). The corresponding curves  $\alpha_{\perp}(T)$  and  $\alpha_{\parallel}(T)$  are presented on fig.14. As it is seen from fig.14 the both curves have clearly expressed peculiarities in temperature interval  $\sim 120 \text{ K} \div \sim 240 \text{ K}$ . It is seen that monotonous step of  $\alpha_{\perp}(T)$  curve destroys at temperature  $\sim 240 \text{ K}$  where the small anomaly in the form of little step is observed in  $\alpha_{\perp}(T)$  behavior (the jump-like cancellation of sample length at its cooling takes place). Beginning from  $\sim 180 \text{ K}$  up to  $\sim 140 \text{ K}$   $\alpha_{\perp}(T)$  it anomalously increases with temperature decrease and below  $\sim 140 \text{ K}$  endures the significant changes moreover maximal value of  $\alpha_{\perp}(T)$  achieves in PhT point in INC-phase at  $T_i \sim 120 \text{ K}$ . From the fig.14 it is seen that  $\alpha_{\parallel}(T)$  dependence has the anomalous behavior in temperature interval  $\sim 120 \text{ K} \div 180 \text{ K}$ : beginning from  $\sim 180 \text{ K}$   $\alpha_{\parallel}(T)$  decreases with temperature decrease and below  $\sim 140 \text{ K}$   $\alpha_{\parallel}(T) = (dL/dT)/L < 0$  (the jump increase of sample length along layer plane takes place). The peak value of  $\alpha_{\parallel}(T)$  curve also falls on PhT point in INC-phase at  $T_i \sim 120 \text{ K}$  (as behavior of  $\alpha_{\perp}(T)$  and  $\alpha_{\parallel}(T)$  curves in the temperature region below  $T_i$  aren't shown on the fig.14, let's note only the fact that  $\alpha_{\perp}(T)$  and  $\alpha_{\parallel}(T)$  anomalies near  $T_i$  have  $\lambda$ -shaped character).

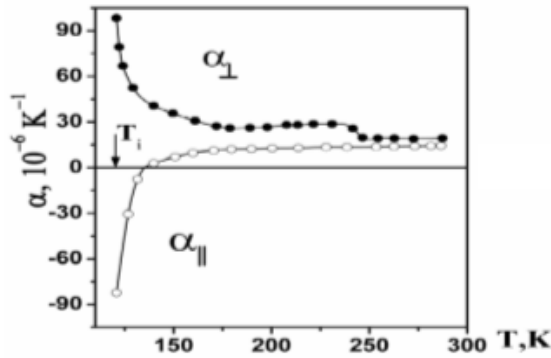


Fig.14. Temperature dependences of thermal-expansion coefficients in directions perpendicular ( $\alpha_{\perp}$ ) and parallel ( $\alpha_{\parallel}$ ) to  $\text{TiGaSe}_2$  layer plane. The data of figure corresponds to [10, 11, 16].

The temperature dependence of effective Young's module measured in ref [16] also endures the significant changes in the above mentioned temperature interval  $\sim 140 \text{ K} \div \sim 220 \text{ K}$ , i.e. in paraelectric phase far from structural PhT points, moreover the points of structural PhT on Young's module curve reveal in the form of character maximums at  $T_i \sim 120 \text{ K}$  and  $T_c \sim 110 \text{ K}$ . The nontrivial

character of temperature dependence of thermal-expansion coefficients  $\alpha_{\perp}(T)$  and  $\alpha_{\parallel}$  of  $\text{TiGaSe}_2$  described above is explained by the fact that PhT consistency exists in crystal structure. But many questions don't have the answers. For example, why the anomalous behavior of  $\alpha_{\perp}(T)$  and  $\alpha_{\parallel}(T)$  in cooling process begins in paraelectric phase far from structural PhT points or why the peak values of  $\alpha_{\perp}(T)$  and  $\alpha_{\parallel}(T)$  of investigated substance coincide with PhT point in INC-phase in spite of conclusions of conventional phenomenological theories [69, 70], though the given anomalies should take place near  $T_c$ ? Finally, the main question arises according to new experimental results above mentioned: what is interconnection of electric instabilities observed in temperature region  $\sim 140 \text{ K} \div \sim 205 \text{ K}$  with described peculiarities of thermal expansion.

Let's see on the fig.14. It is obvious that both curves  $\alpha_{\perp}(T)$  and  $\alpha_{\parallel}(T)$  endure the critical behavior at approach to  $\sim 120 \text{ K}$  that isn't expected in the experiment if point  $\sim 120 \text{ K}$  were only PhT temperature in INC-phase [69, 70]. Let's try to explain the anomalous behavior of  $\alpha_{\perp}(T)$  and  $\alpha_{\parallel}(T)$  in temperature interval  $\sim 120 \text{ K} \div \sim 220 \text{ K}$  on the base of other model. Let's base on quasi-harmonic model of crystal thermal expansion of hexagonal symmetry ( $\text{TiGaSe}_2$  structure with good approximation can be considered as quasi-hexagonal because of physical properties of  $\text{TiGaSe}_2$  don't reveal the anisotropy in layer plane [15, 16]). Besides, let's suppose the weak anisotropy of phonone spectrum and consider  $\gamma_{\perp} \approx \gamma_{\parallel}$  ( $\gamma$  are Grunaisen parameters) that is totally acceptable from the point of view of having data about phonon spectrums of these compounds [72, 73]. In this case the formulas for  $\alpha_{\perp}$  and  $\alpha_{\parallel}$  calculations [74] strongly simplify and have the form:

$$\alpha_{\perp} \approx \frac{C}{V} \gamma \frac{C_{11} + C_{12} - 2C_{13}}{(C_{11} + C_{12}) \cdot C_{33} - 2C_{13}^2}$$

and

$$\alpha_{\parallel} \approx \frac{C}{V} \gamma \frac{C_{33} - C_{13}}{(C_{11} + C_{12}) \cdot C_{33} - 2C_{13}^2}$$

Here,  $C$  is heat capacity,  $V$  is molar volume,  $C_{ik}$  are elastic constants. It is obvious that thermal expansion anomalies given on fig.14 can't be caused by specific behavior of heat capacity or  $\gamma$ . We suppose the temperature dependences of elastic modules  $\text{TiGaSe}_2$  in particular the nontrivial temperature behavior of elastic constant  $C_{13}$  are responsible for special behavior of  $\alpha_{\perp}(T)$  and  $\alpha_{\parallel}(T)$  in temperature interval  $\sim 120 \text{ K} \div \sim 220 \text{ K}$ . The joint analysis of experimental results obtained by investigation of temperature dependences of elastic constants  $C_{11}$ ,  $C_{12}$ ,  $C_{33}$  and effective Young's modulus [15, 16] of  $\text{TiGaSe}_2$  allows to authors of the present work to make conclusion about unusual strong temperature dependence of coefficient of elasticity  $C_{13}$  in temperature interval  $\sim 120 \text{ K} \div \sim 220 \text{ K}$ , moreover the enough strong increase with temperature decrease beginning from  $\sim 220 \text{ K}$  up to  $\sim 140 \text{ K}$  with small change of inclination  $\sim 180 \text{ K}$  should be observed in behavior of  $C_{13}(T)$  constant. The dependences of elastic compliances on value of coefficient of elasticity  $C_{13}$  are given on the fig.15 (taking into consideration the data [15, 16]).



$$S_{zz} = \frac{C_{11} + C_{12} - 2C_{13}}{(C_{11} + C_{12}) \cdot C_{33} - 2C_{13}^2}$$

and

$$S_{xx} = \frac{C_{33} - C_{13}}{(C_{11} + C_{12}) \cdot C_{33} - 2C_{13}^2}$$

As it is seen from this figure the behavior of elastic compliances  $S_{xx}$  and  $S_{zz}$  with increase of elastic constant  $C_{13}$  with accuracy corresponds to anomalous temperature behavior of  $\alpha_{\perp}(T)$  and  $\alpha_{\parallel}(T)$  curves in the interval  $\sim 120\text{K} \div \sim 220\text{K}$ .

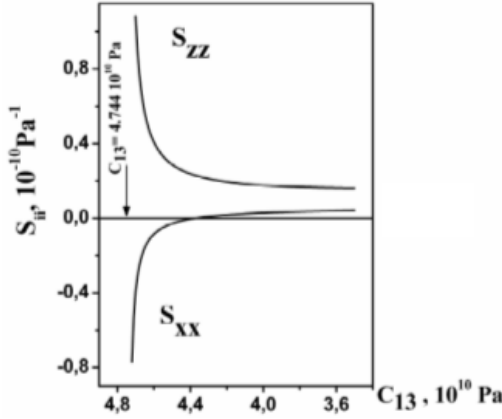


Fig.15. The dependences of elastic compliances  $S_{xx}$  and  $S_{zz}$  on the coefficient of elasticity value  $C_{13}$ . The arrow on the figure corresponds to numerical value  $C_{13} = 4,744 \cdot 10^{10}$  Pa defining the boundary of mechanical stability of TiGaSe<sub>2</sub> layered crystal.

As it is known [71] the mechanical stability of crystal lattice meaning its stability in relation to small homogeneous deformations is defined from generalized criterion of Born stability. According to this criterion at the given temperature all determinants of main matrix minors  $C_{ij}$  ( $i, j = 1, \dots, 6$ ) of isothermal modules of crystal elasticity in the Fogt designations should be positively defined. Born criterion of mechanical stability for hexagonal crystal includes the conditions:  $C_{44} > 0$ ;  $C_{11} > |C_{12}|$ ;  $(C_{11} + C_{12}) \cdot C_{33} > 2C_{13}^2$ ;  $C_{66} > 0$ . The theoretical estimations carried out by the attraction of experimental data [15, 16] show that the stability condition  $(C_{11} + C_{12}) \cdot C_{33} > 2C_{13}^2$  destroys at coefficient of elasticity module  $C_{13} = 4,744 \cdot 10^{10}$  Pa, consequently, this value  $C_{13}$  defines the boundary of mechanical stability of layered crystal TiGaSe<sub>2</sub> (the found boundary of crystal mechanical stability by Born is shown on fig.15 by the arrow). As it is seen from the fig.15 the numerical value of  $C_{13}$  corresponding to the boundary of crystal mechanical stability is such one that allows us to describe all main peculiarities in behavior of  $\alpha_{\perp}(T)$  and  $\alpha_{\parallel}(T)$ . Thus, the given circumstance shows on the fact that especially the increase of elastic constant  $C_{13}$  (but not PhT in INC-phase at  $T_i \sim 120$  K) with temperature decrease causes the anomalous temperature behavior of  $\alpha_{\perp}(T)$  and  $\alpha_{\parallel}(T)$  curves in paraelectric phase far from structural PhT points. The closeness of  $C_{13}$  to critical value at which the condition of crystal mechanical stability destroys is the precursor of low-temperature PhT in these compounds totally proving the earlier made conclusions [16]

about importance of coefficient of elasticity modulus role  $C_{13}$  in the nature of phase transformations in TiGaSe<sub>2</sub>.

The effects of negative thermal expansion similar to described above for TiGaSe<sub>2</sub> are observed in many layered metal-oxide high-temperature supersemiconductors [75]. The direct experiment evidence of the fact that anomalies of thermal expansion of high-temperature semiconductors have the electron nature and are connected with WCD (so-called charge on bonds) is given in present scientific works.

Taking into consideration the fact that temperature interval in which the peculiarities in the behavior of thermal-expansion coefficients of layered crystal TiGaSe<sub>2</sub> are observed, coincides with temperature region of electric instability appearance in this compound and also the absence of any macroscopic structural changes in this temperature interval, one can conclude that the instability in electronic subsystem of investigated crystal is the peculiarity of unusual transport, heat, elastic, spectroscopic [43, 44], optical [20-22] and other physical properties of TiGaSe<sub>2</sub> in temperature interval  $\sim 140\text{K} < T < \sim 205\text{K}$ . The last one means that anomalous increase of elastic constant  $C_{13}(T)$  and peculiarities in  $\alpha_{\perp}(T)$  and  $\alpha_{\parallel}(T)$  behaviors connected with it in the given temperature interval is defined by the contribution of electronic subsystem but not by crystal lattice anharmonicity. Let's note that as  $C_{13}$  is "interlayer elastic" constant, then it is the more sensitive to internal electric fields directed perpendicular to TiGaSe<sub>2</sub> crystal layers.

Thus, one can confirm that formation and dynamics of electric domains appearing because of electric instability considered as inequilibrium PhT in crystal electronic subsystem of TiGaSe<sub>2</sub> in temperature interval  $\sim 140\text{K} < T < \sim 205\text{K}$  because of strong interaction by crystal electron and elastic subsystem is accompanied by the appearance of internal fields of elastic deformations in TiGaSe<sub>2</sub> structure, moreover only such components of internal stress tensor are not equal to zero, which have non-zero projections in the direction perpendicular to plane of crystal layers. The long-distance field of elastic determinations formed by these fields are similar to electrostrictive fields in crystals. The electrostriction overlapping on  $T_c$  phonon part of thermal-expansion coefficient leads to anomalies in  $\alpha_{\perp}(T)$  and  $\alpha_{\parallel}(T)$  above described behaviors.

As the concurrence of two mechanisms of thermal-expansion coefficients, which are "charge" component and atomic anharmonicity, exists in real crystal TiGaSe<sub>2</sub> in temperature interval  $\sim 140\text{K} < T < \sim 205\text{K}$  then the unique possibility to strengthen or weaken "charge" component of thermal expansion appears in this crystal because of external influence on internal electric fields and to influence on lattice stability of TiGaSe<sub>2</sub> and anomaly form (suppress or strengthen) on  $\alpha_{\perp}(T)$  and  $\alpha_{\parallel}(T)$  curves. From this point of view, the layered crystal TiGaSe<sub>2</sub> is the fine model medium not only for study of appearance mechanisms, development of electric instabilities and their revealing in behavior of different crystal physical parameters, but for control of such crystal fundamental characteristics as thermal-expansion coefficients, transport and optical properties.

## 6. Conclusion.

Thus, in the present work the unusual transport properties of layered crystal of TiGaSe<sub>2</sub> in the direction perpendicular to the layers in temperature interval  $\sim 140\text{K} < T < \sim 205\text{K}$  are discussed in effective medium model appearing as the

consequence of PhT semiconductor – dielectric in crystal electronic subsystem and presenting itself the crystal inclusion regions with dielectric properties in semiconductor matrix (phase splitting). The electric instability observable in these samples because of strong electron-phonon bond

reveals by the anomalous behavior of thermal expansion and elastic properties of TlGaSe<sub>2</sub> in paraelectric phase, i.e. in temperature interval which are far from structural PhT points in this crystal.

- [1] *V.D.Muller, H.Hahn. Z. Anorg.Allg.Chem.* 438, 258, 1978.
- [2] *H.Hahn, B.Wellmann. J.Naturwissenschaften* 54, 42, 1967.
- [3] *T.J.Isaacs, J.D.Feichtner. J.Solid State Chem.* 14, 260, 1975.
- [4] *T.J.Isaacs. J.Appl.Crystallogr.* 6, 413, 1973.
- [5] *S.Kashida, Y.Kobayashi. J. Korean Phys. Soc.* 32, S 40, 1998.
- [6] *G.D.Guseinov, A.M.Ramazanade, E.M.Kerimova, M.Z.Ismailov. Phys.Stat.Sol.* 22, K 117, 1967.
- [7] *G.E.Delgado, A.J.MoraI, F.V.Perez, J.Gonzalez. Cryst. Res. Technol.* 42, 663, 2007.
- [8] *D.F. Mc.Moorrow, R.A.Cowley, P.D.Hatton, J.Banys. J.Phys.: Condens. Matter* 2, 3699, 1990.
- [9] *E.S. Krupnikov, F.Yu. Aliyev. FTT.* 30, 3158, 1988. (in Russian).
- [10] *N.A. Abdullayev, T.G. Mamedov, R.A. Suleymanov. FNT,* 27, 915, 2001. (in Russian).
- [11] *N.A.Abdullayev, T.G. Mammadov, R.A. Suleymanov. Phys.Stat.Sol.(b)* 242, 983, 2005.
- [12] *S.G. Abdullayeva, A.M. Abdullayev, K.K. Mamedov, N.T. Mamedov. FTT,* 26, 618, 1984. (in Russian).
- [13] *M.A.Aldzhanov, N.G.Guseinov, Z.N.Mamedov. Phys. Stat. Sol.(a)* 100, K 145, 1987.
- [14] *O.B. Plyush, A.U. Sheleg. Kristallographiya.* 44, 873 1999. (in Russian).
- [15] *Yu.V. Ilisavskiy, V.M. Sternin, R.A. Suleymanov, F.M. Salayev, M.Yu. Seidov. FTT,* 33, 104, 1991. (in Russian).
- [16] *R.A. Suleymanov, M.Yu. Seyidov, F.M. Salayev. FTT,* 33, 1797, 1991. (in Russian).
- [17] *Yu.G. Gololobov, V.P. Perga, I.N. Salivonov, E.E. Shigol. FTT,* 34, 115, 1992. (in Russian).
- [18] *Yu.P. Gololobov, I.N. Salivonov. FTT,* 33, 298, 1991. (in Russian).
- [19] *H.D.Hochheimer, E.Gmelin, W.Bauhofer, Ch von Schnering-Schwarz, H.G.von Schnering, J.Ihringer. W. Appel, Zeitschrift fur Physik B-Condensed Matter* 73, 257 (1988)
- [20] *S.G. Abdullayeva, N.T. Mamedov, Sh.S. Mamedov, F.A. Mustafayev. Neorg. Mat.* 25, 35, 1989. (in Russian).
- [21] *S.G. Abdullayeva, N.T. Mamedov, Sh.S. Mamedov, F.A. Mustafayev. FTT,* 29, 3147, 1987. (in Russian).
- [22] *N.Yamamoto, N.Mamedov, T.Shinohara. J. Crystal Growth* 237, 2023, 2002.
- [23] *K.R. Allakhverdiyev, N.D. Akhmedzade, T.G. Mamedov, T.S. Mamedov, M.Yu. Seidov. FNT,* 26, 76 2000. (in Russian).
- [24] *V. P.Aliyev, S.S.Babayev, T.G.Mammadov, M.Yu.Seyidov, R.A.Suleymanov. Sol. St. Comm.* 128, 25, 2003.
- [25] *F.A.Mikhailov, E.Basaran, E.Senturk, L.Tumbek, T.G.Mammadov, V.P.Aliev. Phase Transitions* 76, 1057, 2003.
- [26] *F.A.Mikhailov, E.Basaran, E.Senturk, L.Tumbek, T.G.Mammadov, V.P.Aliev. Sol. St. Comm.* 129, 761, 2004.
- [27] *F.A.Mikhailov, E.Senturk, L.Tumbek, T.G.Mammadov, T.S.Mammadov. Phase Transitions* 78, 413. 2005.
- [28] *F.A.Mikhailov, E.Basaran, E.Senturk, L.Tumbek, T.G.Mammadov. Journal of Non-Crystalline Solids* 351, 2809, 2005.
- [29] *R.M.Sardarly, O.A.Samedov, I.Sh.Sadikov, E.I. Mordukhaeva, T.A.Gabibov. Sol. St. Comm.* 77, 453, 1991.
- [30] *Yu. Banis, A.Brilingas, I.Grigas, G. Guseynov. FTT* 29, 3324, 1987. (in Russian).
- [31] *A.K. Abiyev, N.A. Bakhishov, A.E. Bakhishov, M.S. Gadjiyev. Izvestiya vuzov. Fizika.* 12, 84, 1989. (in Russian).
- [32] *S.S.Babaev, E.Basaran, T.G.Mammadov, F.A.Mikhailov, F.M.Salehli, M-H.Yu. Seyidov, R.A.Suleymanov. J.Phys.: Condens. Matter* 17, 1985 (2005)
- [33] *M.Yu. Seyidov, R.A. Suleymanov, R.Khamoyev. FTT.* 48, 1270, 2006. (in Russian).
- [34] *S.P. Gabuda, S.G. Kozlova, N.T. Mamedov, N.K. Moroz. FTT,* 32, 1708, 1990. (in Russian).
- [35] *A.M. Panich, D.C. Ailion, S. Kashida, N. Gasanly. Phys. Rev. B* 69, 245319, 2004.
- [36] *F.A.Mikhailov, B.Z.Rameev, S.Kazan, F.Yildiz, T.G.Mammadov, B.Aktas. Sol. St. Comm.* 133, 389, 2005.
- [37] *N.I. Agladze, B.P. Antonyuk, V.M. Burlakov, E.A. Vinogradov, G.N. Jijin. FTT,* 23, 3289, 1981. (in Russian).
- [38] *Yu.I.Durnev, B.S.Kulbuzhev, A.U.Malsagov, L.M.Rabkin, V.I.Torgashev, Yu.I.Yuzyk. Phys. Stat. Sol. (b)* 153, 517, 1989.
- [39] *Yu.G.Goncharov, G.V.Kozlov, B.S.Kulbuzhev, V.B.Shirokov, V.I.Torgashev, A.A.Volkov, Yu.I.Yuzyk. Phys. Stat. Sol. (b)* 153, 529, 1989.
- [40] *V.M. Burlakov, S.Nurov, A.P. Ryabov. FTT,* 30, 3616, 1988. (in Russian).
- [41] *V.M.Burlakov, M.R. Yahkeev. Phys. Stat. Sol. (b),* 151, 337, 1989.
- [42] *A.A.Volkov, Yu.G.Goncharov, G.V.Kozlov, V.I.Torgashev, V.B. Shirokov. FTT,* 30, 3621, 1988. (in Russian).
- [43] *A.A. Volkov, Yu.G. Goncharov, G.V.Kozlov, S.P. Lebedev, A.M. Prokhorov, R.A. Aliyev, K.R. Allakhverdiyev. Pisma v JETF,* 37, 517, 1983. (in Russian).
- [44] *A.A. Volkov, Yu.G. Goncharov, G.V. Kozlov, R.M. Sardarli. Pisma v JETF,* 39, 293, 1984. (in Russian).
- [45] *B.R. Gadjiyev, Kh.M. Pashayev. FNT,* 17, 644, 1991. (in Russian).
- [46] *B.R. Gadjiyev. FNT,* 17, 889, 1991. (in Russian).
- [47] *F.A.Mikhailov, E.Basaran, T.G.Mammadov, M.Yu.Seyidov, E.Senturk. Physica B* 334, 13, 2003.
- [48] *S.G. Abdullayeva, V.A.Aliyev, N.T. Mamedov, M.K. Sheynmak. FTP.* 17, 1787, 1983. (in Russian).

- [49] S.G.Abdullaeva, V.A.Aliev. Phys.Stat.Sol.(a) 69, K33, 1982.
- [50] Yu.Yu. Kopayev, V.V. Tutushev. Pisma v JETF, 41, 320, 1985. (in Russian).
- [51] B. R.Gadjiev. Ferroelectrics 291, 111, 2003.
- [52] V.A. Golovko, A.P. Levanyuk. JETF, 77, 1556, 1979. (in Russian).
- [53] V.A. Golovko, A.P. Levanyuk. JETF, 81, 2296, 1981. (in Russian).
- [54] V.A. Golovko, A.P. Levanyuk. Pisma v JETF, 32, 104, 1980. (in Russian).
- [55] V.A.Golovko, A.P.Levanyuk. Ferroelectrics 26, 699 (1980)
- [56] M.Yu.Seyidov, Y.Sahin, M H.Aslan, R.A.Suleymanov. Semicond. Sci. Technol. 21, 1633, 2006.
- [57] M.Yu.Seyidov, Y.Sahin, D.Erbahar, R.A.Suleymanov. Phys. Stat. Sol. (a) 203, 3781 (2006)
- [58] V.M. Fridkin. Segnetoelektriki-poluprovodniki. M. 1976. 408 c. (in Russian).
- [59] V.M. Fridkin. Fotosegnetoelektriki. M. 1979. 284 c. (in Russian).
- [60] R. A.Smith. Semiconductors. Cambridge. 1978. 561 p.
- [61] I.A. Karpovech, A.A. Chernova, L.I. Demidova, E.I. Leonov, V.M. Orlov. Neorg. Mater., 8, 70, 1972. (in Russian).
- [62] V.A.Aliev,E.F.Bagirzade, N.Z.Gasanov, G.D.Guseinov. Phys. Stat.Sol.(a) 102, K109 (1987)
- [63] S.N. Mustafayeva, V.A. Aliyev, M.M. Asadov. FTT, 40, 48, 1998. (in Russian).
- [64] A.Neumann. Appl. Phys. Rev. 90, 1 (2001)
- [65] E.A. Lebedev, M.Ya. Goykhman, K.D. Cendin, I.V. Podeshvo, I.E. Terukov, V.V. Kudryavcev. FTP. 38, 1115, 2004. (in Russian).
- [66] K.D. Cendin, E.A. Lebedev, A.B. Shmelkin. FTT, 47, 427, 2005. (in Russian).
- [67] L.I. Bulayevskiy. UFN, 115, 263, 1975. (in Russian).
- [68] L.I. Bulayevskiy. UFN, 116, 449, 1975. (in Russian).
- [69] Incommensurate Phase in Dielectrics I. Fundaments / R.Blin, A.P.Levanyuk (ed.). North Holland, Amsterdam, 1986.
- [70] H.Z.Cummins. Physics Reports 185, 211, 1990.
- [71] M.Born, K.Huang. Dynamical theory of crystal lattices. Oxford, 1964, 489 p.
- [72] K.R.Allakhverdiev, T.G.Mammadov, R.A.Suleymanov, N. Z.Gasanov. J. Phys. Condens. Matter 15, 1291, 2003.
- [73] T.G. Mamedov, R.S. Suleymanov. FTT, 45, 2141, 2003. (in Russian).
- [74] N.A.Abdullaev, K.R.Allakhverdiev, G.L.Belenkii, T.G.Mamedov, R.A.Suleymanov, Y.N.Sharifov .Sol.St.Comm. 53, 601, 1985.
- [75] A.I. Golovashkin, A.P. Rusakov. FTT, 49, 1363, 2007. (in Russian).

**M.Yu. Seyidov, R.A. Süleymanov, T.Q. Məmmədov, R.A. Xamoyev**

### **TiGaSe<sub>2</sub> – PAYERLS DİELEKTRİKİ**

Laylı TiGaSe<sub>2</sub> segnetoelektrik-yarımkeçirici kristalda dielektrik nüfuzluğunun ( $\epsilon$ ), qaranlıq və piroelektrik cərəyanlarının temperatur asılılıqları və həmçinin 77-300K temperatur intervalında stabil temperaturlarda volt-ampere xarakteristikaları və qaranlıq cərəyanının zamana görə dəyişməsi tədqiq edilmişdir. Kiçik tezliklərdə laylara perpendikulyar istiqamətdə ölçülən  $\epsilon(T)$  əyrisində ilk dəfə olaraq 150K və 200K temperaturlarla sərhədlənən “çökük” formalı anomaliya müşahidə olunmuşdur. Həmçinin ilk dəfə təcrübə olaraq 145-205K temperatur intervalı ilə məhdudlanan nümunənin volt-ampere xarakteristikasında cərəyanın alçaq tezlikli kvaziperiodik rəqsləri şəklində müşahidə olunan elektrik qeyri-tarazlıqlarının təkamülü qeydə alınmışdır. Cərəyan qeyri-tarazlıqlarının zaman xarakteri müəyyən edilmişdir. Bu qeyri-tarazlıqların müşahidə olunması üçün elektrik sahəsinin nümunəyə verilməsi kontaktsiz, nazik lövhə şəkilli slyüdədən hazırlanmış potensialötürən elektrodlar vasitəsilə verilməsinin vacibliyi göstərilmişdir. Qeyri-tarazlıqların təbiəti və onun laylı TiGaSe<sub>2</sub> kristalının müxtəlif fiziki parametrlərinə təsiri öyrənilmişdir.

**М.Ю. Сеидов, Р.А. Сулейманов, Т.Г. Мамедов, Р.А. Хамоев**

### **TiGaSe<sub>2</sub> – ПАЙЕРЛСОВСКИЙ ДИЭЛЕКТРИК**

В работе представлены результаты исследований температурных зависимостей диэлектрической проницаемости ( $\epsilon$ ), темнового и пироэлектрического токов, а также вольт-амперные характеристики и временные эволюции темнового тока слоистого сегнетоэлектрика-полупроводника TiGaSe<sub>2</sub>, полученные при фиксированных температурах в интервале 77K ÷ 300K. На кривой  $\epsilon(T)$ , измеренной в направлении перпендикулярном к слоям, в области низких часто впервые обнаружена ярко выраженная аномалия в виде “ям”, с визуально заметными температурными границами ~ 150K и ~ 200K. Также впервые экспериментально зафиксировано развитие электрических неустойчивостей, проявляющихся в виде низкочастотных квазипериодических колебаний тока на вольт-амперных характеристиках образца в строго ограниченном температурном интервале 145K ÷ 205K. Установлен временной характер токовых неустойчивостей. Показано, что для наблюдения указанных неустойчивостей важно, чтобы электрическое поле к образцу подавалось посредством бесконтактных, потенциалоподающих электродов, выполненных в виде тонких прокладок из слюды. Обсуждается природа неустойчивости и её влияние на различные физические параметры слоистого кристалла TiGaSe<sub>2</sub>.

Received: 10.09.08